STATE OF CALIFORNIA • DEPARTMENT OF TRANSPORTATION
TECHNICAL REPORT DOCUMENTATION PAGE
TR-0003 (REV 04/2024)

1. REPORT NUMBER	2. GOVERNMENT ASSOCIATION NUMBER	3. RECIPIENT'S CATALOG NUMBER
CA24-3684		

4. TITLE AND SUBTITLE	5. REPORT DATE
Second-Order Effects on the Design of Slender Reinforced Concrete Bridge Columns	October 1, 2024
	6. PERFORMING ORGANIZATION CODE OSU, UTK

7. AUTHOR	8. PERFORMING ORGANIZATION REPORT NO.
Mark D. Denavit, Javad Esmaeelpour, Michael H. Scott, Minjie Zhu	None

9. PERFORMING ORGANIZATION NAME AND ADDRESS	10. WORK UNIT NUMBER
Oregon State University, School of Civil and Construction Engineering, 101 Kearney Hall, 1491 SW Campus Way, Corvallis, OR 97331 University of Tennessee, Department of Civil and Environmental Engineering, 325 John D. Tickle Engineering Building, 851 Neyland Drive, Knoxville, TN 37996-2313	
	11. CONTRACT OR GRANT NUMBER 65A0774 TO 004

12. SPONSORING AGENCY AND ADDRESS	13. TYPE OF REPORT AND PERIOD COVERED
California Department of Transportation Division of Engineering Services 1801 30th Street, MS #9-2/5i Sacramento, CA 95816	Final Report
	14. SPONSORING AGENCY CODE

15. SUPPLEMENTARY NOTES
Prepared in cooperation with the State of California Department of Transportation

16. ABSTRACT
The AASHTO LRFD Bridge Design Specifications (AASHTO, 2017), hereafter referred to as AASHTO LRFD, includes an approximate method for the design of slender RC bridge columns. This approximate method, the method most commonly used by bridge engineers, was adapted from building design codes such as the ACI Building Code Requirements for Structural Concrete (ACI,2019), hereafter referred to as ACI 318. Accordingly, the AASHTO LRFD approximate method applies to a specific range of parameters and configurations based on floor framing stiffness, building story heights, and material properties and reinforcing ratios common to buildings. While some analogies carry over to bridge columns, the superstructure stiffness and unbraced column lengths can be quite different for bridge systems compared to buildings. The assumptions built into the approximate AASHTO LRFD method can lead to unsafe bridges in some cases and inefficient designs that are more costly than necessary in other cases.

The purpose of this research is to develop improved guidelines for the efficient design of slender RC bridge columns using the approximate method (moment magnification) and the refined method(second-order analysis). This work evaluates the AASHTO LRFD approximate moment magnification method against advanced second-order inelastic analyses. Parametric studies were conducted on single column models and common Caltrans bridge types. The impact of major parameters,e.g., slenderness, out-of-plumbness, and superstructure stiffness, on structural response according to both the approximate method and advanced analysis were quantified. Refinements to the approximate method were developed in cases where these methods differ substantially. This work provides the guidance necessary for engineers to make justifiable decisions with confidence when designing slender RC columns. The increased accuracy will result in more efficient, cost-effective designs while maintaining safety.

17. KEY WORDS	18. DISTRIBUTION STATEMENT
Reinforced concrete, Stability, Moment Magnification, Nonlinear analysis, Creep and shrinkage, Effective flexural rigidity	No restrictions

19. SECURITY CLASSIFICATION (of this report)	20. NUMBER OF PAGES	21. COST OF REPORT CHARGED
None	154	

Reproduction of completed page authorized.

DISCLAIMER STATEMENT

This document is disseminated in the interest of information exchange. The contents of this report reflect the views of the authors who are responsible for the facts and accuracy of the data presented herein. The contents do not necessarily reflect the official views or policies of the State of California or the Federal Highway Administration. This publication does not constitute a standard, specification or regulation. This report does not constitute an endorsement by the Department of any product described herein.

For individuals with sensory disabilities, this document is available in alternate formats. For information, call (916) 654-8899, TTY 711, or write to California Department of Transportation, Division of Research, Innovation and System Information, MS-83, P.O. Box 942873, Sacramento, CA 94273-0001.

Second-Order Effects on the Design of Slender Reinforced Concrete Bridge Columns: Final Report

Mark D. Denavit[1], Javad Esmaeelpour[1], Michael H. Scott[2], Minjie Zhu[2]

Revision 0: December 22, 2023
Revision 1: February 29, 2024
Revision 2: May 14, 2024
Revision 3: July 31, 2024
Revision 4: October 1, 2024

[1]University of Tennessee
[2]Oregon State University

Contents

List of Abbreviations

AASHTO   The American Association of State Highway and Transportation Officials

ACI   American Concrete Institute

CEN   European Committee for Standardization

GMNIA   Geometrically and Materially Nonlinear Analysis with Imperfections

LRFD   Load and Resistance Factor Design

OpenSees   Open System for Earthquake Engineering Simulation

RC   Reinforced Concrete

Chapter 1

Introduction

Stability effects can dominate the design of slender reinforced concrete (RC) bridge columns. Yet, bridge engineers are often forced to make assumptions in the stability design of RC columns that are not rigorously justified by data.

The AASHTO LRFD Bridge Design Specifications (AASHTO, 2017), hereafter referred to as AASHTO LRFD, includes an approximate method for the design of slender RC bridge columns. This approximate method, the method most commonly used by bridge engineers, was adapted from building design codes such as the ACI Building Code Requirements for Structural Concrete (ACI, 2019), hereafter referred to as ACI 318. Accordingly, the AASHTO LRFD approximate method applies to a specific range of parameters and configurations based on floor framing stiffness, building story heights, and material properties and reinforcing ratios common to buildings. While some analogies carry over to bridge columns, the superstructure stiffness and unbraced column lengths can be quite different for bridge systems compared to buildings. The assumptions built into the approximate AASHTO LRFD method can lead to unsafe bridges in some cases and inefficient designs that are more costly than necessary in other cases.

Bridge engineers can obtain safer and more efficient designs using the refined method based on second-order finite element analysis. In fact, if the slenderness ratio exceeds 100, AASHTO LRFD requires the refined method. Although the refined method can be more accurate than the approximate method, the refined method is rarely used in practice because of the computational effort and the need to make choices about uncertain parameters of a finite element model.

The purpose of this research is to develop improved guidelines for the efficient design of slender RC bridge columns using the approximate method (moment magnification) and the refined method (second-order analysis). This work evaluates the AASHTO LRFD approximate moment magnification method against advanced second-order inelastic analyses. Parametric studies were conducted on single column models and common Caltrans bridge types. The impact of major parameters, e.g., slenderness, out-of-plumbness, and superstructure stiffness, on structural response according to both the approximate method and advanced analysis were quantified. Refinements to the approximate method were developed in cases where these methods differ substantially. This work provides the guidance necessary for engineers to make justifiable decisions with confidence when designing slender RC columns. The increased accuracy will result in more efficient, cost-effective

designs while maintaining safety.

This report is organized as follows. A review of relevant literature and development of a database of experimental data is presented in Chapter 2. Chapter 3 introduces the advanced second-order inelastic analysis model used in this work. Validation studies comparing results from the refined model to previously published experimental results are presented in Chapter 4. Chapter 5 presents an evaluation of current AASHTO LRFD design provisions. The development of potential modifications to the design provisions is described in Chapter 6. The work is summarized, conclusions are stated, and overall recommendations are made in Chapter 7. A comparison of methods, including the recommended methods and their use in the software package CSiBridge, for an archetype bridge is presented in Appendix A.

Chapter 2

Literature Review

The literature review is divided into three general areas: physical experiments, analytical modeling, and design of slender reinforced concrete columns.

2.1   Physical Experiments on Slender Reinforced Concrete Columns

Thousands of physical experiments on RC columns are documented in the literature. Given the goals of the project, this literature review and database development are focused primarily on columns that were either slender, subjected to long-term loading, or both. Tests using common configurations (e.g., cross-sectional shape, boundary conditions, and loading) were added to a highly-quantitative database to enable automated evaluation. Testing with less common configurations is described more qualitatively.

The experimental database is the primary means of validating the numerical models from which the new design recommendations are calibrated. The database includes hundreds of tests on short-term loaded, uniaxially loaded, eccentrically loaded RC columns. Table 2.1 lists the references and number of specimens from each reference included in the database.

Fields in the database are sufficient to perform a second-order inelastic analysis of each specimen and compare experimental results to numerical results when paired with information common to all specimens in the database (e.g., all specimens that have a rectangular cross section). Note that while the focus of the project is on RC columns with circular or obround cross sections, the data on RC columns with rectangular cross sections is still useful for validation. The differences in cross section will be handled via the definition of fiber cross sections in the finite element analyses. The fields in the database include:

- Author and year of reference (`author`, `year`)
- Specimen name (`specimen`)
- Column length (`L`)
- Maximum load from experiment (`Pexp`)
- Deflection at maximum load (`dmax_at_Pexp`)

Table 2.1: References included in the database of short-term eccentrically loaded columns.

Reference	Number of Specimens
Viest et al. (1956)	13
Chang and Ferguson (1963)	6
Saenz and Martin (1963)	52
MacGregor and Barter (1966)	4
Martin and Olivieri (1966)	8
Goyal and Jackson (1971)	26
Drysdale and Huggins (1971)	4
Dracos (1982)	36
Iwai et al. (1986)	11
Kim and Yang (1995)	28
Lloyd and Rangan (1996)	36
Foster and Attard (1997)	68
Chuang and Kong (1997)	20
Claeson and Gylltoft (1998)	12
Lee and Son (2000)	32
Kim and Lee (2000)	6
Claeson and Gylltoft (2000)	4
Khalil et al. (2001)	11
Sarker and Rangan (2003)	18
Germain and Espion (2005)	12
Pallarés et al. (2008)	21
Jenkins and Frosch (2015)	8
Total	**436**

- Load eccentricity at top and bottom of column (`et`, `eb`)

- Overall height and width of the cross section (`H`, `B`)

- Concrete compressive strength and type of sample use to determine concrete compressive strength (`fc`, `fc_type`)

- Yield strength of longitudinal reinforcing bars (`fy`)

- Distance from edge of cross section to center of longitudinal reinforcing bars (`dp`)

- Diameter of longitudinal reinforcing bars (`db`)

- Number of longitudinal reinforcing bars along each face (`nbx`, `nby`)

- Diameter, spacing, and yield strength of transverse reinforcing bars (`dbt`, `s`, `fyt`)

- Transverse reinforcing configuration (`lat_config`)

- Miscellaneous notes (`notes`)

For each parameter with units, two fields are defined: the value and the units. For example, for

steel yield stress, the two fields are `fy` and `fy_units`. Separate fields for values and units allows for more efficient and accurate data entry and checking. Parameters are converted to consistent units programmatically prior to analysis. Figure 2.1 shows some of the cross-sectional parameters stored in the database. Cases where load eccentricity is near the edge or outside the section are achieved in the physical experiments by enlarging the ends of the column.
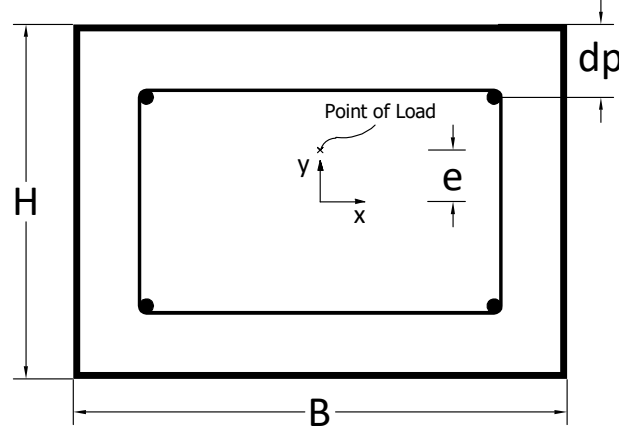

Figure 2.1: Cross-sectional parameters of the database columns

Not all data are available for each specimen. If a major piece of data (i.e., concrete compressive strength) was not reported, then the specimen was not included in the database. Other data, such as the yield strength of transverse reinforcing bars, is less important. Analyses were conducted to evaluate the sensitivity of the strength of these columns to the missing data. In cases where the difference in column strength for the anticipated range of the values of the missing field is negligible, such as for the yield strength of transverse reinforcing bars, the specimens were included in the database, and the field of missing data was left blank.

Some specimens were excluded from the database because they failed in ways that could not be simulated using the numerical model in this work (e.g. if failure occurred due to imperfect compaction of ends).

The information in the database is visualized with several histograms. Figures 2.2–2.9 demonstrate the frequency and range of selected parameters from the database.

The following list describes other series of experimental tests which relevant to this work but fall outside the scope of the database (e.g., long-term loaded columns and biaxially loaded columns).

- Babazadeh et al. (2016) tested 3 slender RC bridge columns in a cantilever configuration with constant axial compression and cyclically applied lateral displacements. This work is also described in other references Burgueño et al. (2016); Babazadeh et al. (2017); Babazadeh-Naseri (2017).

- Barrera et al. (2011) tested 44 slender RC members which were simply-supported and subjected to axial load and a transverse load at the midpoint.

- Breen and Ferguson (1969) tested 10 slender RC columns in a cantilever configuration.

- Green and Breen (1969) tested 10 slender RC columns under eccentric sustained load.

- Hsu et al. (1995) tested 14 slender RC columns under biaxial loading. 5 of the columns had fiber reinforced concrete.

- Hung et al. (2024) tested 4 slender RC bridge columns bent in double curvature with constant axial compression and cyclically applied lateral displacements.

- Ibrahim and MacGregor (1996) tested 20 high-strength RC columns under a non-proportional loading scheme.

- Kim and Lee (2000) tested 10 RC column under biaxial eccentric load in addition to the 6 already included in the database.

- Mavichak and Furlong (1976) tested 24 RC columns under biaxial load, including 15 with "partial circlar" cross sections.

- Pancholi (1977) tested 39 RC columns.

- Ramamurthy (1966) tested 50 RC columns in biaxial bending.

- Sarker et al. (2001) tested 12 RC columns in biaxial bending.

- Schofield (1983) tested 50 RC columns under non-proportional loading.

- Taso and Hsu (1994) tested 14 RC columns in biaxial bending, including 8 with "L-shaped" cross sections.

- Wang and Hsu (1992) tested 6 RC columns in biaxial bending.

- Wu and Huggins (1977) tested 34 RC columns in biaxial bending and under sustained load.
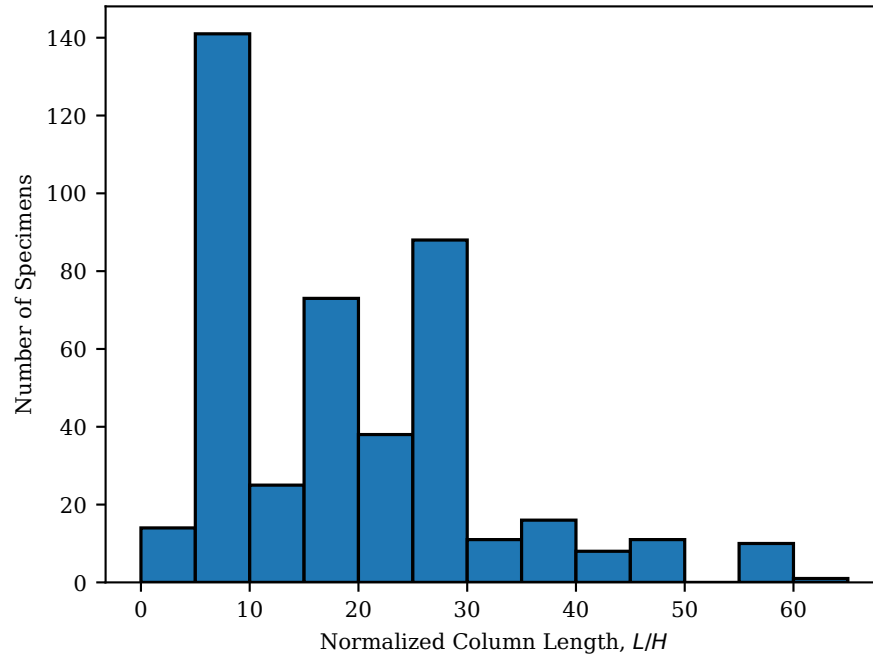
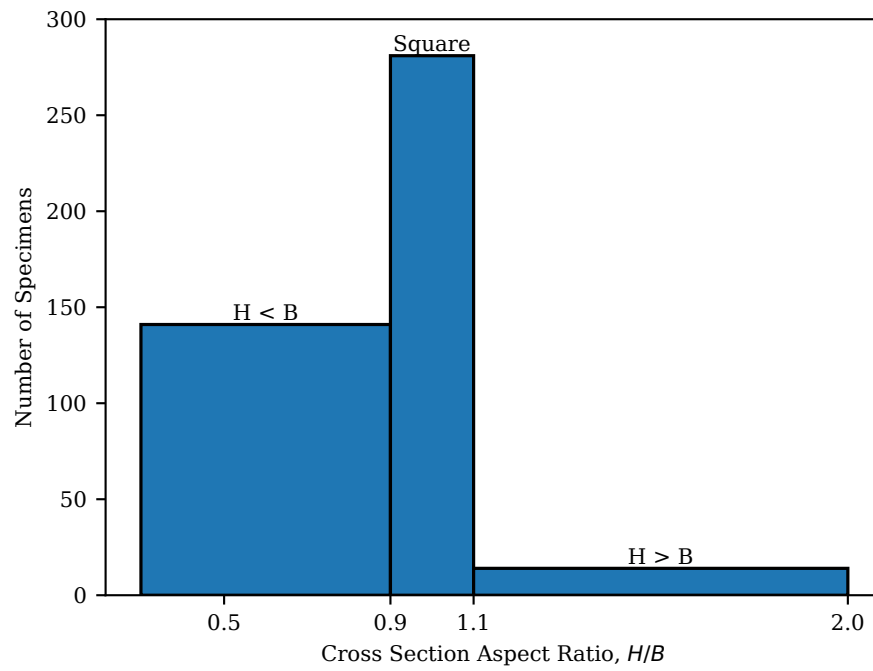Figure 2.2: Column slenderness ratio histogram

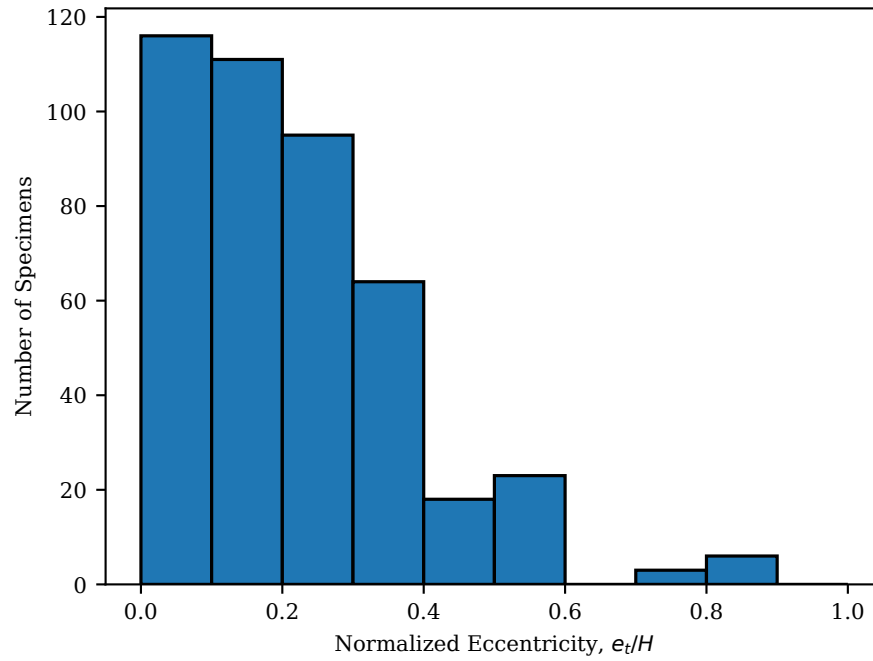Figure 2.3: Cross section aspect ratio histogram

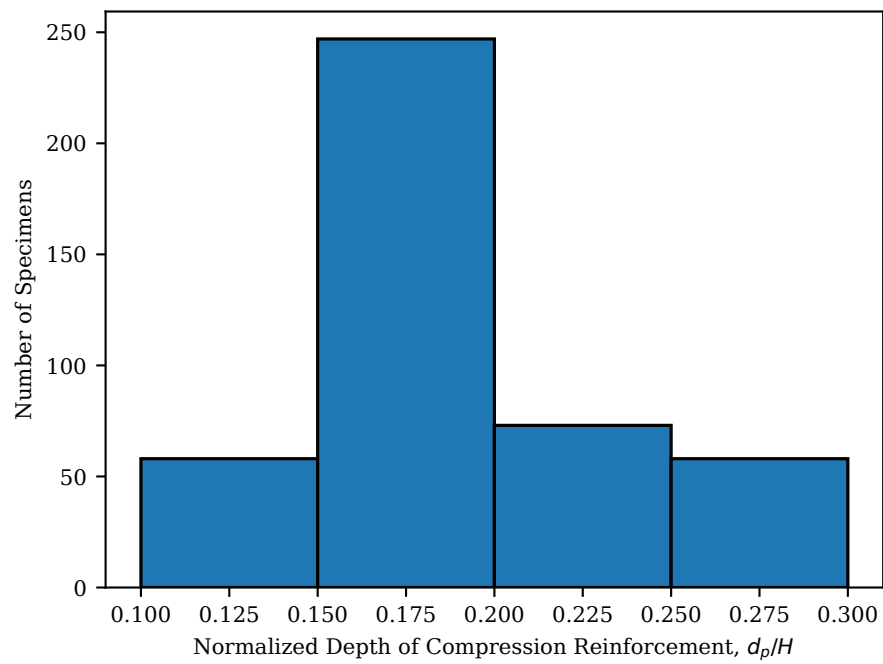Figure 2.4: Normalized load eccentricity histogram

Figure 2.5: Normalized depth of compression reinforcement histogram
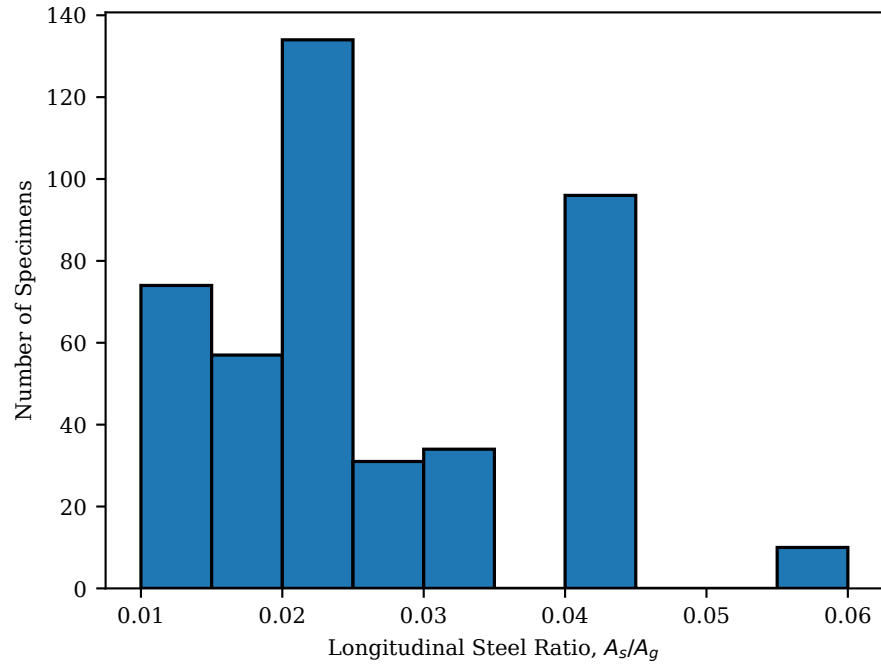
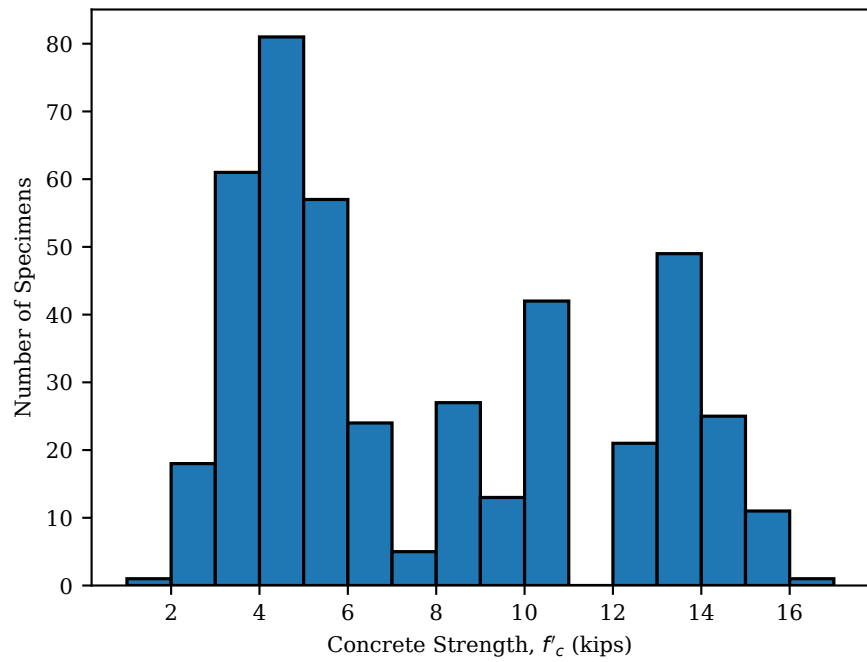Figure 2.6: Longitudinal steel ratio histogram

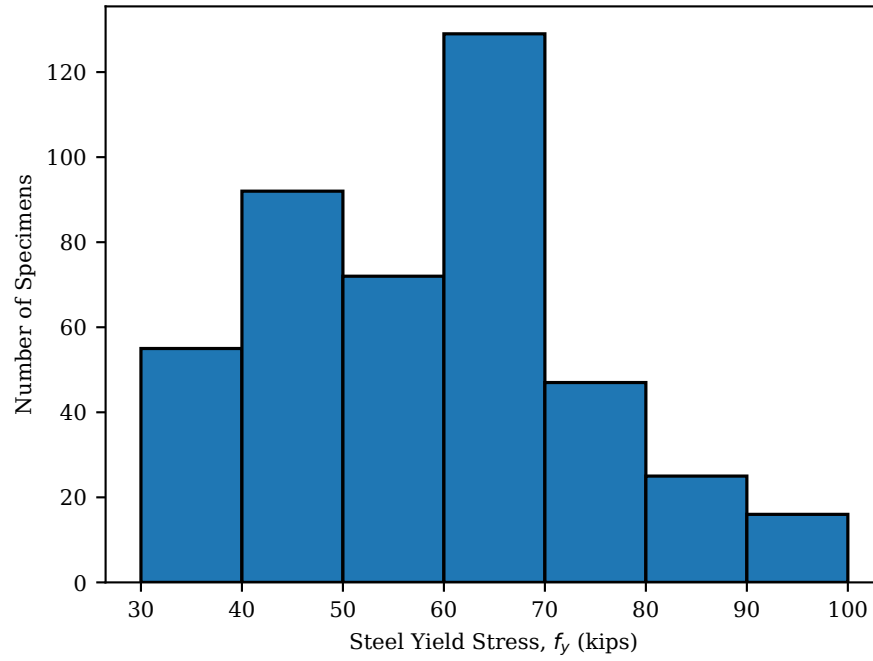Figure 2.7: Concrete compressive strength histogram
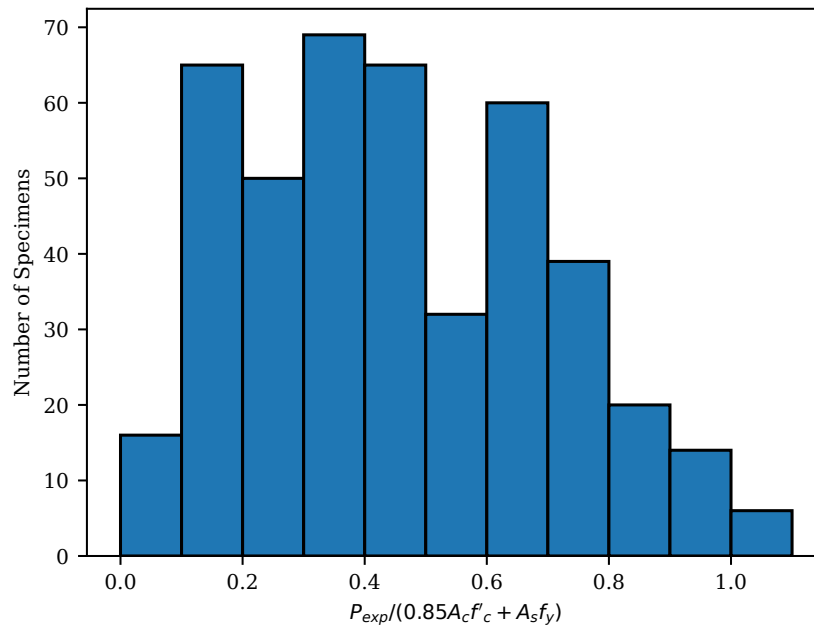
Figure 2.8: Steel yield strength histogram

Figure 2.9: Experimental peak load over the nominal strength of reinforced concrete column histogram

2.2 Analytical Modeling of Slender Reinforced Concrete Columns

Simulating the response of reinforced concrete columns ranges from elastic models based on effective section properties to nonlinear finite element models that incorporate the stress-strain behavior of concrete and steel. Due to the slenderness of columns, frame or beam-column line elements are commonly employed because, compared to solid finite elements, line elements strike a balance between computational efficiency and accuracy. Owing to their prevalence in modeling reinforced concrete column response, this review will focus on beam-column line elements and the constitutive models typically employed with these elements.

2.2.1 Finite Element Formulations

Formulations for material nonlinear beam-column finite elements are typically categorized as either distributed plasticity or concentrated plasticity. While concentrated plasticity formulations are popular in earthquake simulation of columns in lateral load resisting systems, these formulations are less suitable for stability analysis. Concentrated plasticity formulations assume the largest bending moments are confined to the ends of the member; however, for stability analysis, the largest bending moment can occur along the member due to P-δ effects. Distributed plasticity formulations account for material nonlinearity (concrete cracking, steel yielding, etc.) along the member length and will thus be the focus of this project.

There are three major approaches to distributed plasticity: displacement-based, force-based, and mixed formulations. In the displacement-based formulation, a strain field is imposed along the element. In the presence of material nonlinearity, the displacement-based approach requires mesh refinement (multiple elements per member) in order to obtain an accurate representation of the member deformation field. The force-based and mixed formulations do not require mesh refinement to capture material nonlinearity; however, the computed response can be sensitive to the numerical integration used for the element state determination.

To account for geometric nonlinearity along a column member (P-δ effects), moderate to large deformation formulations for displacement-based, force-based, and mixed elements are available. For displacement-based elements, second-order Green-Lagrange strain is computed from the element displacement fields Hjelmstad (2005) while for the force-based formulation, curvature-based displacement interpolation approximates the transverse displacement along an element Neuenhofer and Filippou (1998). In the mixed formulation, both the displacements and the stress resultants are treated as interpolated fields along each element using the Hellinger-Reissner principle Hjelmstad and Taciroglu (2003). The displacement-based formulation for geometric nonlinearity typically requires mesh refinement while the force-based and mixed formulations can use a single element per member to capture combined material and geometric nonlinearity. However, using a single element per member for combined material and geometric nonlinearity is uncommon as it is desirable to define intermediate nodes to track deflections. Comparisons of the three formulations are given by Alemdar and White (2005).

Instead of a single member, a mesh of material nonlinear, but geometrically linear elements, each with the corotational large displacement transformation Crisfield (1991) can also capture geometric nonlinearity. This "corotational mesh" approach requires multiple elements, but can be a more suitable approach for stability analysis of reinforced concrete columns because the high

number of elements per member, typically four or five, will also capture the change in stiffness along the member. Because the mesh is already refined to capture geometric effects, the displacement-based formulation is typically used in this "corotational mesh" approach because this formulation is the most computationally simple among the three formulations.

2.2.2 Constitutive Models

Fiber-discretized cross-sections provide a convenient approach to modeling the change in stiffness along a member under combined axial and flexural loads. With this approach, the force-deformation response at each integration point along an element is computed from the stress-strain response at discrete locations (fibers) over the section area. Although the computed force-deformation response improves as the number of fibers increases, a relatively low number of fibers is required to obtain accurate response for reinforced concrete members in compression Kostic and Filippou (2012).

With the fiber section approach, one-dimensional, or uniaxial, stress-strain relationships are assigned to each fiber. For monotonic (non-cyclic) loading such as the conditions expected for stability analysis, basic models of concrete and steel stress-strain behavior typically suffice. For concrete, the compressive backbone is often defined by Mander et al. (1988) or the Kent and Park (1971) approximation. The increase in concrete stiffness and strength due to confinement in compression is typically represented with the Mander model based on transverse steel strength and spacing Mander et al. (1988). Although it is conservative to ignore the beneficial effects of concrete tension strength and strain hardening of steel when computing member strength, these effects can be included with little additional modeling effort when using fiber sections.

A schematic of a corotational mesh with the fiber section modeling approach is shown in Figure 2.10. Note that, without complication, rotational and translational springs can be added at the ends of the corotational mesh in order to model bent cap and foundation stiffnesses. All of these modeling components (corotational mesh, fiber section, stress-strain relationships for concrete and steel, and rotational and translational springs) are available in the widely-used OpenSees finite element software framework McKenna et al. (2010).

2.2.3 Long-Term Load Effects

Reinforced concrete column stability under long-term loads is an important consideration due to the additional strains, curvatures, and deformations owing to creep and shrinkage. Goel et al. (2007) compared several models for concrete creep and shrinkage, comparing the model effects on long-term behavior. Although none of the models give an explicit expression for the change in concrete compressive strength because the models are intended for service level loads, expressions are available for the change in elastic modulus as a function of time. Without a change in strength, the change in stiffness will have an effect on column stability under long-term loading.

Several time-dependent concrete material models by Knaack and Kurama (2018) are available in OpenSees Tošić et al. (2020), along with a general material wrapper that applies creep and shrinkage evolution equations to any uniaxial material. In the time-dependent concrete models available in OpenSees, the evolution equations for creep and shrinkage are based on either Eurocode 2010 fib (2013) or ACI 209-92R ACI Committee 209 (1997). The models employed in this project are based on ACI 209-92R evolution equations. These time-dependent models can be used directly in the fiber section models described in the previous section.
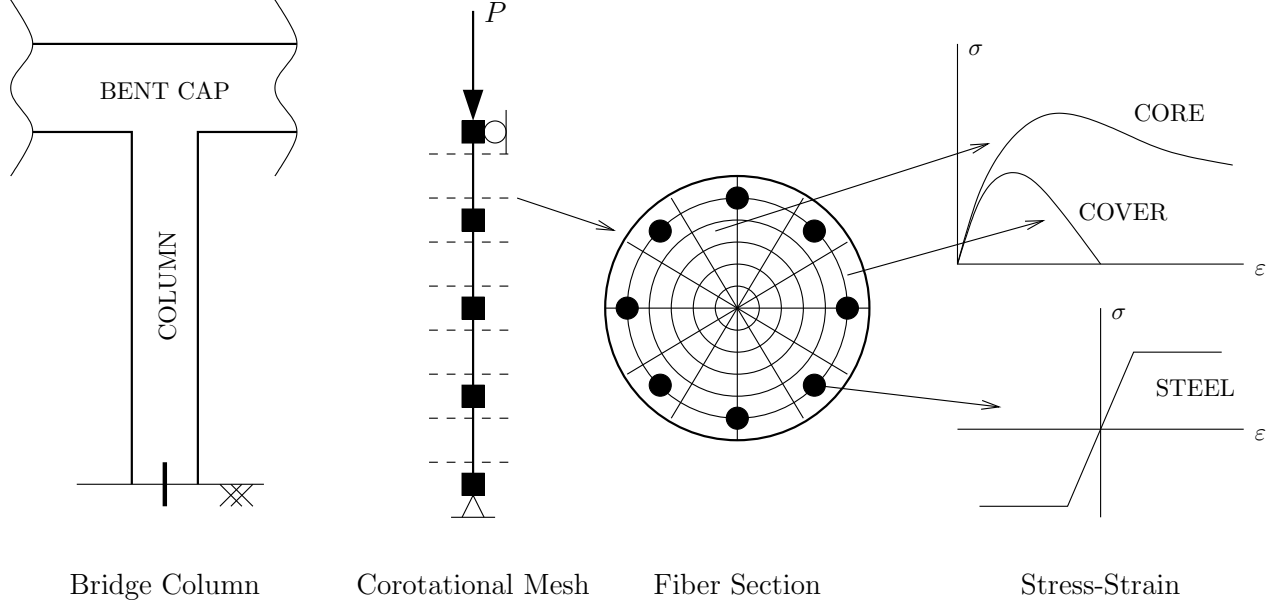
14

Figure 2.10: Analytical model of a bridge column using corotational mesh and fiber sections with uniaxial stress-strain relationships for concrete and steel.

2.3 Design of Slender Reinforced Concrete Columns

Standards that include provisions for the design of slender reinforced concrete columns often describe several methods. These methods of design are most generally categorized by the method of analysis they employ, including second-order inelastic analysis, second-order elastic analysis, and first-order elastic analysis with moment magnification.

Several standards, including AASHTO LRFD, the 2019 edition of ACI 318, and Eurocode 2, permit the use of second-order inelastic analysis for design of slender reinforced concrete columns. The design provisions in each of these standards are general with little guidance beyond which physical effects need to be considered. Provisions for design using second-order elastic analysis are typically general as well.

The most detailed provisions for the design of slender reinforced concrete columns are for methods that utilize first-order elastic analysis and moment magnification. Key aspects of these methods include: 1) a limit at which second-order effects may be neglected, 2) approximate formulas for effective flexural stiffness, and 3) equations for determining the moment magnification factors. The provisions in AASHTO LRFD are largely based on those in ACI 318.

AASHTO LRFD presents two equations (Equations 5.6.4.3-1 and 5.6.4.3-2) for computing the effective flexural rigidity of RC columns.

$$EI = \frac{0.4E_cI_g}{1 + \beta_d} \tag{2.1}$$

15

$$EI = \frac{0.2E_cI_g + E_sI_{se}}{1 + \beta_d} \tag{2.2}$$

where:

E_c = modulus of elasticity of concrete

E_s = modulus of elasticity of longitudinal steel

I_g = moment of inertia of the gross concrete section about the centroidal axis

I_{se} = moment of inertia of longitudinal steel about the centroidal axis

β_d = ratio of maximum factored permanent load moments to maximum factored total load moment

Basing the effective flexural rigidity on more precise calculation is also permitted by AASHTO LRFD.

ACI 318 includes a third equation for the flexural rigidity based on the work of Khuntia and Ghosh (2004).

$$EI = \frac{\left(0.80 + 25\frac{A_{st}}{A_g}\right)\left(1 - \frac{M_u}{P_u h} - 0.5\frac{P_u}{P_o}\right)E_cI_g \leq 0.875E_cI_g}{1 + \beta_d} \tag{2.3}$$

where:

A_{st} = total area of longitudinal reinforcement

A_g = gross area of concrete section

M_u = factored moment at section

P_u = factored axial force

h = overall depth of member

P_o = nominal axial strength at zero eccentricity

Note that ACI 318 permits other, larger, values of stiffness for second-order elastic analysis.

Eurocode 2 governs reinforced concrete bridge design in Europe. Part 1-1 of this standard CEN (2004) contains general rules. Part 2 of this standard CEN (2005) contains design and detailing rules specific to concrete bridges. For analysis of second-order effects with axial load, the specific provisions in Part 2 are minimal.

The simplified method based on nominal stiffness presented in Eurocode 2 is similar to the moment magnification methods in AASHTO LRFD and ACI 318. The effective stiffness used in the analysis is

$$EI = K_cE_cI_g + E_sI_{se} \tag{2.4}$$

where $K_c = k_1k_2/(1 + \phi_{ef})$, with a creep parameter ϕ_{ef}. The parameter k_1 is based on the concrete compressive strength

$$k_1 = \sqrt{\frac{f'_c}{20 \text{ MPa}}} \tag{2.5}$$

while k_2 is based on axial load

$$k_2 = \left(\frac{P}{A_cf'_c}\right)\left(\frac{\lambda}{170}\right) \leq 0.20 \tag{2.6}$$

where f'_c is the specified compressive strength of concrete, psi, and λ is a slenderness ratio.

Eurocode 2 also includes a simplified method based on nominal curvature. This method is similar to that described by CEB-FIP *Manual of Buckling and Instability*, which Bažant et al. (1991) found provides highly accurate results. However, this method is mainly intended for isolated members.

Other researchers have proposed equations for the flexural rigidity of reinforced concrete columns. Mirza (1990) developed equations that depend on the column length and eccentricity while Jenkins and Frosch (2015) developed equations that depend on required axial strength, required flexural strength, and steel ratio.

Chapter 3

Refined Second-Order Analysis

Refined second-order analysis capabilities are necessary for this work to form the "best guess" of true behavior and provide a benchmark against which current and proposed design provisions can be evaluated. The refined second-order analyses performed in this work utilize frame elements to model bridge columns and capture both material and geometric nonlinearity. The analyses are not necessarily intended for use in practice. This chapter describes the models while the following chapter describes validation studies that confirm the models produce accurate results.

3.1   General Modeling

Models of columns were developed in the OpenSees finite element framework using Python and the `OpenSeesPy` interpreter Zhu et al. (2018). Columns were modeled with frame elements, specifically a mixed beam column-element although displacement- and force-based beam-column elements are available and interchangeable with the mixed element. Eight elements along the length of the column and a corotational transformation between element basic and local coordinate systems were used to capture geometric nonlinearity and initial geometeric imperfections (by definition of initial nodal coordinates). The Gauss-Lobatto quadrature rule with three integration points was used to integrate the section response. The constitutive response at each section was obtained from a fiber section approach where stress-strain response is assigned to each cell of the discretized cross-section area.

Three cross-sectional shapes are considered in this work: 1) rectangular, 2) circular, and 3) obround. Circular and obround shaped columns are common on Caltrans bridges. Rectangular columns are not standard Caltrans design, however, the vast majority of experimental results on RC columns identified in the literature are with rectangular cross sections. Fiber discretized models have been developed for rectangular (Figure 3.1), circular (Figure 3.2), and obround cross sections (Figure 3.3). The cross sections shown in these figures have only been discretized in one direction as is accurate and efficient for two-dimensional analyses.

Each fiber discretization consists of a) concrete patches that are subdivided into fibers and b) individually defined fibers for the longitudinal steel reinforcing bars. The patches were assigned either a core concrete or cover concrete stress-strain relationship to capture the effects of confinement
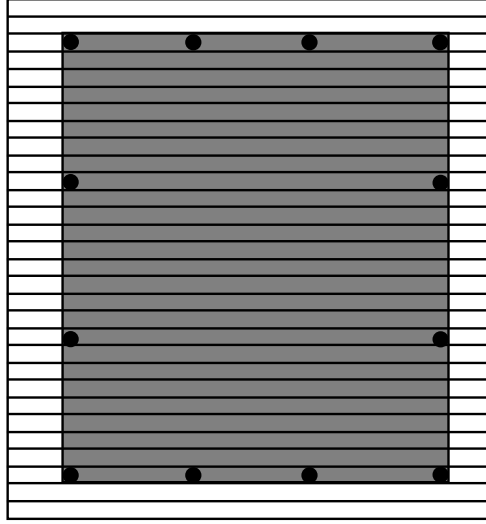
Figure 3.1: Rectangular section fiber discretization
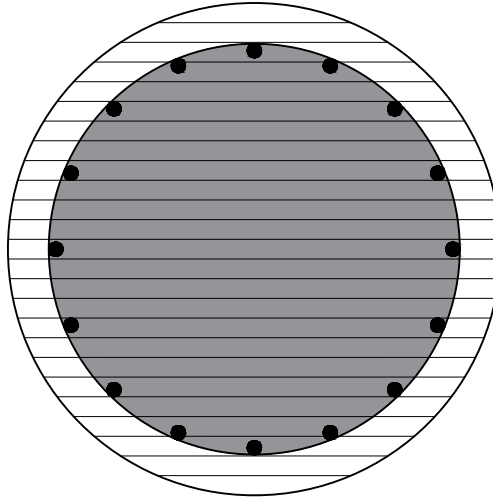
with uniaxial materials as described below.

Figure 3.2: Circular section fiber discretization

For circular cross sections, several concentric circular patches were used to make the size of the individual fibers more uniform. Each individual fiber representing a steel reinforcing bar was paired with a second individual fiber of negative area and concrete material in order to avoid double counting of steel and concrete areas.

For each cross-sectional type, a Python function was written to define the fiber discretization. To simplify input, the number of fibers is defined for the overall cross section as the approximate
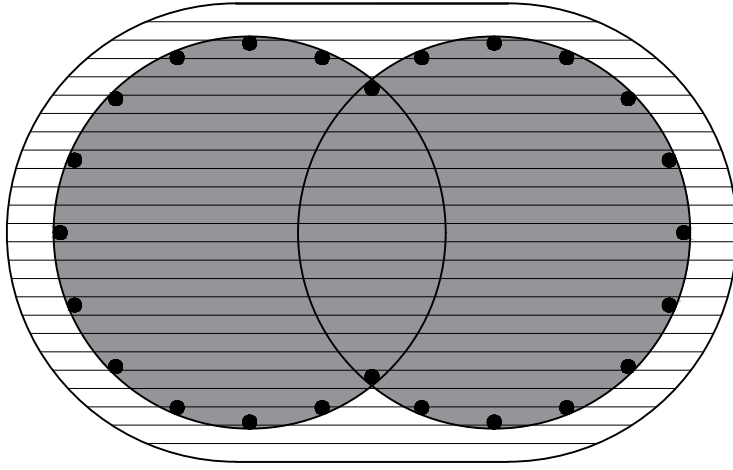
(a)
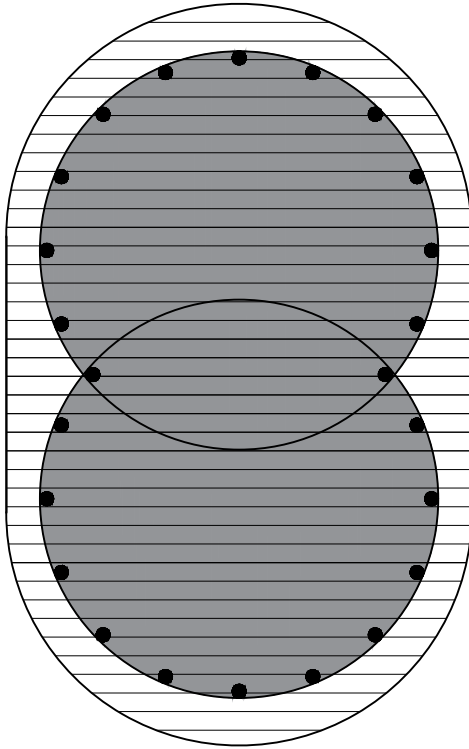
(b)

Figure 3.3: Obround section fiber discretization (a) bending about the x-axis (b) bending about the y-axis

number of fibers in the x and y directions. The number of fibers in specific concrete patches was computed using these values and cross-sectional properties.

OpenSees includes a variety of uniaxial constitutive relations for reinforcing steel. A relatively simple elastic-perfectly plastic material (Figure 3.4) was used because this model captures yielding and requires only two input parameters, the modulus of elasticity and yield stress, both of which are generally known. Due to conservatism in the results, neglecting steel strain-hardening is common in the development of design recommendations for RC members.
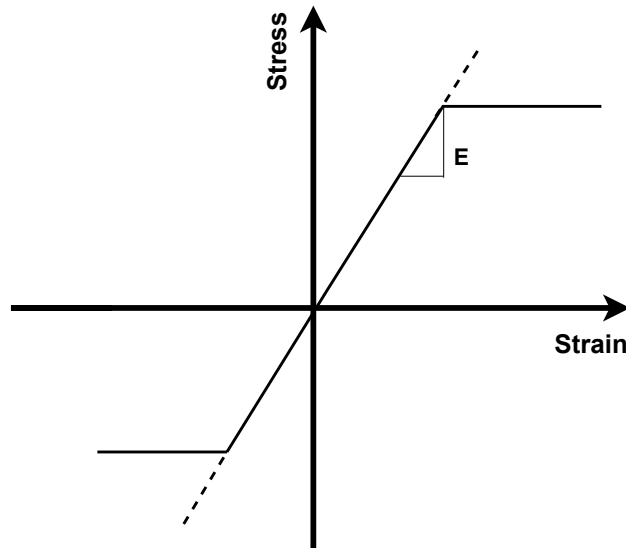
Figure 3.4: Elastic-perfectly plastic material used for modeling reinforcing steel

OpenSees also includes a variety of uniaxial constitutive relations for concrete. Many models are available for capturing the short-term behavior of concrete. The model described by Mander et al. (1988) was selected for this work as it is commonly used (Figure 3.5). The available concrete constitutive relations that capture creep and shrinkage in OpenSees are discussed in Chapter 4. A creep and shrinkage material wrapper was developed for this project so that modeling choices for short-term and long-term loading are as consistent as possible.
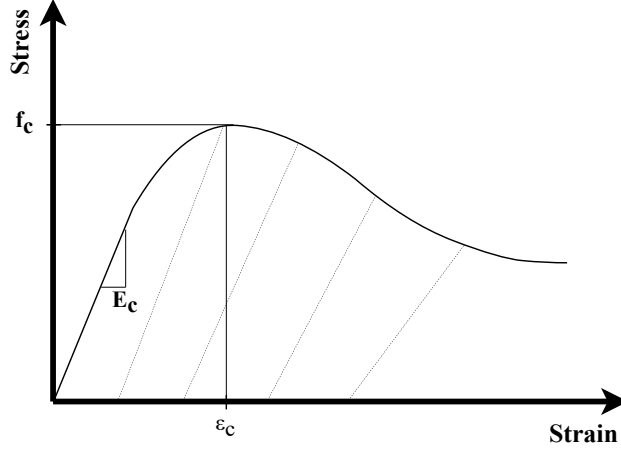
Figure 3.5: Mander material used for modelling concrete

3.2 Concrete Constitutive Modeling for Short-Term Loading

The stress-strain relationship described by Mander et al. (1988) was adopted for modeling concrete under short-term loading, with the exception of equations for E_c and ε_c which were taken from other references. The model describes a backbone curve for the compressive response and confinement model. The strength and stiffness of concrete in tension are neglected. For GMNIA, the `Concrete04` uniaxial material is used to capture this behavior.

The elastic modulus of the concrete is calculated as

$$E_c = 57000\sqrt{f_c'} \tag{3.1}$$

where E_c is the elastic modulus of the concrete and f_c' is the compressive strength of the concrete, both in units of psi.

The strain at maximum compressive strength for unconfined concrete (ε_c) is calculated as

$$\varepsilon_c = \frac{(f_c')^{1/4}}{4000} \tag{3.2}$$

where f_c' is in units of psi.

Eq. (3.1) is based on ACI 318 while Eq. (3.2) is based on Chang and Mander (1994).

The concrete in the core of the cross-section is confined by the transverse steel reinforcement, thus increasing its strength and ductility. The peak compressive strength for confined concrete (f_{cc}) is calculated as

For rectangular sections confined by rectangular hoops with or without cross ties

$$f_{cc}' = f_c'(1 + k_1\bar{x}) \tag{3.3}$$

For sections confined by spirals or circular hoops

22

$$f'_{cc} = f'_c(-1.254 + 2.254\sqrt{1 + 7.94\bar{x}} - 2.0\bar{x}) \tag{3.4}$$

with k_1 and $\bar{x}$ defined as

$$k_1 = A\left[0.1 + \frac{0.9}{1 + B\bar{x}}\right] \tag{3.5}$$

For rectangular sections confined by rectangular hoops

$$\bar{x} = \frac{f_{l1} + f_{l2}}{2f'_c} \tag{3.6}$$

For sections confined by spirals or circular hoops

$$\bar{x} = \frac{f_l}{f'_c} \tag{3.7}$$

where f_l, f_{l1}, and f_{l2} are the lateral confining pressure on the concrete (in x and y direction for f_{l1} and f_{l2}, respectively), and defined as:

For rectangular sections confined by rectangular hoops:

$$f_{l1} = k_e \rho_{sx} f_{yh} \tag{3.8}$$

$$f_{l2} = k_e \rho_{sy} f_{yh} \tag{3.9}$$

For sections confined by spirals or circular hoops:

$$f_l = \frac{1}{2} k_e \rho_s f_{yh} \tag{3.10}$$

where ρ_s is the ratio of the volume of transverse confining steel to the volume of confined concrete core (in x and y direction for $\rho_s f_{yh}$ and $\rho_s f_{yh}$, respectively); f_{yh} is the yield strength of the transverse reinforcement; k_e is the confinement effectiveness coefficient as defined by Mander et al. (1988).

The factors A and B are calculated as below

$$A = 6.886 - (0.6069 + 17.275q)e^{-4.989q} \tag{3.11}$$

$$B = \frac{4.5}{\frac{5}{A}[0.9849 - 0.6306e^{-3.8939q}] - 0.1} - 5 \tag{3.12}$$

with q defined as

$$q = \frac{f_{l1}}{f_{l2}}, \qquad f_{l2} \geq f_{l1} \tag{3.13}$$

23

The strain at maximum compressive strength for confined concrete is calculated as

$$\varepsilon_{cc} = \varepsilon_c(1 + k_2\bar{x}) \tag{3.14}$$

where $k_2 = 5k_1$.

Table 3.1 summarizes the parameters used for modelling core concrete versus cover concrete. The optional parameters to define the tensile strength of concrete were omitted since the tensile strength of concrete was neglected in this work.

Table 3.1: Concrete04 material parameters for core and cover concrete.

Input Parameter	Core Concrete	Cover Concrete
Concrete Compressive Strength, `fc`	f'_{cc} (Eq. (3.3), Eq. (3.4))	f'_c
Concrete Strain at Maximum Strength, `epsc`	ε_{cc} (Eq. (3.14))	ε_c (Eq. (3.2))
Concrete Strain at Crushing Strength, `epscu`	$2\varepsilon_{cc}$	$2\varepsilon_c$
Modulus of Elasticity, `Ec`	E_c (Eq. (3.1))	E_c (Eq. (3.1))

3.2.1 Example Results

Interaction diagrams computed using the refined second-order analysis model are among the primary analysis results that will be used in this project. Example interaction diagrams are presented in this section for a base case and variations from the base case. The structure examined for these example interaction diagrams is a simply-supported column subject to axial compression and equal end moments producing single-curvature bending (Figure 3.6). The parameters for the base case are as follows:

- Column length, $L = 200$ in.

- Section Diameter, $D = 10$ in.

- Longitudinal steel ratio, $\rho_s = A_{sr}/A_g = 0.02$

- 6 bars in circumference direction

- Distance from center of reinforcing to outside edge of concrete $= 1$ in.

- Steel yield strength, $f_y = 60$ ksi

- Initial geometric imperfection, $\delta_o = L/1000$

A series of analyses was performed to construct each interaction diagram. The first analysis subjects the column to axial load only. The analysis is performed in displacement control until a maximum applied load was observed. Once the maximum applied axial load was determined, a series of equally spaced axial loads between the maximum axial load and zero were selected. For each of these selected axial loads a non-proportional analysis was performed, first applying the axial load, then increasing the applied moment (while holding the applied axial load constant) until a maximum applied moment was observed. The maximum applied moment was recorded as M_1. The maximum internal moment along the length of the member when the applied load reached its maximum was recorded as M_2. For this case, the two moments differ by the P-δ moment occurring
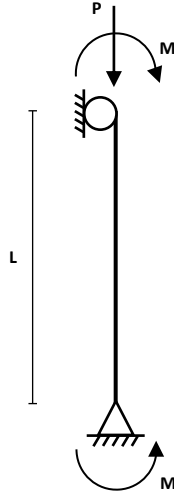
Figure 3.6: Example column and loading

at mid-height of the columns (Figure 3.7). The resulting interaction diagrams for the base case are presented in Figure 3.8.

To evaluate the model and ensure that the results align with known behavior of RC columns several series of interaction diagrams were produced each varying a single structural parameter. Interaction diagrams with variations in column slenderness ratio (Figure 3.9), concrete compressive strength (Figure 3.10), steel yield stress (Figure 3.11), and longitudinal steel ratio (Figure 3.12) were produced.

The interaction diagrams shown in these figures align with expectations based on known behavior of RC columns. In the base case, the shape of the interaction diagram is as exceed with a bulge near the balance point. The moments for the internal force interaction diagram are larger than for the applied load interaction diagram for all except the case with zero axial load where P-$\delta = 0$ because $P = 0$. The internal moment for case with zero applied axial load is greater than zero because of the initial geometric imperfections. A reduction in maximum applied loads is seen with increasing member slenderness (Figure 3.9) due to the larger P-δ efforts that occur for longer columns. The internal moments are less sensitive to changes in member slenderness and only decrease for longer columns where the failure becomes more stability dominated. Increasing the concrete compressive strength has a much larger effect on the axial strength than the moment strength (Figure 3.10). Conversely, increasing the steel yield stress or steel ratio has a much larger effect on the moment strength than the compressive strength (Figure 3.11 and Figure 3.12). Increasing the steel yield stress or steel ratio also has the effect of changing the shape of the interaction diagram with the bulge at the balance point becoming less pronounced with more steel-dominant columns.
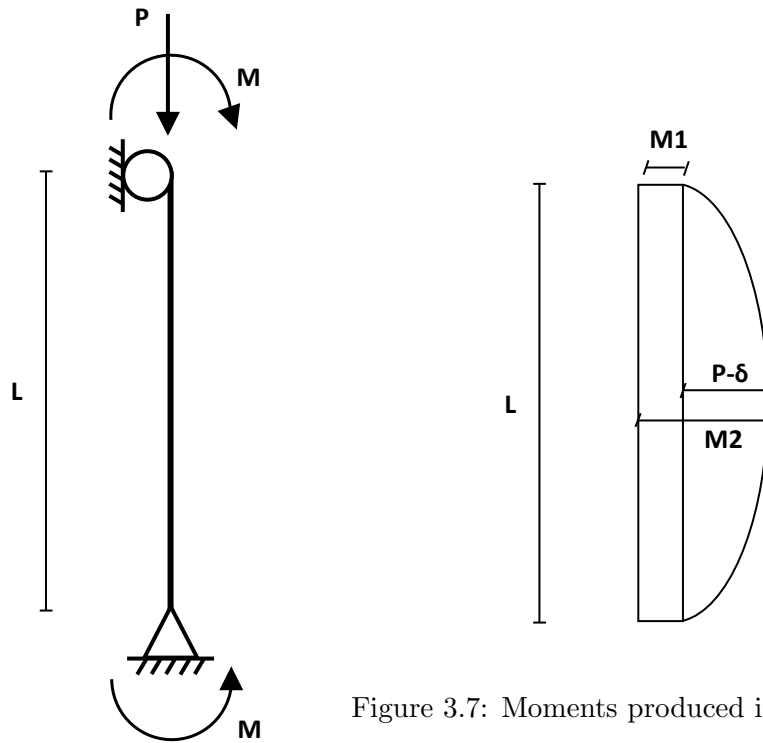
Figure 3.7: Moments produced in the column
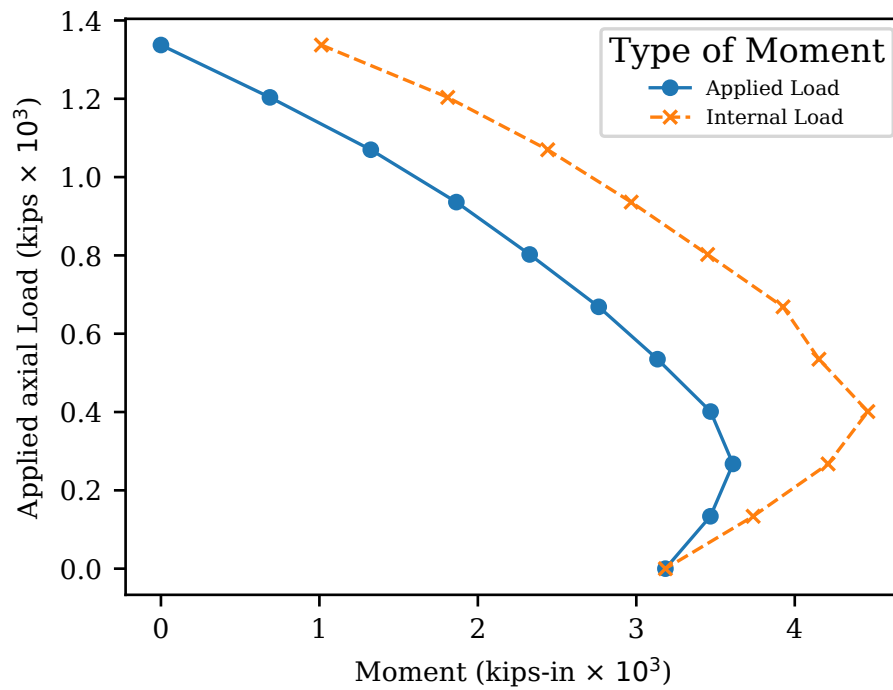
Figure 3.8: P-M interaction diagram of the base case

26

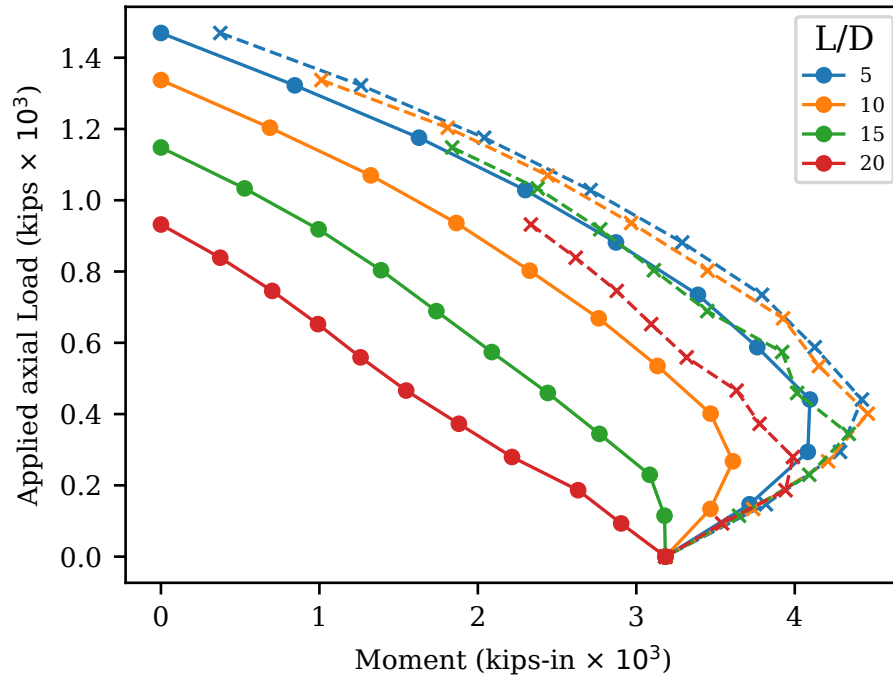Figure 3.9: P-M interaction diagram for different slenderness ratio values (diameter held constant)
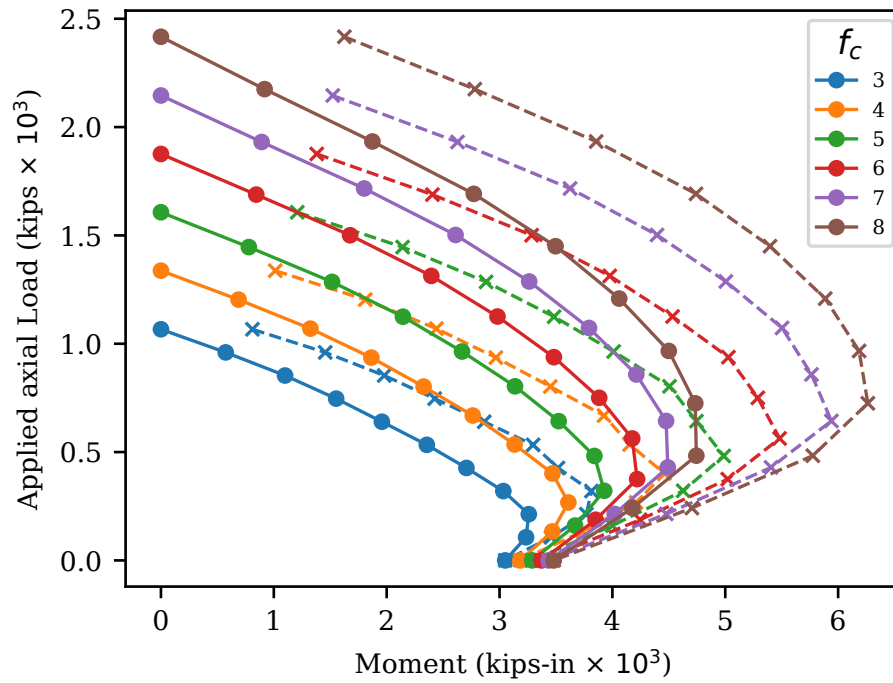

Figure 3.10: P-M interaction diagram for different concrete compressive strength values
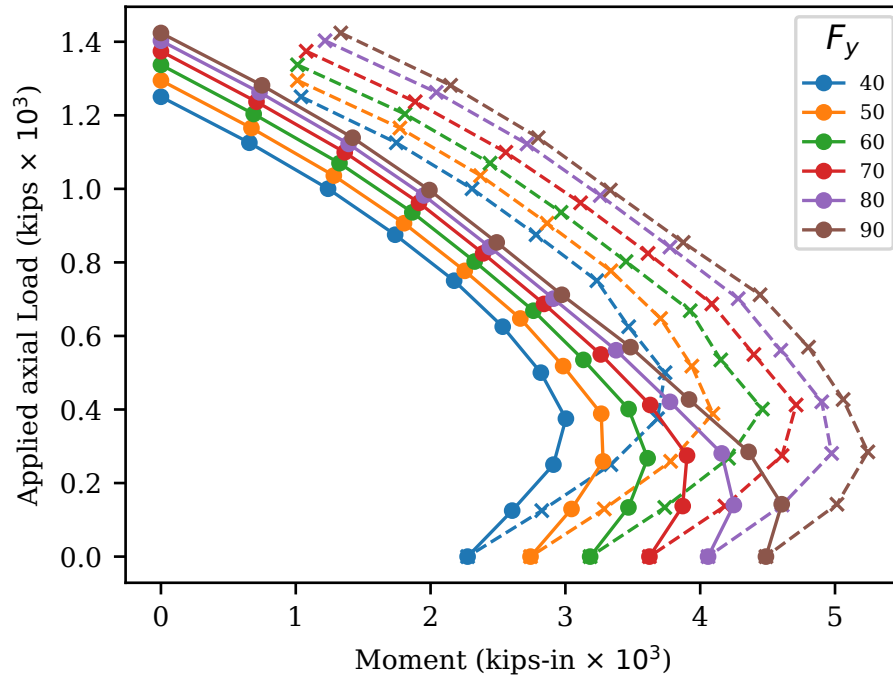
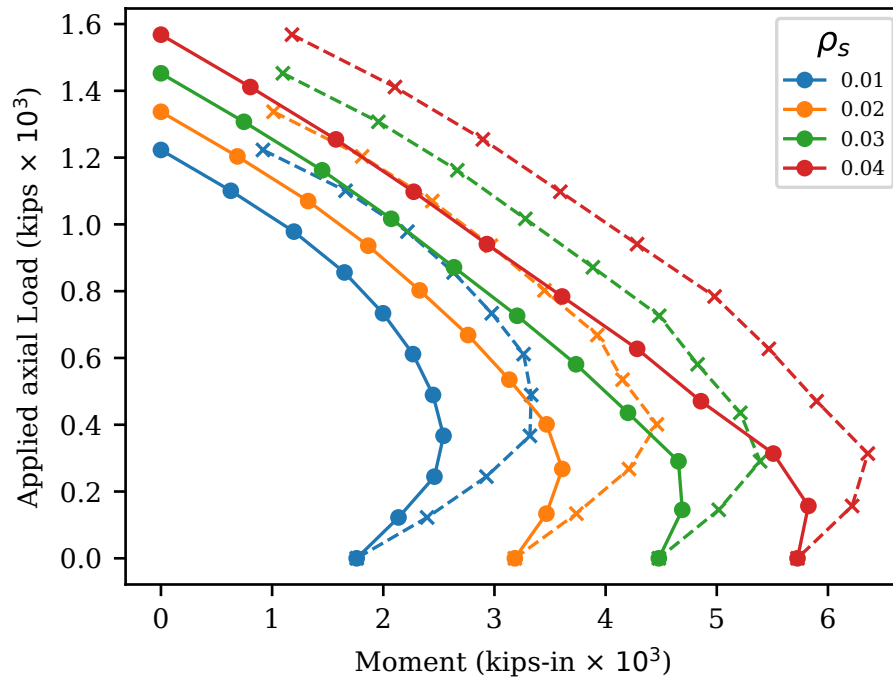Figure 3.11: P-M interaction diagram for different steel yield strength values

Figure 3.12: P-M interaction diagram for different longitudinal steel ratio values (diameter and number of bars held constant)

3.3 Concrete Constitutive Modeling for Long-Term Loading

To account for the effect of concrete shrinkage and creep over long periods (several decades) of bridge service life, the concrete stress-strain relationship used for short-term loading was modified within the OpenSees model.

3.3.1 OpenSees Time-Dependent Concrete Models

Although several time-dependent uniaxial material models are available in OpenSees for modeling creep and shrinkage of concrete, none of the models meet the needs of this project. For example, the `TDConcrete` model uses ACI209R-92 creep evolution equations, but does not not incorporate peak compressive strength, f'_c, i.e., the model assumes concrete is linear in compression. On the other hand, the `TDConcreteMC10NL` model incorporates compressive strength but uses creep evolution equations from Model Code 2010. And even though the `TDConcreteNL` model uses ACI209R-92 evolution equations, the concrete compressive behavior is based on the `Concrete02` model in OpenSees whereas the column interaction diagrams generated in this report for short-term loading use the `Concrete04` material model.

Rather than implement another "TDConcrete" model that is derivative of `TDConcreteNL`, differing by only the concrete stress-strain behavior, a generic `CreepMaterial` wrapper was developed. This wrapper is able to apply ACI209R-92 creep and shrinkage evolution equations to *any* uniaxial material model, ranging from `Elastic` material to the `Concrete04` used previously in this report. The OpenSees input format for the wrapper material model is shown below:

```
uniaxialMaterial Concrete04 $concTag $fc $epsc $epscu $Ec
```

```
uniaxialMaterial Creep $matTag $concTag $tD $epsshu $psish \
$Tcr $phiu $psicr1 $psicr2 $tcast
```

where `matTag` is the material tag of the wrapper and `concTag` is the material tag of the wrapped material (shown above with `Concrete04` inputs).

The parameters `tD`, `epsshu`, and `psish` control the evolution of concrete shrinkage, respectively defined as the analysis time at the start of drying, the ultimate shrinkage strain, and a fitting parameter based on the cross-section dimensions.

The parameters `Tcr`, `phiu`, `psicr1`, and `psicr2` define the evolution of creep in the concrete material. The parameter `Tcr` is the creep model age in days and `phiu` is the ultimate creep coefficient. The parameters `psicr1` and `psicr2` are fitting parameters where the former is typically taken as 1.0 while the latter is based on the cross-section dimensions.

The final parameter, `tcast`, is the analysis time when the concrete was cast. All analysis times input for the `CreepMaterial` wrapper are in days. Additional details on the time-dependent concrete models available in OpenSees, as well as utilities for calculating creep and shrinkage fitting parameters, are provided by Tošić et al. (2020).

3.3.2 Analysis Sequence for Long-Term Loading

The concrete models that account for long-term load effects (creep and shrinkage) in OpenSees require additional analysis considerations beyond typical short-term loading scenarios. The creep concrete models use the time step from analysis domain in order to determine incremental stress, creep, and shrinkage effects. The models interpret the time unit as days, so some caution is required in order to mix long-term and short-term analyses in OpenSees.

1. Adjust creep and shrinkage parameters based on member size.

2. Define the model with the `CreepMaterial` wrapper for concrete fibers.

3. Analyze the model for zero load with creep turned on (`setCreep 1`) and with the domain time set to after the start of drying. Note that self-weight of the concrete is not included in the analyses performed for this report.

4. Define gravity loads.

5. Analyze the model for the sustained gravity load with creep turned off (`setCreep 0`). This step puts the column into static equilibrium.

6. Analyze the model for shrinkage effects with creep turned on (`setCreep 1`) and the domain time set to when the column can sustain loads, e.g., 28 days after casting. This step accounts for initial shrinkage.

7. Leaving creep on, analyze the model for long-term creep effects inside a loop. Due to the long time scale, the stepping should be logarithmic and the time step should be passed to the `LoadControl` integrator at each analysis step inside the time loop.

8. Turn creep off (`setCreep 0`), then perform one static analysis at the post-creep state.

9. Analyze the model for remaining (post-creep) load capacity. If using displacement control, set the domain time to zero and define a linear time series with reference loading for the capacity analysis. Assuming the model did not fail during the creep analysis, load the model to a specified failure criterion.

3.3.3 Minimal Long-Term Loading Examples

To account for long-term load effects, only the concrete material model (`Concrete04` used in this report) must be wrapped with the `CreepMaterial` wrapper. To demonstrate the evolution of creep and shrinkage strains, simulations of long-term loading were carried out in OpenSees for the base case and nominal parameters shown in Figure 3.6 along with the following additional parameters:

- Constant axial load, 50 kip, held for 10,000 days (approximately 30 years)

- Load eccentricity, $0.1D$ (one-tenth of column diameter)

- After holding the axial load for 10,000 days, the axial load is increased in order to determine the axial load carrying capacity of the column

Although there is zero moment applied, the initial $L/1000$ geometric imperfection will cause P-δ moments to increase under sustained, long-term loading due to concrete creep and shrinkage. Long-term analyses are performed over the following parameter ranges:

- Ultimate creep factor, ϕ_u; base = 2.8, range = [1.3, 2.3, 2.8, 3.3, 4.3]

- Ultimate shrinkage strain, $\varepsilon_{sh,u}$; base = 780×10^{-6}, range = [480×10^{-6}, 630×10^{-6}, 780×10^{-6}, 930×10^{-6}, 1080×10^{-6}]

- Concrete compressive strength, f_c'; base = 4 ksi, range = [3, 4, 5, 6] ksi

Analyses are repeated for the range of values for each parameter listed above. Rather than analyze for all possible parameter combinations, when a parameter is varied, the other parameters are held fixed at their base value.

Prior to analysis, the concrete creep and shrinkage parameters are adjusted based on the member size using spreadsheet tools developed by Tošić et al. (2020). In addition to member size, the adjustments accounts for relative humidity, aggregate size, cement type, and other factors. Default values are used for every factor except for member size. The important parameter is the ratio of volume to surface area for the member, which for a straight member reduces to the ratio of cross-section area to circumference.

For a circular cross-section of diameter, D, the ratio of cross-section area to circumference is $D/4$. Using the spreadsheet tools developed by Tošić et al. (2020), the adjusted creep and shrinkage values for the D=10 inch diameter column are shown in Table 3.2. The parameters adjustments assume the nominal creep and shrinkage parameters are measured at 1000 days and that concrete drying begins seven days after casting.

Table 3.2: Adjusted creep and shrinkage parameters for D=10 inch circular column with f_c'=4 ksi.

CREEP, ϕ_u		SHRINKAGE, $\varepsilon_{sh,u}$	
Nominal	Adjusted	Nominal	Adjusted
1.8	1.00	480×10^{-6}	234×10^{-6}
2.3	1.28	630×10^{-6}	307×10^{-6}
2.8	1.56	780×10^{-6}	380×10^{-6}
3.3	1.84	930×10^{-6}	454×10^{-6}
3.8	2.12	1080×10^{-6}	527×10^{-6}

Figure 3.13 shows the variation in column response over the range of nominal creep factors 1.8–3.8. As expected, the lateral deflection at column mid-height increases as the creep factor increases. There is little difference in the ultimate axial load capacity of the column, with ultimate strength of about 160 kip in all cases, about a 10% reduction compared to the case of no creep and shrinkage (short-term loading).

Likewise, Figure 3.14 shows little effect on the ultimate capacity of the column over the range of nominal shrinkage strain (480×10^{-6}–1080×10^{-6}); however, the inclusion of long-term load effects causes a reduction in axial strength compared to the short-term loading case.
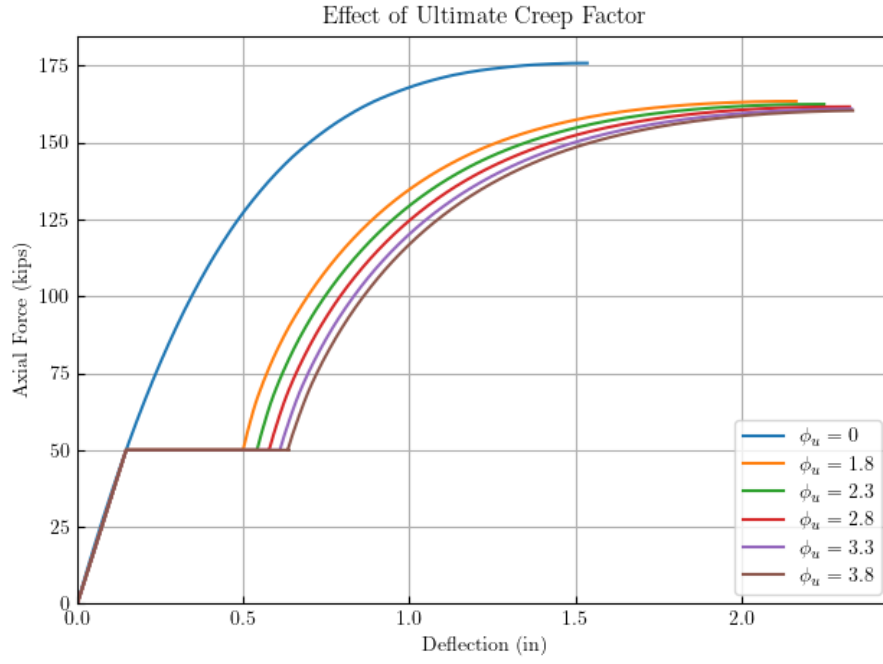
Figure 3.13: Axial force-lateral deflection response for long-term loading on column with range of ultimate creep factors.
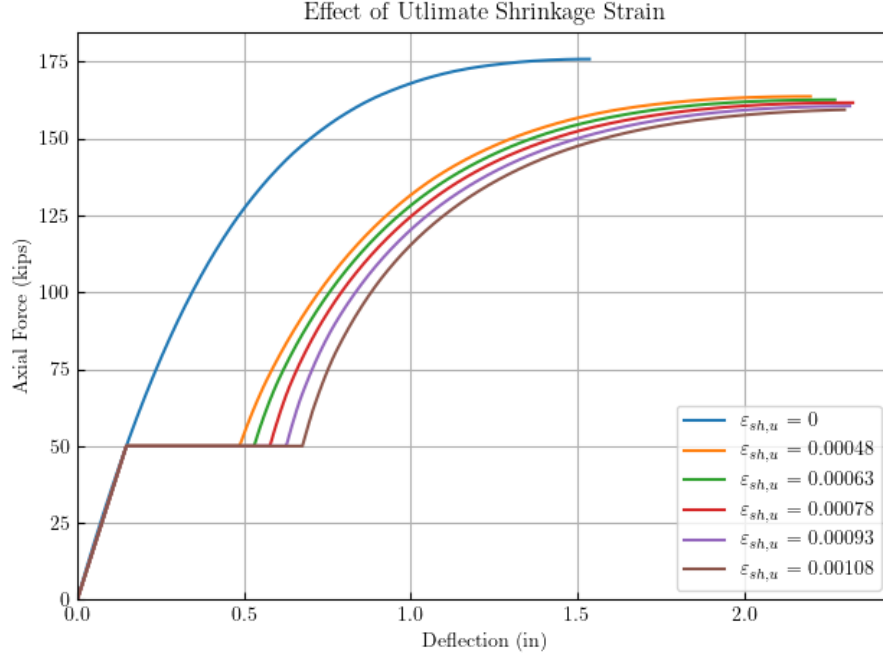

Figure 3.14: Axial force-lateral deflection response for long-term loading on column with range of ultimate shrinkage strain.

The final parametric variation shown in Figure 3.15 is over the concrete strength f'_c. As expected, the lateral deflection during the hold phase decreases and the axial strength of the column increases as the concrete compressive strength increases. In all cases, the inclusion of long-term creep and shrinkage effects leads to an approximately 10% reduction in column axial strength.
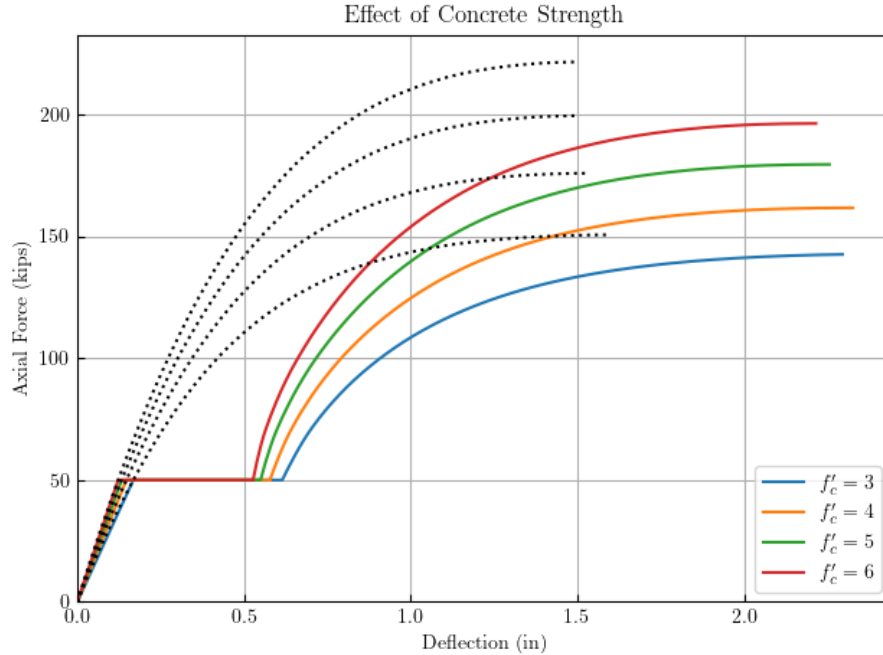

Figure 3.15: Axial force-lateral deflection response for long-term loading on column with range of concrete strength.

These examples demonstrate the long-term loading capabilities and the relative effect of the creep and shrinkage parameters that affect column axial strength. The results indicate that the long-term axial capacity is not sensitive to the ultimate creep factor and ultimate shrinkage strain; however, the axial capacity is sensitive to the presence of long-term load effects, i.e., *that* the model includes long-term load effects, but not *what* the parameters are. The conclusions are preliminary and cannot be generalized before performing additional column analyses over various cross-section sizes, column slenderness ratios, and load eccentricities. In addition to further parametric analyses, the `Concrete04` with `CreepMaterial` wrapper model will be validated against a series of experimental results in Chapter 4.

Chapter 4

Model Validation

To validate the model described in Chapter 3, a series of analyses were performed to compare against experimental data compiled as described in Chapter 2. The comparisons are currently limited to short-term loading of rectangular RC columns using the database of experiments described in Table 2.1.

4.1   Short-Term Loading of Rectangular Reinforced Concrete Columns

Analyses were performed for each of the 436 RC columns listed in Table 2.1. These columns were all simply-supported single columns that were proportionally loaded with defined eccentricities. Each column was modeled as described in Chapter 3. Eight elements were used along the length of the column.

The yield strength of lateral reinforcement was not reported for some of the columns in the database. According to trial evaluations, the exact value of f_{yt} had minimal effect on the resulting peak load had little effect on the column strength, hence this has no relevant effect on the results. For these cases, a yield strength of $f_{yt} = 60$ ksi was assumed. Note, however, some references that did not report the yield strength were published as early the 1960s when lower strength steel may have been common.

Additionally, the concrete compressive strength for some columns in the database were reported as cubic specimen strength. As the value used in the model is cylinder specimen strength, the cubic ones needed to be converted to the equal cylinder values. This was done using conversion factors described by Reineck et al. (2003), specifically

$$f'_{c,cyl} = 0.78 f'_{c,cube} \tag{4.1}$$

Initial out-of-straightnesses were included through definition of the initial nodal coordinates. The magnitude of initial imperfection of the column specimens was not typically reported. Three sets of analyses were performed, with different magnitudes of initial out-of-straightness. Statistics on the resulting ratio of maximum load from the OpenSees model, P_{GMNIA} to the maximum load
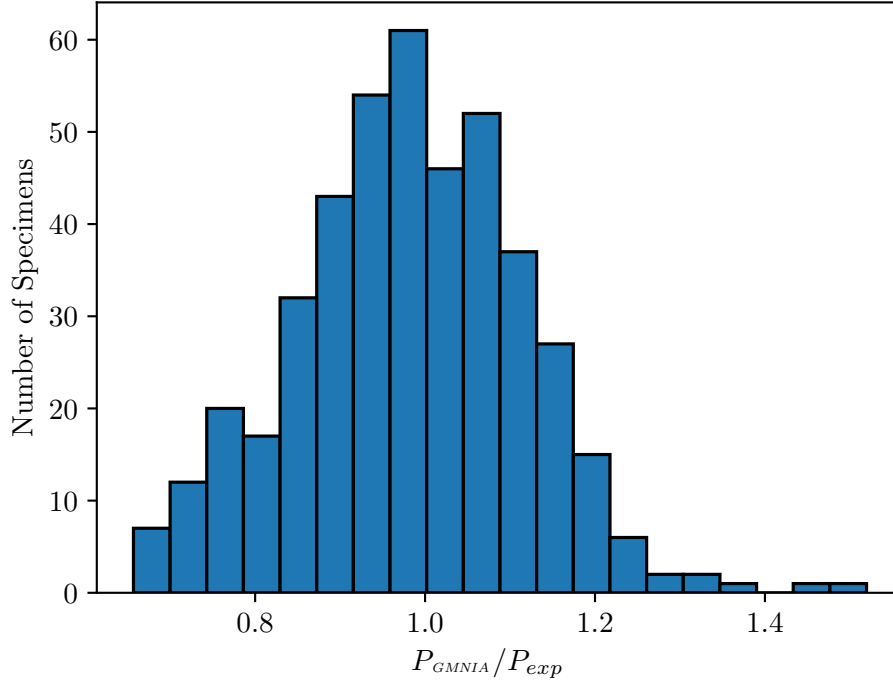
Figure 4.1: Histogram of validation results ($\delta_o = L/1000$)

from the experiment, P_{exp} are shown in Table 4.1. A histogram of the P_{GMNIA}/P_{exp} ratio for the case of $\delta_o = L/1000$ is shown in Figure 4.1.

Based on these results, the model is capable of accurately capturing the strength of RC columns. The mean value is closest to unity for initial out-of-straightness of $L/1333$. However, this does not necessarily mean that $L/1333$ is best representative of the actual out-of-straightness of the columns in the experimental database. It is likely still most appropriate to assume $L/1000$ as a conservative value for the development of design provisions.

Table 4.1: Statistical data of P_{GMNIA}/P_{exp} based on assumed initial geometric imperfection.

Initial Imperfection	Mean	St. Dev.	CoV
$\delta_o = L/1000$	0.981	0.135	0.138
$\delta_o = L/1333$	0.995	0.139	0.140
$\delta_o = L/2000$	1.014	0.140	0.138

To further investigate the accuracy of the model, scatter plots were produced showing the P_{GMNIA}/P_{exp} ratio as a function of column slenderness ratio (Figure 4.2), section aspect ratio (Figure 4.3), concrete compressive strength (Figure 4.4), and steel yield stress (Figure 4.5). No discernible relationship between P_{GMNIA}/P_{exp} and the parameters is noted, indicating that the model is not biased for any of these parameters.
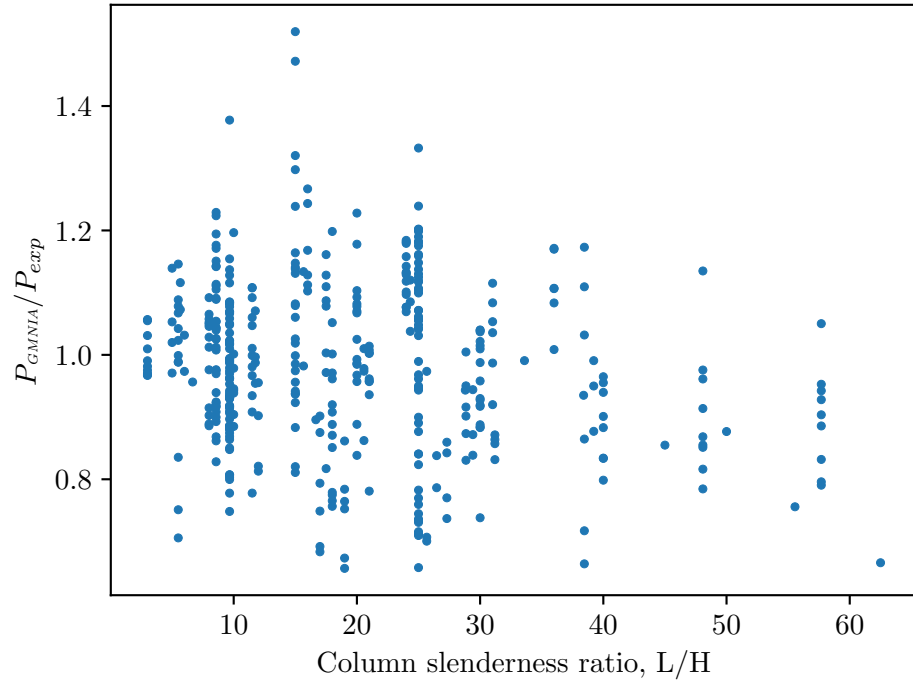
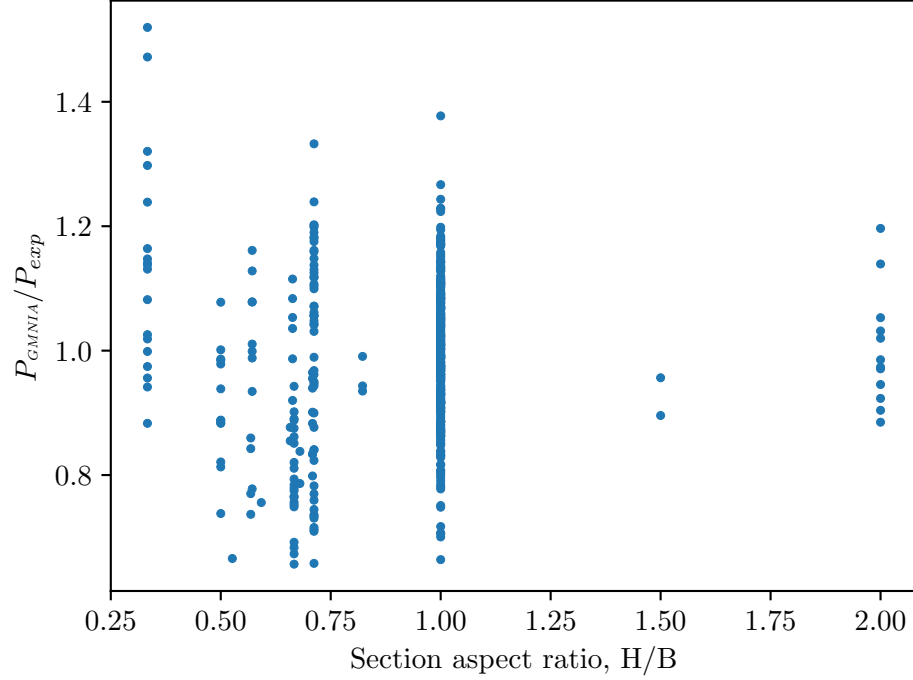Figure 4.2: Scatter plot of validation results vs. column slenderness ratio ($\delta_o = L/1000$)

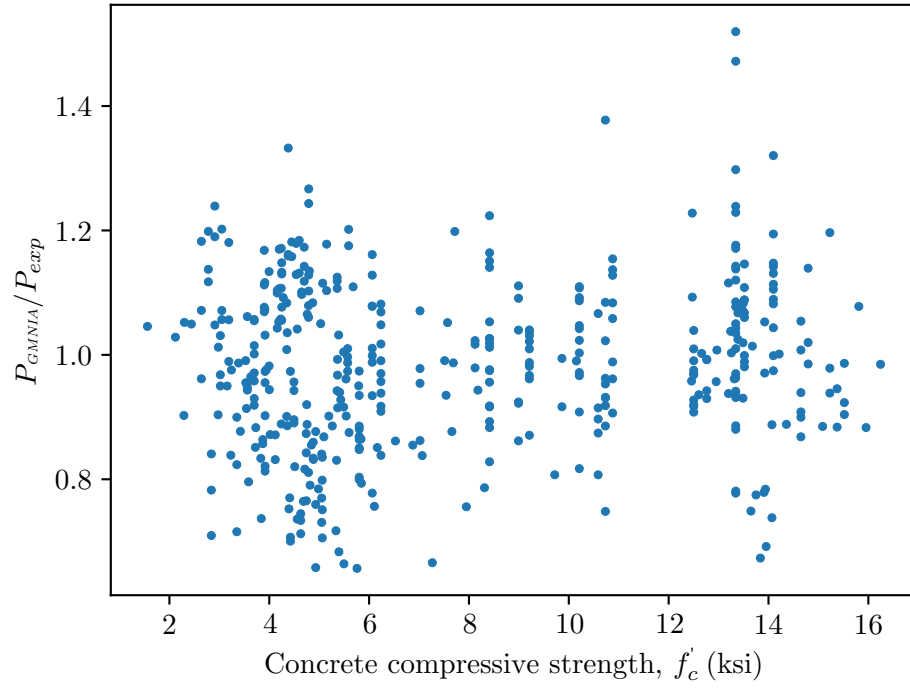Figure 4.3: Scatter plot of validation results vs. section aspect ratio ($\delta_o = L/1000$)

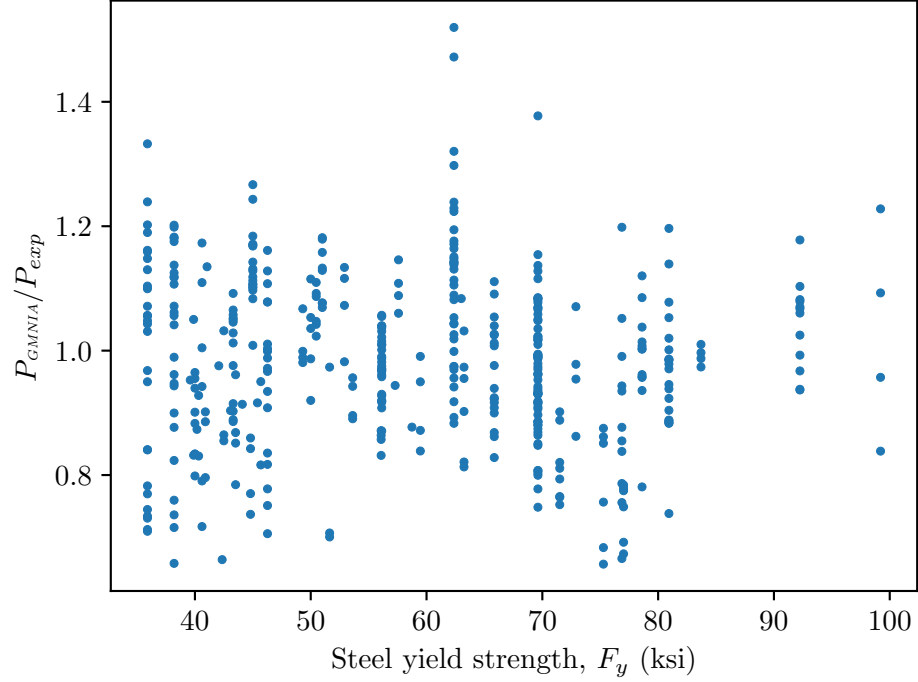Figure 4.4: Scatter plot of validation results vs. concrete compressive strength ($\delta_o = L/1000$)

Figure 4.5: Scatter plot of validation results vs. steel yield stress ($\delta_o = L/1000$)

4.2 Long-Term Loading of Rectangular Reinforced Concrete Columns

OpenSees models were developed for validation of long-term loading simulations against the experimental results.

4.2.1 Long-Term Loading Experiments

Jenkins and Frosch (2015) performed a series of long-term loading experiments on slender reinforced concrete columns of rectangular cross-section shown in Figure 4.6. The slenderness ratio, L/r, for the columns was either 40 or 70 giving column lengths L=6 ft and 10 ft. The section dimensions and steel reinforcing pattern are shown in Figure 4.6. In addition to slenderness ratios of 40 and 70, Jenkins and Frosch varied the bar sizes (#3 and #5) along with the load eccentricity, e/h, equal to 0.10 and 0.25.
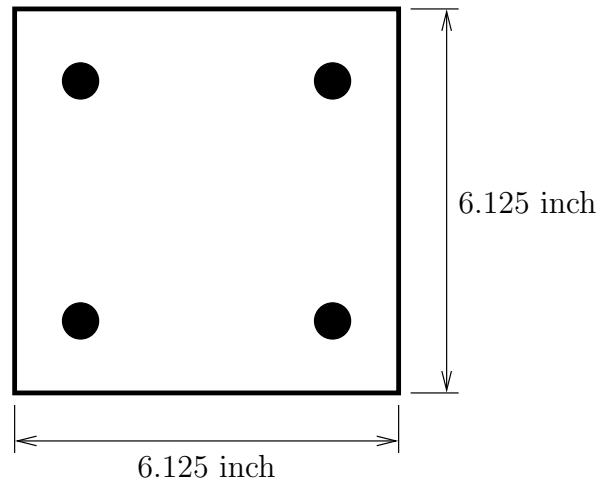
Figure 4.6: Reinforced concrete section details for experiments in Jenkins and Frosch (2015).

From the eight combinations of slenderness, bar size, and load eccentricity, the 12 specimens listed in Table 4.2 were tested under sustained loading. In four cases, two specimens of the same configuration were tested (denoted (2) in the table).

Table 4.2: Specimens tested by Jenkins and Frosch (2015) for sustained loading.

Specimen	Bar Size	Slenderness, L/r	Load Eccentricity, e/h
R3-40-10-LT	#3	40	0.10
R5-40-10-LT	#5	40	0.10
R3-40-25-LT (2)	#3	40	0.25
R5-40-25-LT (2)	#5	40	0.25
R3-70-10-LT (2)	#3	70	0.10
R5-70-10-LT (2)	#5	70	0.10
R3-70-25-LT	#3	70	0.25
R5-70-25-LT	#5	70	0.25

In the experiments, an axial load (with specified eccentricity) is held constant for about 100

days. If the column specimen did not fail during this "hold phase", the axial load is subsequently increased to determine the long-term column capacity.

Jenkins and Frosch (2015) report experimentally obtained values for the ultimate shrinkage strain, $\varepsilon_{shu}=750 \times 10^{-6}$, and ultimate creep factor, $\phi_u=3.3$. These values are input to the `CreepMaterial` wrapper along with $\psi_{cr1}=1$ and $\psi_{sh}=\psi_{cr2}=45.168$. The values for concrete strength, stiffness, and axial load during the "hold phase" are detailed by Jenkins and Frosch (2015), along with reinforcing steel material properties.

The subsequent figures compare the experimentally obtained a) displacement-time and b) load-displacement relationships for each column. Note that the recorded displacement is the lateral displacement at mid-height of each column. OpenSees models used a corotational mesh of eight `mixedBeamColumn` frame elements (to capture P-δ effects) with fiber sections defined by `Concrete04` and `Steel01` materials. Each section uses 40 concrete fibers (layers) through the section depth and one fiber for each reinforcing bar. Concrete fibers of negative bar area are collocated with the steel fibers so that the concrete contribution is not double counted.

In addition to simulations of short-term load effects with `Concrete04`, the following sections also present simulations of long-term loading using the `CreepMaterial` wrapper around `Concrete04`. This wrapper accounts for creep and shrinkage effects according to ACI209R-92 using the ultimate shrinkage strain and ultimate creep factor reported by Jenkins and Frosch (2015). Note that under short-term loading, a corotational mesh of displacement-based elements would be sufficient; however, the distribution of strain across each section will evolve under long-term creep and shrinkage effects, and the mixed formulation will maintain equilibrium along each element.

4.2.2 R3-40-10-LT and R5-40-10-LT

The first comparisons are for the case of $L/r=40$ and load eccentricity $e/h=0.1$ with #3 and #5 reinforcing bars. These conditions produce the least geometric effects and the specimens should pass the "hold phase" and be able to take on more axial load up to failure. As shown in Figure 4.7, the simulation does a good job of predicting the long-term displacement as well as the ultimate axial load after the "hold phase". For references, the short-term simulation predicts an ultimate column capacity of 172 kip while the long-term simulation predicts a capacity of 157 kip, closer to the experimental capacity of 150 kip.

Figure 4.7: Comparison of short-term and long-term OpenSees simulations with experimental results for specimen R3-40-10-LT: (a) displacement-time and (b) load-displacement.

The second specimen for the $L/r=40$ slenderness and $e/h=0.1$ load eccentricity uses #5 instead of #3 steel bars. With more steel, the axial load carrying capacity of the section should increase and the long-term load effects should decrease slightly compared to the case with #3 bars. As shown in Figure 4.8, the long-term deflection decreases while the axial load capacity increases compared to the previous case with #3 bars.

Figure 4.8: Comparison of short-term and long-term OpenSees simulations with experimental results for specimen R5-40-10-LT: (a) displacement-time and (b) load-displacement.

4.2.3 R3-40-25-LT and R5-40-25-LT

The second set of specimens maintains slenderness L/r=40 but has a higher axial load eccentricity, e/h=0.25, which should increase the bending moment in the column and thus the P-δ effect under long-term loading.

Two specimens, designated R3-40-25-LT-1 and R3-40-25-LT-2 were tested with #3 bars. As shown in the load-displacement plots of Figures 4.9 and 4.10, these specimens had little to no axial load capacity after the "hold phase". The simulated long-term models had difficulty capturing the loss of capacity due to creep and predicted gains in strength after the hold phase. However, the models of long-term concrete behavior generally predicted less capacity than the short-term models.
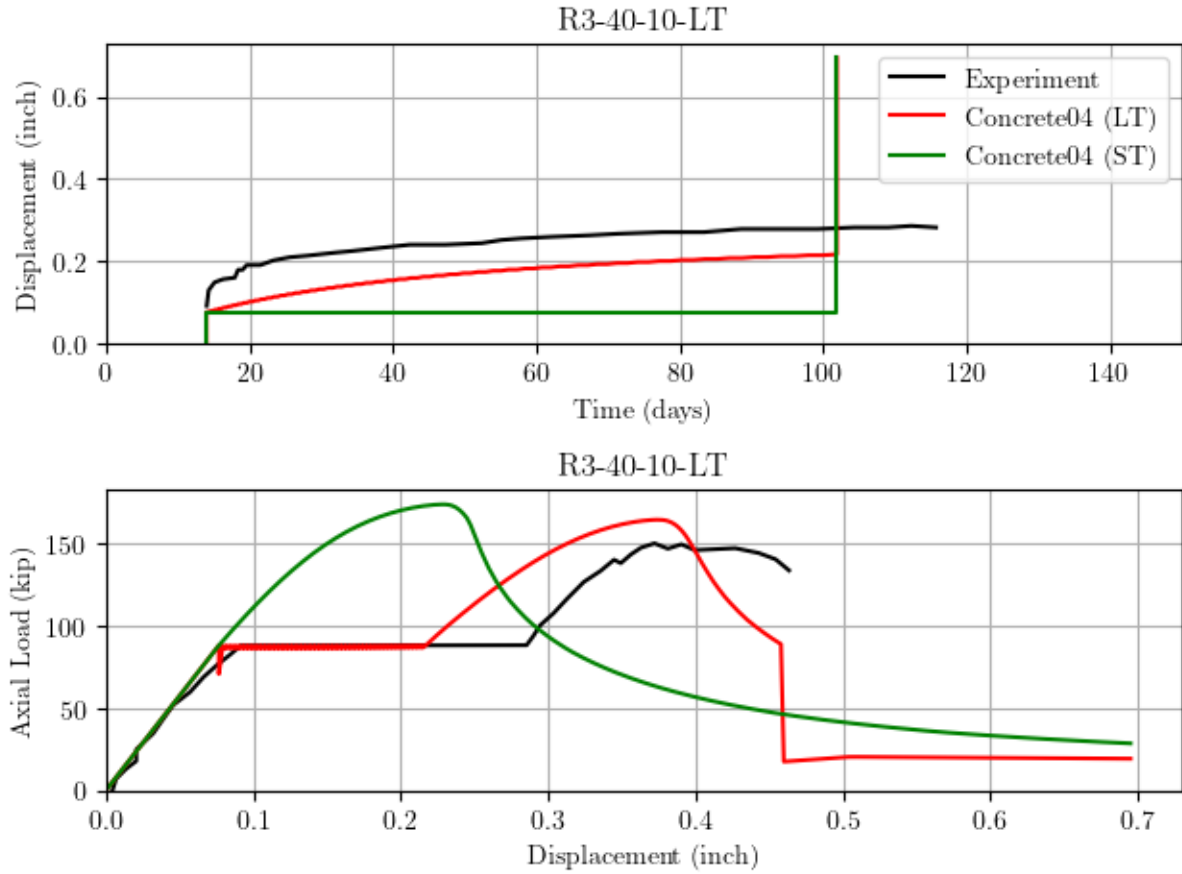

Figure 4.9: Comparison of short-term and long-term OpenSees simulations with experimental results for specimen R3-40-25-LT-1: (a) displacement-time and (b) load-displacement.
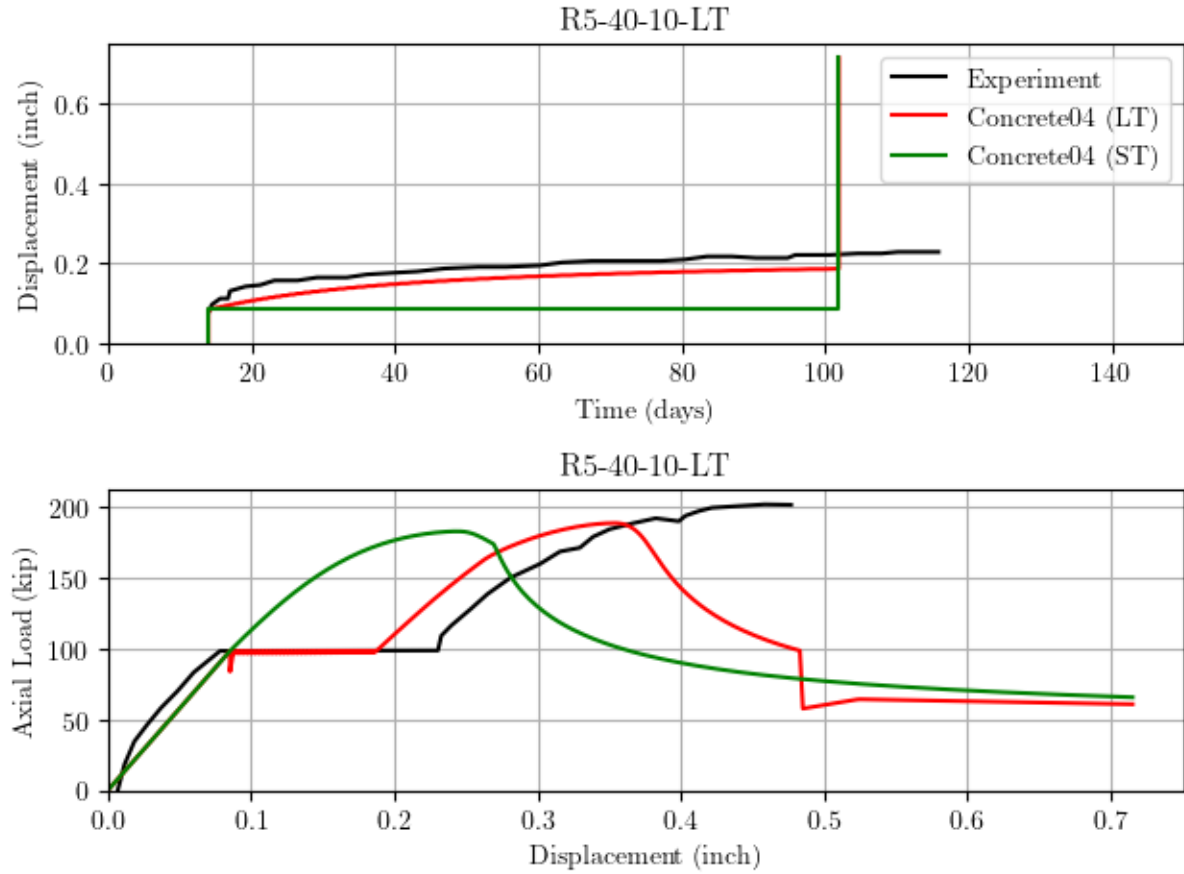
Figure 4.10: Comparison of short-term and long-term OpenSees simulations with experimental results for specimen R3-40-25-LT-2: (a) displacement-time and (b) load-displacement.

Two specimens were tested with #5 bars and slenderness and eccentricity of $L/r{=}40$ and $e/h{=}0.25$, respectively. With more steel, these columns fared better after the hold phase, able to take on additional axial load. The simulated results using long-term concrete showed lower axial load capacity than the simulations based on short-term concrete behavior; however, the simulated results did not match the experiments very well, perhaps due to the high amount of flexure resulting from the increased load eccentricity.

Figure 4.11: Comparison of short-term and long-term OpenSees simulations with experimental results for specimen R5-40-25-LT-1: (a) displacement-time and (b) load-displacement.
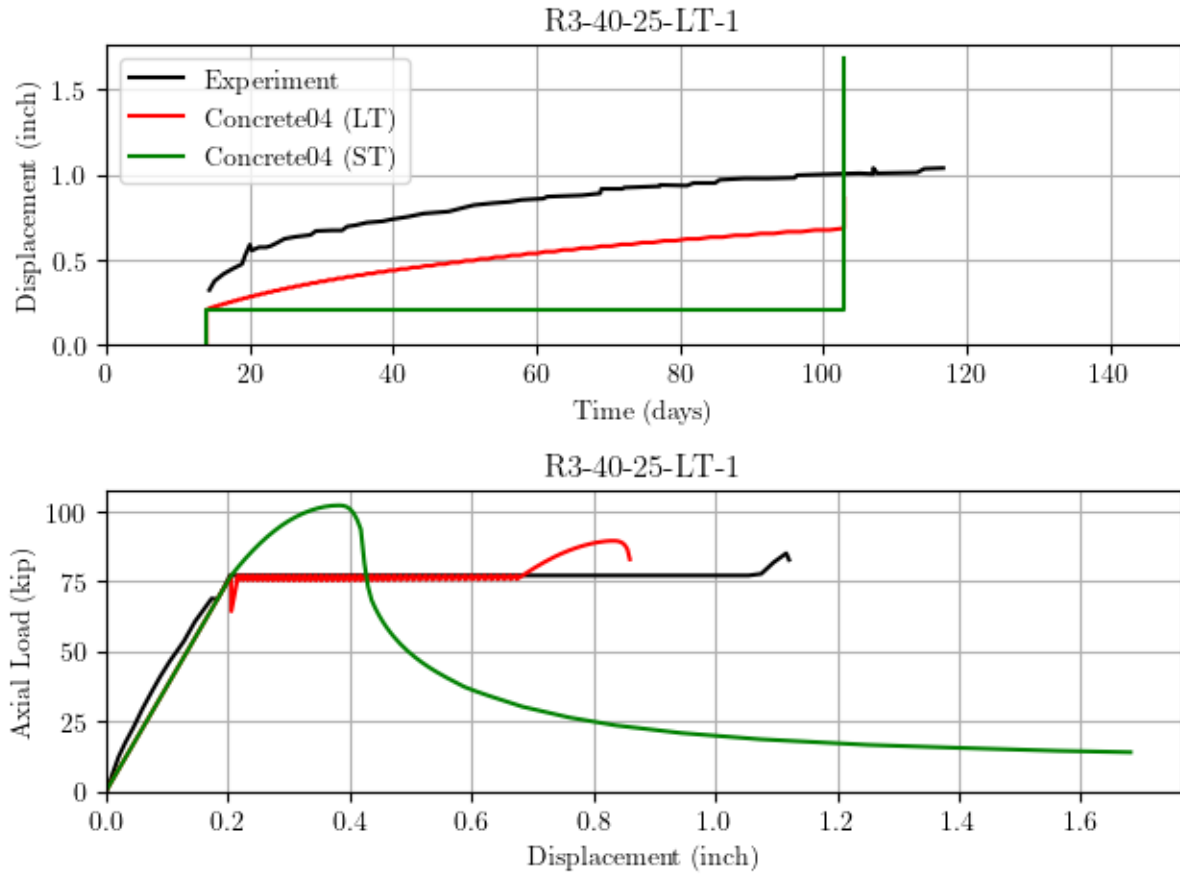
Figure 4.12: Comparison of short-term and long-term OpenSees simulations with experimental results for specimen R5-40-25-LT-2: (a) displacement-time and (b) load-displacement.

4.2.4 R3-70-10-LT and R5-70-10-LT

The next set of specimens were for higher slenderness, L/r=70, and low load eccentricity, e/h=0.10. The experimental and simulated results for two specimens using #3 bars are shown in Figures 4.13 and 4.14. Although both specimens had the same sustained load, only the R3-70-10-LT-1 specimen was able to carry additional axial load after the hold phase. The long-term concrete model was able to simulate this case well, but the simulated results did not predict the failure during the hold phase for R3-70-10-LT-2.

Figure 4.13: Comparison of short-term and long-term OpenSees simulations with experimental results for specimen R3-70-10-LT-1: (a) displacement-time and (b) load-displacement.
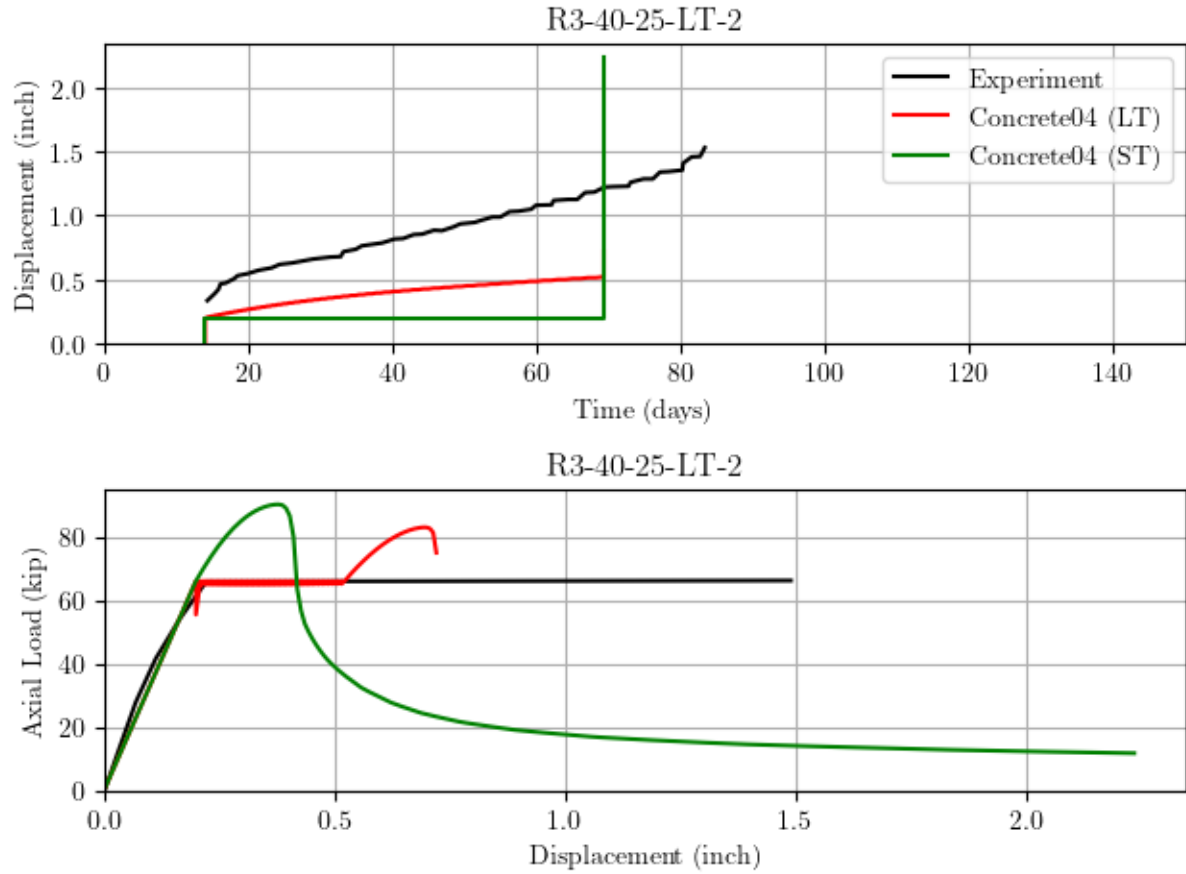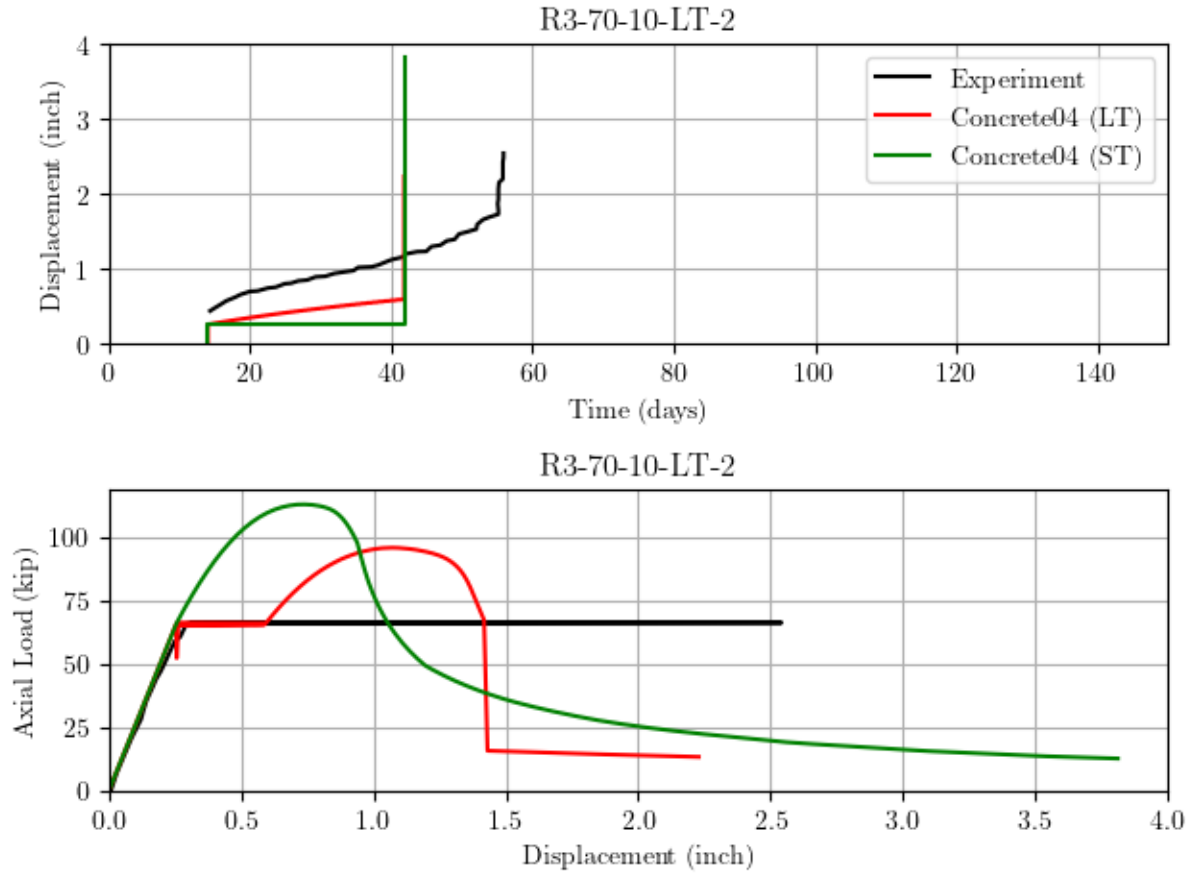
Figure 4.14: Comparison of short-term and long-term OpenSees simulations with experimental results for specimen R3-70-10-LT-2: (a) displacement-time and (b) load-displacement.

With the larger steel area owing to #5 bars, both specimens shown in Figures 4.15 and 4.16 are able to pass the hold phase and resist additional axial load. The prediction of axial load capacity using long-term concrete models is reasonable for both specimens with #5 bars.
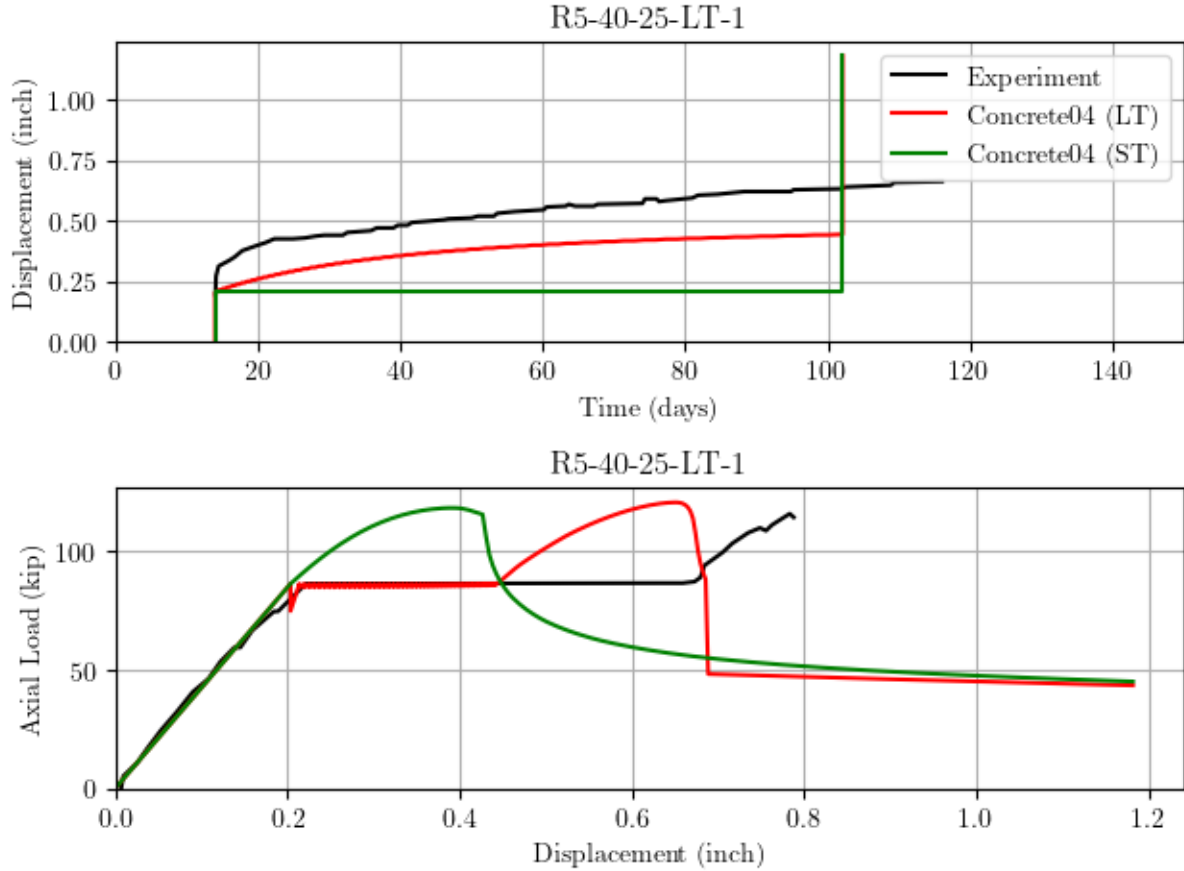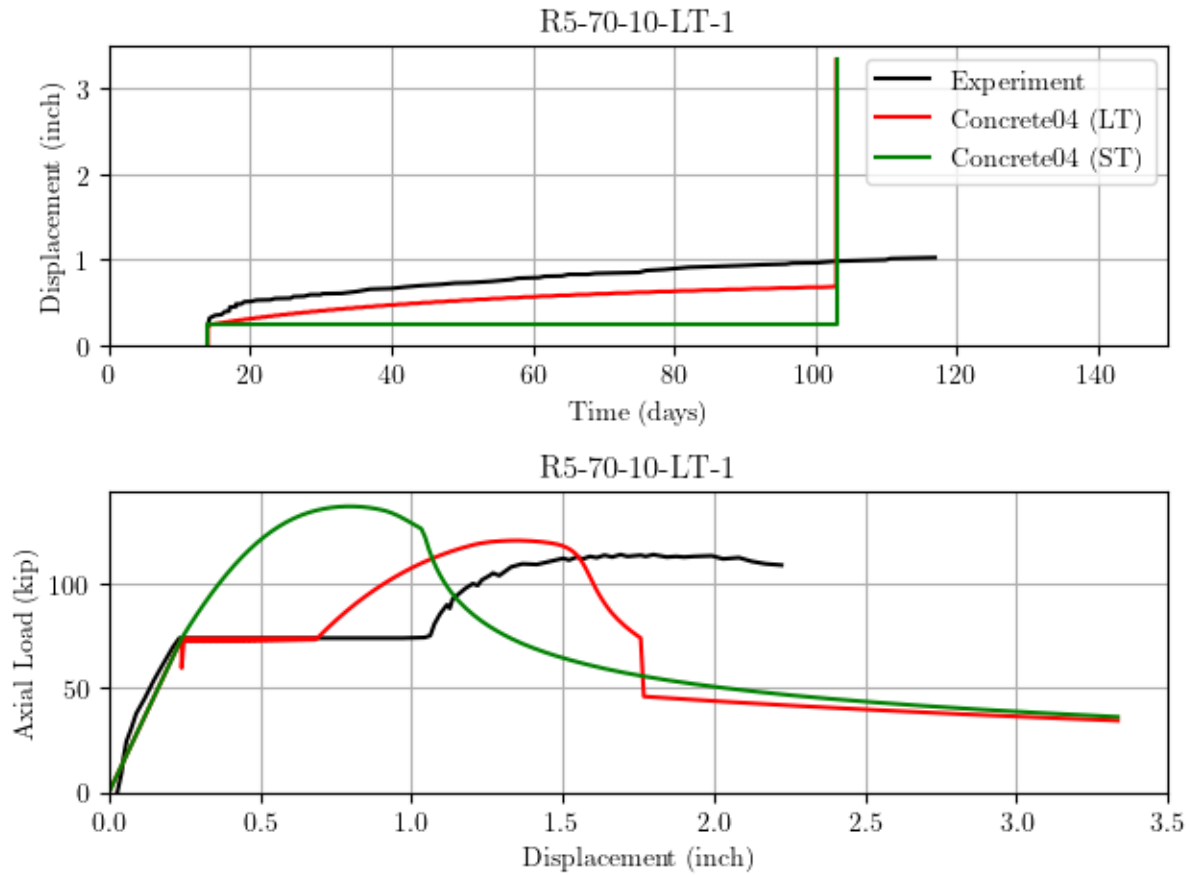

Figure 4.15: Comparison of short-term and long-term OpenSees simulations with experimental results for specimen R5-70-10-LT-1: (a) displacement-time and (b) load-displacement.
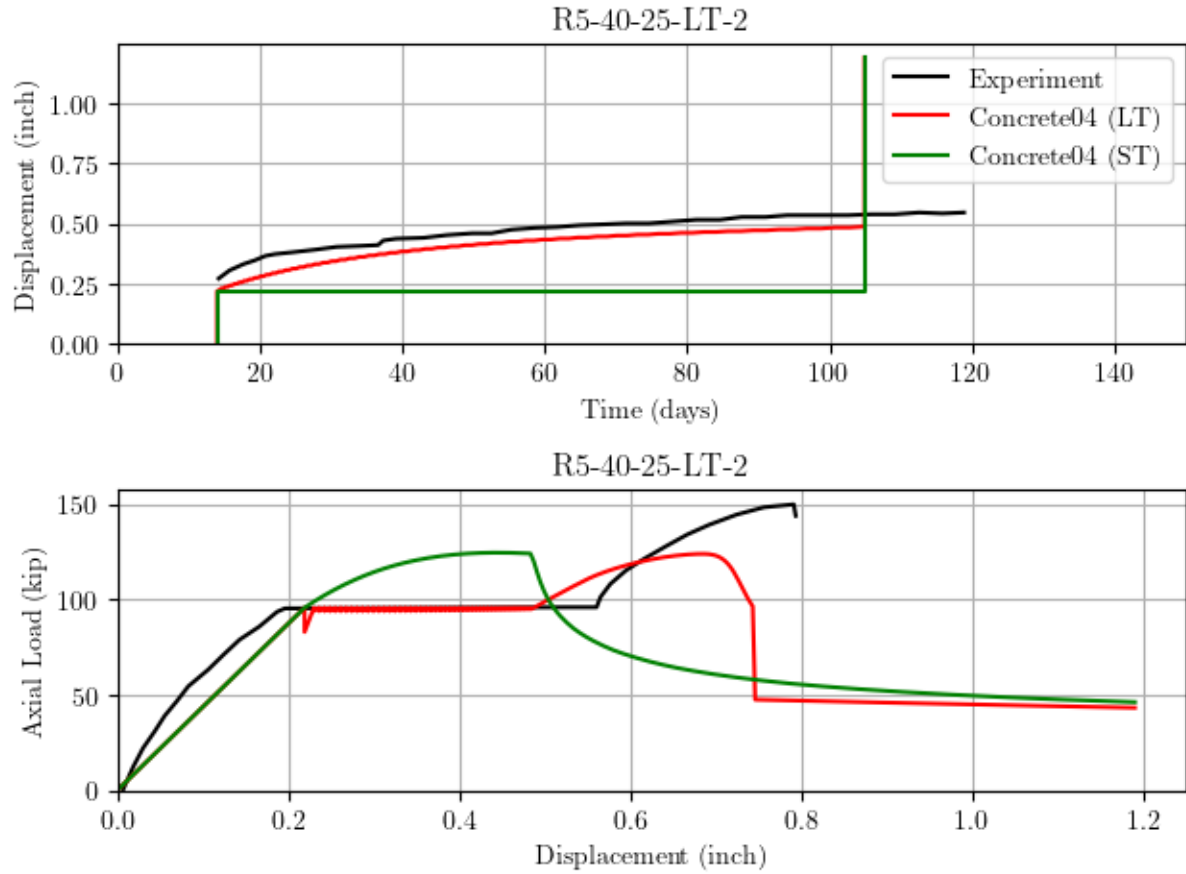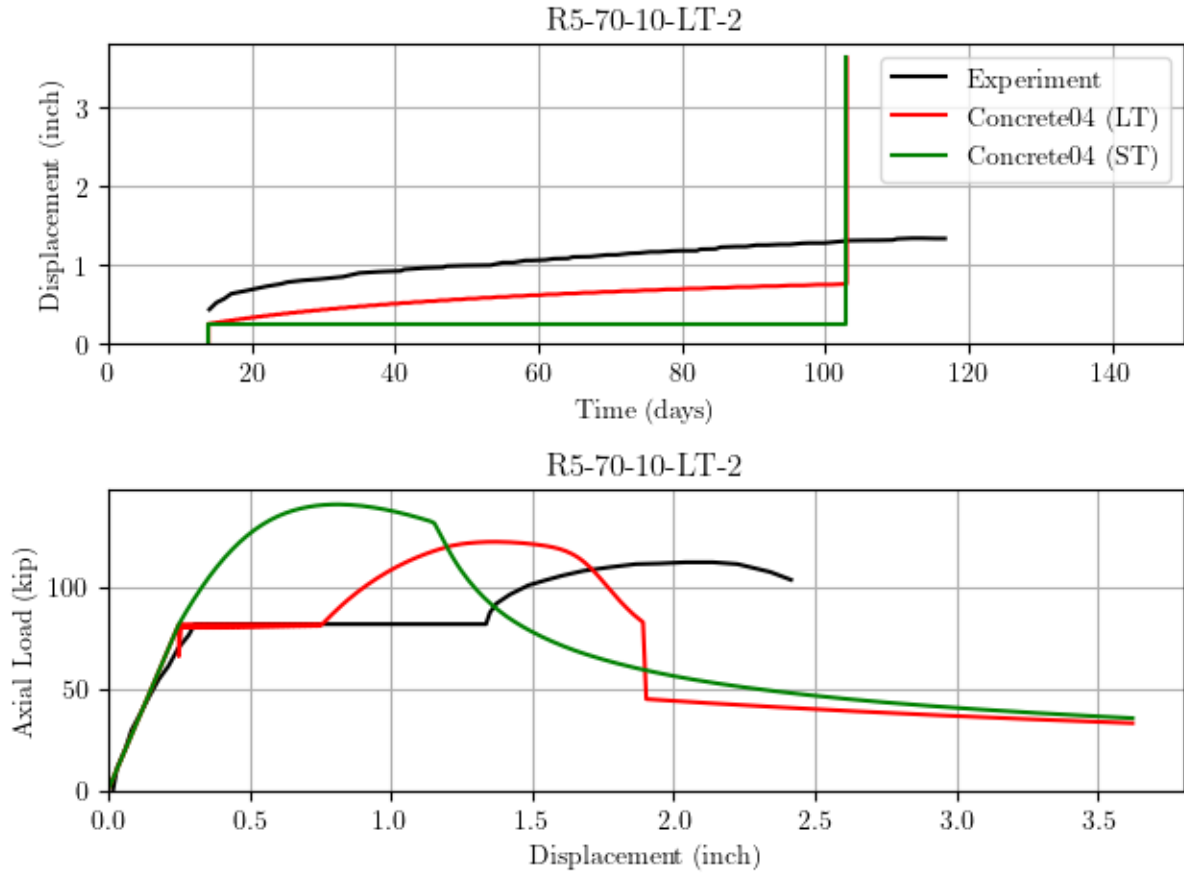
Figure 4.16: Comparison of short-term and long-term OpenSees simulations with experimental results for specimen R5-70-10-LT-2: (a) displacement-time and (b) load-displacement.

4.2.5 R3-70-25-LT and R5-70-25-LT

The final group of specimens were of high slenderness, $L/r=70$, and high axial load eccentricity, $e/h=0.25$. For these cases, the magnitude of the sustained load was reduced to under 40 kip. As shown in Figure 4.17, the long-term concrete model does a good job of simulating the experimental results, both in deflection and load. For the case of #5 bars shown in Figure 4.18, the long-term concrete simulation adequately predicts the ultimate strength, but under predicts the lateral deflections.
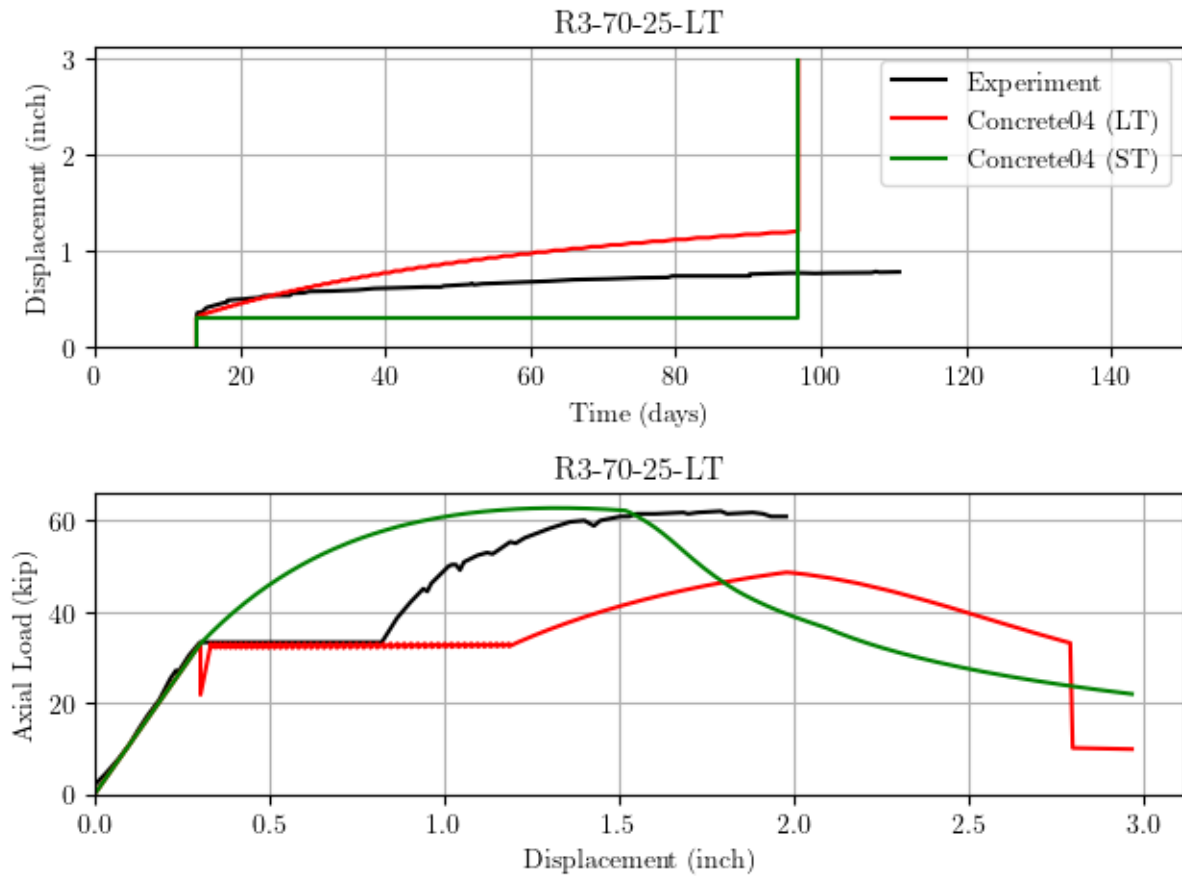
Figure 4.17: Comparison of short-term and long-term OpenSees simulations with experimental results for specimen R3-70-25-LT: (a) displacement-time and (b) load-displacement.
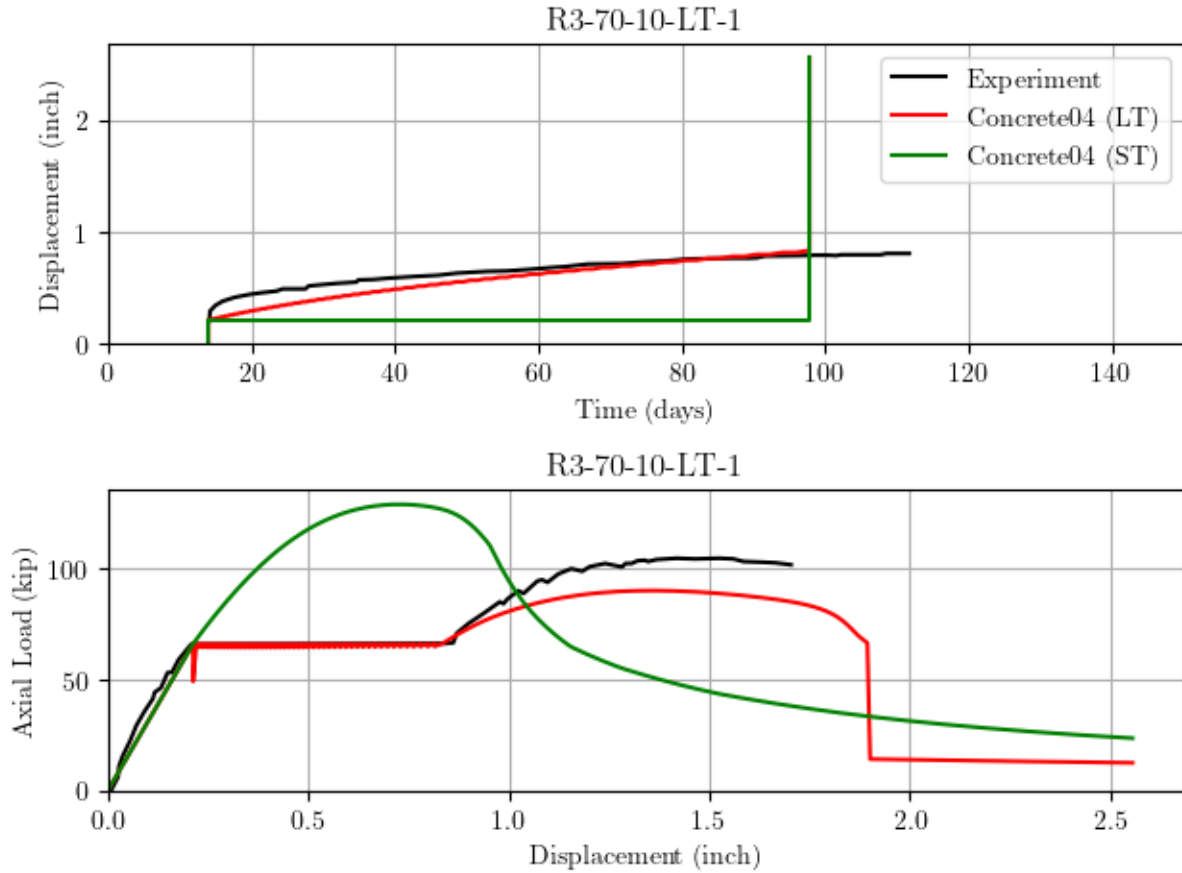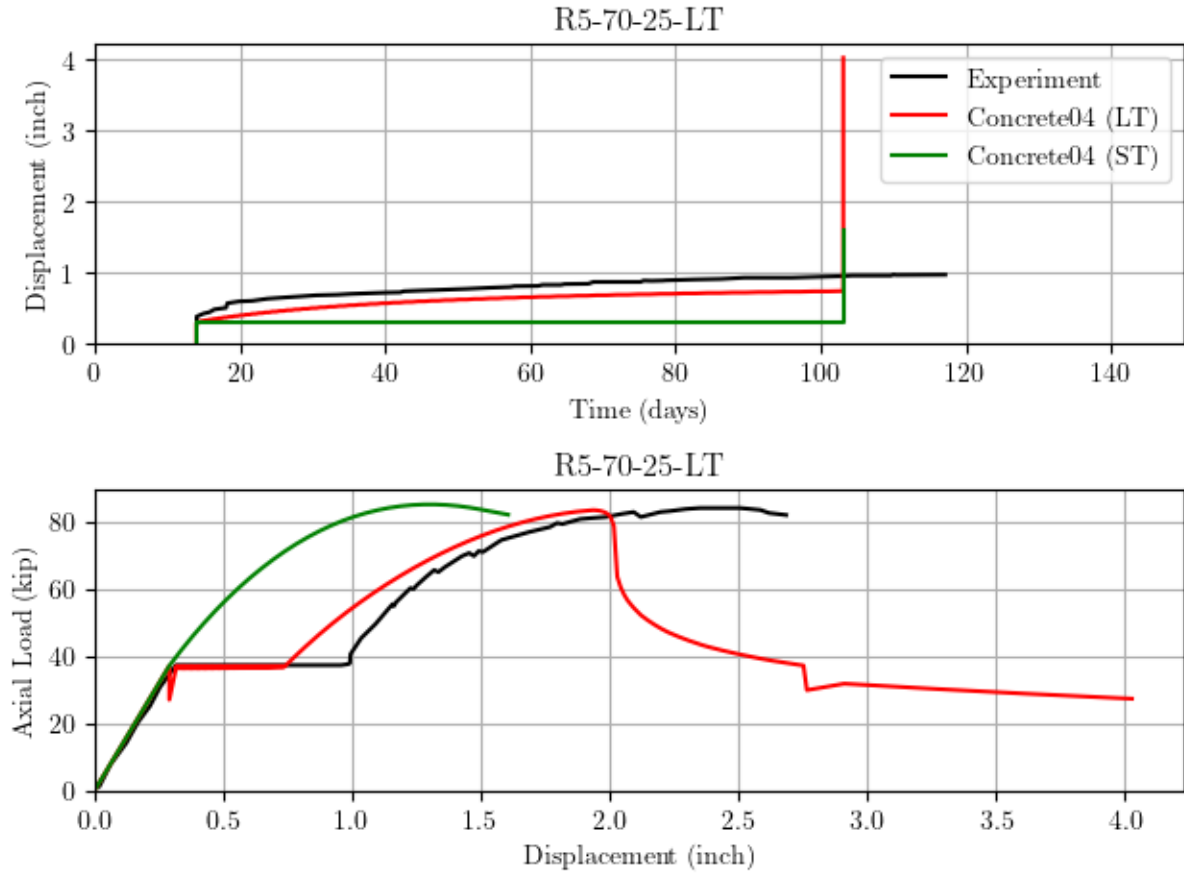
Figure 4.18: Comparison of short-term and long-term OpenSees simulations with experimental results for specimen R5-70-25-LT: (a) displacement-time and (b) load-displacement.

### 4.2.6 Summary of Results

Across all specimens, the maximum axial load predicted using long-term concrete models tended to be 10-20% less than the maximum axial load predicted using short-term concrete models. However, the simulated results did not always predict lower axial load capacity than that recorded in the experiments. Table 4.3 shows the maximum axial loads observed and predicted for all specimens while Figure 4.19 gives a graphical summary of the maximum axial loads.

Table 4.3: Summary of maximum axial load (kip) recorded in the long-term load experiments of Jenkins and Frosch (2015) and simulated OpenSees results using the long-term creep wrapper (LT) around `Concrete04` and short-term (ST) model of standalone `Concrete04`.

Specimen	Experiment	Concrete04 (LT)	Concrete04 (ST)
R3-40-10-LT	150	164	174
R3-40-25-LT-1	84.9	89.3	102
R3-40-25-LT-2	66.1	82.9	90.1
R3-70-10-LT-1	105	90	129
R3-70-10-LT-2	66.1	95.7	113
R3-70-25-LT	62	48.6	62.7
R5-40-10-LT	202	189	183
R5-40-25-LT-1	115	120	118
R5-40-25-LT-2	150	124	124
R5-70-10-LT-1	114	121	137
R5-70-10-LT-2	112	122	140
R5-70-25-LT	83.9	83.3	85
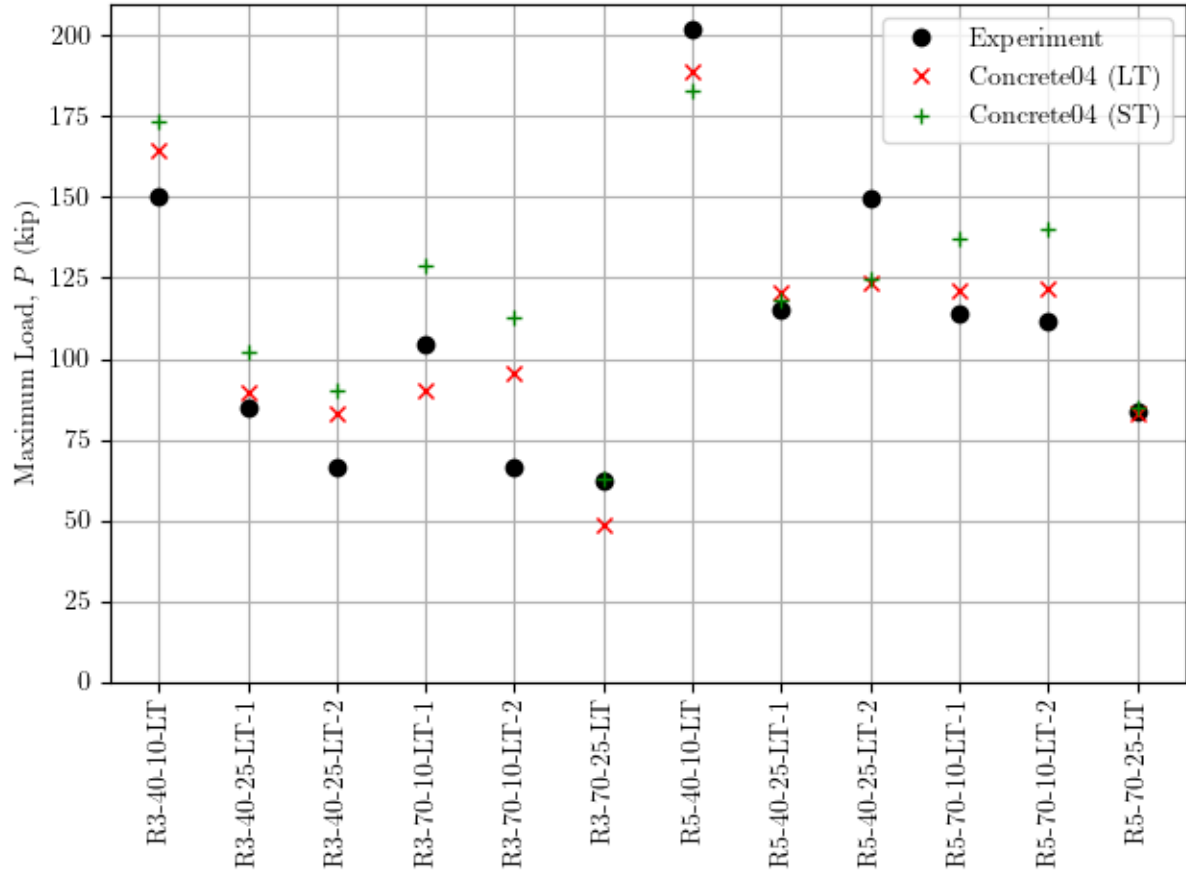
Figure 4.19: Maximum axial loads (kip) recorded in the long-term load experiments of Jenkins and Frosch (2015) and simulated OpenSees results using the long-term creep wrapper (LT) around `Concrete04` and short-term (ST) model of standalone `Concrete04`.
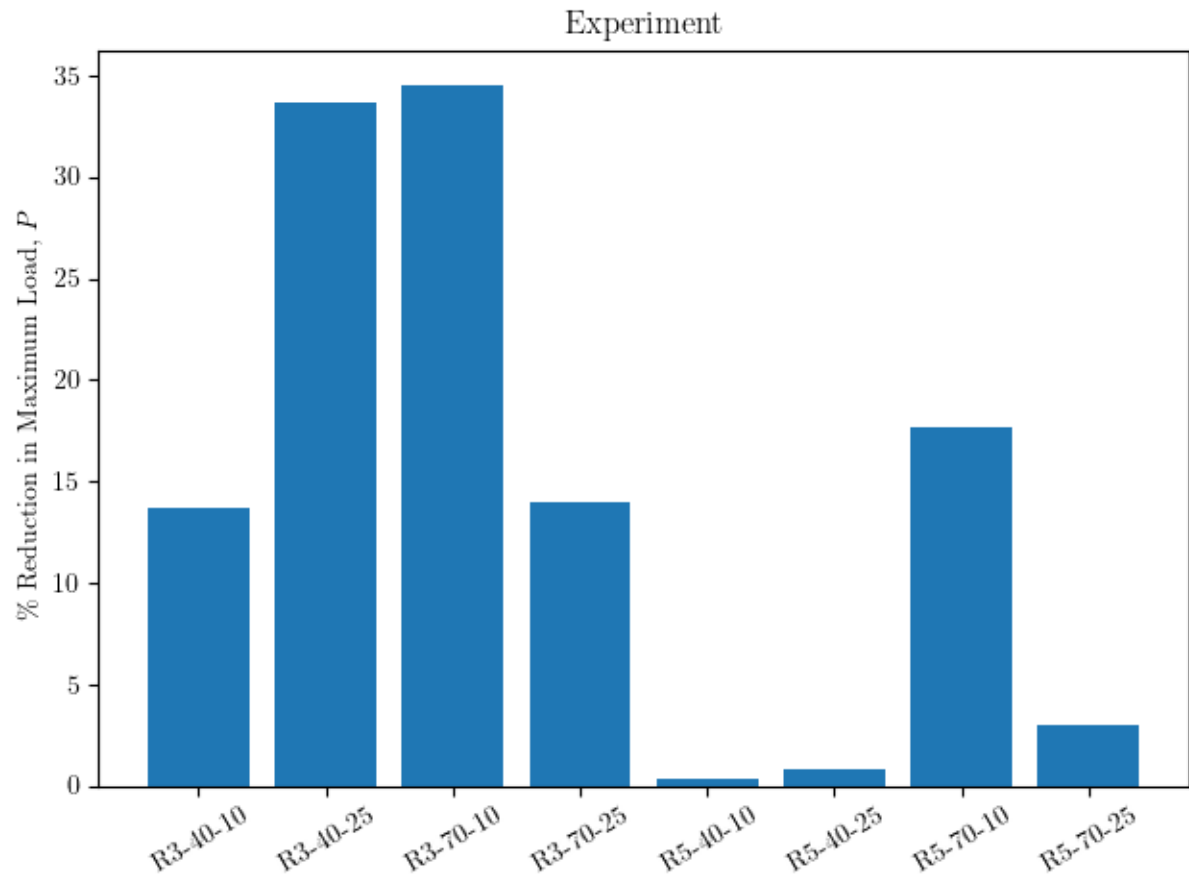
Figure 4.20: Reduction in maximum axial load capacity observed in experiments of short-term and long-term loading.
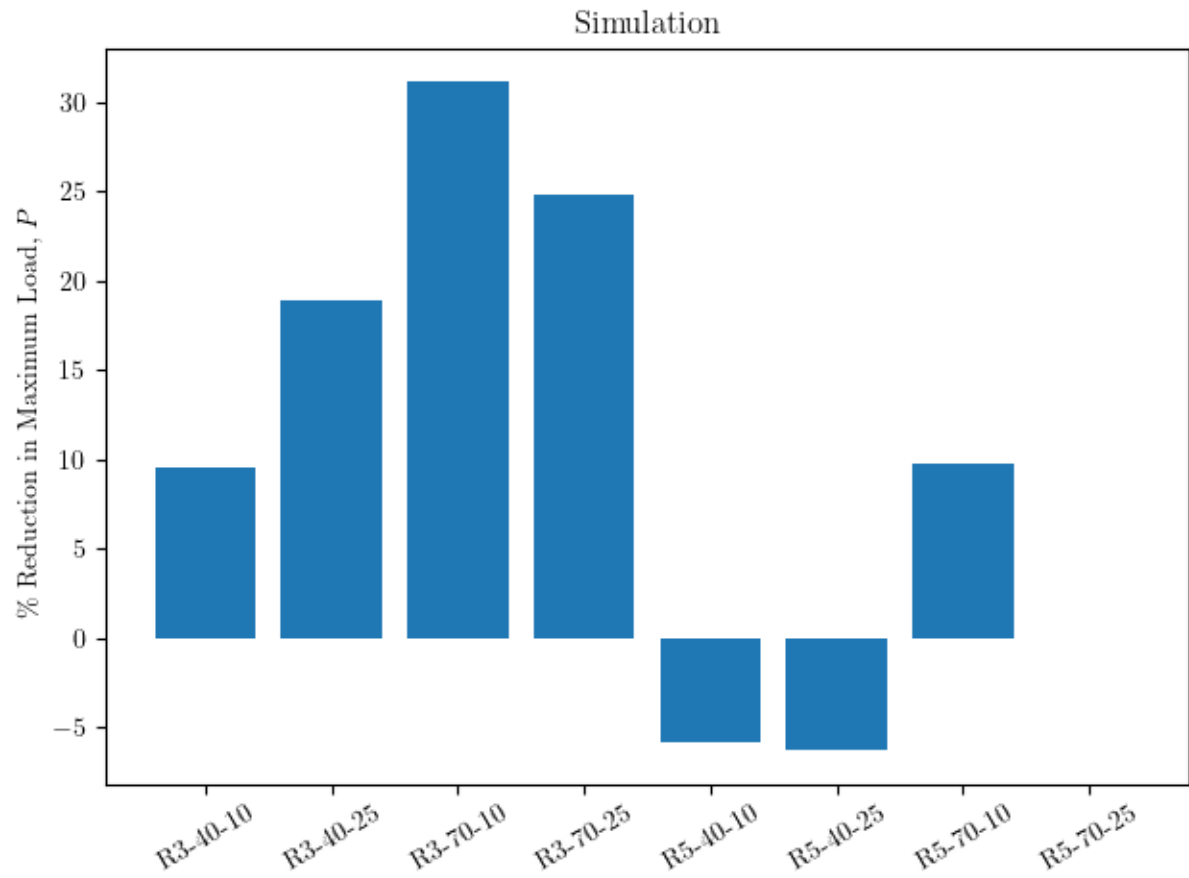
Figure 4.21: Reduction in maximum axial load capacity based on simulation of short-term and long-term loading.
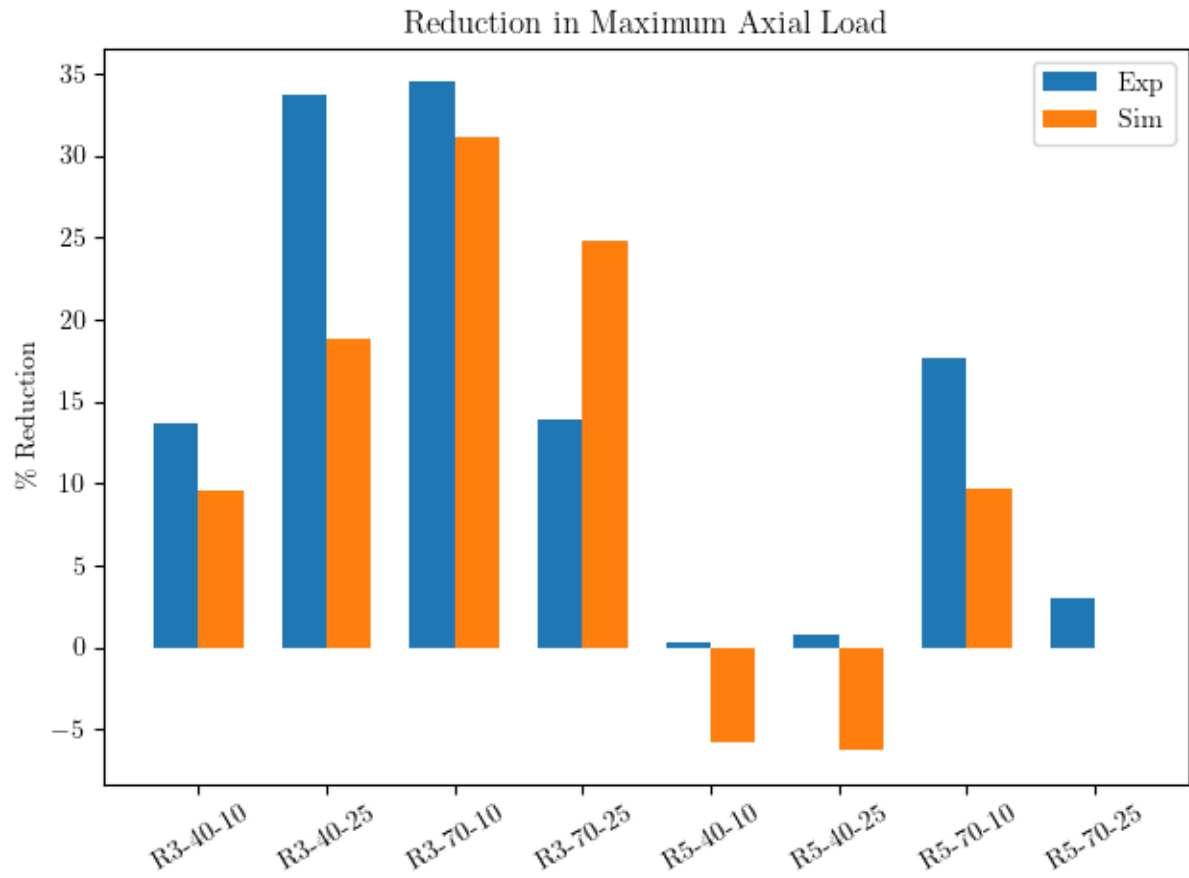
Figure 4.22: Comparison of simulated and experimentally observed reduction in maximum axial load capacity for short-term and long-term loading.

Chapter 5

Evaluation of the Current Design Method

To evaluate the current AASHTO LRFD approximate method for design of slender reinforced concrete bridge columns, comparisons were made between the maximum applied loads permitted by the design methodology and maximum applied loads from a second-order inelastic analysis using the model described in Chapter 3. The comparisons were made for a wide range of cases and are described separately for short-term loading and long-term loading. To evaluate many cases, the comparisons were automated to the maximum extent possible with code written in the Python programming language.

5.1 Short-Term Loading

This section evaluates the short-term strength of bridge columns. While bridges are always subject to long-term loading, it remains important to investigate short-term behavior. The behavior of a column subject to short-term loading represents a bound of the range of long-term behavior with short-term strength being an upper limit of the time-dependent strength. Additional deformations due to creep and shrinkage will only reduce the apparent strength of the column. Additionally, current design provisions for long-term loading are based on short-term behavior with a correction for long-term effects and it is unclear that an alternative approach, not based on short-term behavior, would provide any benefit. Furthermore, a broader evaluation of cases is possible when investigating short-term loading given the extra computational expense of evaluating columns subject to long-term loading.

5.1.1 Parametric Suite

This section describes the parametric suite of individual column cases that are investigated for short-term loading. The suite includes cases with different cross-sectional shapes and sizes, different steel ratios, different member lengths, different boundary conditions, different bending axis (for obround columns), and sway condition (sway or nonsway).

Cross Sections

The RC cross sections selected for investigation in this work represent the range of typical practice for Caltrans for the parameters most important to strength and stability. The parameters varied among the selected cross sections are:

- **Cross-sectional shape**, circle or obround as shown in Figure 5.1. An obround is a shape that consists of two semicircles connected by parallel lines tangent to their endpoints.

- **Bending axis**, x axis or y axis (only for obround shapes). Unlike circular sections, obround sections are not rotationally symmetric, which results in different response characteristics depending on the orientation of the applied bending moments. The bending axis of an obround shape refers to the axis about which the bending moments are applied. The x axis is the minor axis of the shape, while the y axis is the major axis of the shape, as denoted in Figure 5.1.

- **Cross-sectional dimensions**. Three different diameters, D, were considered for the columns: 16, 48, and 72 in. In the case of obround shapes, the diameter corresponds to the diameter of the semicircles that make up the ends of the shape. The diameter is also the smaller of the two lateral dimensions of the obround. Caltrans guidelines specify that the obround lengths should range from 1.25 times the diameter $(1.25D)$ to 1.75 times the diameter $(1.75D)$. As a result, the distance between the centers of each semicircle within the obround shape, a (Figure 5.1b), varies from 0.25 times the diameter $(0.25D)$ to 0.75 times the diameter $(0.75D)$. A middle value of a equal to 0.5 times the diameter (i.e., $a = 0.5D$) was selected as representative.

- **Longitudinal steel ratio**. The nominal longitudinal steel ratio, $\rho_{nominal}$, was varied at 1%, 2%, 3%, and 4%. The actual longitudinal steel ratio, denoted as ρ or ρ_{actual}, is defined as the ratio of the cross-sectional area of the longitudinal steel reinforcement (A_s) to the gross cross-sectional area of the column (A_g). The number of bars and bar sizes were selected for each cross-sectional size and nominal steel ratio as described in Table 5.1 for circular cross sections and Table 5.2 for obround cross sections. These reinforcing configurations are reasonably representative of typical practice. For example, configurations were selected such that the spacing between the bars was between 3.8 in. and 8.4 in. However, in practice, bundled bars are often used in lieu of large bar sizes (e.g., #18). Also, #5 bars are not commonly used for longitudinal reinforcing. The large and small bar sizes are used in this work for simplicity.

Other parameters are constant among the selected cross sections, including:

- Concrete compressive strength, $f'_c = 4$ ksi

- Yield strength of longitudinal reinforcement steel, $f_y = 60$ ksi

- Yield strength of transverse reinforcement, $f_{yt} = 60$ ksi

- Cover to transverse reinforcing, 2 in. This value is based on Table 5.10.1-1 of California Amendments to AASHTO LRFD (Caltrans, 2019) for columns in a non-corrosive exposure condition.

- Transverse reinforcing of #4 hoops at 8 in. on center. Transverse reinforcing has a minor effect on the strength of the column determined from GMNIA since the model considers

(a)

Interior bars used for
constructability are
not modeled

(b)
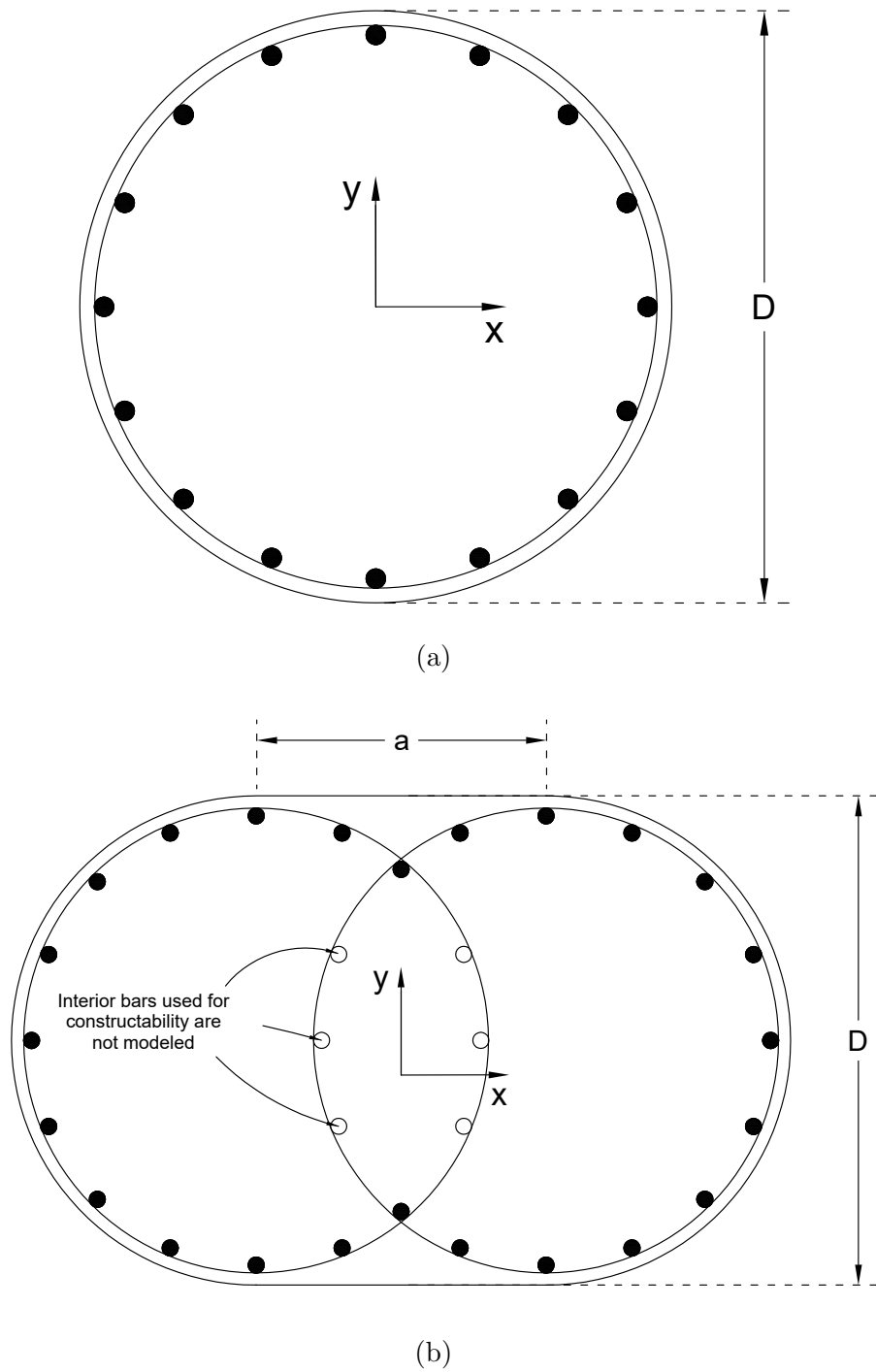
Figure 5.1: Dimensions and coordinate axes of cross sections, (a) circle and (b) obround.

Table 5.1: Longitudinal reinforcing for circular sections

D (in.)	ρ_{nominal} (%)	ρ_{actual} (%)	Number of bars	Bar size
16	1	1.23	8	#5
	2	2.16	14	#5
	3	2.98	10	#7
	4	3.93	10	#8
48	1	0.99	18	#9
	2	2.07	24	#11
	3	2.98	24	#14
	4	3.98	32	#14
72	1	1.00	26	#11
	2	1.99	36	#14
	3	2.98	54	#14
	4	3.93	40	#18

Table 5.2: Longitudinal reinforcing for obround sections

D (in.)	$\rho_{nominal}$ (%)	ρ_{actual} (%)	Number of bars	Bar size
16	1	1.13	12	#5
	2	2.14	16	#6
	3	2.92	16	#7
	4	4.01	22	#7
48	1	1.07	40	#8
	2	2.03	60	#9
	3	3.06	58	#11
	4	3.95	52	#14
72	1	0.99	52	#10
	2	2.01	86	#11
	3	3.04	90	#14
	4	3.98	118	#14

confinement. The interaction strength per AASHTO LRFD does not depend on the transverse reinforcing. Accordingly, to produce conservative results, the single-column analyses in this project will use reinforcing representative of a lower bound of Caltrans practice. Note that Section 5.10.4.3 of AASHTO LRFD requires 1) a minimum tie bar size of #3 if the longitudinal bars are #10 or smaller and #4 bars otherwise; and 2) a maximum spacing of 12 in. or the least dimension of the member, whichever is less.

For the obround shapes, no bars are included in the middle of the cross section. These middle bars are typically included for constructability, but not considered for strength and not subject to the same detailing requirements (e.g., splicing) as the main longitudinal reinforcing bars (Figure 5.1).

Across the parametric suite, 36 cross sections were selected for investigation: 3 cross-sectional types (circular, obround bent about the x-axis, obround bent about the y-axis) $\times$ 3 diameters $\times$ 4 longitudinal steel ratios = 36.

Column Configurations

Each cross section was investigated with a variety of sway (sidesway uninhibited) and nonsway (sidesway inhibited) column configurations as shown in Figure 5.2. Each configuration had a different member length and boundary conditions. The member length was defined using eight length-to-diameter (L/D) values: 5, 10, 15, 20, 25, 30, 35, and 40. The boundary conditions were different for sway and nonsway columns.

For sway columns, the boundary conditions were defined by the rotational stiffness of the springs at the top and bottom of the column, k_{top} and k_{bot}, respectively. The spring stiffnesses were defined relative to the column stiffness using parameters $G_{n,top}$ and $G_{n,bot}$ as

$$k_{top} = \frac{6(0.4E_cI_g)}{G_{n,top}L} \tag{5.1}$$

$$k_{bot} = \frac{6(0.4E_cI_g)}{G_{n,bot}L} \tag{5.2}$$

where L is the length of the column and I_g is the gross moment of inertia of the concrete section about its centroidal axis, neglecting reinforcement.

Values for $G_{n,top}$ and $G_{n,bot}$ were back-calculated from selected nominal values of the effective length factor K. The nominal K in the table corresponds to a scenario where the column's flexural rigidity (EI) equals $0.4E_cI_g$. In this case, the values of $G_{n,top}$ and $G_{n,bot}$ are selected to achieve the desired length factor K. Selected values of $G_{n,top}$ and $G_{n,bot}$ are listed in Table 5.3.

For nonsway columns, the boundary conditions are defined by the ratio of end moments, β, as shown in Figure 5.2. The values of β, 1.0, 0.5, 0.0, and -0.5, define the ratio of applied moment at the top of the column to applied moment at the bottom of the column. These β values explore different load distributions and configurations that affect the bending behavior and overall response of nonsway columns.

The chosen L/D ratios and boundary conditions in the parameter suite explore individual column behavior under varying column slenderness and load conditions. Systematic analysis shed light on the stability and strength of columns subjected to axial compression and bending.
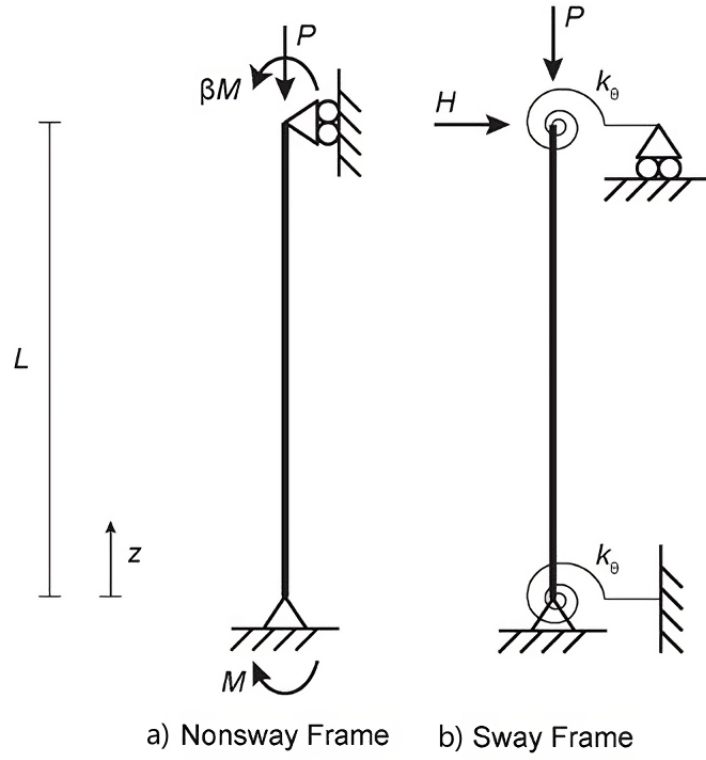
Figure 5.2: Example nonsway (left) and sway (right) columns.

Table 5.3: Boundary conditions for sway columns

Pair	$G_{n,top}$	$G_{n,bot}$	K (nominal)
1	0 (Fixed)	∞ (Pinned)	2.0
2	0.604	∞ (Pinned)	2.2
3	1.228	∞ (Pinned)	2.4
4	0 (Fixed)	0 (Fixed)	1.0
5	0.614	0.614	1.2
6	1.288	1.228	1.4
7	2.042	2.042	1.6

With the aforementioned parameters, 88 column configurations are selected: 8 member lengths × (7 sway boundary condition options + 4 nonsway boundary condition options) = 88. Each cross section analyzed for each column configuration results in 3,168 individual cases (2,016 sway cases and 1,152 nonsway cases) for investigation.

Each case is named using a specific format, e.g., "C08-L35-NS02" and "Ox04-L15-S01" The first letter designates the cross-sectional shape, with "C" representing circular sections and "Ox" and "Oy" representing obround sections. The second letter indicates the bending axis orientation for obround sections, with "x" denoting the x-axis and "y" indicating the y-axis. The subsequent two digits signify the unique identifier for the cross-section. The letter "L" is followed by a numerical value, representing the length-to-depth ratio of the cross-section. In the provided example, "L35" indicates a length-to-depth ratio of 35. The final component represents the sway condition, with "NS" indicating nonsway condition and "S" indicating sway condition. The final number, e.g., "02", represents the column's end condition, signifying β for nonsway cases and boundary condition for sway cases.

5.1.2 Maximum Permitted Applied Loads According to AASHTO LRFD

AASHTO LRFD includes provisions for assessing the strength of slender reinforced concrete columns. In general, the strength of a column is adequate if the required strength is less than or equal to the available strength. Accordingly, the maximum permitted applied loads per the AASHTO LRFD provisions are those that cause required strengths equal to the available strengths.

The available strength of an RC column is that of the cross section based on the strain compatibility method. In design, resistance factors are applied to the nominal strength to compute the available strength. In this work, analyses are performed at the nominal strength level and thus resistance factors are not applied.

The strain compatibility method was evaluated in this work using a fiber-based approach implemented in the Python programming language. Note that the fiber discretization used for the strain compatibility method was different that that used in OpenSees for GMNIA, notably many more fibers were used. Approximately 200 fibers were used along each of the lateral dimensions of the cross section, resulting in approximately 30,000 total fibers for the circular sections and 45,000 total fibers for the obround sections. The large number of fibers enabled calculation of a smooth interaction diagram and did not significantly affect calculation time since the strain compatibility method was performed outside any finite element simulation. Examples of fiber discretization, with a reduced number of fibers for clarity, are shown in Figures 5.3 and 5.4.

Once the fiber discretization was established for a cross section, axial load and bending moment pairs were computed for assumed neutral axis locations. For a given neutral axis position, an axial strain was calculated for each fiber assuming a linear strain distribution and that the maximum compressive strain in the concrete was 0.003. A stress was assigned to each fiber based on the strain using an elastic perfectly plastic model for the steel (Figure 3.4) and a rectangular stress block model for the concrete. The resulting axial load and bending moment were determined by numerically integrating the stresses over the cross section. Repeating this process for many different neutral axis locations procures many different pairs of axial load and bending moment, which when plotted produce an interaction diagram. According to AASHTO Eq. 5.7.4.4-2, the
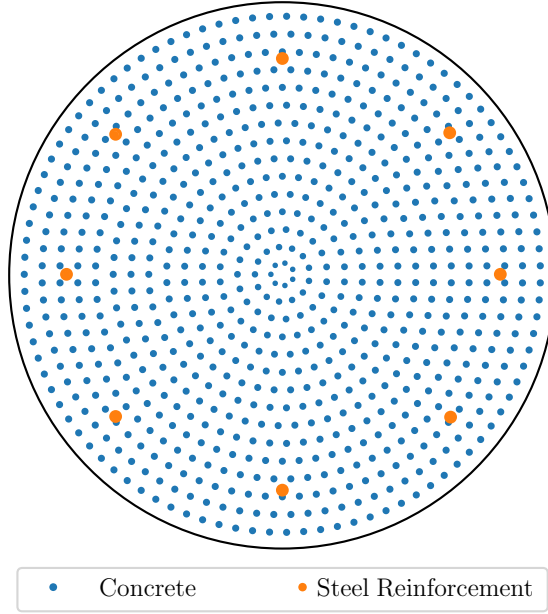
Figure 5.3: Fiber discretization used in the strain compatibility method for circular cross sections

nominal axial compressive strength was capped at $0.8P_0$ where P_0 is the nominal axial strength at zero eccentricity:

$$P_0 = 0.85f'_c(A_g - A_{st}) + f_y A_{st} \tag{5.3}$$

The required strength includes second-order effects and is calculated using the moment magnification approach defined in AASHTO LRFD Sections 4.5.3.2.2b and 5.6.4.3. While AASHTO LRFD does not allow use of the moment magnification approach when $KL/r > 100$, the moment magnification approach was used on all of the columns in the parameter suite. Use of the moment magnification approach for all cases enables a reevaluation of the $KL/r > 100$ limit.

The required moment strength, M_c, is calculated using AASHTO LRFD Eq. 4.5.3.2.2b-1 as

$$M_c = \delta_b M_{2b} + \delta_s M_{2s} \tag{5.4}$$

where

M_{2b} = moment on compression member due to factored gravity loads that result in no appreciable sidesway, calculated by conventional first-order elastic frame analysis; always positive

M_{2s} = moment on compression member due to factored lateral or gravity loads that result in sidesway, Δ, greater than $L/1500$, calculated by conventional first-order elastic frame analysis; always positive
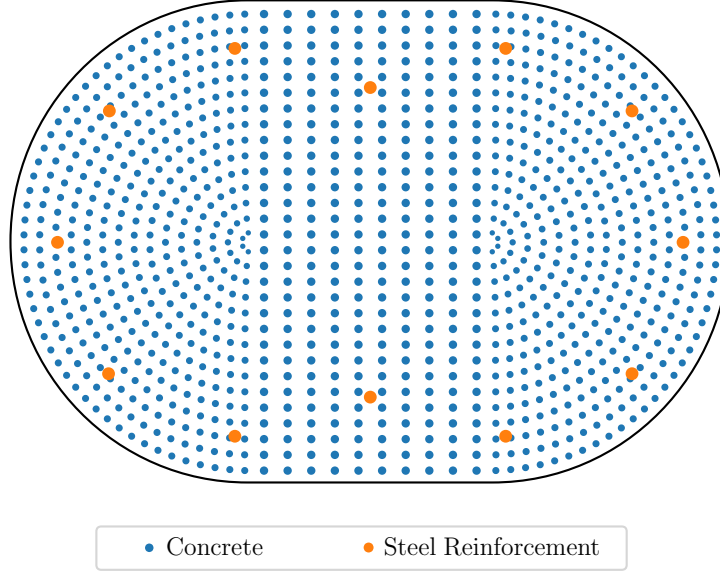
Figure 5.4: Fiber discretization used in the strain compatibility method for obround cross sections

δ_b = nonsway moment magnifier (Eq. 5.6)

δ_s = sway moment magnifier (Eq. 5.9)

For the nonsway columns investigated in this work, $M_{2s} = 0$ and the required strength reduces to

$$M_c = \delta_b M_{2b} \tag{5.5}$$

The moment M_{2b} is equal to the applied moment, M, shown in Figure 5.2 since $|\beta| \leq 1$ for all cases investigated in this study. Unlike ACI 318, AASHTO LRFD does not have a minimum value of nonsway moment to account for initial geometric imperfections.

The nonsway moment magnifier, δ_b, is calculated as

$$\delta_b = \frac{C_m}{1 - \dfrac{P_u}{\phi_K P_e}} \tag{5.6}$$

where

C_m = equivalent uniform moment factor, Eq. (5.7)

P_u = factored axial load

ϕ_K = stiffness reduction factor

P_e = Euler buckling load, Eq. (5.10)

The coefficient C_m is defined as:

$$C_m = 0.6 + 0.4\frac{M_{1b}}{M_{2b}} \tag{5.7}$$

where

M_{1b} = smaller end moment

M_{2b} = larger end moment

In cases where the column is bent in single curvature, the ratio M_{1b}/M_{2b} is positive, while in cases of double curvature, the ratio is negative. This translates to a C_m value of 1.0, 0.8, 0.6, 0.4 for nonsway cases with β values of 1.0, 0.5, 0.0, -0.5, respectively.

For the sway columns investigated in this work, $M_{2b} = 0$ and the required strength reduces to

$$M_c = \delta_s M_{2s} \tag{5.8}$$

The sway moment magnifier, δ_s, is calculated as

$$\delta_s = \frac{1}{1 - \dfrac{\Sigma P_u}{\phi_K \Sigma P_e}} \tag{5.9}$$

where the summation of P_u and P_e indicates that these values should be computed as the total for the bridge in the direction of translation being considered. For the sway frame (Figure 5.2b), there is only one column, therefore $\Sigma P_u = P_u$ and $\Sigma P_e = P_e$.

The stiffness reduction factor, ϕ_K, in Equations 5.6 and 5.9 is a parameter that accounts for potential variations in material properties and workmanship in the analysis. It it specified as 0.75 for concrete members in AASHTO LRFD, but taken as 1.0 in this work given that comparisons are made at the nominal strength level and strength reduction factors are also not applied. This simplifying assumption is made for the sake of clarity and to focus on other aspects of the structural behavior without introducing unnecessary complexity related to these factors.

The Euler buckling load, P_e, in Equations 5.6 and 5.9 is calculated as

$$P_e = \frac{\pi^2 EI}{(KL)^2} \tag{5.10}$$

where

EI = flexural stiffness of the reinforced concrete column

K = effective length factor in the plane of bending.

L = unsupported length of the column

AASHTO LRFD provides two equations, Equations 2.1 and 2.2 which are described in Section 2, for the EI to be used in Eq. (5.10). Determination of the appropriate value of flexural stiffness is an objective of this work therefore additional options for the flexural stiffness, beyond those that appear in AASHTO LRFD, are examined in this study.

For the nonsway columns, the effective length factor, K, is taken as 1. For the sway columns, the effective length factor, K, is calculated based on the stiffness of the rotational springs. Stiffness parameters G_{top} and G_{bot} are computed based on the stiffness of rotational springs and the assumed flexural stiffness of the columns as:

$$G_{top} = \frac{6(EI)L}{k_{top}} \tag{5.11}$$

$$G_{bot} = \frac{6(EI)L}{k_{bot}} \tag{5.12}$$

These computed values of G_{top} and G_{bot} differ from the defined values of $G_{n,top}$ and $G_{n,bot}$ used to define the spring stiffness because $EI = 0.4E_c I_g$ is always used with $G_{n,top}$ and $G_{n,bot}$ while various values of EI are used to define G_{top} and G_{bot}.

The effective length factor, K, is determined iteratively as the value of K that solves the AASHTO LRFD Equation C.4.6.2.5-2:

$$\frac{G_{bot}G_{top}(\pi/K)^2 - 36}{6(G_{bot} + G_{top})} - \frac{(\pi/K)}{\tan(\pi/K)} = 0 \tag{5.13}$$

Eq. (5.14) from Geschwindner et al. (2017), is used as an initial guess for the iterations.

$$K = \sqrt{\frac{1.6G_{bot}G_{top} + 4(G_{bot} + G_{top}) + 7.5}{G_{bot} + G_{top} + 7.5}} \tag{5.14}$$

The maximum permitted applied axial load is equal to the lesser of P_e computed using Eq. (5.10) and $0.8P_0$ where P_0 computed using Eq. (5.3). The maximum permitted applied moment (for the nonsway columns) or lateral load (for the sway columns) is computed for a range of applied axial loads linearly spaced from zero to the maximum permitted axial load. At each level of applied axial load, the available flexural strength is determined from the cross-sectional interaction diagram and the applied moment or lateral load is back-calculated using the equations described above.

5.1.3 Maximum Applied Loads from Second-Order Inelastic Analysis

Results from a second-order inelastic analysis, also referred to as a geometrically and materially nonlinear analysis with imperfections included (GMNIA) form the best approximation of the true behavior of the column and are the benchmark against which results from the design methods are compared.

The analyses are performed using the OpenSees model described in Chapter 3 and validated in Chapter 4. The modeling of the columns included an initial out-of-straightness of $L/1000$ for both sway and nonsway columns, as well as an initial out-of-plumbness of $L/500$ for sway columns.

The limit point of each analysis was defined as when the lowest eigenvalue of the system reached zero or a strain limit was reached, whichever occurred first. The lowest eigenvalue of the system reaching zero corresponds with a true maximum of applied loads. In some cases, especially those with low or no axial compression, a true maximum of applied loads is not reached due to post-yield hardening and one of the strain limits defines limit point. Two strain limits were used: 0.01 for concrete in compression and 0.05 for steel in tension.

Applied loads and internal forces at the limit point were recorded and taken as the maximum applied loads from the second-order inelastic analysis.

5.1.4 Error Calculation

Error in the design method exists if the applied load interaction diagram representing the maximum applied load permitted by the design method does not coincide with the applied load interaction diagram calculated from second-order inelastic analysis. In this study, second-order inelastic analysis is taken as the best approximation of true behavior and the benchmark against which results from the design provisions are measured.

If the design interaction curve lies outside the interaction curve from second-order inelastic analysis, the design method permits applied loads that the inelastic analysis indicates would cause failure. This error in the design method is unconservative. On the other hand, if the design interaction curve is within the interaction curve from second-order inelastic analysis, then the inelastic analysis indicates that there are some applied loads that are safe, but not permitted by the design method. This error in the design method is conservative.

A radial error measure is used to quantify the error as shown in Figure 5.5. The interaction diagrams for a typical case are plotted with the axial compression normalized by P_0 and the bending moment normalized by M_n. P_0 is the nominal axial load capacity of the RC cross section calculated using Eq. (5.15). M_n is the nominal moment capacity of the RC section determined using the strain compatibility method. With this normalization, the design interaction curve will intersect the x axis at a value of 1.0.

$$P_0 = 0.85 f'_c A_c + f_y A_s \tag{5.15}$$

Two lines are drawn from the origin at a given angle, θ, with respect to the x axis. The first line terminates at the intersection with the interaction diagram representing the maximum applied loads from the second-order inelastic analysis. The length of this line is r_{GMNIA}. The second line terminates at the intersection with the interaction diagram representing the maximum permitted applied loads according to AASHTO LRFD. The length of this line is r_{design}. The error is defined as

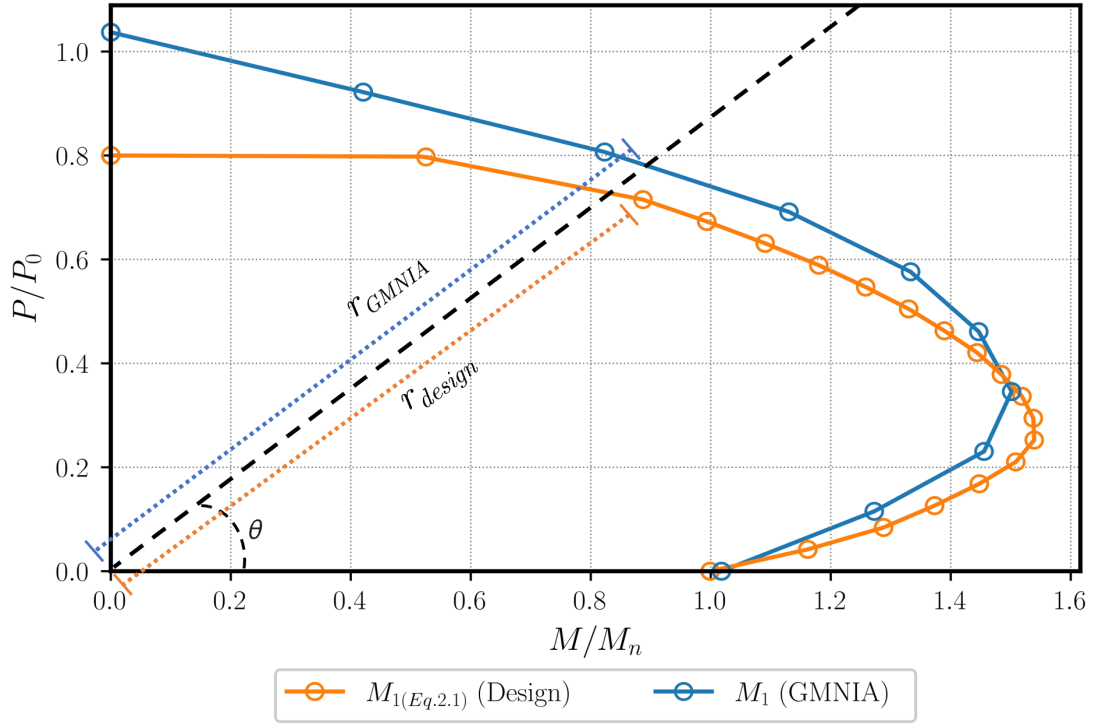$$\varepsilon = \frac{r_{GMNIA} - r_{design}}{r_{GMNIA}} \tag{5.16}$$

Figure 5.5: The essential parameters utilized in the calculation of errors

Using this measure, positive values of error are conservative and negative values of error are un-conservative. The error is quantified at many different angles for a full assessment of the interaction diagrams.

5.1.5 Results

Example interaction diagrams using both Eq. (2.1) and Eq. (2.2) and the corresponding plots of error are shown in Figures 5.6a through 5.11b for the following cases:

- Case C08-L35-NS02, a circular nonsway column with a diameter of 48 in., length to diameter ratio of 35, steel ratio of 4% and a $\beta = 0.5$ (Figure 5.6).

- Case Ox05-L20-NS02, an obround nonsway column with a diameter of 48 in., length to diameter ratio of 20, steel ratio of 1% and a $\beta = 0.5$, bending around the minor axis (Figure 5.7).

- Case Oy01-L15-NS01, an obround nonsway column with a diameter of 16 in., length to diameter ratio of 15, steel ratio of 1% and a $\beta = 1$, bending around the major axis (Figure 5.8).

- Case C01-L5-S05, a circular sway column with a diameter of 16 in., length to diameter of 5, steel ratio of 1% and a $K_{nominal} = 1.2$ (Figure 5.9).

- Case Ox02-L15-S02, an obround sway column with a diameter of 16 in., length to diameter of 15, steel ratio of 2%, bending around the minor axis with a $K_{nominal}$ of 2.2 (Figure 5.10).

- Case Oy01-L40-S04, an obround sway column with a diameter of 16 in., length to diameter of 40, steel ratio of 1%, bending around the major axis with a $K_{nominal}$ of 1.0 (Figure 5.11).

Error plots for individual cases using both AASHTO LRFD equations are plotted together in Figures 5.12 through 5.15. Eight plots are shown, where error lines that are computed using EI from Eq. (2.1) are separated by sway condition and shown in Figures 5.12 and 5.13, while error lines that are computed using EI from Eq. (2.2) are similarly shown in Figures 5.14 and 5.15. Subplot (a) of each figure shows all cases in the group while subplot (b) of each figure shows only cases where $KL/r < 100$.

The error lines of each case are plotted as thin gray lines, giving a graphical representation of which values of error are more frequent based on the darkness in each region. Additionally, the envelope of maximum error is shown as a green line and the envelope of minimum error is shown as a red line.

Unconservative errors due to the overprediction of EI are observed when the axial loads are low across all of the plots. This unconservatism is more prominent for the cases with a higher slenderness ratio. Additionally, Eq. (2.2) tends to have lower overprediction error when compared to Eq. (2.1).

Tables 5.4 through 5.7 list maximum and minimum errors. The cases identified in each table caption are grouped by length-to-diameter ratio and steel ratio. The maximum and minimum errors were computed over each case in the group and over all angles. The average error in each group is not shown in this table, or generally in this work, because the distribution of cases investigated in this work is not representative of the distribution of actual bridge columns. The cases were selected to be representative of the range of actual bridge columns, but include a higher proportion of very slender columns than is used in construction.
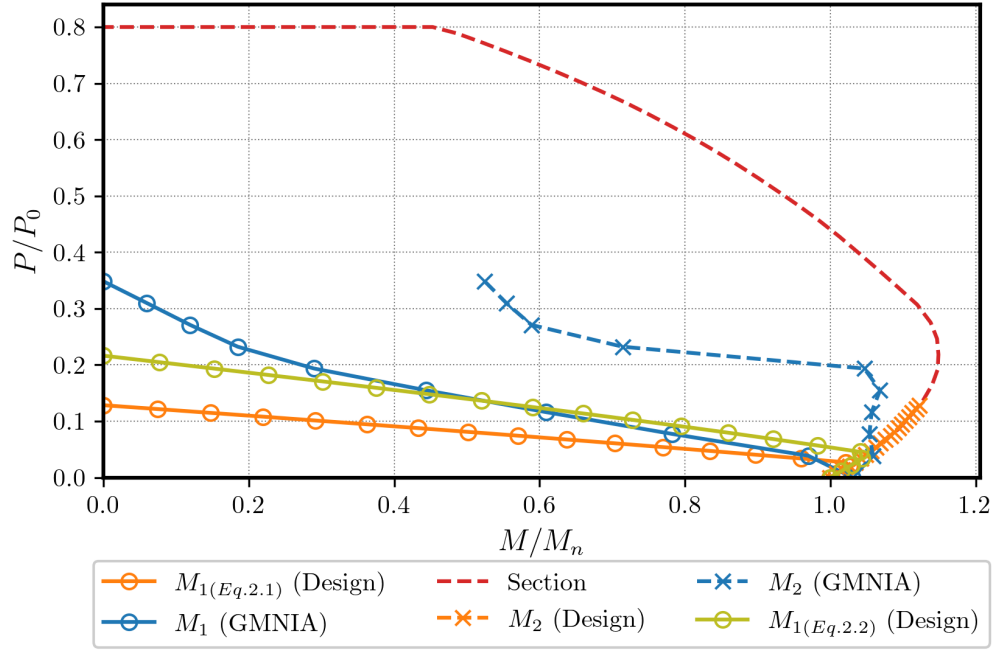
(a)
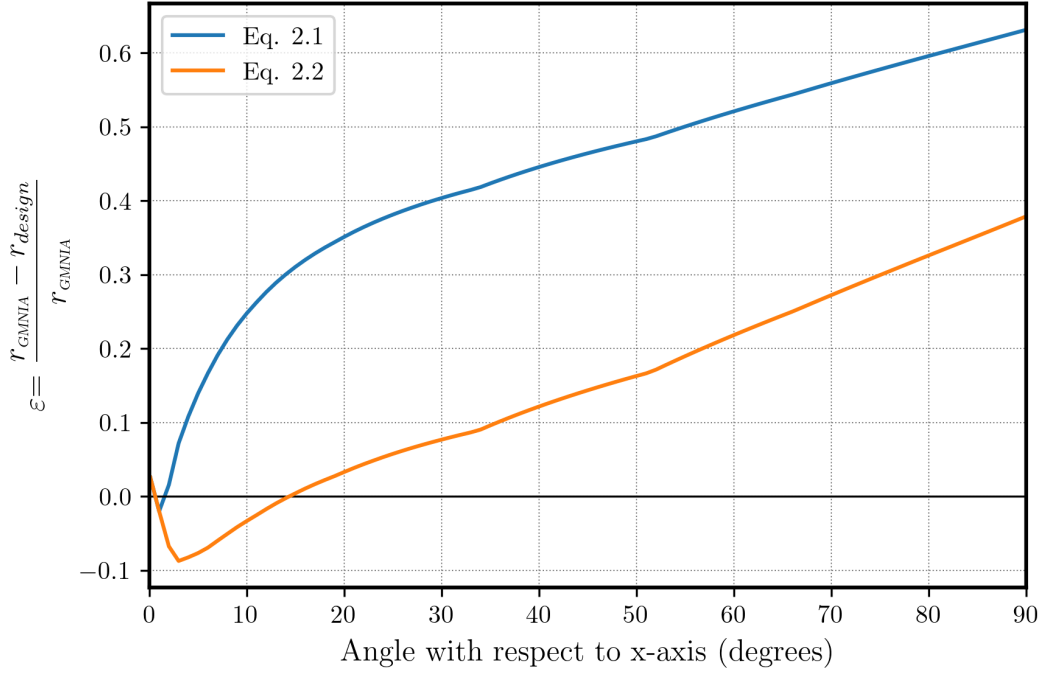
(b)

Figure 5.6: Interaction diagram (a) and error plot (b) for case C08-L35-NS02
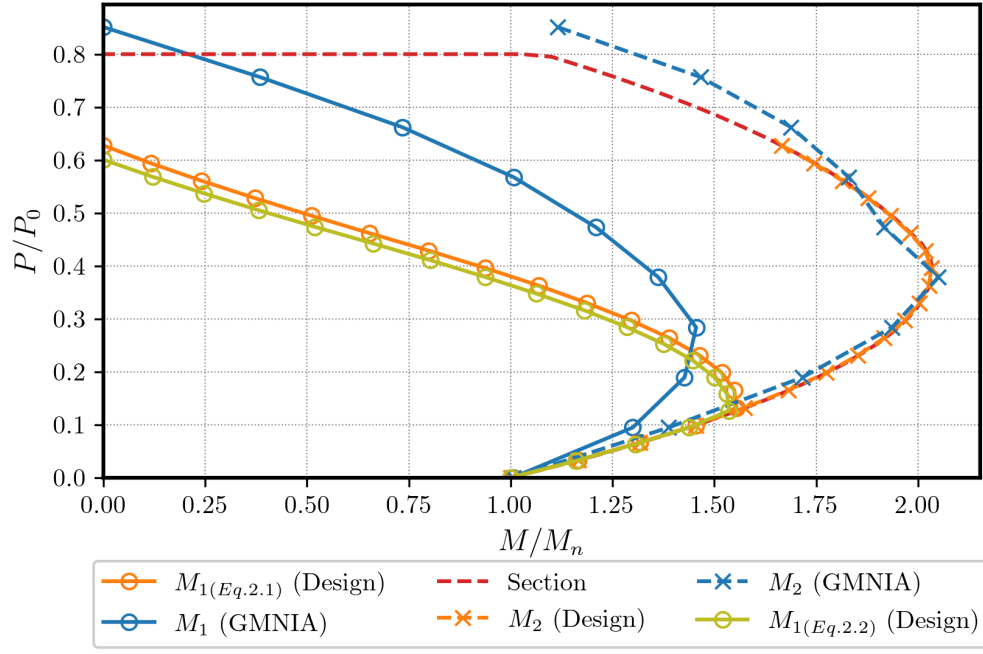
(a)
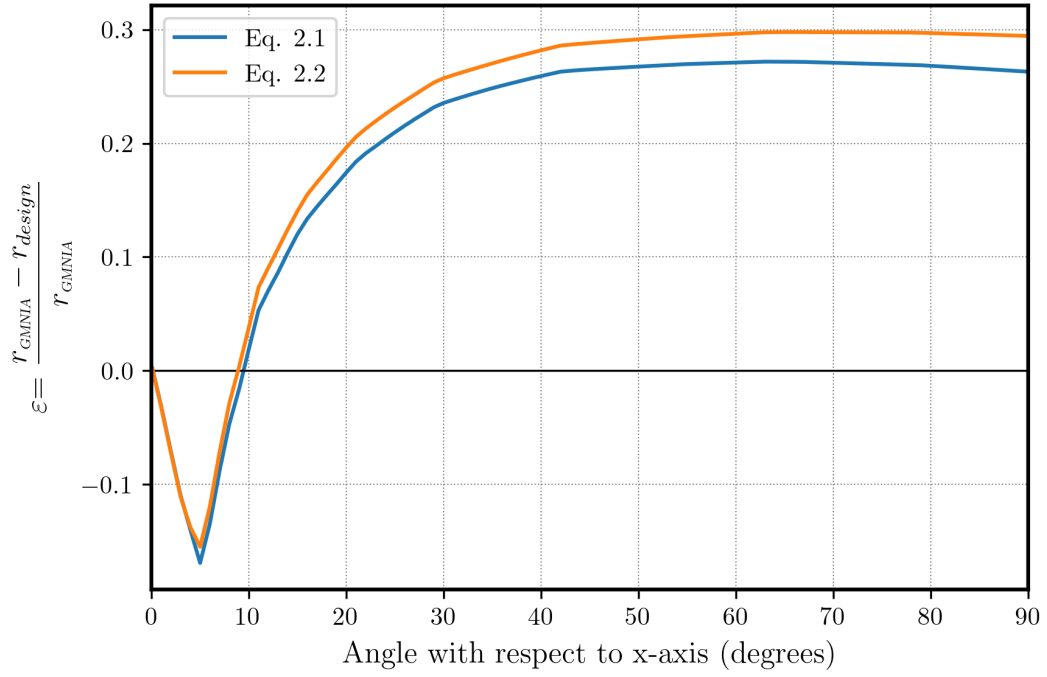
(b)

Figure 5.7: Interaction diagram (a) and error plot (b) for case Ox05-L20-NS02
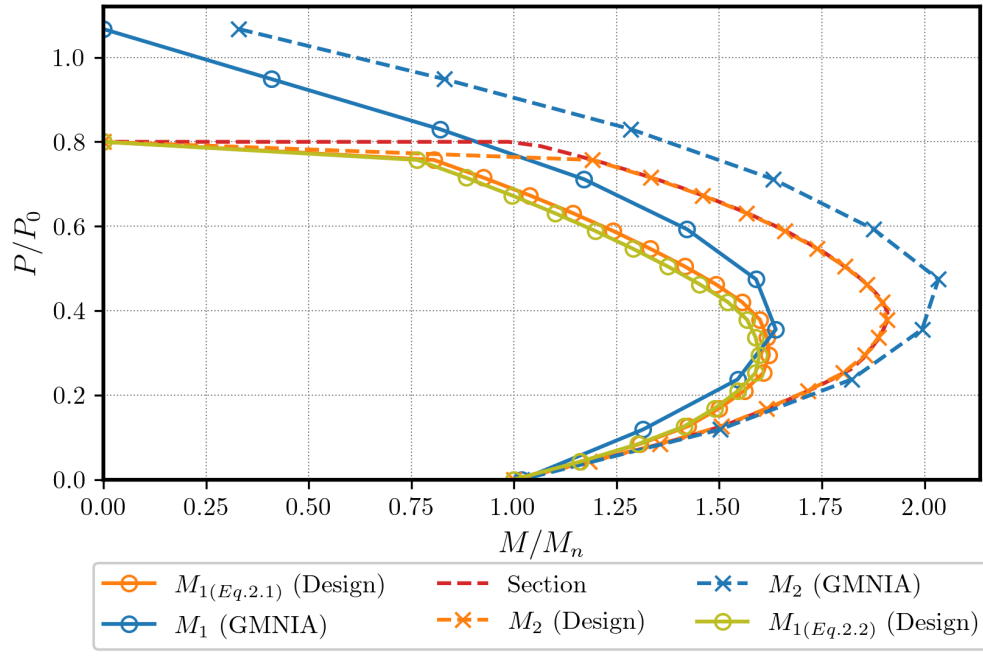
(a)
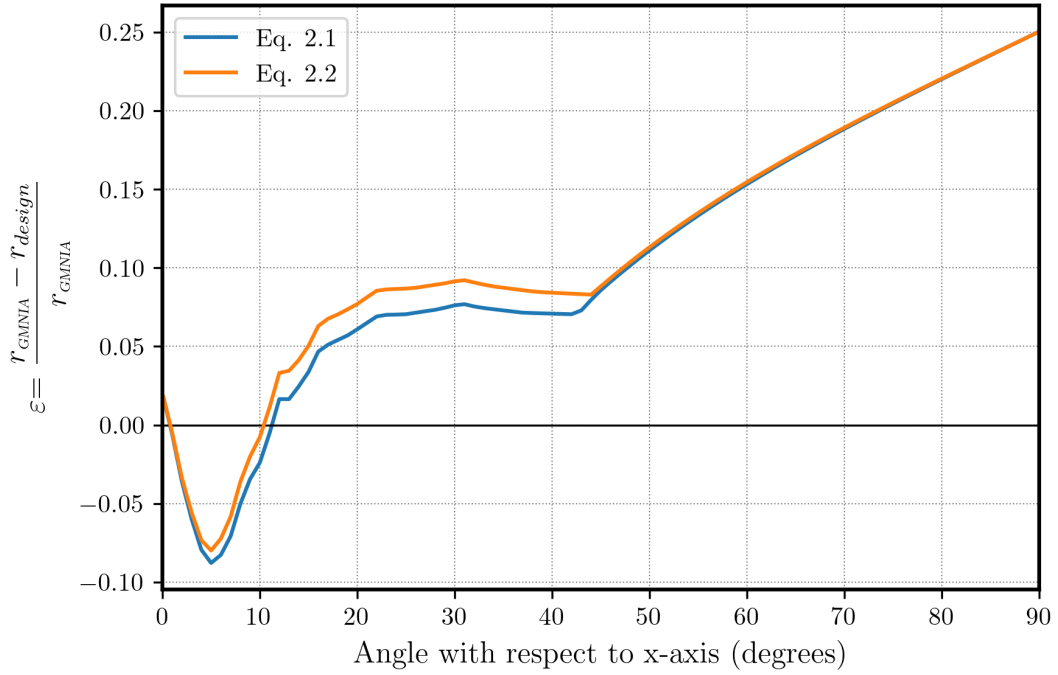
(b)

Figure 5.8: Interaction diagram (a) and error plot (b) for case Oy01-L15-NS01
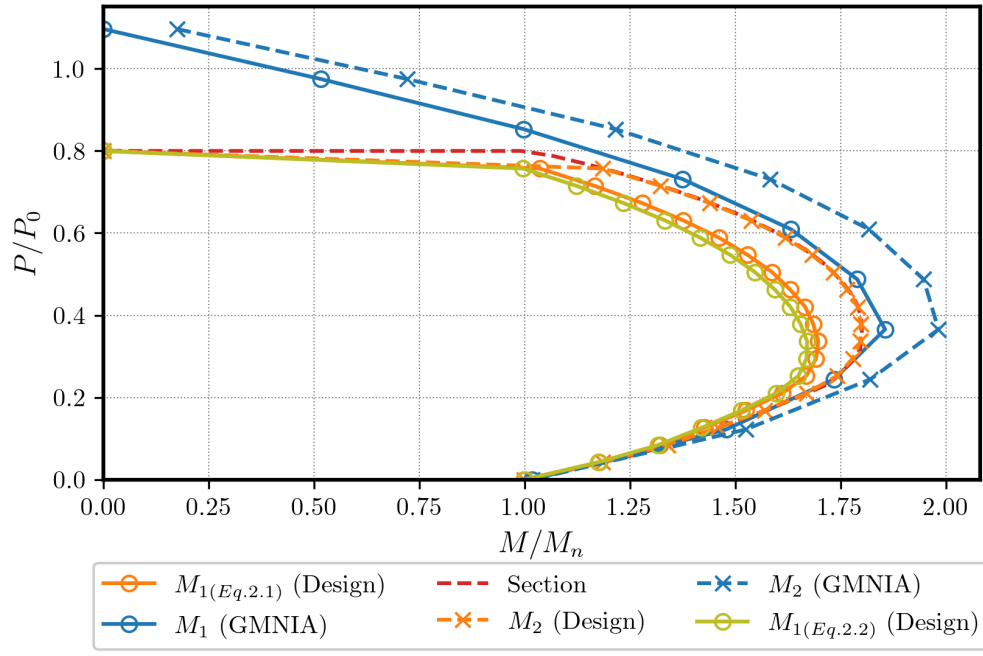
(a)
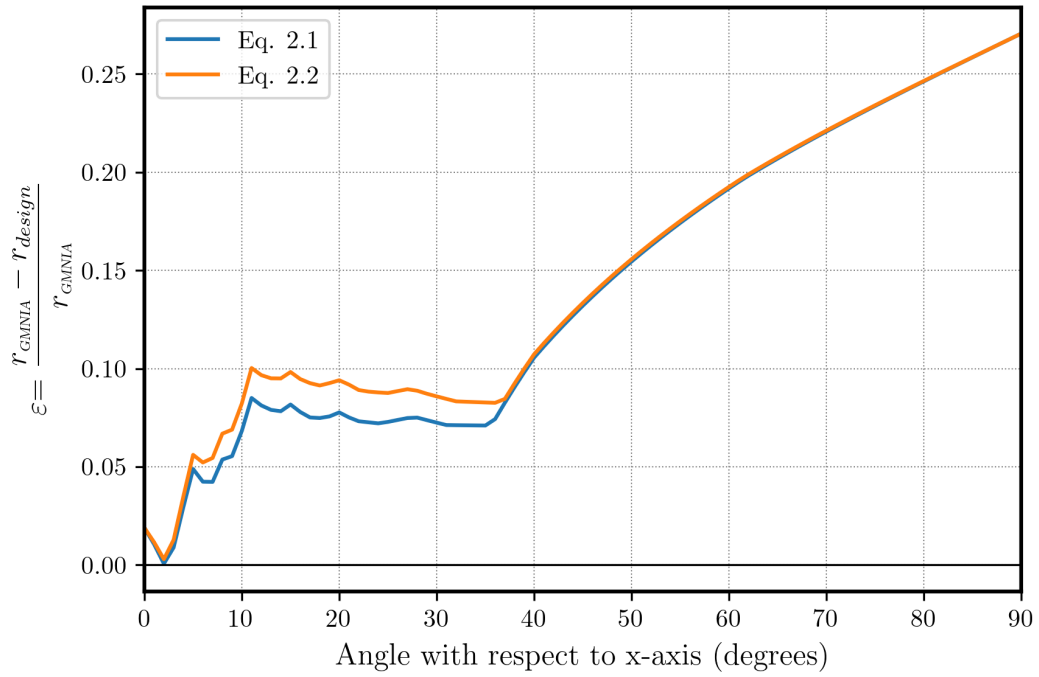
(b)

Figure 5.9: Interaction diagram (a) and error plot (b) for case C01-L5-S05
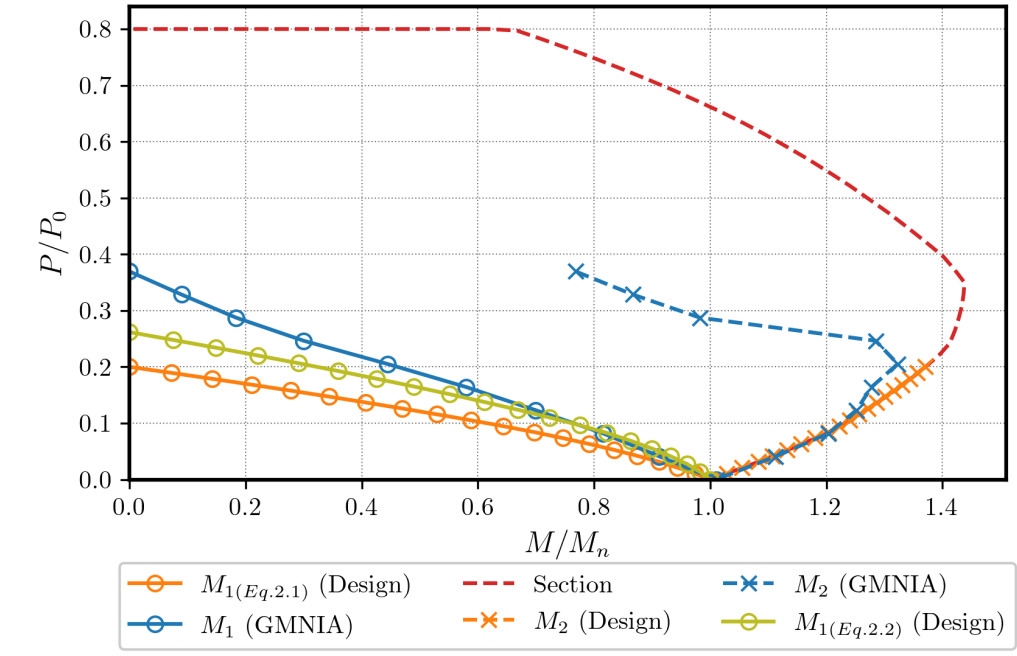
(a)
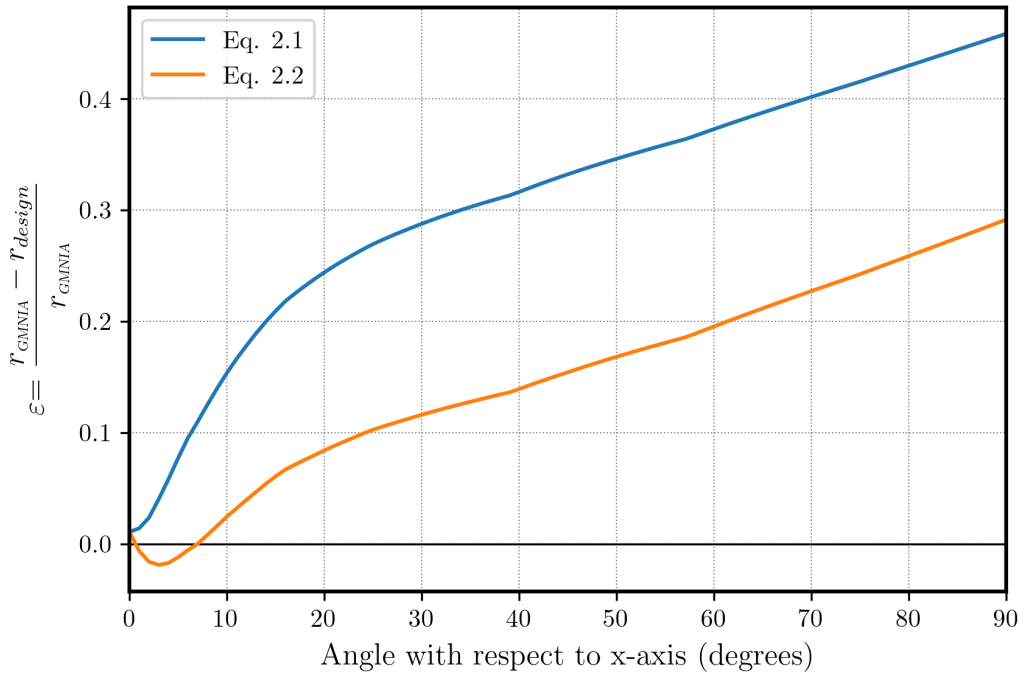
(b)

Figure 5.10: Interaction diagram (a) and error plot (b) for case Ox02-L15-S02
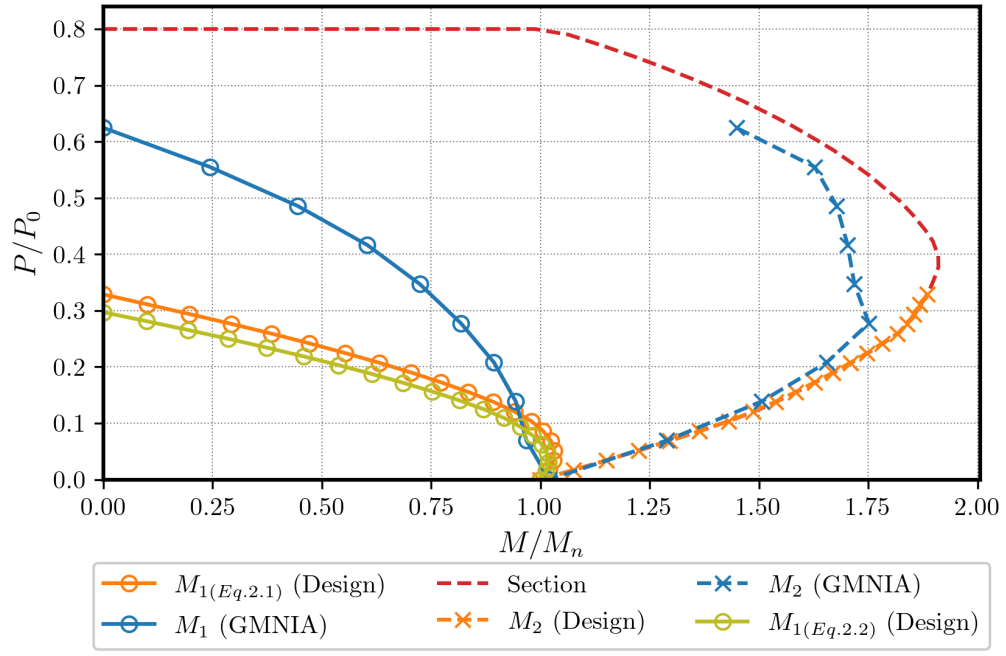
(a)
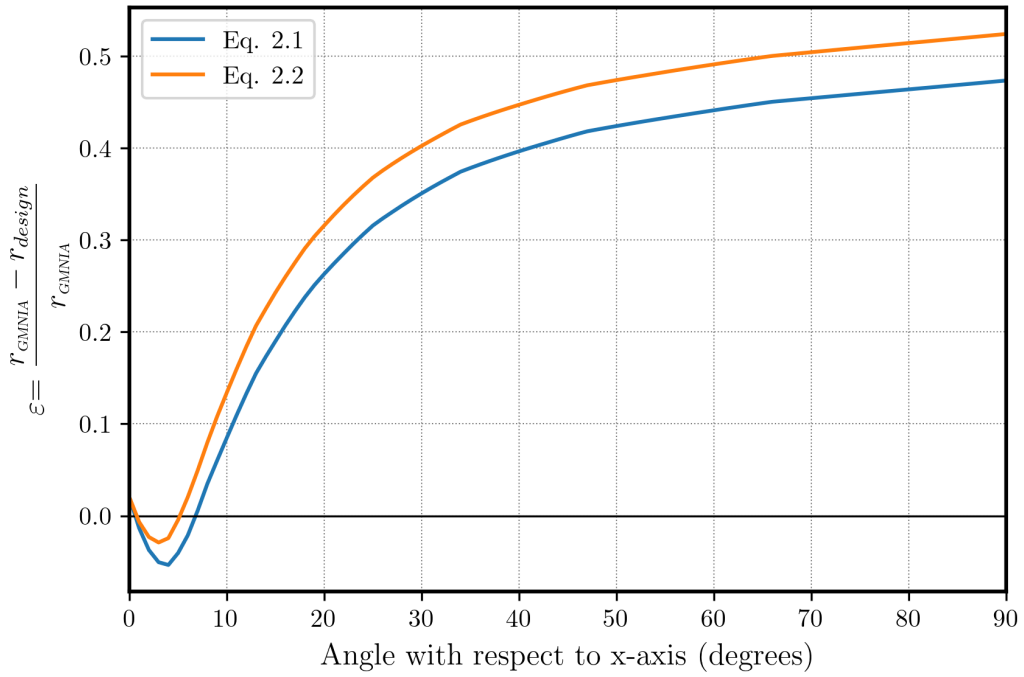
(b)

Figure 5.11: Interaction diagram (a) and error plot (b) for case Oy01-L40-S04
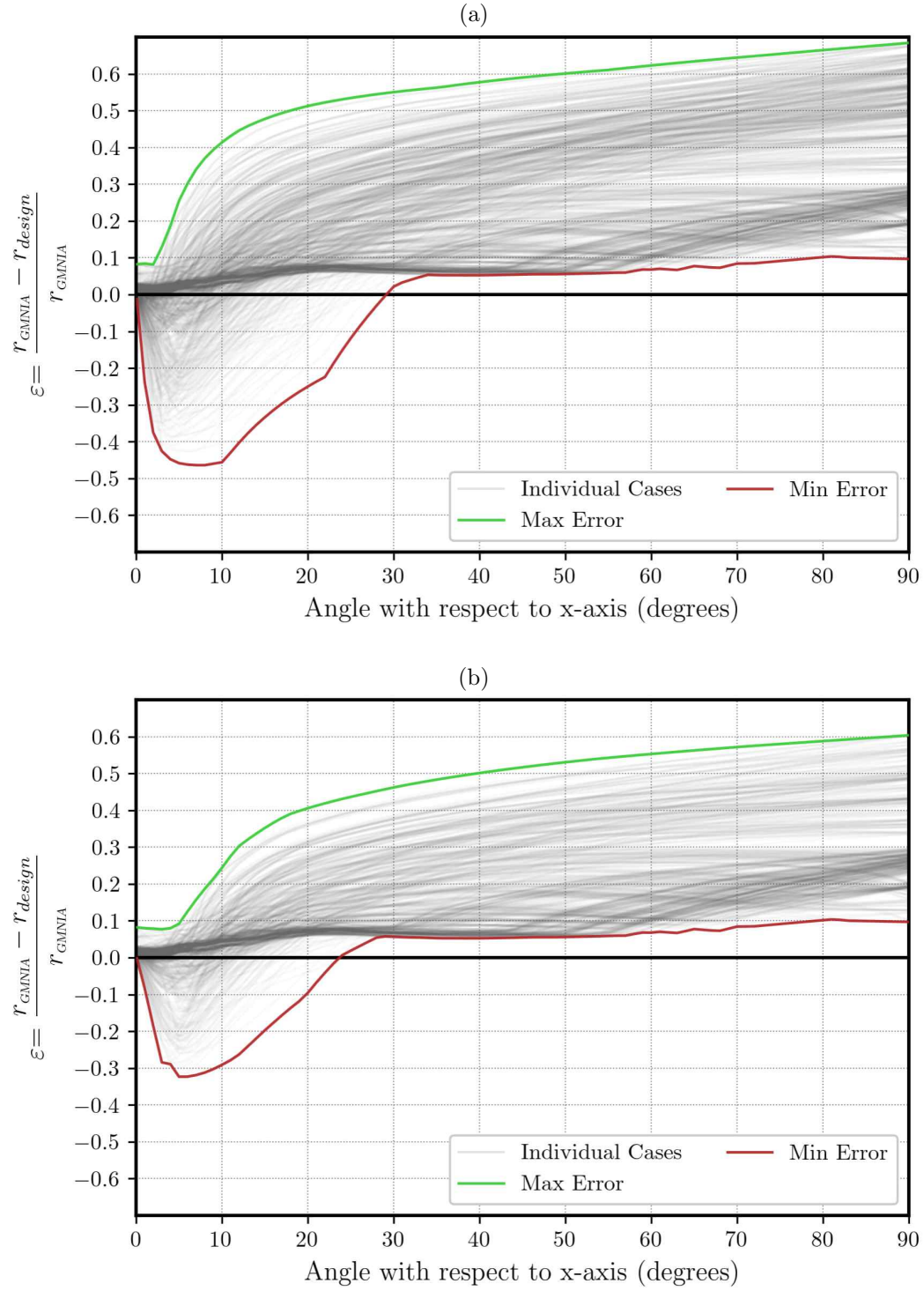
Figure 5.12: Error plot of (a) all nonsway cases and (b) nonsway cases with $KL/r < 100$, based on the results obtained with EI calculated using Eq. (2.1).
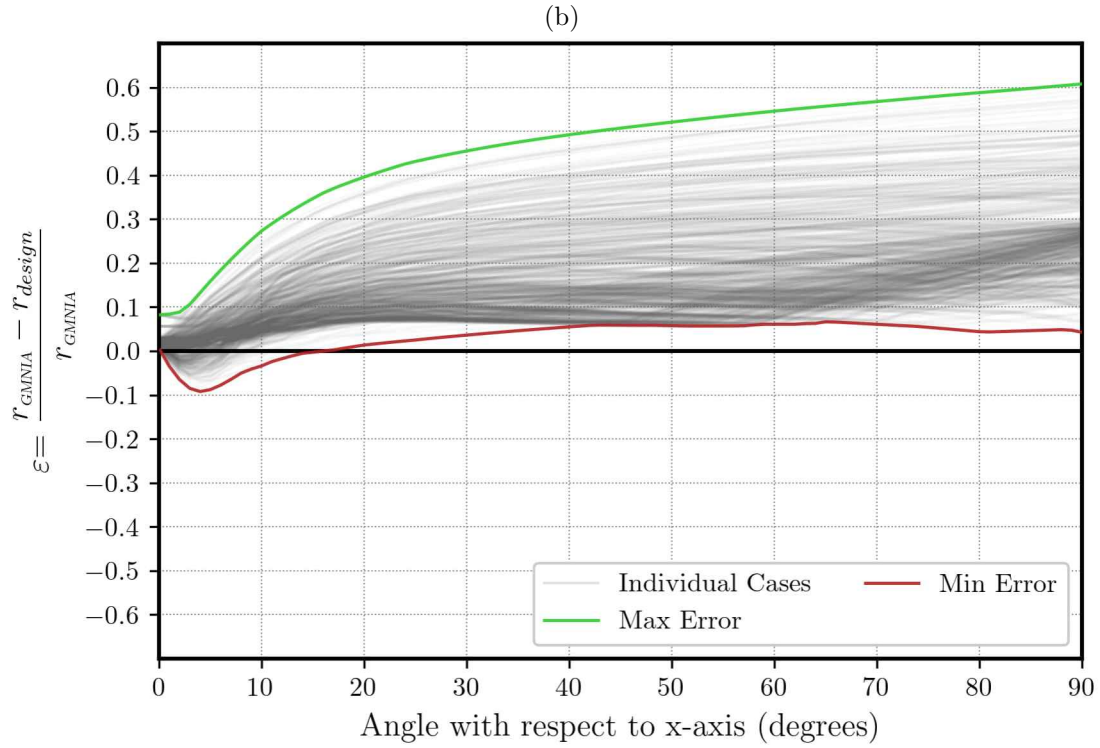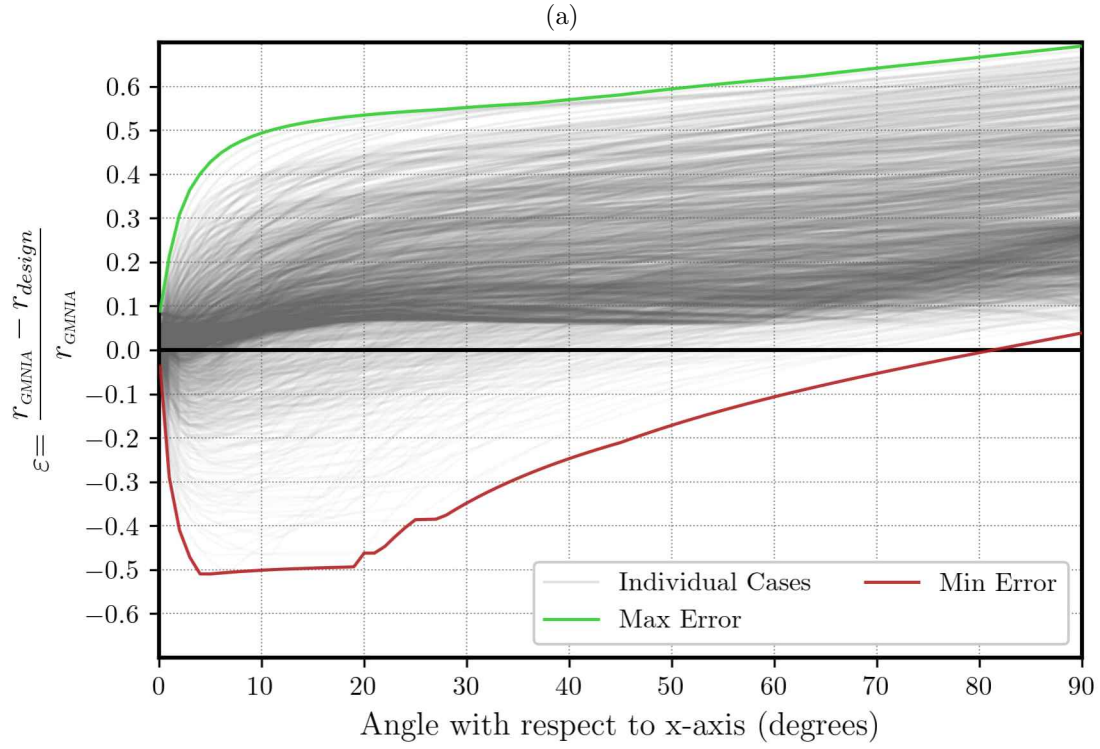
Figure 5.13: Error plot of (a) all sway cases and (b) sway cases with $KL/r < 100$, based on the results obtained with EI calculated using Eq. (2.1).

78
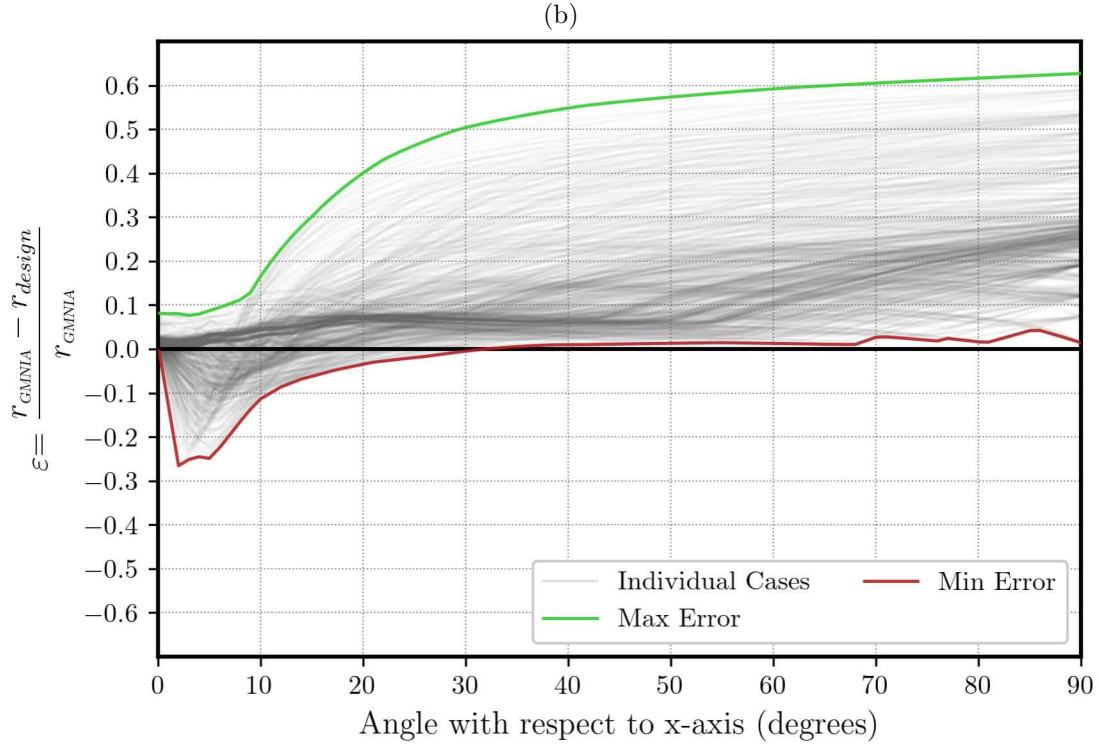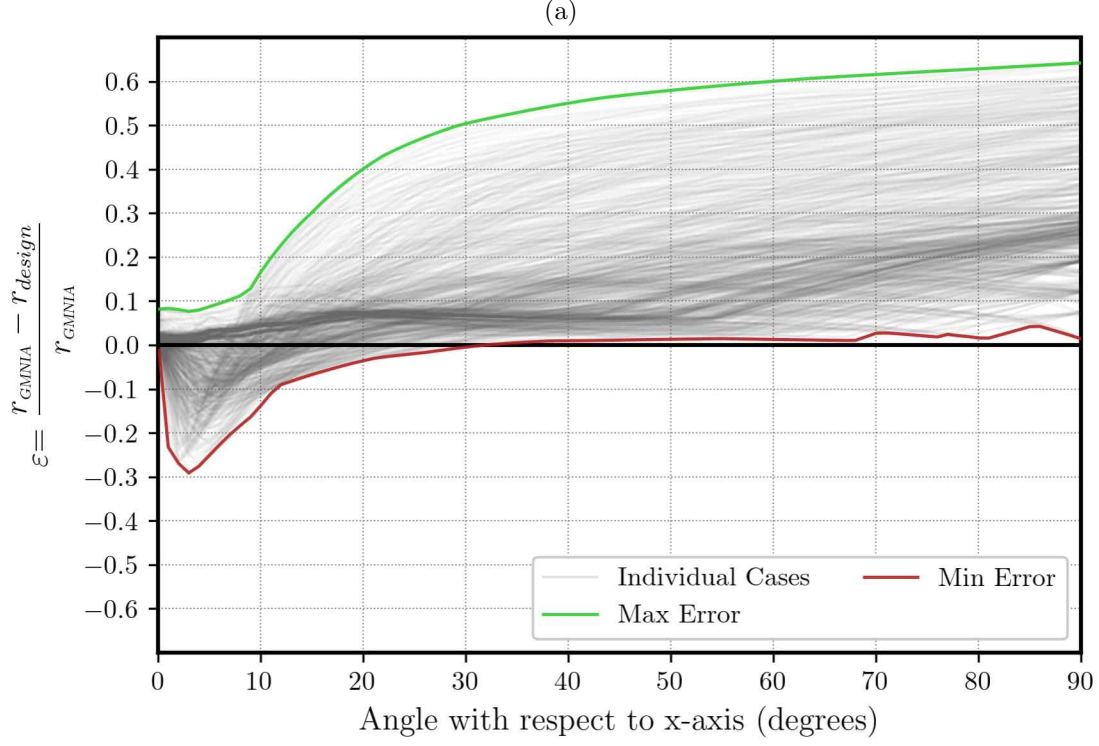
Figure 5.14: Error plot of (a) all nonsway cases and (b) nonsway cases with $KL/r < 100$, based on the results obtained with EI calculated using Eq. (2.2).
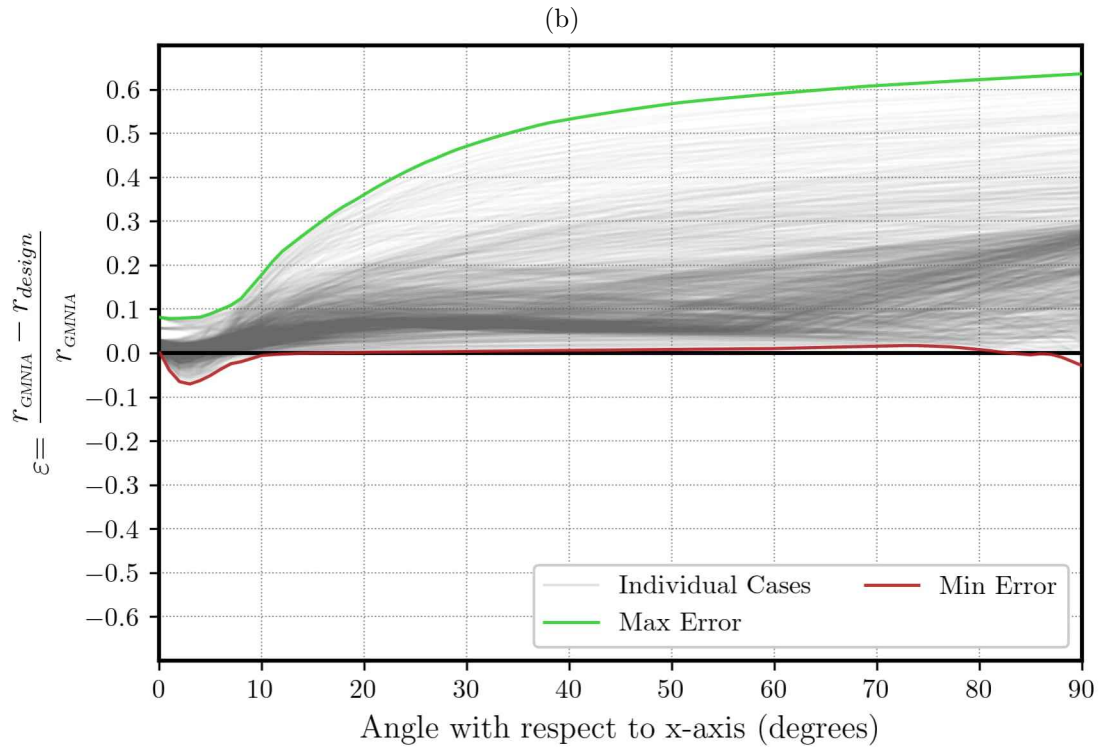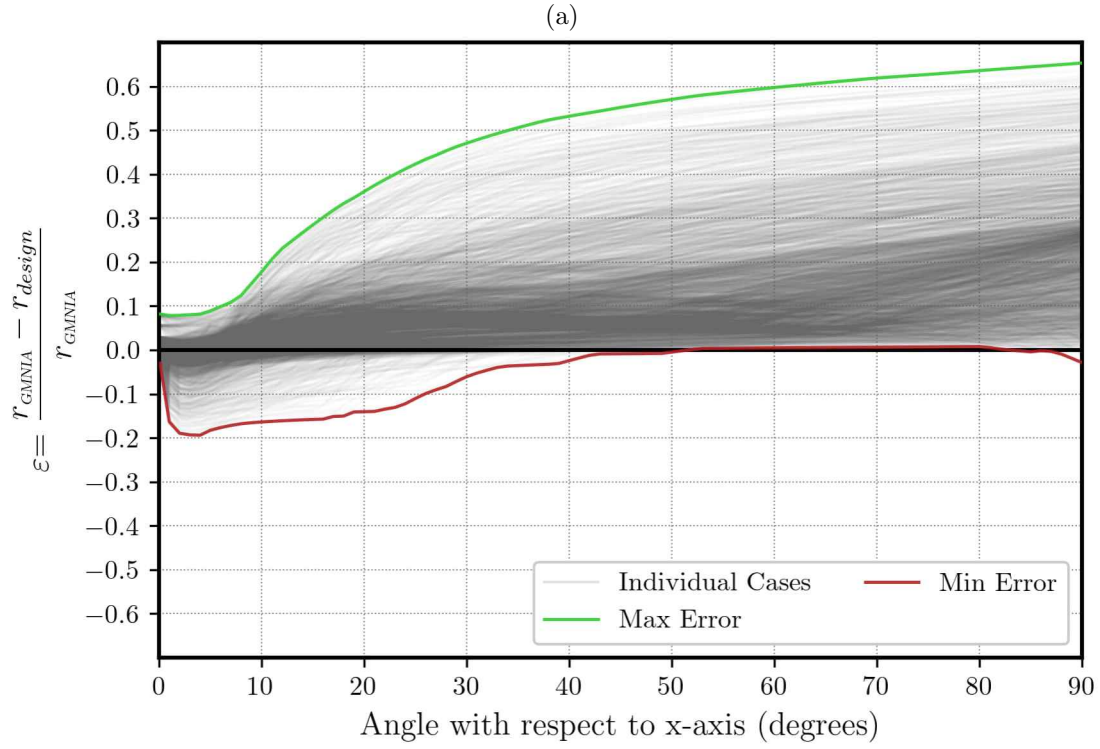
Figure 5.15: Error plot of (a) all sway cases and (b) sway cases with $KL/r < 100$, based on the results obtained with EI calculated using Eq. (2.2).

Table 5.4: Upper and lower error bounds for nonsway columns as determined by slenderness using Eq. (2.1).

ρ	ε	Slenderness Range					
		0-25	25-50	50-75	75-100	100-125	≥ 125
1%	Min	-0.036	-0.107	-0.196	-0.323	-0.380	-0.464
	Max	0.295	0.280	0.204	0.436	0.503	0.545
2%	Min	-0.011	-0.029	-0.076	-0.147	-0.167	-0.195
	Max	0.283	0.270	0.248	0.504	0.567	0.605
3%	Min	-0.009	-0.014	-0.024	-0.068	-0.079	-0.094
	Max	0.274	0.262	0.297	0.559	0.615	0.649
4%	Min	0.008	0.009	0.010	-0.011	-0.022	-0.031
	Max	0.266	0.255	0.348	0.604	0.653	0.684

Table 5.5: Upper and lower error bounds for sway columns as determined by slenderness using Eq. (2.1).

ρ	ε	Slenderness Range					
		0-25	25-50	50-75	75-100	100-125	≥ 125
1%	Min	-0.014	-0.024	-0.038	-0.092	-0.154	-0.510
	Max	0.291	0.285	0.233	0.445	0.512	0.557
2%	Min	0.002	-0.001	0.001	0.003	-0.006	-0.128
	Max	0.279	0.274	0.273	0.511	0.575	0.615
3%	Min	-0.003	-0.005	0.000	0.007	0.007	-0.001
	Max	0.271	0.265	0.313	0.564	0.622	0.658
4%	Min	0.010	0.009	0.012	0.015	0.018	0.020
	Max	0.263	0.258	0.355	0.608	0.659	0.692

Table 5.6: Upper and lower error bounds for nonsway columns as determined by slenderness using Eq. (2.2).

ρ	ε	Slenderness Range					
		0-25	25-50	50-75	75-100	100-125	≥ 125
1%	Min	-0.037	-0.087	-0.159	-0.237	-0.254	-0.284
	Max	0.295	0.280	0.300	0.587	0.627	0.642
2%	Min	-0.015	-0.042	-0.090	-0.148	-0.164	-0.181
	Max	0.283	0.270	0.240	0.529	0.571	0.586
3%	Min	-0.011	-0.030	-0.065	-0.110	-0.137	-0.157
	Max	0.274	0.262	0.209	0.492	0.534	0.548
4%	Min	0.003	-0.020	-0.048	-0.093	-0.108	-0.129
	Max	0.266	0.255	0.193	0.451	0.494	0.507

Table 5.7: Upper and lower error bounds for sway columns as determined by slenderness using Eq. (2.2).

ρ	ε	Slenderness Range					
		0-25	25-50	50-75	75-100	100-125	≥ 125
1%	Min	-0.015	-0.023	-0.029	-0.038	-0.062	-0.193
	Max	0.291	0.285	0.328	0.594	0.635	0.653
2%	Min	-0.002	-0.006	-0.008	-0.012	-0.020	-0.058
	Max	0.279	0.274	0.271	0.537	0.581	0.599
3%	Min	-0.005	-0.008	-0.009	-0.005	-0.008	-0.040
	Max	0.271	0.265	0.242	0.501	0.545	0.562
4%	Min	0.007	0.005	-0.029	-0.012	-0.003	-0.023
	Max	0.263	0.258	0.215	0.462	0.506	0.522

5.1.6 Discussion

Examining the individual results of Figures 5.6 through 5.11, there is a distinct difference between shorter columns and longer columns. The axial capacity of the shorter columns is higher compared to longer columns (i.e., the intersection of the interaction diagram and the y axis is closer to 1.0). There is also a smaller difference between the first-order moment, M_1, and second-order moment, M_2, for shorter columns compared to longer columns. The difference between M_1 and M_2 represents the P-δ and P-Δ effects.

In several cases, the second-order moment from the inelastic analysis (i.e., M_2 (GMNIA)) is similar to the available strength from design (i.e., M_2 (design)), indicating that failure of the column is largely due to the internal forces reaching their cross-sectional strength. However, for longer columns near their axial capacity, the second-order moment from the inelastic analysis can be significantly less than the available strength from design, indicating stability failure.

The error is generally smaller at zero axial load and high moments (i.e., $\theta = 0°$) but increases to higher values as the axial load increases (i.e., θ approaches $90°$). However, for low angles there is a dip in the error, often to the unconservative range, before increasing to conservative error for high axial loads. Low angles represent cases with high bending moment and some axial compression. In these cases, significant cracking is expected, reducing the stiffness of the column even below the effective values used in design.

The graphs presented in Figures 5.12a through 5.15b show that the unconservative error trends observed for the individual examples generally apply, meaning unconservative error is concentrated at low angles and for longer columns. However, significant unconservative error is observed for columns at higher angles (i.e., $\theta > 30°$) especially for the cases with a slenderness ratio (KL/r) of more than 100.

The data in Tables 5.4 through 5.7 further reinforces the observed trends with respect to length-to-diameter ratio and uncovers further trends with respect to steel ratio. The greatest unconservative and conservative errors are for low steel ratio cases. The worst case unconservative error observed for results obtained using Eq. (2.1) overall is for a sway column with a slenderness ratio (KL/r) greater than 125 and a steel ratio (ρ) of 1% which has an error (ε) of -0.510. While the worst case for the results from Eq. (2.2) is a nonsway column with a KL/r of greater than 125 and a ρ of 1%, which has a ε of -0.284.

It was observed that in general, nonsway cases exhibit greater maximum unconservative errors than sway cases, likely due to the $\beta = 1$ cases where concrete cracking occurs along the entire length of the column. The spread of error values is also greater for nonsway cases than for sway cases.

5.2 Long-Term Loading

Select cases from the parametric study conducted for short-term loading are repeated for long-term loading effects using the cross-sectional shapes, bending axes, cross-section dimensions, and longitudinal steel ratios described in the previous section. In addition to the parameters held constant across the short-term parametric study (concrete compressive strength, steel yield strengths, clear cover, and transverse hoop details), the long-term loading parametric study assumes the following

creep and shrinkage parameters are held constant:

- Ultimate concrete shrinkage strain, $\varepsilon_{sh,0}$=600 × 10^{-6}

- Ultimate concrete creep factor, φ_0=3.0

Each analysis simulates the column holding a sustained load for 10,000 days (approximately 27 years). For long-term analysis, the sustained load is set to 5% of the peak axial capacity from the interaction diagram for short-term loading of the column.

After the hold phase, the capacity of the column is calculated. Similar to the short-term analysis in the previous section, the long-term simulation is repeated over several eccentricities of the sustained load in order to develop an interaction diagram.

5.2.1 Results

Interaction diagrams based on GMNIA with OpenSees are shown for the following cases. All columns are nonsway with β=1.

- Case C06-L15-NS01 – Nonsway, D=48 inch diameter circular column with 2% steel and L/D=15

- Case Oy01-L15-NS01 – Nonsway, D=16 inch obround column with 1% steel and L/D=15, bending about the major axis

- Case Ox05-L20-NS01 – Nonsway, D=48 inch diameter obround column with 1% steel and L/D=20, bending about the minor axis

In the cases listed above, for each level of eccentricity, the sustained long term load was set to 50% of the axial load capacity for short term loading at the same eccentricity.

For the C06-L15-NS01 case, the axial force-lateral deflection curves (Figure 5.16) for the column reveal significant long-term lateral deflections under sustained loads. In addition, as shown in Figure 5.17, the applied loads that cause failure are lower when long-term effects are considered, but the internal forces at failure are not affected. The load-deflection and axial-moment interaction diagrams for the Oy01-L15-NS01 case (Figure 5.18 and Figure 5.19) show similar trends with significant long-term deflection adding to the second-order effects and reducing the applied load at failure.

For the Ox05-L20-NS01 case, a more slender column than the previous two cases, Figure 5.20 and Figure 5.21 show, in addition to sustained long-term deflections, that both the applied loads and internal forces at failure are less when considering long-term effects for higher axial loads (i.e., over 40% of the pure axial capacity of the column). These results indicate that this column, with its greater slenderness, is experiencing a stability failure, not precipitated by reaching the cross-sectional strength of the column.

The methodology shown here indicates a roughly 10-20% reduction in strength due long-term effects. Evaluating strength reductions across a broader range of columns and loading conditions can enable the development of more refined design recommendations.

Figure 5.16: Load-deflection curves for long-term loading of column case C06-L15-NS01.

Figure 5.17: Interaction diagram for short-term and long-term loading for case C06-L15-NS01.
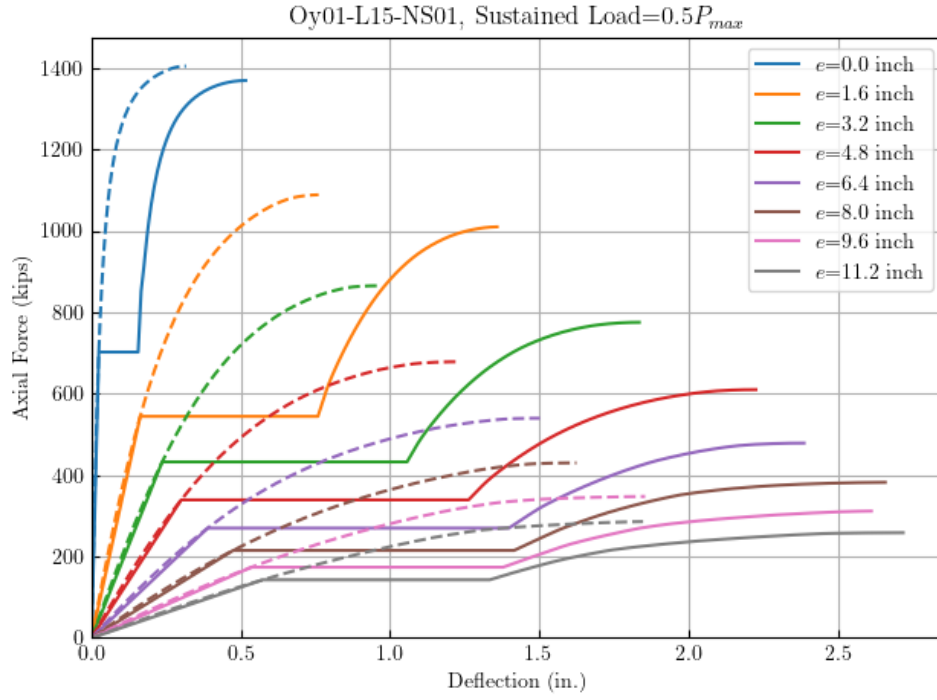
Figure 5.18: Load-deflection curves for long-term loading of column case Oy01-L15-NS01.
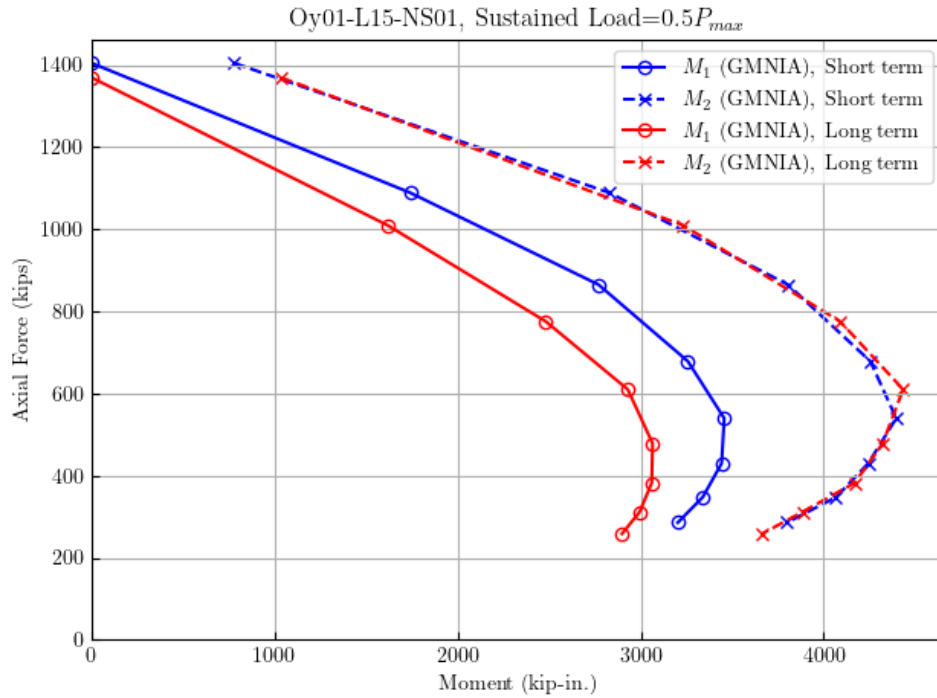
Figure 5.19: Interaction diagram for short-term and long-term loading for case Oy01-L15-NS01.
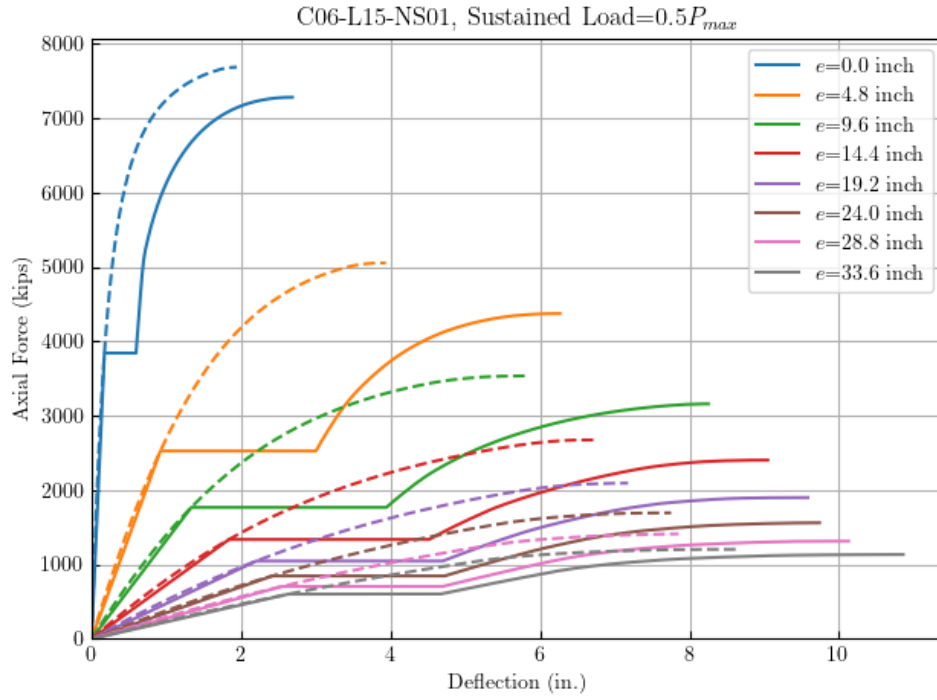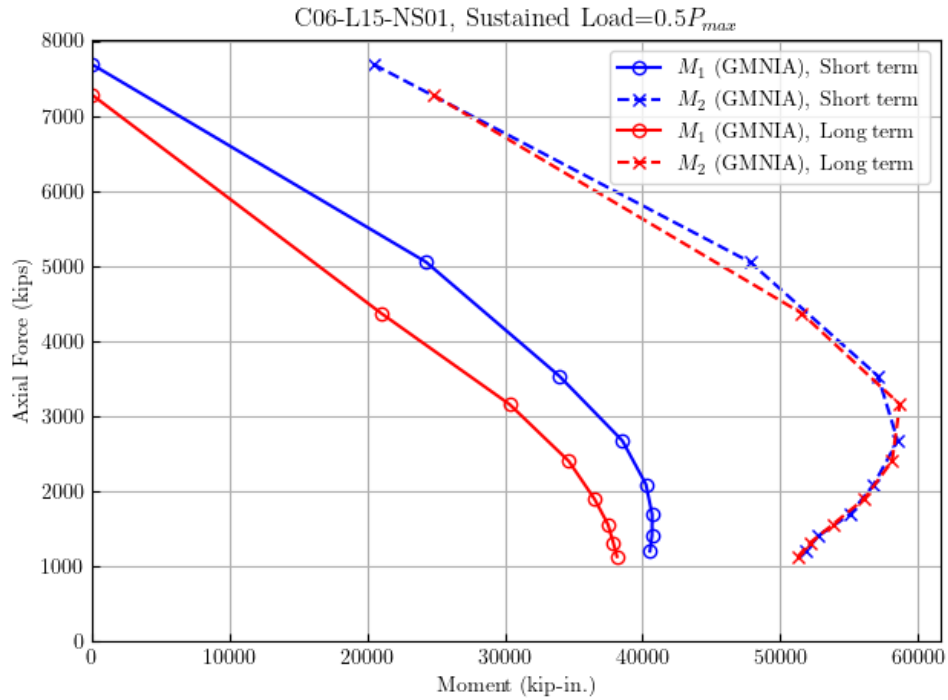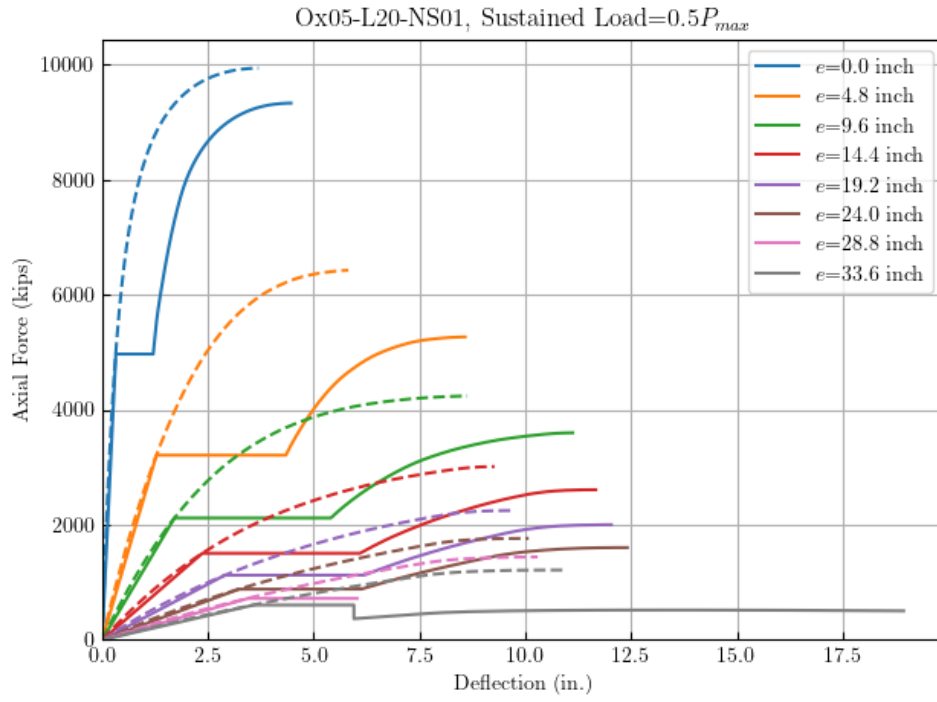
Figure 5.20: Load-deflection curves for long-term loading of column case Ox05-L20-NS01.
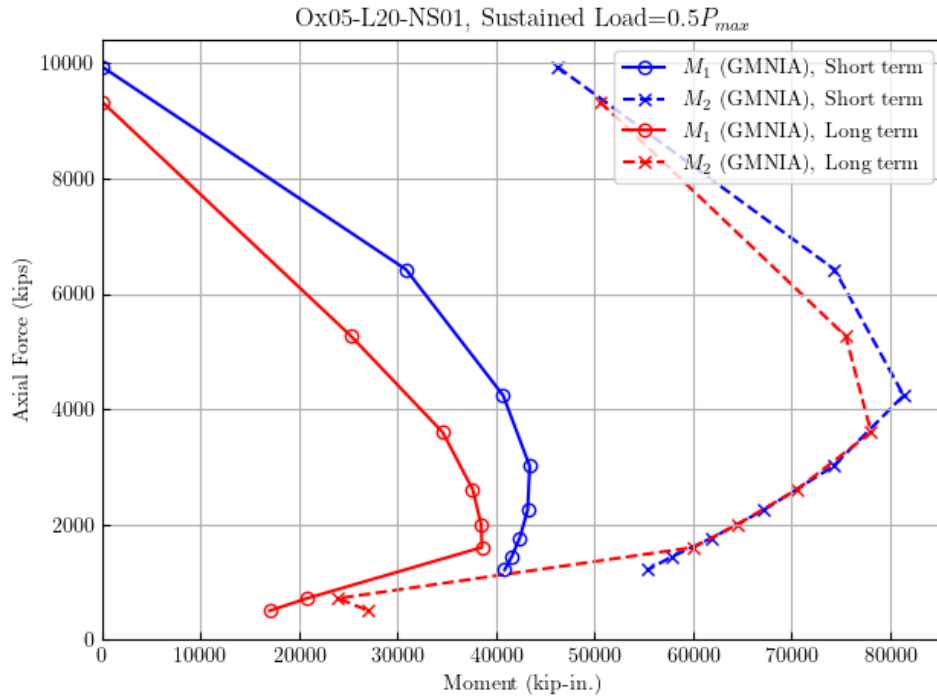
Figure 5.21: Interaction diagram for short-term and long-term loading for case Ox05-L20-NS01.

Chapter 6

Modifications to Design Methods

This chapter describes the development of several potential modifications to the AASTHO LRFD method of design for slender RC columns. First, alternative equations for the flexural rigidity, EI, for use in the moment magnification procedure are evaluated and developed. Then, slenderness ratio limits on the use of the moment magnification procedure are evaluated. A new effective length factor for the transverse buckling mode of single column bents is developed. Finally, rules of thumb for preliminary design are proposed.

6.1 Flexural Rigidity

The results of Chapter 5 show that there is both conservative and unconservative error associated with the evaluation of strength of RC bridge columns using the AASHTO LRFD moment magnification approach. The flexural rigidity used in the approach, i.e., Eq. (2.1) or Eq. (2.2), is the largest source of the observed error because of its simplicity in comparison to the complex behavior that it stands in for. This section evaluates alternative equations for the flexural rigidity. Noting the limitations of equations that only depend on cross-sectional properties, the equations for flexural rigidity evaluated in this section depend on the axial load in the member, the maximum bending moment in the member, or both. They are the variable flexural rigidity equation in ACI 318, the equations developed by Jenkins and Frosch (2015), and new equations developed in this work.

More emphasis is placed in this work on reducing unconservative error than reducing conservative error. This is because of the greater consequences of unconservative error, but also because bridge columns often have relatively low axial loads in comparison to their cross-sectional axial strength. The unconservative errors observed in Chapter 5 were primarily seen at low axial loads and high bending moments.

To create design interaction diagrams when using effective stiffness equations that vary with axial load or bending moment, e.g., Eq. (2.3), some modifications to the approach described in Section 5.1.2 were necessary. An iterative solution method is required here because the flexural stiffness, EI, can depend on both the maximum factored moment along the length of the column and this moment, in turn, depends on EI. For a given axial load, factored internal bending moment was incrementally increased from zero to the section's strength at the given axial load to find the

corresponding applied moment. The flexural stiffness was calculated at each value of internal moment. This flexural stiffness was used to calculate the buckling load. If the applied axial load is less than the computed buckling load, δ was computed and the applied moment was computed by dividing the internal moment by δ. If the applied axial load was greater than the buckling load, then the remaining moments increments were disregarded, the previous step was identified as the limit point, and the applied moment from the previous step was identified as the maximum permitted applied moment.

6.1.1 ACI's Variable Effective Flexural Stiffness

ACI 318 includes provisions for slender RC column design that are similar to those in AASHTO LRFD. Eq. (2.1) and Eq. (2.2) are options for use as the flexural rigidity in ACI 318. However, ACI 318 has a third equation to calculate the effective flexural rigidity of RC columns based on the work of Khuntia and Ghosh (2004). In the third equation, ACI 318 Equation 6.6.4.4.4c or Eq. (2.3) in this report, EI depends on the axial load and bending moment experienced by the column.

In order to gain a deeper understanding of this equation, a contour plot of EI_{eff} according to Eq. (2.3) normalized by $E_c I_g$ was created for the cross section of the first column of the parameter suite, case C01-L5-NS01 (a circular column with a D=16 in./ and $\rho_{nominal}$=0.01, note that the member properties such as L/D do not effect the evaluation of EI_{eff}). The contour plot is shown in Figure 6.1. The cross-sectional capacity obtained from the strain compatibility is plotted in Figure 6.1 as a solid black line. For a given axial load, the flexural rigidity computed from Eq. (2.3) decreases as the bending moment increases. For a given bending moment, the flexural rigidity computed from Eq. (2.3) first increases then decreases. Within the cross-sectional strength, the lowest flexural rigidity occurs for low axial loads and high bending moments.

Figure 6.2 shows the error plots for when flexural rigidity is defined by Eq. (2.3). These plots are constructed in the manner as the figures in the Chapter 5 (e.g., Figure 5.12). As can be seen in Figure 6.2, the results obtained from this equation have a lower conservative errors in general compared to AASHTO LRFD equations (Figures 5.12 through 5.15). This is expected since Eq. (2.3) results in values of EI that are greater than from Eq. (2.1) or Eq. (2.2) over most of the cross-sectional strength.

Unconservative errors were identified in the lower axial load region as before with Eq. (2.1) and Eq. (2.2). However, Eq. (2.3) the unconservative errors manifest over a broader range of applied axial loads. The extent of unconservative error is less for cases with a slenderness of less than 100. However, some references (e.g., (Adams et al., 2019)) identify Eq. (2.3) as having superior precision compared to Eq. (2.1) and Eq. (2.2) and suitable for use when the slenderness exceeds 100.
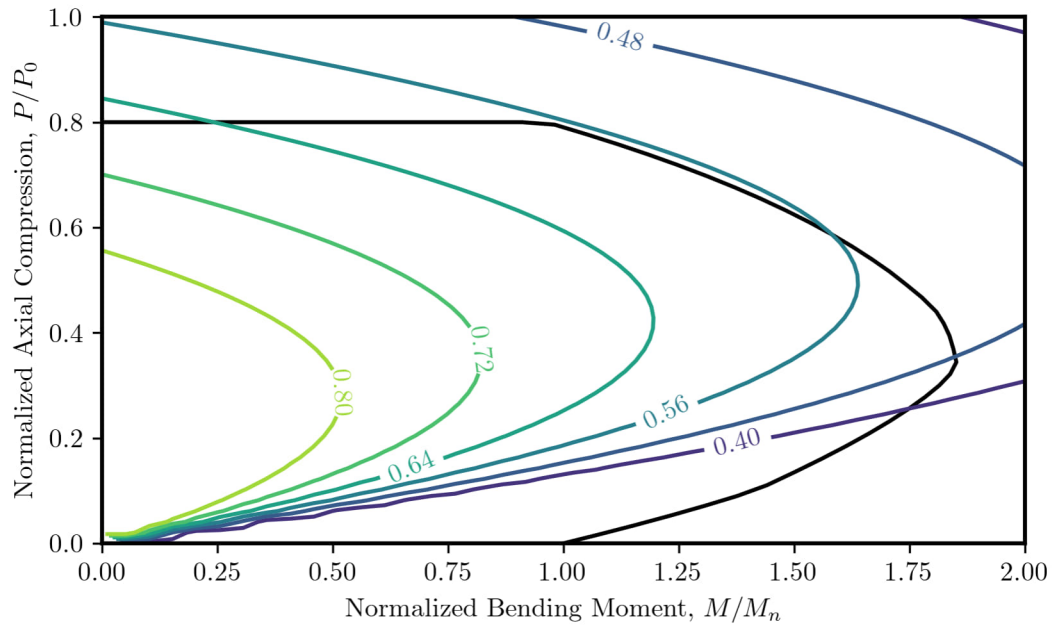
Figure 6.1: Contour plot of $EI_{eff}/E_c I_g$ with EI_{eff} computed using Eq. (2.3). Black line is the cross sectional strength of an example cross section.

Figure 6.2: Error plot of (a) all cases and (b) cases with $KL/r < 100$, based on the results obtained with EI calculated using Eq. (2.3).

Additionally, the error data, separated by nominal steel ratio and slenderness, is shown in Tables 6.1 and 6.2. In general, higher unconservative error was observed for sway columns compared to nonsway columns. This is in direct contrast with the results obtained from Eq. (2.1) and Eq. (2.2). Also, the errors do not exhibit a consistent trend with steel ratio. This, too, is unlike what was observed for the error data based on the AASHTO LRFD EI equations.

Table 6.1: Upper and lower error bounds for nonsway columns as determined by slenderness using Eq. (2.3).

| ρ | ε (%) | Slenderness Range | | | | | |
		0-25	25-50	50-75	75-100	100-125	≥ 125
1%	Min	-0.034	-0.092	-0.207	-0.295	-0.309	-0.393
	Max	0.295	0.280	0.204	0.221	0.241	0.234
2%	Min	-0.009	-0.037	-0.147	-0.250	-0.261	-0.342
	Max	0.283	0.270	0.198	0.298	0.358	0.381
3%	Min	-0.008	-0.043	-0.157	-0.304	-0.313	-0.355
	Max	0.274	0.262	0.195	0.360	0.429	0.492
4%	Min	0.009	-0.037	-0.143	-0.345	-0.328	-0.334
	Max	0.266	0.255	0.215	0.401	0.482	0.565

Table 6.2: Upper and lower error bounds for sway columns as determined by slenderness using Eq. (2.3).

| ρ | ε (%) | Slenderness Range | | | | | |
		0-25	25-50	50-75	75-100	100-125	≥ 125
1%	Min	-0.012	-0.018	-0.041	-0.123	-0.144	-0.578
	Max	0.291	0.285	0.212	0.296	0.302	0.295
2%	Min	0.002	0.000	-0.089	-0.207	-0.142	-0.586
	Max	0.279	0.274	0.217	0.381	0.405	0.433
3%	Min	-0.002	-0.004	-0.147	-0.186	-0.152	-0.537
	Max	0.271	0.265	0.258	0.424	0.482	0.518
4%	Min	0.010	-0.007	-0.161	-0.227	-0.191	-0.411
	Max	0.263	0.258	0.285	0.464	0.528	0.586

6.1.2 Variable Effective Flexural Stiffness Proposed by Jenkins and Frosch

Other equations for the effective flexural stiffness has been proposed by Jenkins and Frosch (2015). They proposed two different sets of equations. The first set of equations, described in Table 6.3, is described as more accurate but requires the steel reinforcement ratio, which may not be known initially in design. The second set of equations, described in Table 6.4, does not require the steel reinforcement ratio. In each set, one equation is provided for lower eccentricity and another equation is provided for higher eccentricity. Each equation has a lower bound of either 0.30 or 0.40 times $E_c I_g$. In the context of these equations P_0 is defined as in Eq. (5.3) and represents the nominal axial strength, while $P_{0g} = 0.85 f'_c A_g$ and represents the axial strength of the gross concrete cross section.

Contour plots like shown in Figure 6.1 for case C01-L5-NS01 are shown in Figures 6.3 and 6.4

Table 6.3: Flexural stiffness equations proposed by Jenkins and Frosch (2015) for detailed analysis or design.

$\dfrac{M}{Ph} = \dfrac{e}{h}$	Flexural Stiffness of Compression Member, EI
≤ 0.1	$\left[1.05 - 0.6\dfrac{P}{P_0}\right]\left[1.0 + 3\left(\dfrac{A_{st}}{A_g} - 0.01\right)\right]E_cI_g \geq 0.30E_cI_g$
> 0.1	$\left[1.05 - 0.6\dfrac{P}{P_0}\right]\left[1.0 + 3\left(\dfrac{A_{st}}{A_g} - 0.01\right)\right]\left[1.2 - 2\dfrac{M}{Ph}\right]E_cI_g \geq 0.30E_cI_g$

Table 6.4: Flexural stiffness equations proposed by Jenkins and Frosch (2015) for general design.

$\dfrac{M}{Ph} = \dfrac{e}{h}$	Flexural Stiffness of Compression Member, EI
≤ 0.1	$\left[1.0 - 0.5\dfrac{P}{P_{0g}}\right]E_cI_g \geq 0.40E_cI_g$
> 0.1	$\left[1.0 - 0.5\dfrac{P}{P_{0g}}\right]\left[1.2 - 2\dfrac{M}{Ph}\right]E_cI_g \geq 0.40E_cI_g$

for the two sets of Jenkins and Frosch equations. These figures show that the Jenkins and Frosch equations exhibit the same general trends with axial load and bending moment as Eq. (2.3).

Error plots are shown in Figures 6.5 and 6.6. The first subplot of each of these figure which shows the results for all cases shows high unconservative errors that significantly surpass any acceptable limit. These errors are prevalent across the entire spectrum of axial loads. However, the unconservative errors are less in Figures 6.5b and 6.6b which show the results only for cases where $KL/r < 100$. The unconservative errors shown in Figure 6.5b for the EI defined by set of equations in Table 6.3 are relatively modest and fall into the same range as errors determined using the AASHTO LRFD equations for EI.

Error data is listed in Tables 6.5 through 6.8. The information presented in Table 6.6 indicates that the error value increases when employing the equations from Table 6.3 for sway columns, particularly when the slenderness ratio is higher than 125. Specifically, the maximum unconservative error observed is 7.6% when $KL/r \leq 125$. Furthermore, data in Tables 6.5 and 6.7 shows a significant increase in unconservative error as the steel ratio decreases when using either set of equations proposed by Jenkins and Frosch.

Figure 6.3: Normalized contour plot for equations in Table 6.3

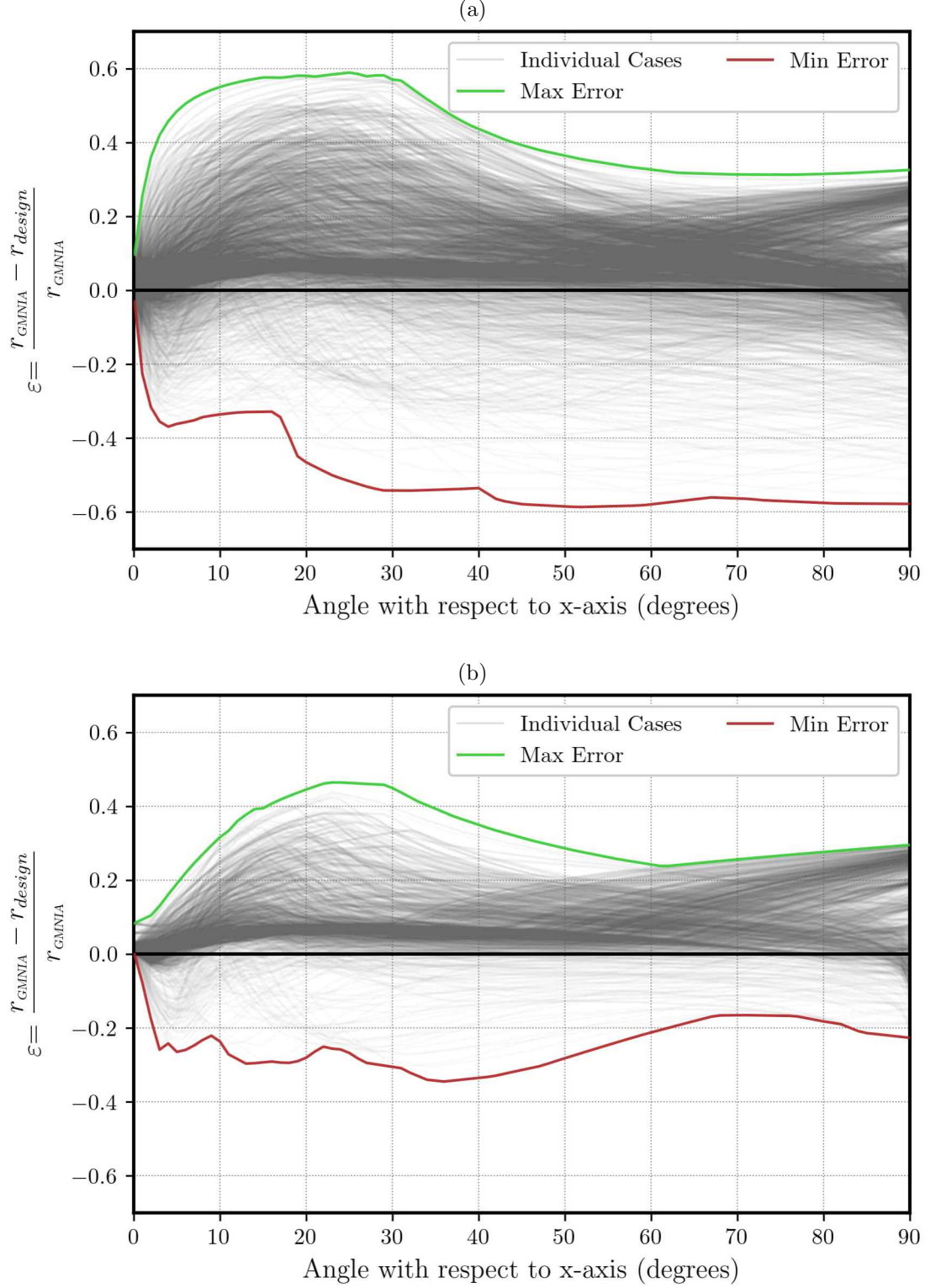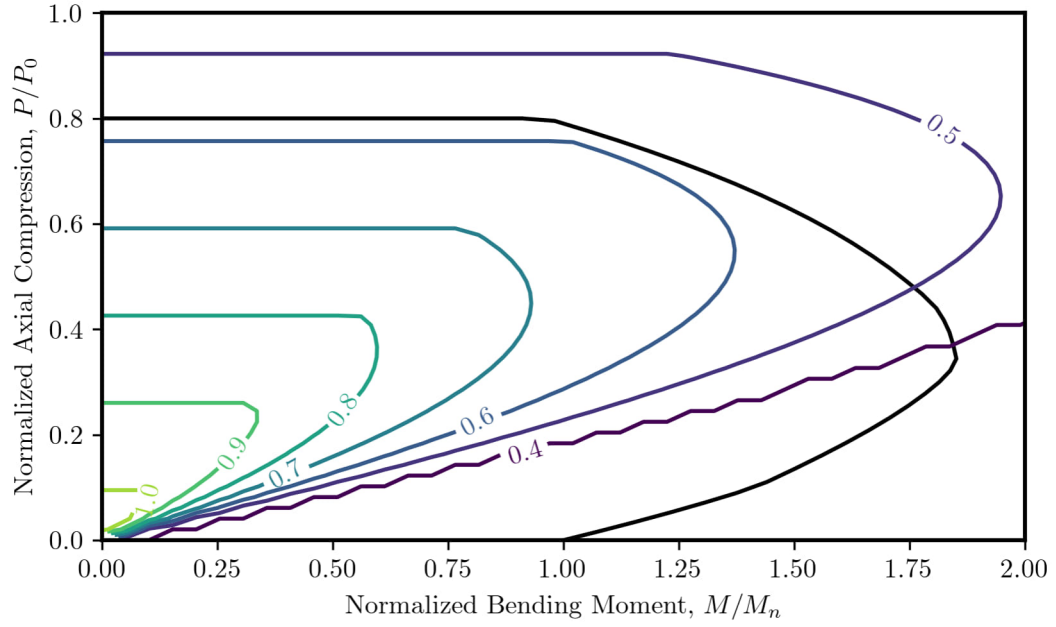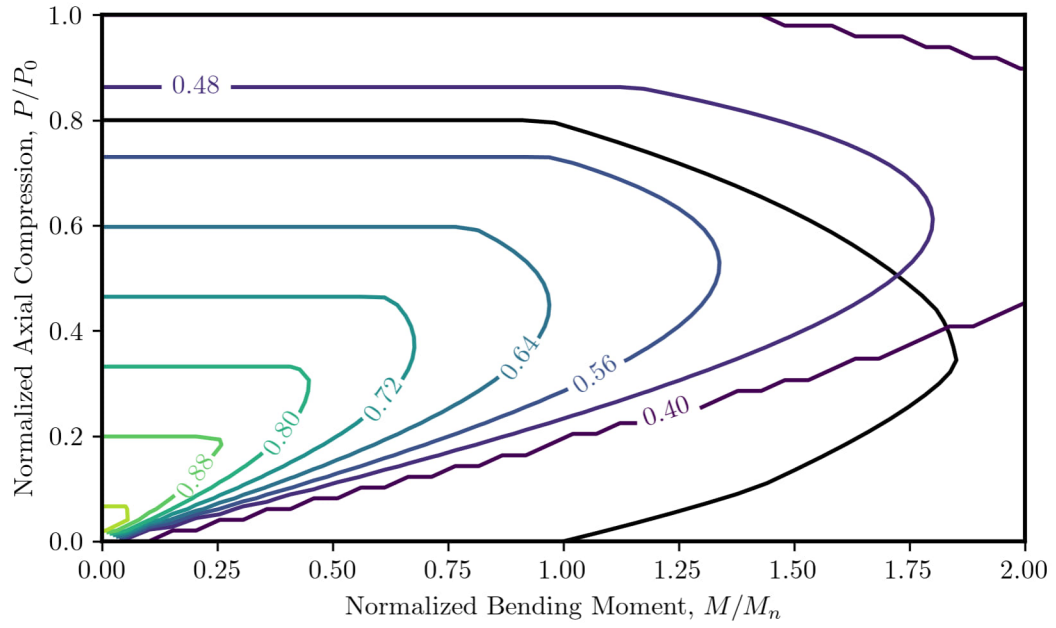
Figure 6.4: Normalized contour plot for equations in Table 6.4
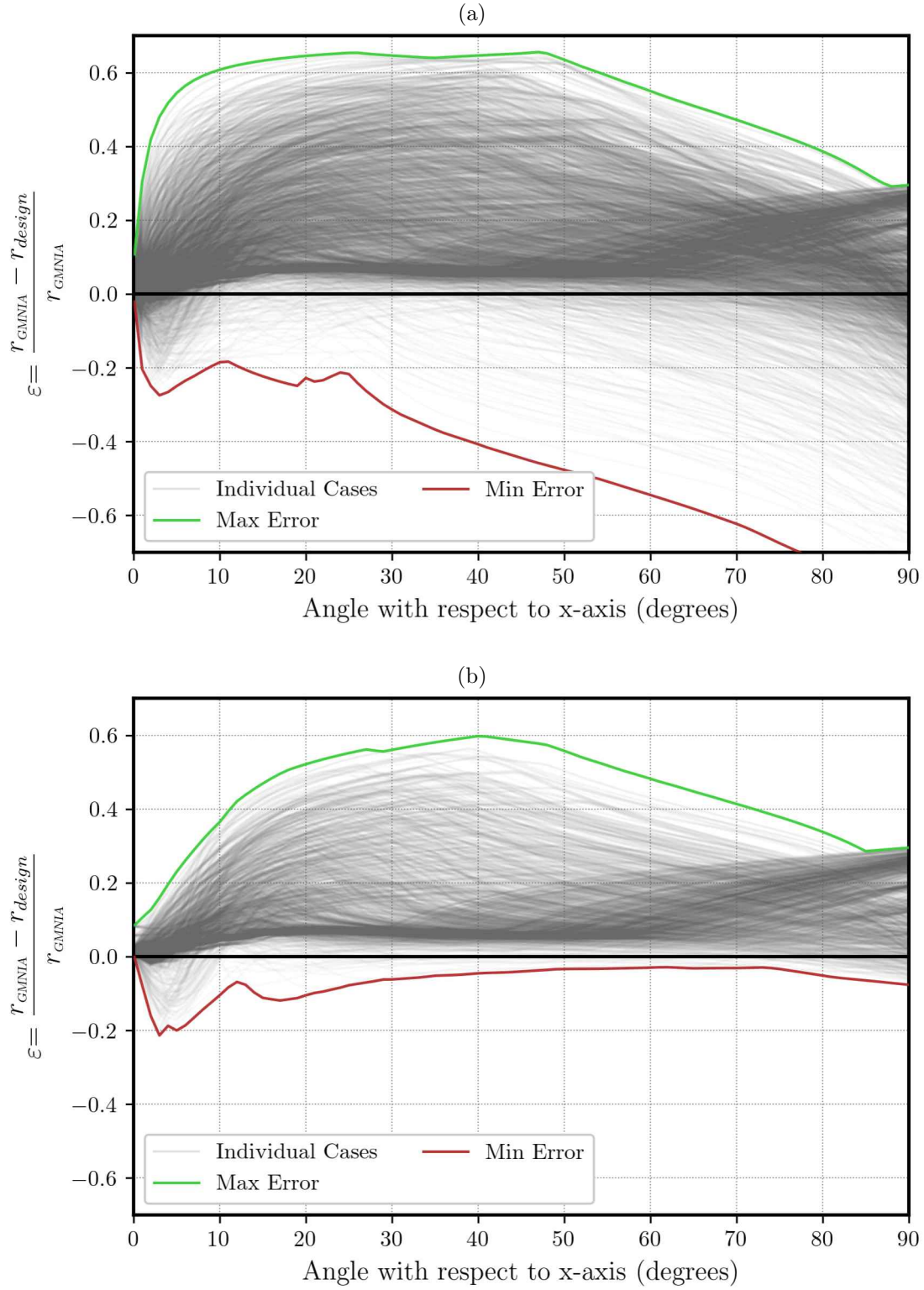
Figure 6.5: Error plot of (a) all cases and (b) cases with $KL/r < 100$, based on the results obtained with EI calculated using Table 6.3.

(a)

(b)
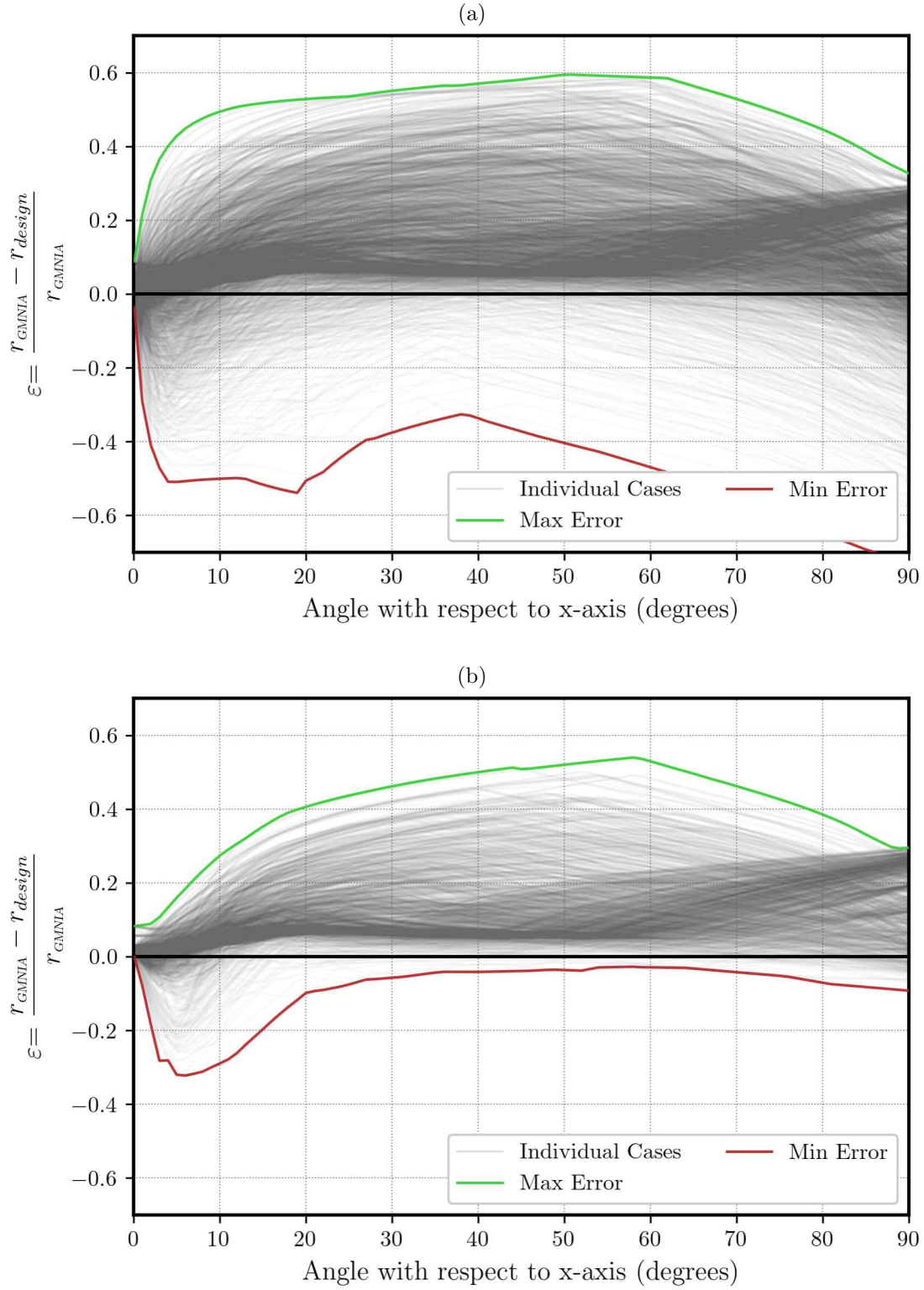
Figure 6.6: Error plot of (a) all cases and (b) cases with $KL/r < 100$, based on the results obtained with EI calculated using Table 6.4.

Table 6.5: Upper and lower error bounds for nonsway columns as determined by slenderness using equations from Table 6.3.

ρ	ε (%)	Slenderness Range					
		0-25	25-50	50-75	75-100	100-125	≥ 125
1%	Min	-0.032	-0.074	-0.122	-0.212	-0.228	-0.274
	Max	0.295	0.280	0.204	0.332	0.374	0.386
2%	Min	-0.007	-0.015	-0.062	-0.055	-0.074	-0.095
	Max	0.283	0.270	0.265	0.444	0.508	0.535
3%	Min	-0.007	-0.006	-0.046	-0.029	-0.022	-0.093
	Max	0.274	0.262	0.314	0.505	0.584	0.605
4%	Min	0.009	0.000	-0.032	-0.019	-0.012	-0.088
	Max	0.266	0.255	0.375	0.557	0.637	0.653

Table 6.6: Upper and lower error bounds for sway columns as determined by slenderness using equations from Table 6.3.

ρ	ε (%)	Slenderness Range					
		0-25	25-50	50-75	75-100	100-125	≥ 125
1%	Min	-0.010	-0.015	-0.032	-0.076	-0.073	-0.813
	Max	0.291	0.285	0.279	0.423	0.433	0.424
2%	Min	0.003	0.001	-0.050	-0.066	-0.067	-0.748
	Max	0.279	0.274	0.336	0.495	0.544	0.543
3%	Min	-0.001	-0.003	-0.058	-0.061	-0.069	-0.719
	Max	0.271	0.265	0.375	0.547	0.600	0.611
4%	Min	0.011	0.010	-0.048	-0.060	-0.068	-0.673
	Max	0.263	0.258	0.423	0.598	0.643	0.655

Table 6.7: Upper and lower error bounds for nonsway columns as determined by slenderness using equations from Table 6.4.

ρ	ε (%)	Slenderness Range					
		0-25	25-50	50-75	75-100	100-125	≥ 125
1%	Min	-0.036	-0.107	-0.196	-0.322	-0.379	-0.463
	Max	0.295	0.280	0.204	0.257	0.291	0.314
2%	Min	-0.011	-0.029	-0.076	-0.146	-0.167	-0.194
	Max	0.283	0.270	0.198	0.387	0.424	0.438
3%	Min	-0.009	-0.014	-0.026	-0.067	-0.079	-0.094
	Max	0.274	0.262	0.243	0.459	0.505	0.518
4%	Min	0.008	0.009	-0.016	-0.012	-0.021	-0.029
	Max	0.266	0.255	0.285	0.515	0.563	0.586

Table 6.8: Upper and lower error bounds for sway columns as determined by slenderness using equations from Table 6.4.

ρ	ε (%)	Slenderness Range					
		0-25	25-50	50-75	75-100	100-125	$\geq$ 125
1%	Min	-0.014	-0.024	-0.040	-0.092	-0.153	-0.729
	Max	0.291	0.285	0.212	0.333	0.360	0.370
2%	Min	0.002	-0.001	-0.055	-0.070	-0.052	-0.623
	Max	0.279	0.274	0.255	0.430	0.455	0.466
3%	Min	-0.003	-0.005	-0.055	-0.046	-0.045	-0.559
	Max	0.271	0.265	0.295	0.491	0.523	0.534
4%	Min	0.010	0.009	-0.037	-0.030	-0.036	-0.478
	Max	0.263	0.258	0.334	0.540	0.575	0.593

6.1.3 Proposed Enhanced Equation for Flexural Rigidity

Chapter 5 and the preceding sections show the unconservative error associated with the existing equations for estimating the flexural rigidity of RC columns. Recognizing the critical need for more accuracy, this section introduces new equations aimed at improving upon the existing ones.

Calculation of Flexural Rigidity Using GMNIA Results

To derive an equation for the effective flexural stiffness of columns, it is important to understand how flexural stiffness varies across different columns properties and under diverse loading conditions. For this purpose, flexural stiffness values are back-calculated for each case in the parameter suite. This calculation ensures that the maximum applied moment allowed by the AASHTO LRFD method equals the maximum applied moment determined from GMINA. This approach aims to achieve zero error when using the calculated EI in design. Given that calculated EI varies with cross-sectional and member properties, as well as loading conditions, the back-calculation is performed at each axial load evaluated by GMNIA.

Alternatively, EI can be back-calculated such that the magnified moment from the AASHTO LRFD method equals the maximum internal moment from the GMNIA. This approach may yield flexural rigidity values that are more physically realistic. However, it may not necessarily minimize errors when applied in the design approach.

In some instances, the maximum applied load obtained from GMNIA exceeds the moment capacity from the strain compatibility method. For these cases, the back-calculated EI is left undefined. In other instances, the maximum applied load obtained from GMNIA is only slightly less than the moment capacity from the strain compatibility method resulting in unrealistically large EI values greater than the gross uncracked stiffness (i.e., $E_c I_c + E_s I_s$). These cases tend to occur for short columns where second-order effects are minimal. For these cases, use of any value for EI equal to or less than the gross uncracked stiffness would be conservative. To avoid skewing the data, the values of EI greater than $E_c I_c + E_s I_s$ were excluded from the analysis.

For both types of back-calculation described above, the resulting value of EI is normalized by $E_c I_g$ and plotted in Figures 6.7 through 6.10. The figures are separated by sidesway condition.

Figure 6.7: Calculated EI of nonsway cases to their respective P/P_0 using moment capacity obtained from strain compatibility

Figure 6.7 shows that for nonsway cases an increase in axial load mostly corresponds to an increase in the flexural rigidity of the column. This result agrees with the findings of Hung et al. (2024), who also observed that the initial stiffness of the column increases under higher axial loading. This increase is nonlinear and exhibits different slopes for different columns. The same cannot be said about sway cases, as Figure 6.8 shows the pattern is not consistent among the cases.

The results in Figures 6.7 through 6.10 are colored by the nominal longitudinal steel reinforcement ratio. Figure 6.7 demonstrates that for nonsway cases, as the steel reinforcement ratio increases, there is a concurrent increase in the minimum flexural stiffness. This pattern is not seen for sway cases.
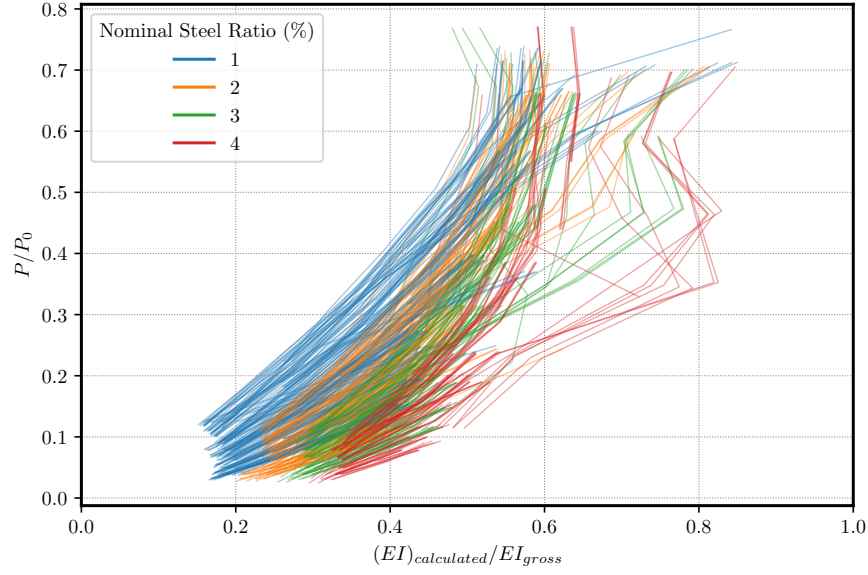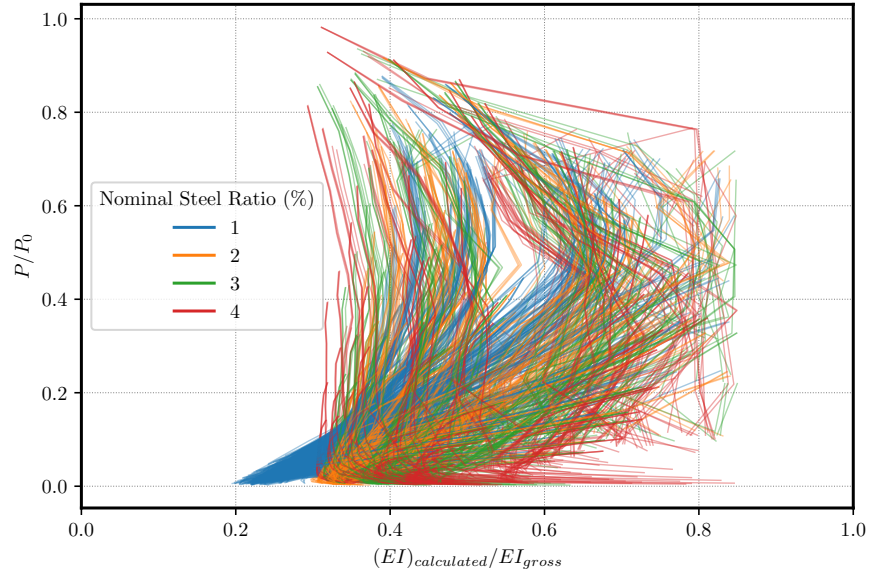
Figure 6.8: Calculated EI of sway cases to their respective P/P_0 using moment capacity obtained from strain compatibility
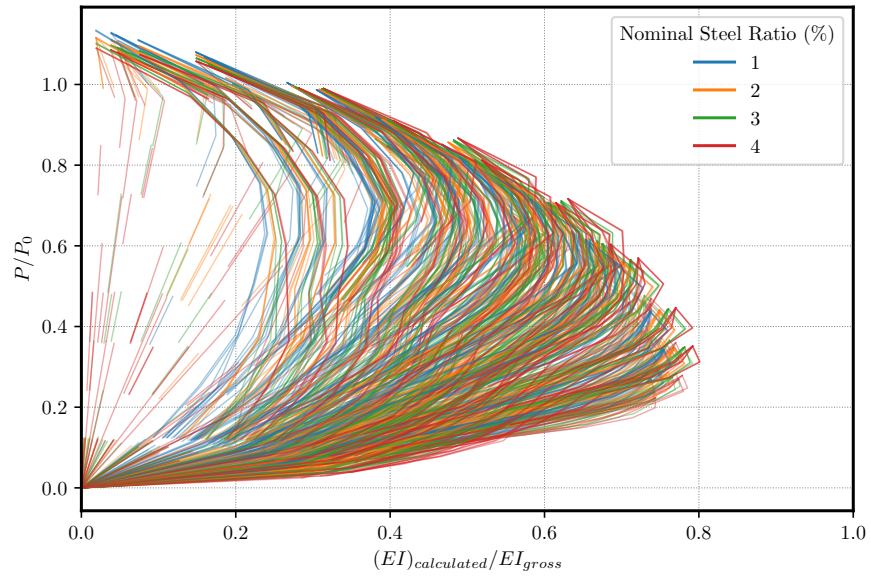
Figure 6.9: Calculated EI of nonsway cases to their respective P/P_0 using moment capacity obtained from GMINA
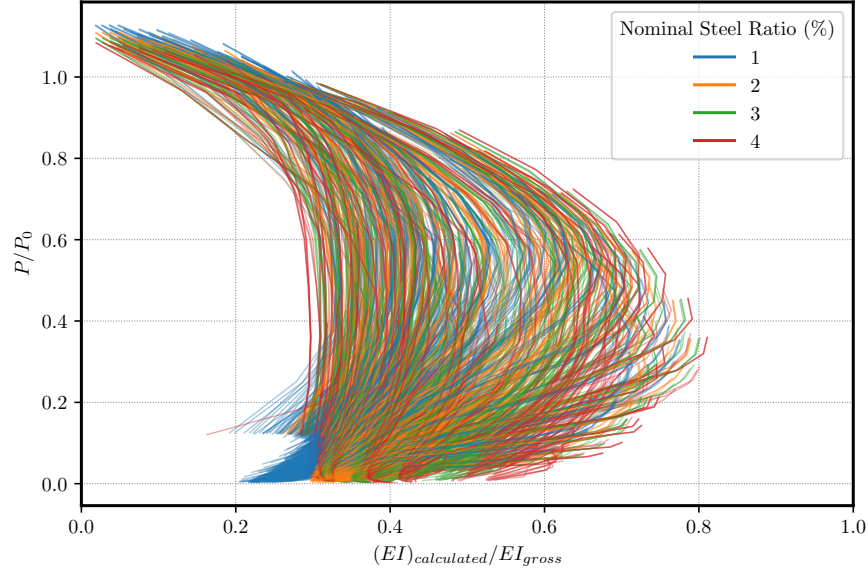
Figure 6.10: Calculated EI of sway cases to their respective P/P_0 using moment capacity obtained from GMINA

Formulation of the New Equations

New equations were developed for the effective flexural rigidity of RC columns based on the back-calculated EI results. These equations were developed with the goal of achieving the least possible unconservative error while controlling the conservative error.

Equation Set 1:

The first set of equations is based on the observation that flexural rigidity of the column decreases as the moment in the column nears the available strength. Flexural rigidity decreases because of cracks in the concrete and near the available strength it decreases further due to steel yielding.

For this equation set, either one of the current AASHTO LRFD equations is used when ratio of maximum internal moment to cross-sectional moment strength at zero axial load is less than or equal to 0.95, i.e., $M/M_n \leq 0.95$, and $EI = 0.4E_sI_s$ is used when $M/M_n > 0.95$. This equation set is described in Table 6.9.

Table 6.9: Flexural stiffness equation using available moment.

$\dfrac{M}{M_n}$	Flexural Stiffness of Compression Member, EI
≤ 0.95	$0.4E_cI_g$ (Eq. 2.1) or $0.2E_cI_g + E_sI_s$ (Eq. 2.2)
> 0.95	$0.4E_sI_s$

Based on the flexural rigidity obtained from the proposed equation defined in Table 6.9, all of the columns in the parameter suite were analyzed and the resulting error plots are shown in Figures 6.11 through 6.14. These plots are divided into sway and nonsway cases as they have shown different results in the equations investigated in the previous chapter. Additionally, the error values only for cases that have a slenderness ratio of less than 100 are plotted separately to understand slenderness effects on the equation accuracy.

These plots show that the new approach using either Eq. (2.1) or Eq. (2.2) results in no significant unconservative error when the slenderness ratio is less than or equal to 100. However, unconservative error is observed for cases with a slenderness ratio greater than 100, especially when Eq. (2.1) is used.

The error results are listed in Tables 6.10 through 6.13 for different slenderness ranges. No significant unconservative errors exist for cases within the range of 0-125 when using Eq. (2.1) and 0-160 when using Eq. (2.2) with the proposed approach. Additionally, the highest unconservative errors are consistently for the cases with the highest slenderness and lowest steel ratio.

Figure 6.11: Error plot of (a) all nonsway cases and (b) nonsway cases with $KL/r < 100$, based on the results obtained with EI calculated using Table 6.9 with Eq. (2.1).

(a)

(b)

Figure 6.12: Error plot of (a) all nonsway cases and (b) nonsway cases with $KL/r < 100$, based on the results obtained with EI calculated using Table 6.9 with Eq. (2.2).

Figure 6.13: Error plot of (a) all sway cases and (b) sway cases with $KL/r < 100$, based on the results obtained with EI calculated using Table 6.9 with Eq. (2.1).
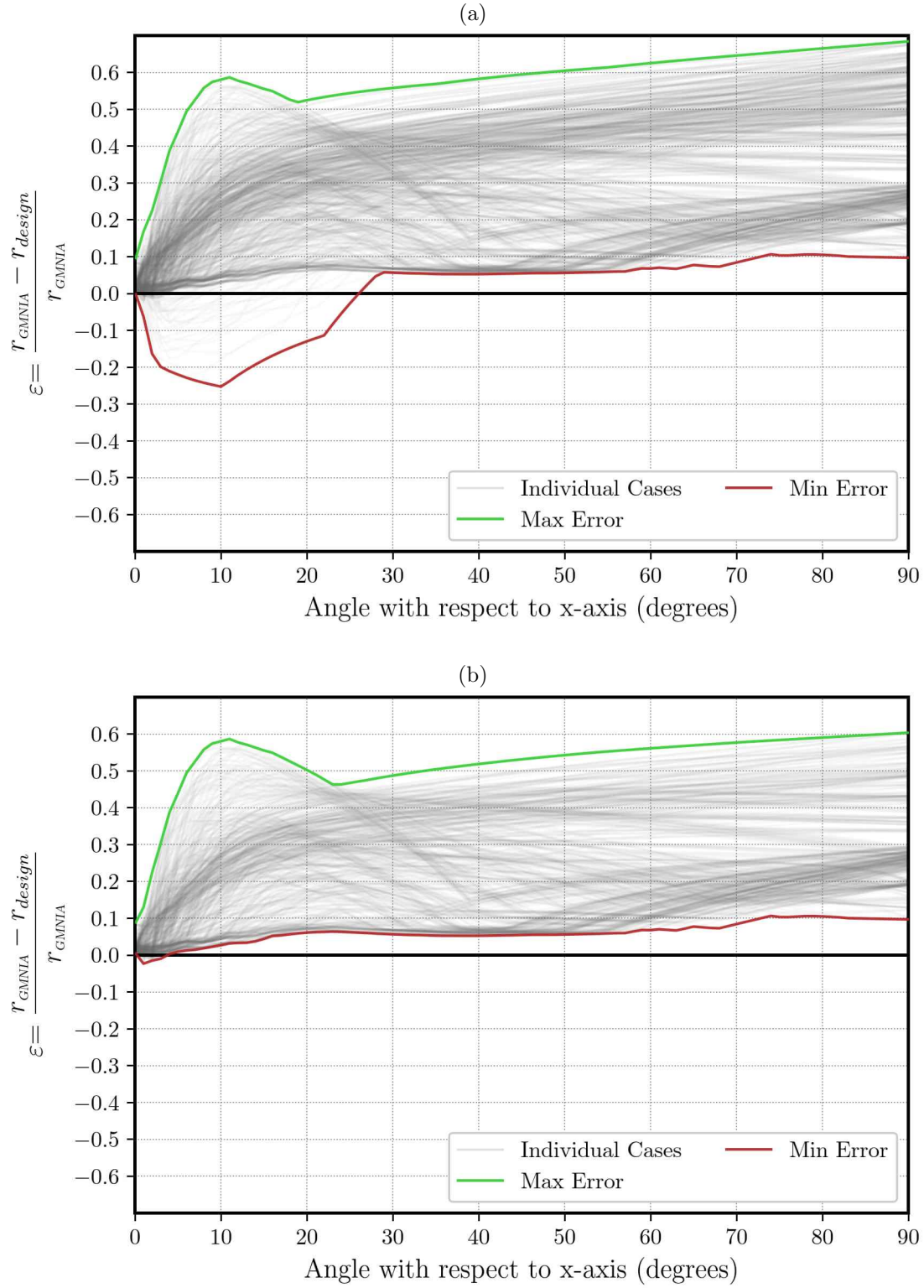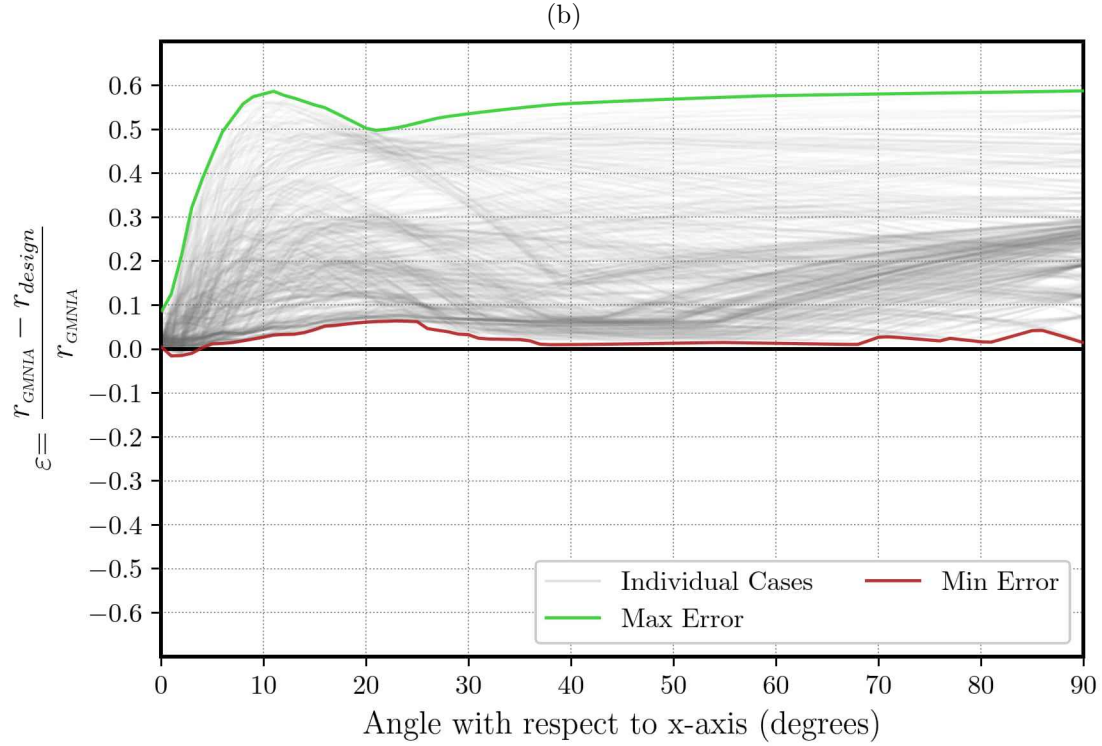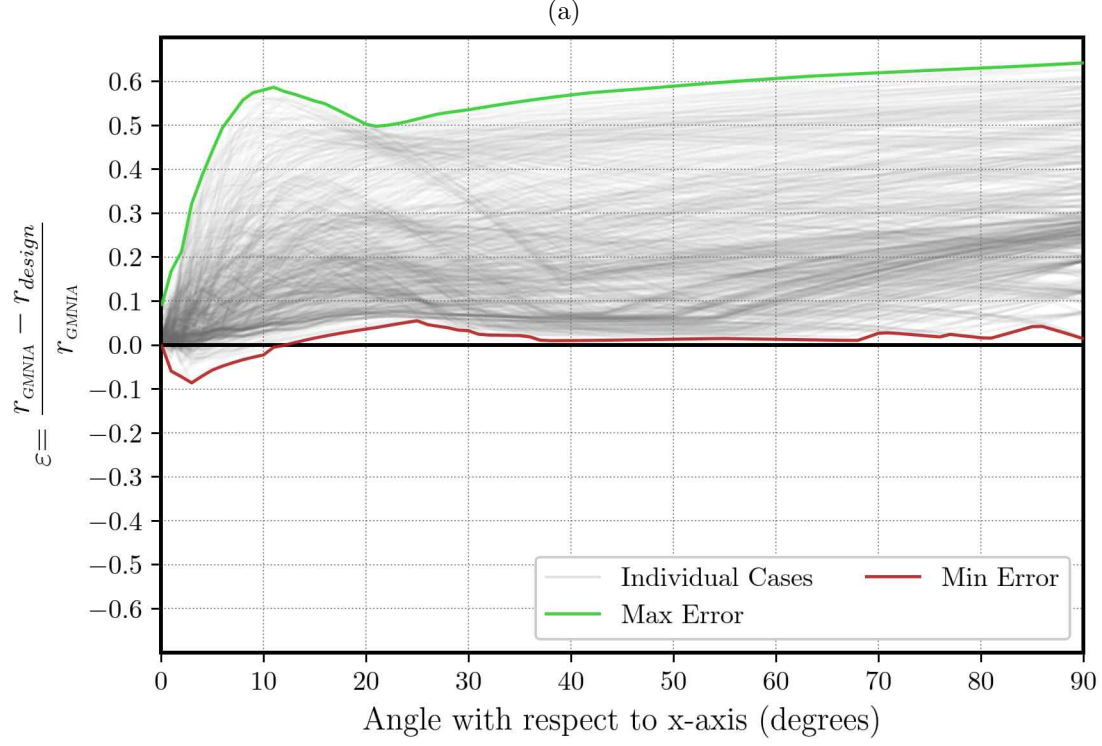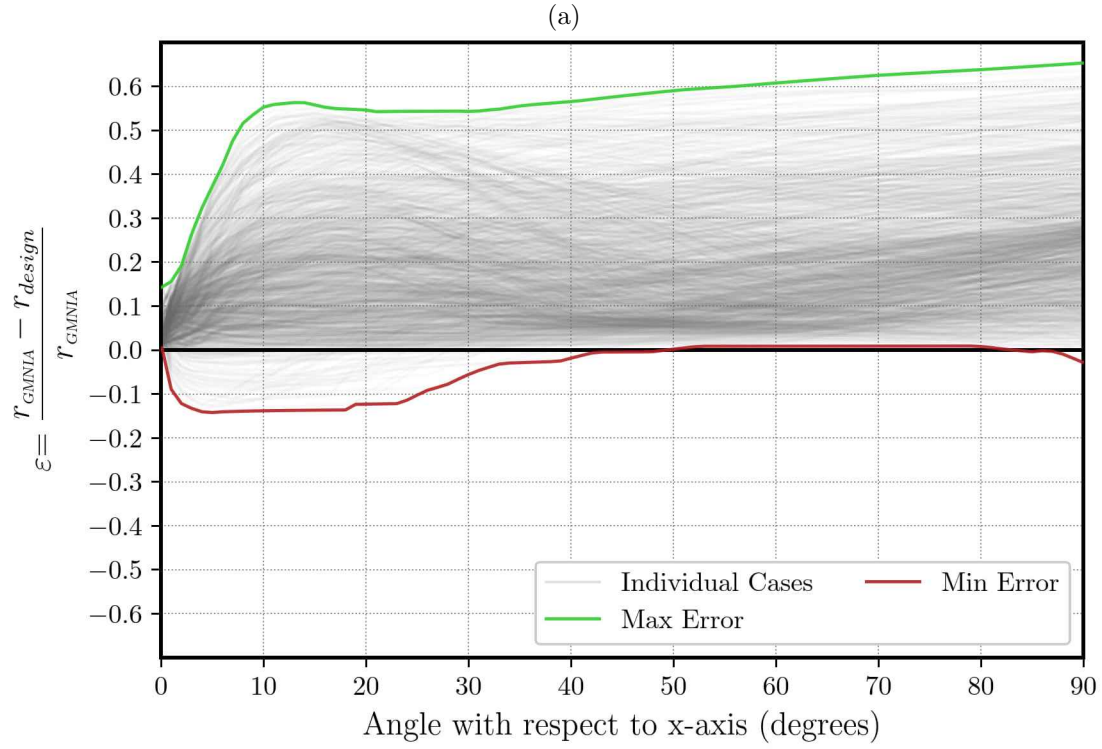
Figure 6.14: Error plot of (a) all nonsway cases and (b) nonsway cases with $KL/r < 100$, based on the results obtained with EI calculated using Table 6.9 with Eq. (2.2).
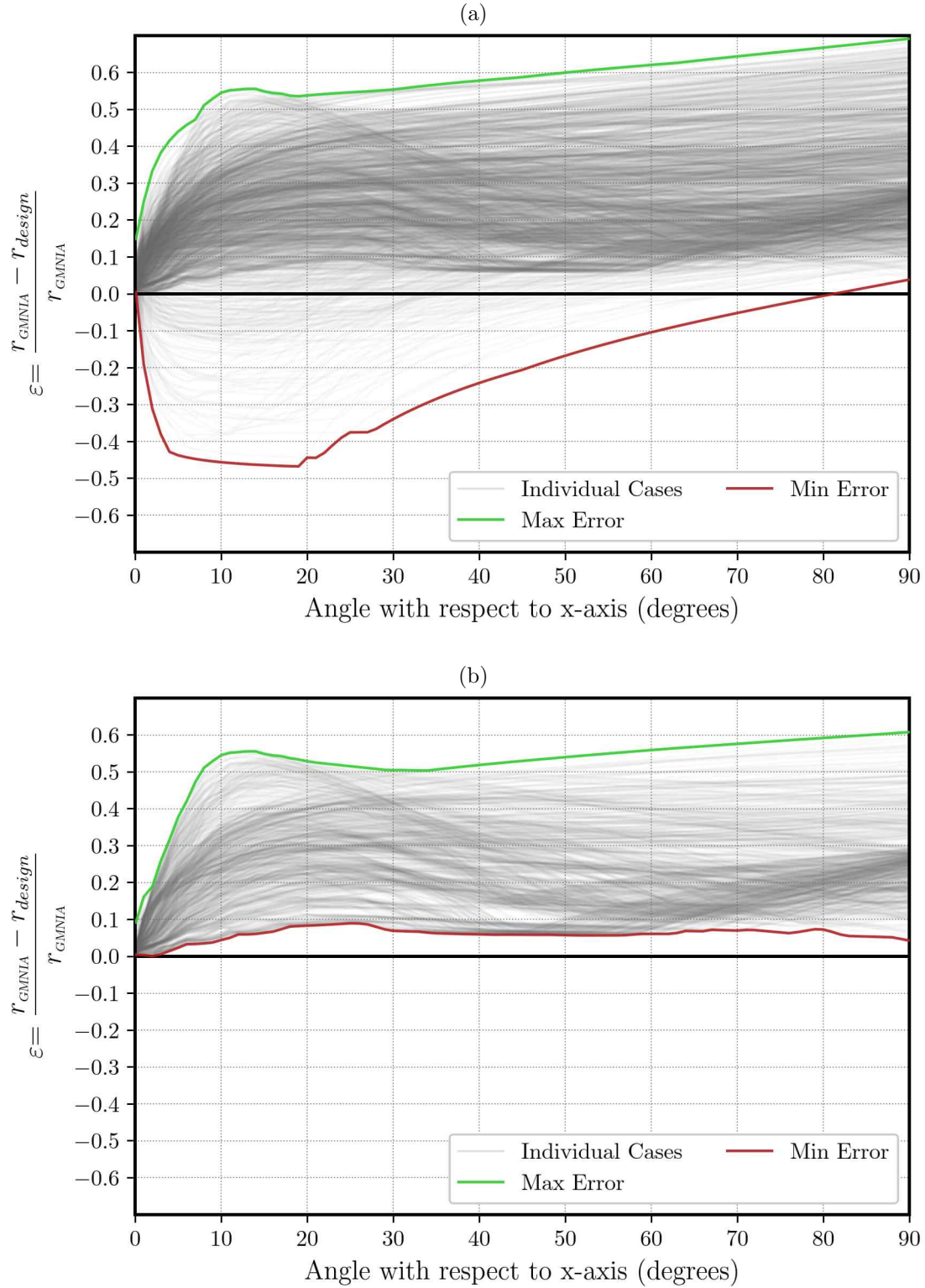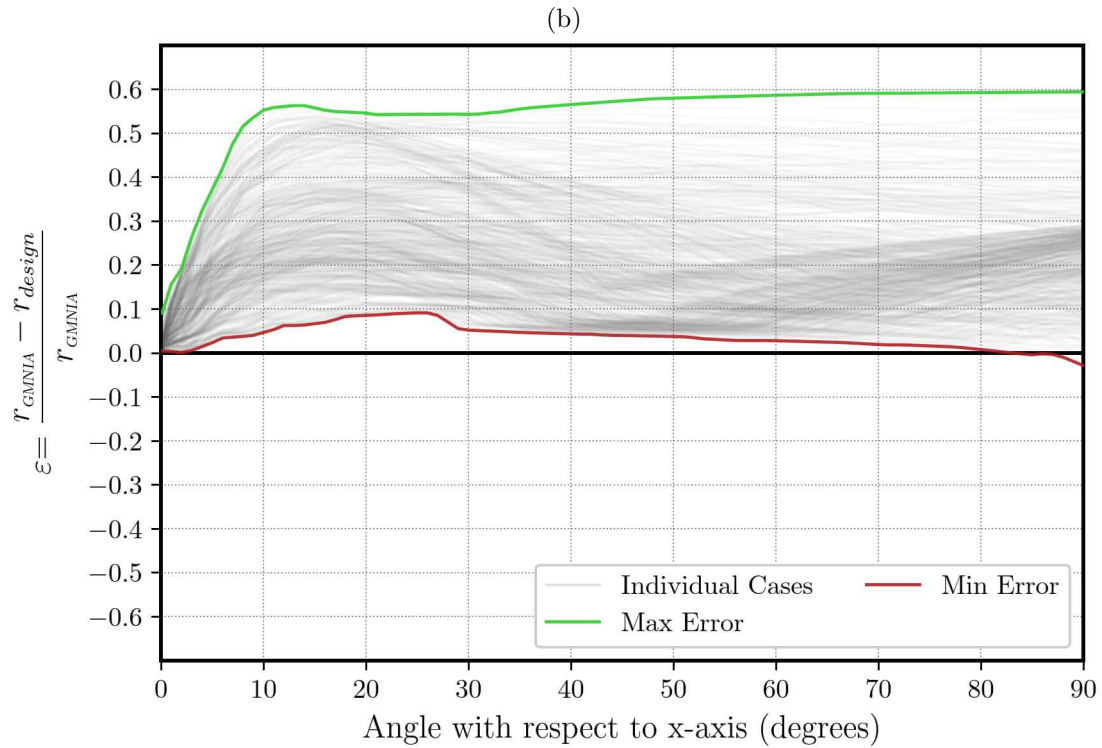
Table 6.10: Upper and lower error bounds for nonsway cases as determined by slenderness based on the results obtained with EI calculated using Table 6.9 with Eq. (2.1).

ρ	ε	Slenderness Range						
		0-24	25-49	50-74	75-99	100-124	125-149	150-160
1%	Min	-0.006	-0.003	-0.002	-0.001	-0.076	-0.164	-0.252
	Max	0.427	0.571	0.579	0.583	0.504	0.535	0.545
2%	Min	0.002	0.003	0.004	-0.018	-0.021	-0.045	-0.080
	Max	0.287	0.388	0.387	0.504	0.567	0.595	0.605
3%	Min	-0.004	-0.003	0.000	-0.007	-0.020	-0.021	-0.033
	Max	0.274	0.305	0.312	0.559	0.615	0.640	0.649
4%	Min	0.009	0.009	0.010	0.000	-0.006	-0.014	-0.005
	Max	0.266	0.272	0.348	0.604	0.653	0.675	0.684

Table 6.11: Upper and lower error bounds for nonsway cases as determined by slenderness based on the results obtained with EI calculated using Table 6.9 with Eq. (2.2).

ρ	ε	Slenderness Range						
		0-24	25-49	50-74	75-99	100-124	125-149	150-160
1%	Min	-0.006	-0.003	-0.002	-0.001	-0.011	-0.043	-0.082
	Max	0.430	0.571	0.579	0.587	0.627	0.641	0.642
2%	Min	0.002	0.003	0.004	-0.001	-0.011	-0.043	-0.082
	Max	0.287	0.388	0.387	0.529	0.571	0.585	0.586
3%	Min	-0.004	-0.003	0.000	-0.007	-0.021	-0.021	-0.024
	Max	0.274	0.305	0.308	0.492	0.534	0.548	0.548
4%	Min	0.009	0.009	0.009	0.000	-0.012	-0.015	-0.025
	Max	0.266	0.272	0.276	0.451	0.494	0.507	0.506

Table 6.12: Upper and lower error bounds for sway cases as determined by slenderness based on the results obtained with EI calculated using Table 6.9 with Eq. (2.1).

ρ	ε	Slenderness Range						
		0-99	100-149	150-174	175-199	200-224	225-249	≥ 250
1%	Min	0.004	0.020	-0.067	-0.250	-0.261	-0.385	-0.468
	Max	0.557	0.545	0.557	0.504	0.478	0.477	0.444
2%	Min	0.007	0.020	0.024	-0.001	-0.036	-0.060	-0.114
	Max	0.511	0.604	0.615	0.575	0.544	0.556	0.533
3%	Min	0.001	0.015	0.020	0.027	0.031	0.043	0.018
	Max	0.564	0.647	0.658	0.626	0.591	0.612	0.596
4%	Min	0.010	0.022	0.028	0.035	0.043	0.053	0.066
	Max	0.608	0.682	0.692	0.666	0.631	0.656	0.643

Table 6.13: Upper and lower error bounds for sway cases as determined by slenderness based on the results obtained with EI calculated using Table 6.9 with Eq. (2.2).

ρ	ε	Slenderness Range						
		0-99	100-149	150-174	175-199	200-224	225-249	≥ 250
1%	Min	0.005	0.020	0.025	0.012	-0.015	-0.059	-0.142
	Max	0.594	0.650	0.653	0.594	0.536	0.563	0.528
2%	Min	0.007	0.020	0.025	0.030	0.019	0.007	-0.017
	Max	0.537	0.597	0.599	0.530	0.434	0.496	0.458
3%	Min	0.001	0.015	0.020	0.021	0.013	0.008	-0.002
	Max	0.501	0.560	0.562	0.487	0.359	0.451	0.410
4%	Min	-0.028	0.023	0.019	0.015	0.010	0.008	0.005
	Max	0.462	0.521	0.522	0.440	0.296	0.401	0.360

Equation Set 2: The second set of equation is based on several observations from the back-calculated EI results. The flexural rigidity depends on the applied axial load on the column. Cross sections with higher steel ratio show higher effective flexural stiffness (Figures 6.7 and 6.8). For the most of the columns, a near sinusoidal pattern is observed for the changes in the EI value with respect to the axial load P with the magnitude of the change increasing as the column gets more slender.

Based on these observations, Eq. (6.1) was developed to evaluate the flexural rigidity of the column. The term $0.45\frac{P}{P_0}E_cI_g$ represents the linear portion of the increase in EI with an increase in axial load. The term $0.35(\frac{K_gL}{100r})^{1.85}\sin(\frac{\pi P}{P_0})E_cI_g$ represents the approximately sinusoidal pattern observed in the variations of the EI concerning the axial load. The term $0.3E_sI_s$ corresponds to the minimum stiffness the columns exhibited, irrespective of the loading and slenderness conditions.

$$EI = \left[0.45\frac{P}{P_0} + 0.35\left(\frac{K_gL}{100r}\right)^{1.85}\sin\left(\frac{\pi P}{P_0}\right)\right]E_cI_g + 0.3E_sI_s \tag{6.1}$$

where K_g is the effective length factor of the column when Eq. (2.1) is used to calculate the effective flexural rigidity. K_g is used instead of K to avoid the need for iterative calculations of EI resulting from a mutual dependence of K on EI and vice versa.

A contour plot of EI according to Eq. (6.1) normalized by E_cI_g for the cross section of case C01-L5-NS01 is shown in Figure 6.15. Unlike the previous contour plots which were investigated in subsections 6.1.1 and 6.1.2, the EI calculated by Eq. (6.1) depends on the slenderness of the column. The values shown in Figure 6.15 are for $K_gL/r = 5$.

To evaluate the efficacy Eq. (6.1) in reducing error, error values were calculated in comparison to results from GMNIA as has been done in this work for other equations of flexural rigidity. Figures 6.16 and 6.17 show the error values plotted against the angle with respect to the x-axis. These plot show nearly no unconservative error for both sway and nonsway cases with a $KL/r < 100$. Looking at the density of the lines from individual cases seen by darkness in the plots of in Figures 6.16 and 6.17, most of the cases with $KL/r < 100$ have a maximum positive error of less than 0.3.
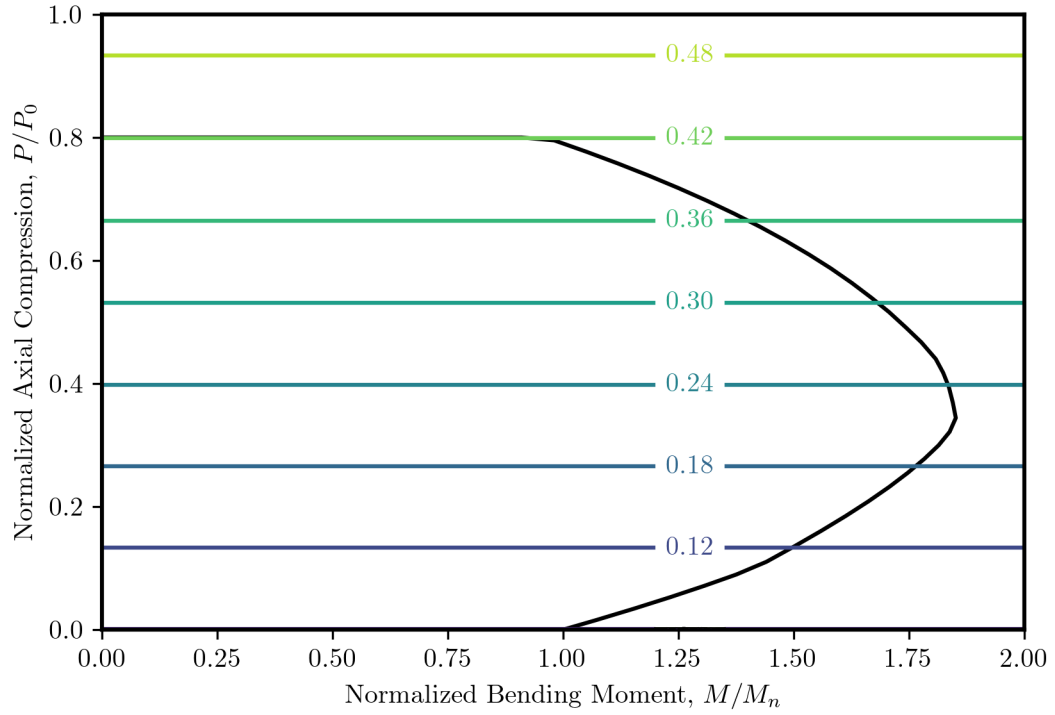
Figure 6.15: Contour plot of EI/E_cI_g with EI computed using Eq. (6.1) and $K_gL/r = 5$. Black line is the cross sectional strength of an example cross section.

Additionally, the maximum conservative error for these cases is decreased up to 50% for different slenderness ratios when compared to the AASHTO LRFD equations (Tables 6.14 and 6.14).

For more slender cases, unconservative errors are observed for sway cases in Figure 6.17. These are limited to a maximum of -10%, which typically happens on the cases with the highest slenderness and low steel ratio. For the cases with a slightly higher slenderness than 100 ($100 < KL/r < 125$), the flexural rigidity obtained from Eq. (6.1) does not show any unconservative error which means the equation can safely be used for the cases near the current AASHTO LRFD slenderness limit of 100.

Figure 6.16: Error plot of (a) all nonsway cases, and (b) nonsway cases with a slenderness of less than 100, using equation in Eq. (6.1).

Figure 6.17: Error plot of (a) all sway cases, and (b) nonsway cases with a slenderness ratio of less than 100, based on the results obtained from Eq. (6.1)

Table 6.14: Upper and lower error bounds for nonsway columns as determined by slenderness using Eq. (6.1).

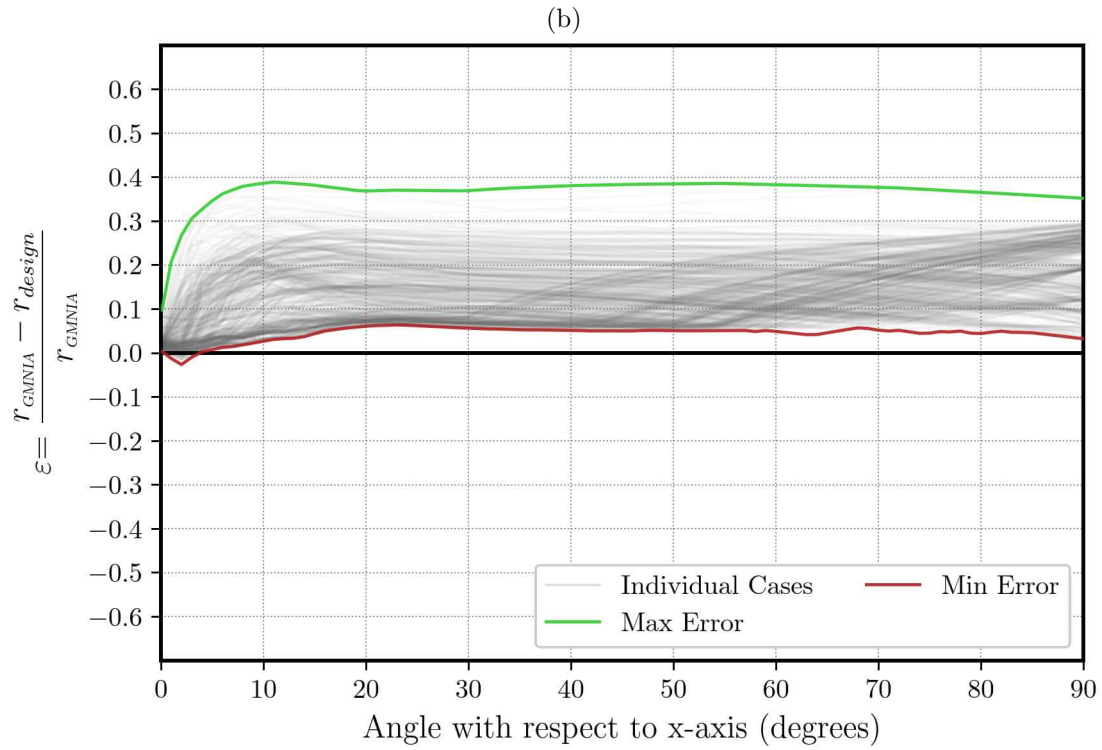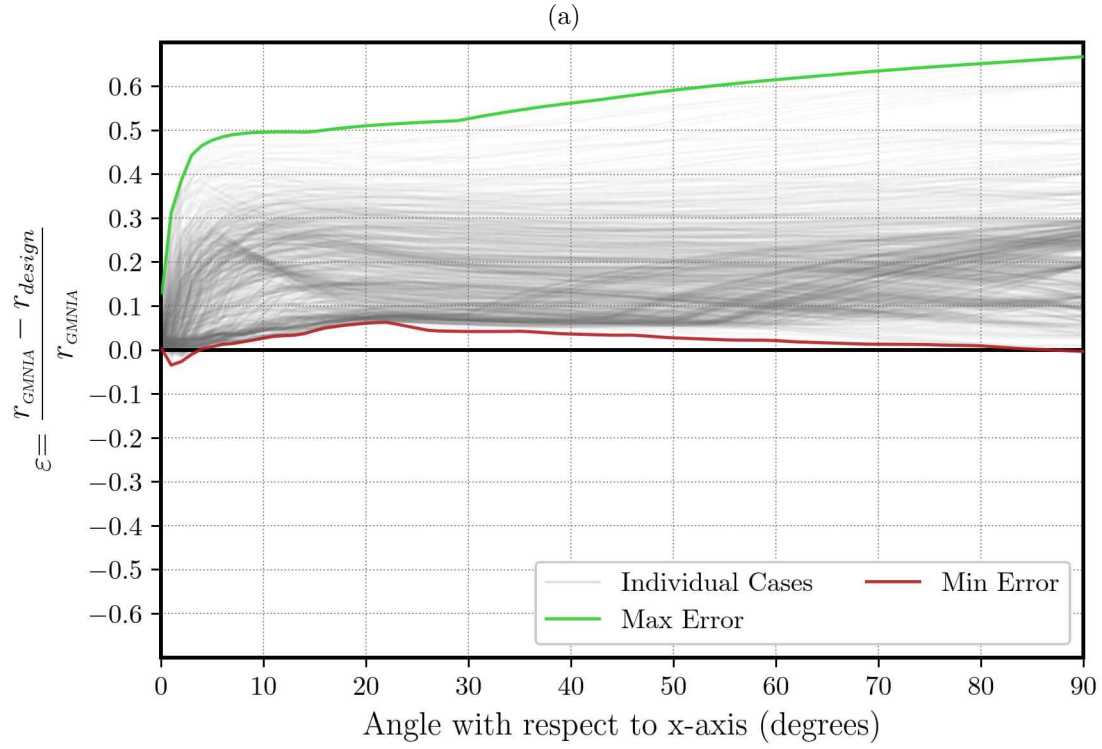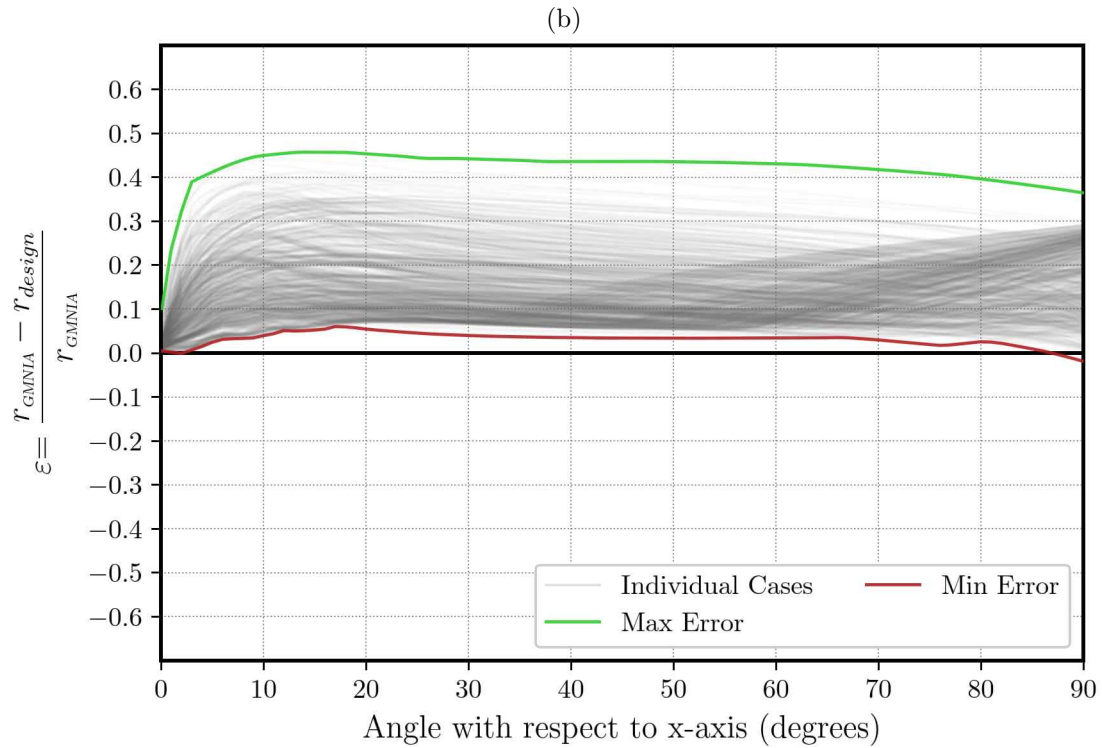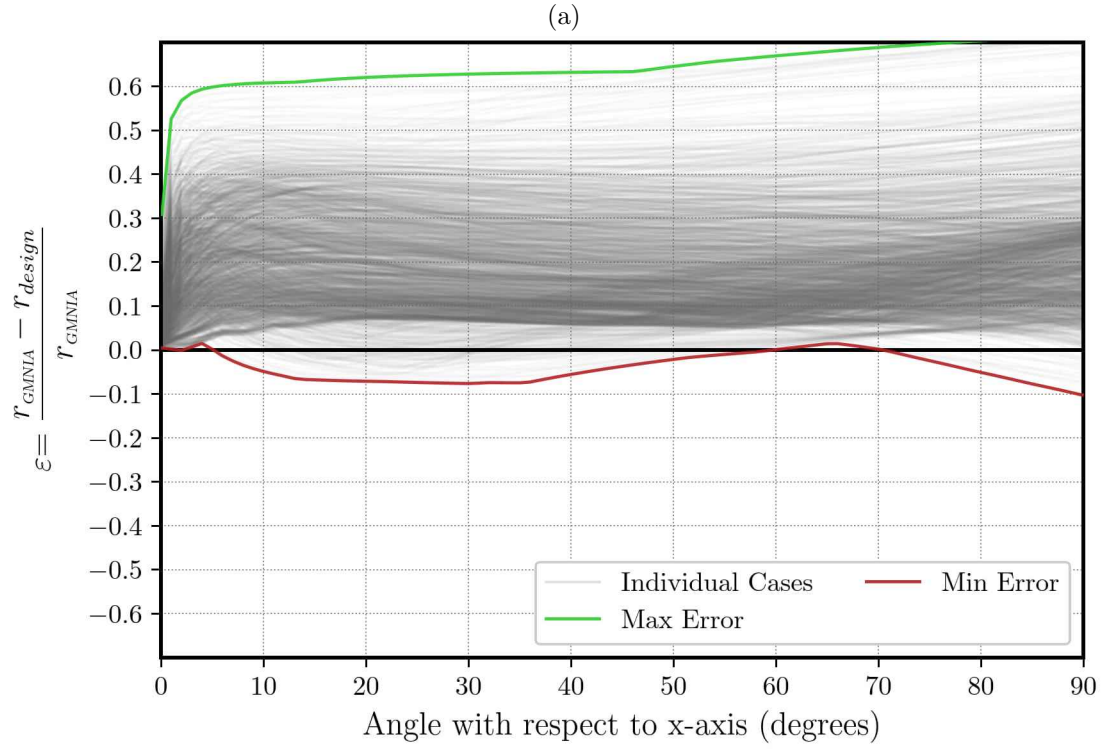| ρ	ε	Slenderness Range						
		0-24	25-49	50-74	75-99	100-124	125-149	150-160
1%	Min	-0.006	-0.003	-0.003	-0.001	-0.016	-0.019	-0.003
	Max	0.295	0.280	0.219	0.310	0.339	0.364	0.390
2%	Min	0.002	0.003	0.004	-0.015	0.007	0.003	0.002
	Max	0.283	0.270	0.229	0.334	0.374	0.417	0.498
3%	Min	-0.004	-0.003	0.000	-0.007	-0.015	-0.010	-0.015
	Max	0.274	0.262	0.252	0.357	0.432	0.523	0.611
4%	Min	0.009	0.009	0.009	0.000	-0.005	-0.014	0.003
	Max	0.266	0.255	0.267	0.407	0.510	0.606	0.667

Table 6.15: Upper and lower error bounds for sway columns as determined by slenderness using Eq. (6.1).

ρ	ε	Slenderness Range						
		0-99	100-149	150-174	175-199	200-224	225-249	≥ 250
1%	Min	0.004	-0.005	-0.074	-0.103	-0.065	-0.038	-0.076
	Max	0.421	0.458	0.470	0.484	0.396	0.602	0.718
2%	Min	-0.018	0.021	0.027	0.035	0.043	0.054	0.058
	Max	0.430	0.474	0.517	0.614	0.457	0.679	0.711
3%	Min	0.002	0.018	0.025	0.033	0.042	0.052	0.103
	Max	0.441	0.535	0.623	0.673	0.517	0.703	0.713
4%	Min	0.011	0.026	0.033	0.042	0.051	0.062	0.110
	Max	0.457	0.618	0.679	0.694	0.548	0.709	0.709

6.2 Slenderness Ratio Limits

Second-order effects, such as P-Δ and P-δ effects, become more significant as member slenderness increases. Like other standards, AASHTO LRFD uses the slenderness ratio, KL/r, to define limits of slenderness where certain provisions apply.

One such limit is the maximum value of KL/r for which second-order effects can be neglected. Neglecting second-order effects simplifies the structural analysis and design process. AASHTO LRFD Section 5.6.4.3 allows second-order effects to be neglected for members not braced against sidesway when the slenderness ratio is less than 22. For members braced against sidesway, second-order effects may be neglected when the slenderness ratio is less than $34 - 12(M_1/M_2)$, where M_1 and M_2 are the smaller and larger end moments, respectively (the term M_1/M_2 is positive if the member is bent in single curvature).

Another important limit is the maximum value of KL/r for which second-order effects can be evaluated using the approximate moment magnification procedure. According to AASHTO LRFD Section 5.6.4.3, the approximate procedure may be used for nonprestressed compression members with KL/r less than 100.

These specified limits and associated design considerations are evaluated in this section. The limits are primarily evaluated as a means of maintaining unconservative error below a tolerance. As a point of reference, 5% is a commonly used tolerance for maximum unconservative error in beam-column design methodologies (ASCE, 1997).

6.2.1 Slenderness Limit to Neglect Second-Order Effects

To examine the slenderness limit to neglect second-order effects, analyses were performed to quantify the unconservative error associated with a design method in which second-order effects are neglected. The analyses were performed as described in Chapter 5, but with second-order effects neglected by setting $\delta_s = 1$ in Eq. (5.5) and $\delta_b = 1$ in Eq. (5.8). Analyses were performed for each column in the parametric suite described in Section 5.1.1 plus additional nonsway cases, with length-to-diameter ratios of 2, 6, 7, 8, 11, 12, 14, and 17. The additional cases had the same cross sections and boundary conditions as the main parametric suite.

The results for sway columns are presented in Figure 6.18. Each point in this figure represents the minimum (i.e., most unconservative) error, computed using Eq. (5.16), over the entire interaction diagram. The current limiting value of $KL/r = 22$ is shown as a vertical dashed line. As expected, the maximum unconservative error increases with slenderness. Unconservative errors greater than 5% (i.e., $\varepsilon < -0.05$) are not observed until a slenderness of 30, indicating that the current limit of 22 is appropriate or could potentially be increased.

The results for nonsway columns are presented in Figure 6.19. Again, each point in this figure represents the minimum (i.e., most unconservative) error over the entire interaction diagram. Different markers are used for different values of β since $\beta = M_1/M_2$ and the the limiting slenderness ratio depends on this parameter. The current limiting values of KL/r for $\beta = 1.0, 0.5, 0.0$, and -0.5 are shown as vertical dashed lines. The maximum unconservative error increases with slenderness but also with β. For $\beta = 1.0$, the current limit of $KL/r < 22$ appears appropriate since the maximum unconservative error starts significantly exceeding 5% for KL/r greater than 22. The other limits appear to be conservative. For example, for $\beta = 0.5$, maximum unconservative error does not exceed 5% until KL/r is greater than 45, significantly higher than the current limiting value of 28.
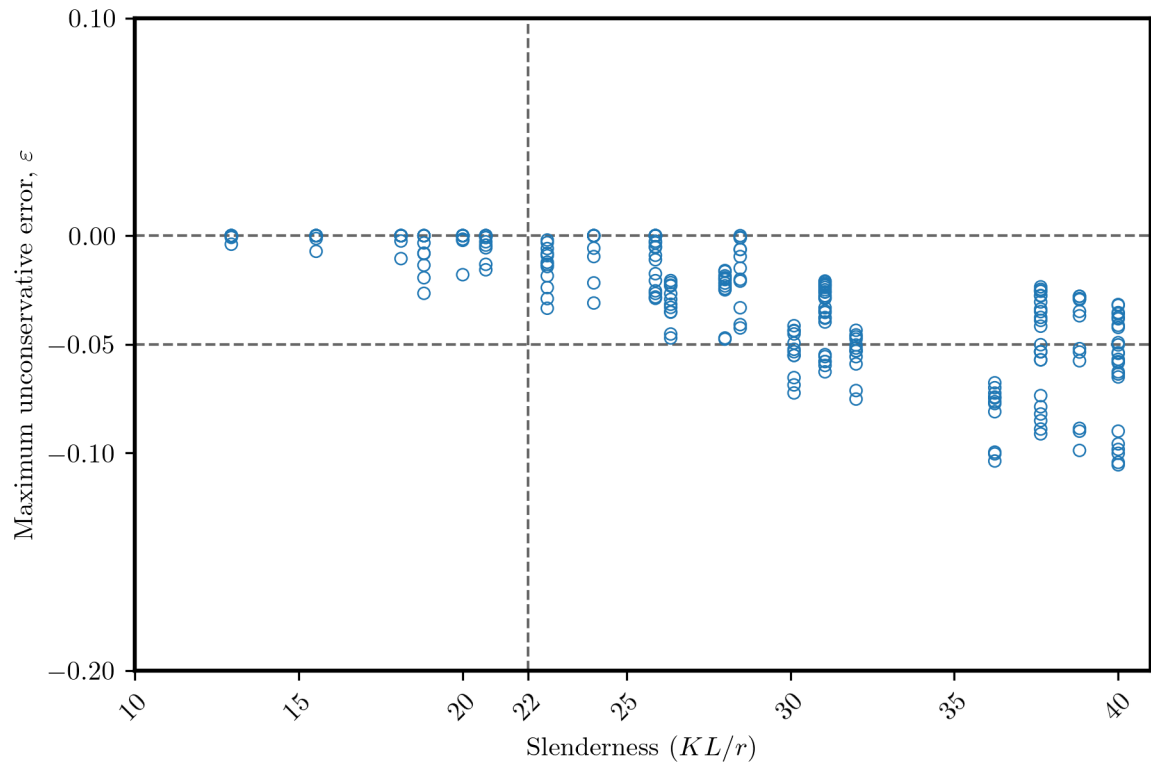
Figure 6.18: Maximum unconservative error when neglecting second-order effects for sway columns
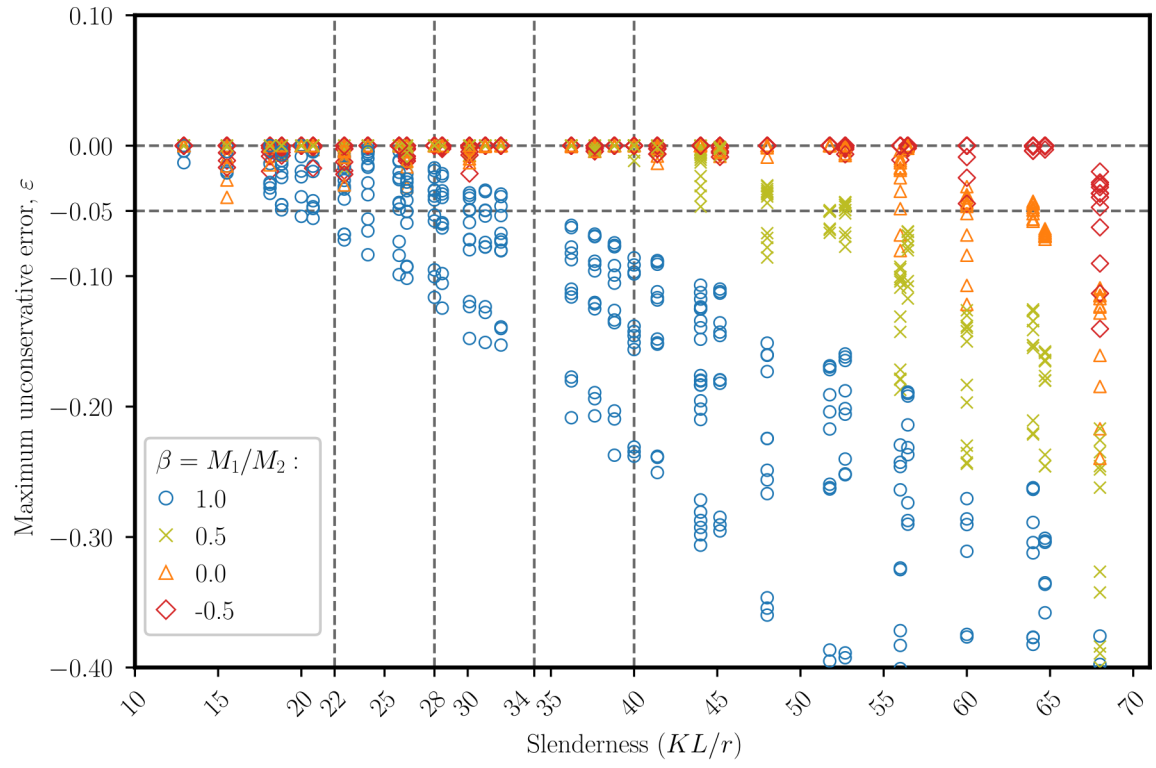
Figure 6.19: Maximum unconservative error when neglecting second-order effects for nonsway columns

6.2.2 Slenderness Limit for the Moment Magnification Approach

The AASHTO LRFD restricts the use of the approximate moment magnification approach to columns with a slenderness ratio (KL/r) less than 100. However, the rationale behind this limitation is not explicitly addressed in the available commentary.

In a design example published by the Federal Highway Administration (Adams et al., 2019), matrix finite elements and the variable EI equation from ACI 318 (Eq. 2.3) are used for a column with $KL/r > 100$. Results using the moment magnification approach and the AASHTO equations for calculating EI (larger value calculated from Eq. 2.1 and Eq. 2.2) are also presented in the example. The results showed that the moment magnification approach and the matrix finite element solution gave nearly identical results for the example structure for a given values of EI. This suggests that the moment magnification approach is an effective method of second-order elastic analysis, even when the slenderness exceeds the AASHTO limitation. This finding challenges the conventional notion that matrix structural analysis is essential for columns with higher slenderness.

The results of Chapter 5 work showed that error in the design of RC columns increases with increasing slenderness. While unconservative error was noted across most of the slenderness range investigated, the value of these errors are greater for more slender columns as shown in Figures 5.12 through 5.15. Greater conservative errors are also observed for more slender columns. In another study, Mirza and MacGregor (1989) found that the slenderness of RC columns impacts their flexural rigidity. They attributed this discrepancy to the relative concentration of cracking in more slender columns, compared to short columns where cracking is distributed more uniformly along the length of the column. Therefore, to accurately predict the flexural rigidity of a column, it is reasonable to consider the slenderness of the column as a major factor.

Tables 5.4 through 5.7 show the maximum unconservative errors associated with the use of Eq. (2.1) and Eq. (2.2). Within the current slenderness limit of $KL/r \leq 100$ the errors exceed the 5% tolerance noted by ASCE (1997). In fact, even with a 10% tolerance for unconservative error, a slenderness limit of 50 would be required to control errors for nonsway cases when using Eq. (2.1) and Eq. (2.2). The current slenderness limit of 100 controls errors for sway cases.

Slenderness remains an important factor even when variable EI equations are used. Error results when using the ACI variable EI equation (2.3) are presented in Tables 6.1 and 6.2. Based on these results, the slenderness limits would need to be 50 and 75 for nonsway and sway columns, respectively, to maintain maximum unconservative error below 10%.

The same slenderness limits may be used while using the equations suggested by Jenkins and Frosch (2015) (Tables 6.3 and 6.4) to confine the non-conservative error below 10%, as indicated by the error values in Tables 6.5 through 6.8, with the exception of an extended sway limit of 125 for the equations presented in Table 6.3.

The proposed equations for EI demonstrate a notable improvement in limiting unconservative error at high slenderness ratio compared to existing equations. When utilizing proposed equation set 1 alongside AASHTO equation 6.6.4.4.4a (Eq. 2.1), no unconservative error surpassing 10% is observed for slenderness (KL/r) less than 125 and 175 for nonsway and sway cases, respectively. This is depicted in Figures 6.20 and 6.21. Similarly, limits of 160 and 250 can be considered when using AASHTO equation 6.6.4.4.4b (Eq. 2.2) to ensure that the unconservative error remains safely below 10% (Figures 6.22 and 6.23).

Table 6.16: Slenderness limit (KL/r) necessary to maintain maximum unconservative error below target maximum percentage.

	Limit for 5%		Limit for 10%	
EI	Nonsway	Sway	Nonsway	Sway
Eq. (2.1)	30	75	50	100
Eq. (2.2)	30	100	50	125
Eq. (2.3)	30	60	50	60
Eqs. in Table 6.3	30	60	50	125
Eqs. in Table 6.4	30	70	50	100
Eq. set 1 (with Eq. 2.1)	100	150	125	175
Eq. set 1 (with Eq. 2.2)	150	225	160	250
Eq. set 2	160	150	160	384

For the second proposed set, the nonsway results consistently exhibit safety, with unconservative errors never exceeding 5% (Figure 6.24). However, some sway cases surpass the 5% unconservative error threshold and one case exceeds 10% error with a maximum error of 10.3% (Figure 6.25). However, unlike with the current AASHTO equations, these errors do not continue to increase with slenderness. Based on these results, it appears that the inclusion of slenderness in the calculation of EI effectively controls the unconservative errors within the extended slenderness range examined in this research (KL/r up to 384).

Table 6.16 provides a summary of slenderness limits for the various equations, categorized according to sway condition and error tolerance.

Given that the current AASHTO equations result in error significantly greater than 10% within their range of applicability, use of limits based on a maximum unconservative error of 10% instead of the commonly referenced error tolerance of 5% may be appropriate. However, it is important to note that not all of the slenderness values examined in this research were explored under all boundary conditions. Therefore, for practical applications, the recommended slenderness limit is 125 for Eq. set 1 with Eq. 2.1 for nonsway conditions and 160 for other applications of the proposed equations. The upper limit of 160 is recommended since this range is evaluated across all boundary conditions considered in this study. Further assessment of the equation under expanded scenarios could potentially result in an extended range of slenderness.

Above the slenderness limit, refined analysis should be used. Such analyses should be refined in their determination of EI or through the use of inelastic analysis where the effects of concrete cracking, concrete crushing, and steel yielding are modeled explicitly.

Figure 6.20: Error values obtained for nonsway cases based on EI values obtained from equation set 1 with AASHTO equation 6.6.4.4.4a (Eq. 2.1).

Figure 6.21: Error values obtained for sway cases based on EI values obtained from equation set 1 with AASHTO equation 6.6.4.4.4a (Eq. 2.1).

119

Figure 6.22: Error values obtained for nonsway cases based on EI values obtained from equation set 1 with AASHTO equation 6.6.4.4.4b (Eq. 2.2).
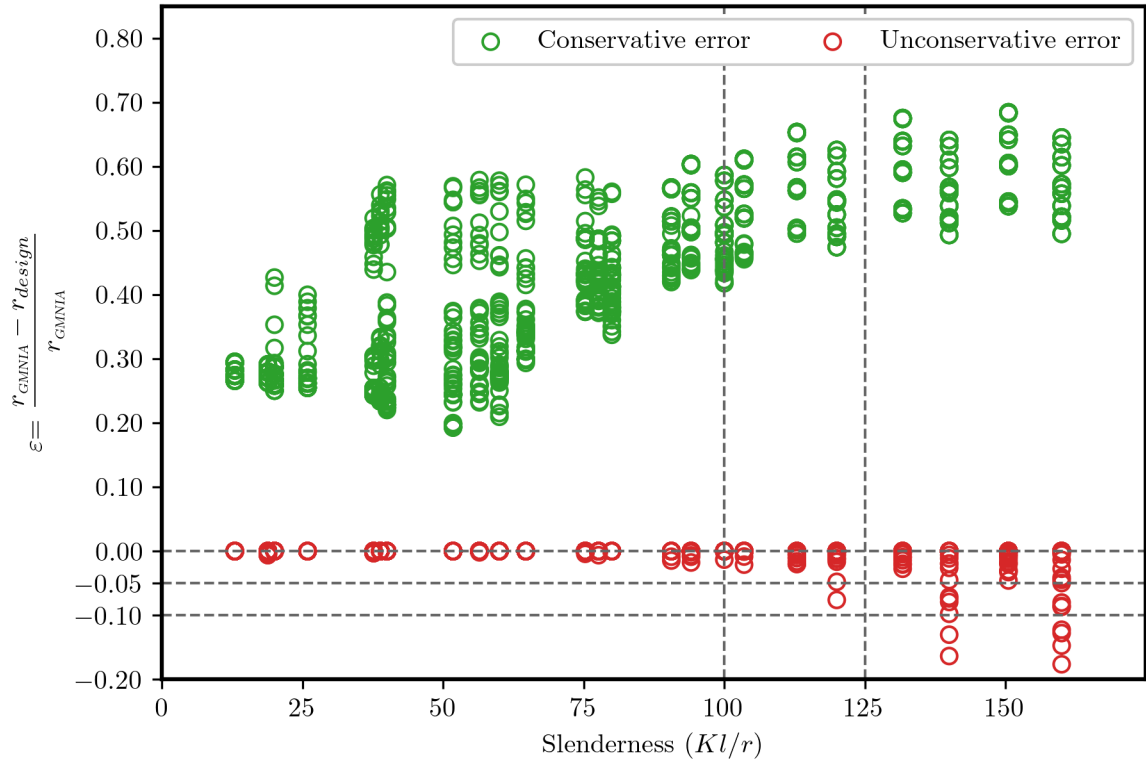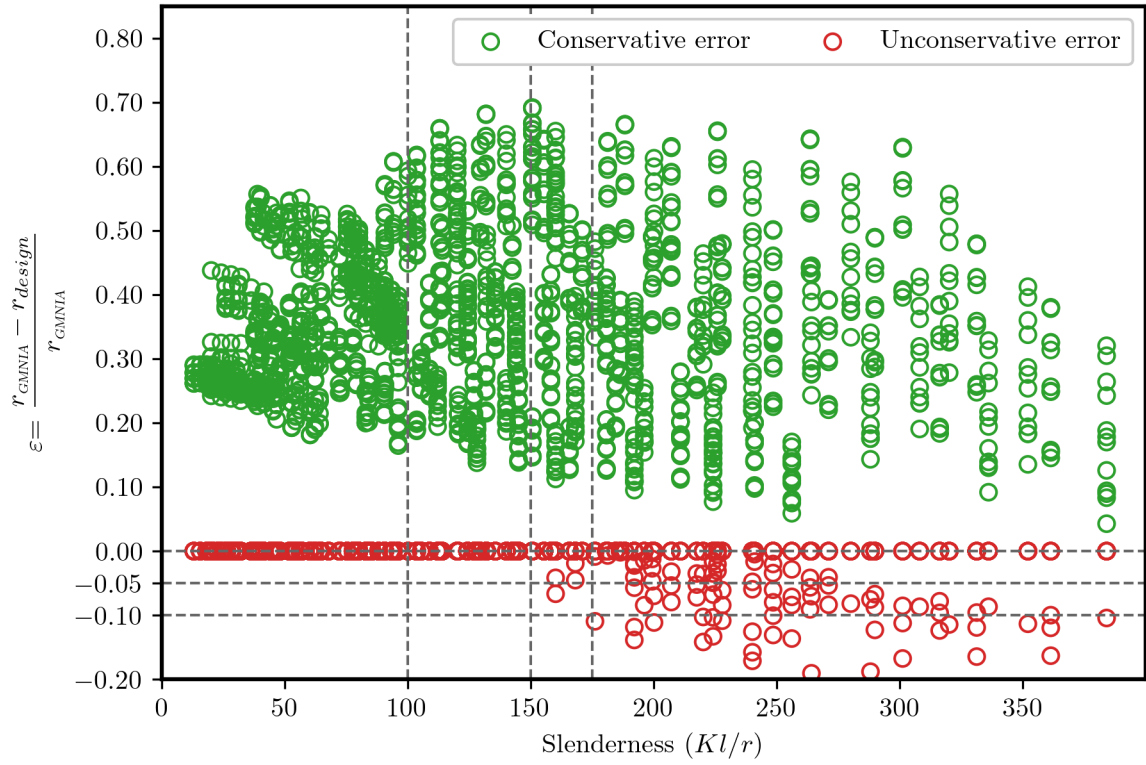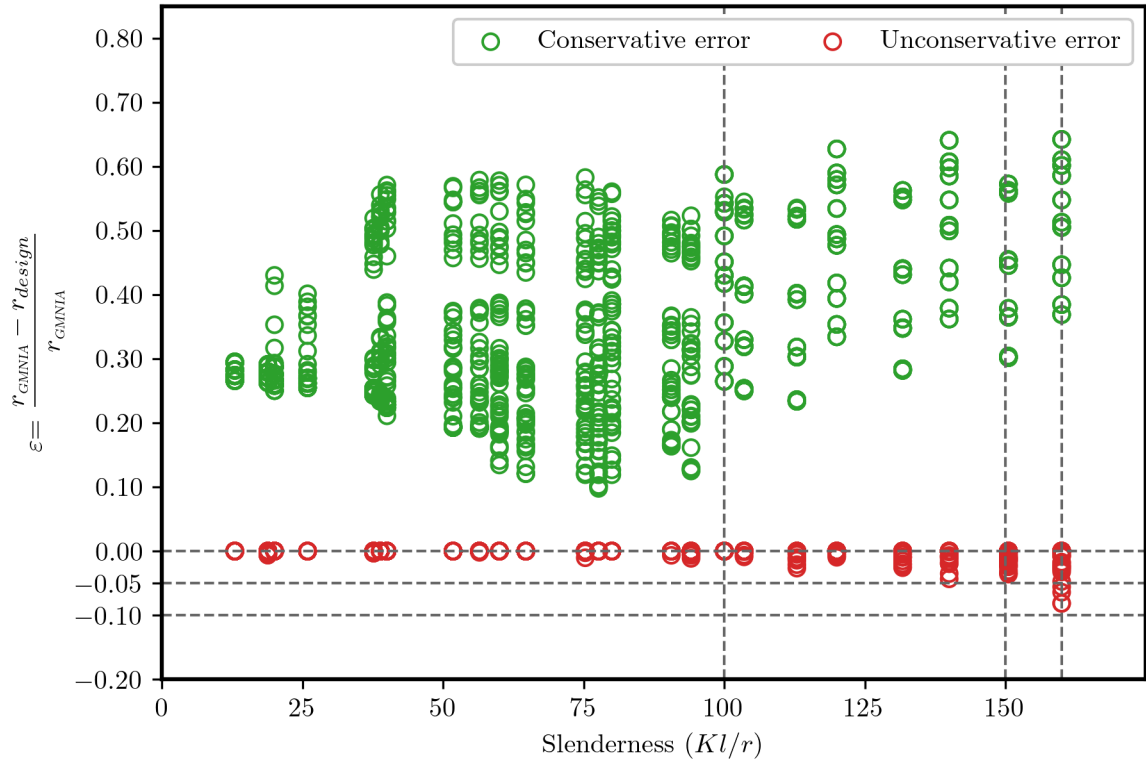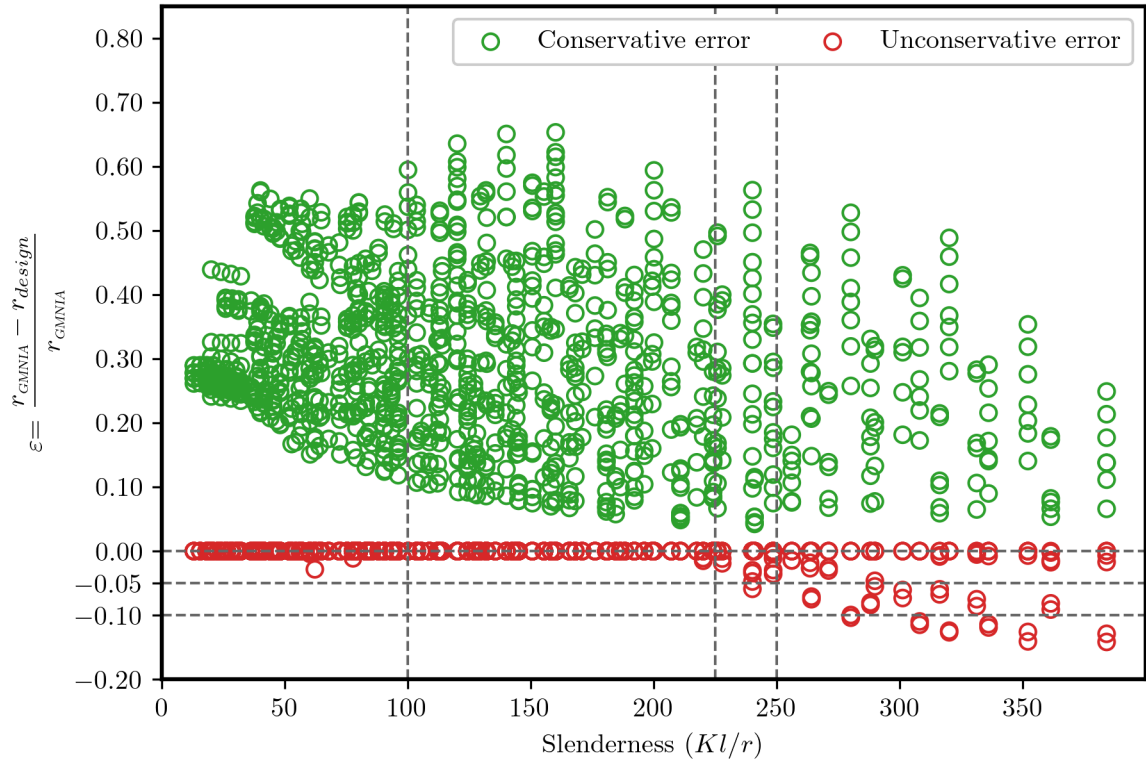
Figure 6.23: Error values obtained for sway cases based on EI values obtained from equation set 1 with AASHTO equation 6.6.4.4.4b (Eq. 2.2).
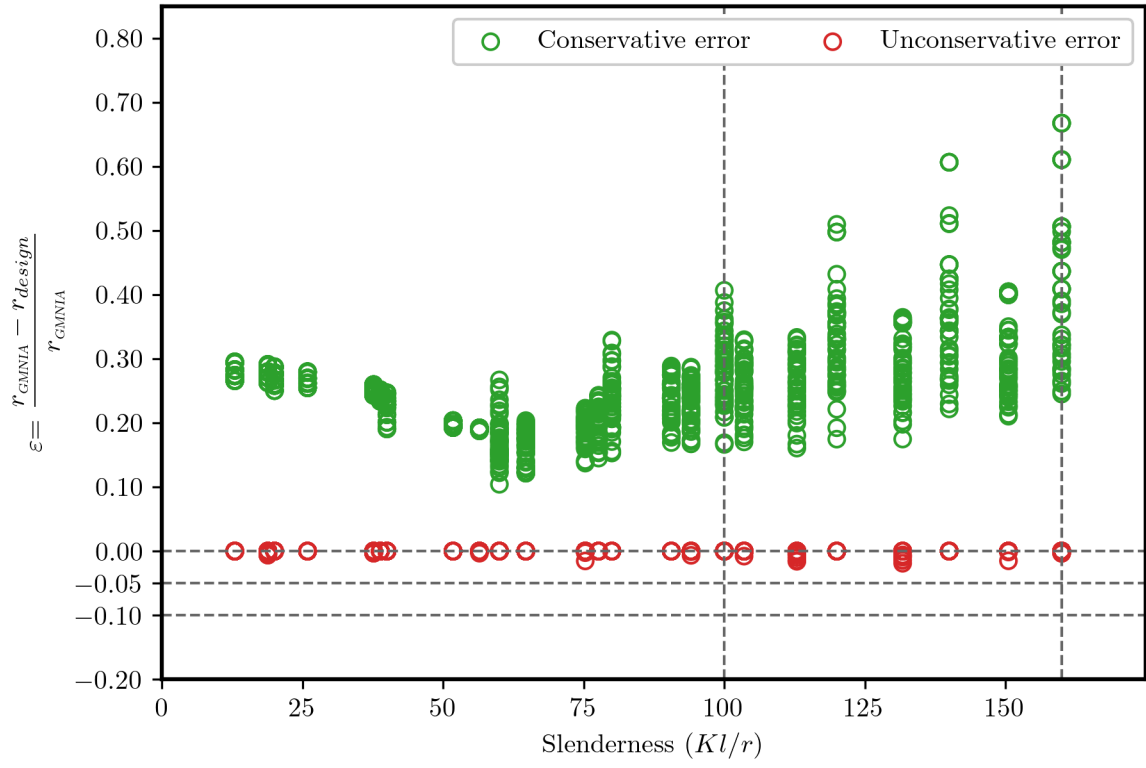
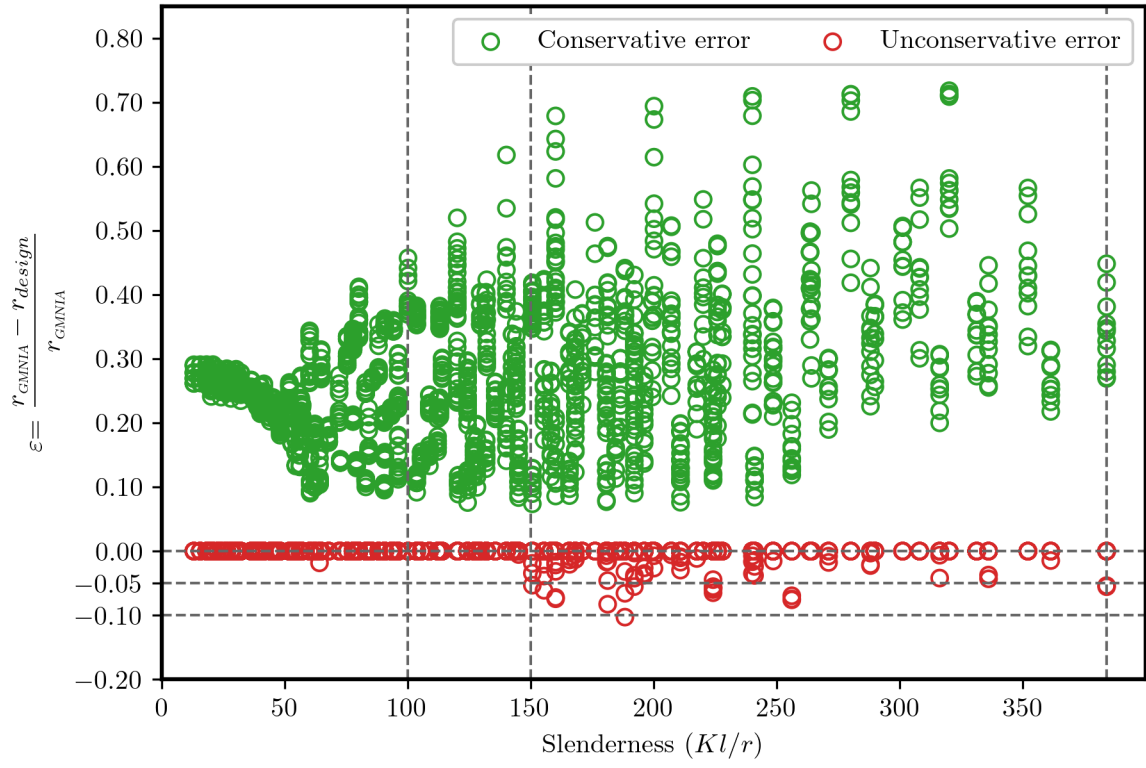Figure 6.24: Error values obtained for nonsway cases based on EI values obtained from equation set 2.

Figure 6.25: Error values obtained for sway cases based on EI values obtained from equation set 2.

6.3 Effective Length Factor

The equation for Euler buckling load in AASHTO LRFD, i.e., Eq. (5.10), includes an effective length factor, K, that reflects the amount of flexural restraint at the column ends. A more restrained column has a higher buckling load and smaller effective length factor while a less restrained column has a lower buckling load and a larger effective length factor.

For multi-column bents where the bases of the columns are designed as pinned and the tops of the columns are fixed to a bent cap or the superstructure, current Caltrans practice is to assume an effective length factor of $K = 2.0$ for both the longitudinal and transverse buckling modes, based on case "(f)" from AASHTO LRFD Table C4.6.2.5-1 (Figure 6.26). This assumption relies on the bending stiffness of the bent cap and superstructure to restrict rotations, but not sway, at the top of the column. Large sways will be restricted by the abutments; however, since the abutments are designed to provide no lateral restraint for small sways, any potential restraint is neglected for stability design.

	(a)	(b)	(c)	(d)	(e)	(f)
Buckled shape of column is shown by dashed line						
Theoretical K value	0.5	0.7	1.0	1.0	2.0	2.0
Design value of K when ideal conditions are approximated	0.65	0.80	1.0	1.2	2.1	2.0
End condition code	Rotation fixed Translation fixed					
	Rotation free Translation fixed					
	Rotation fixed Translation free					
	Rotation free Translation free					

Figure 6.26: AASTHTO Table of Effective Length Factors, K (AASHTO LRFD Table C4.6.2.5-1)

For single column bents where the base of the column is designed as fixed and the top of the column is fixed to the superstructure, current Caltrans practice is to assume effective length factors based on case "(d)" for the longitudinal buckling mode and case "(e)" for the transverse buckling mode. These assumptions rely on the bending stiffness of the superstructure to restrict rotations in the longitudinal buckling mode, but rotational restraint provided by the torsional stiffness of the superstructure is neglected.

While the abutment does not restrict sway of the superstructure or rotation of the super-structure about vertical or transverse axes, it does restrict twist of the superstructure about the superstructure's longitudinal axis. Out-of-plane rotation of the column is thus restrained by the torsional stiffness of the superstructure.

An effective length factor that accounts for the rotational restraint provided by the torsional stiffness of the superstructure can be obtained through eigenvalue buckling analysis of a three-dimensional model of the bridge. However, this type of analysis is typically not practical for design. This section describes the development of practical design tools for determining an effective length factor for out-of-plane buckling of single column bents considering the torsional stiffness of the superstructure.

6.3.1 Governing Differential Equation

The governing differential equation for planar flexure of a column including second-order effects, i.e., P-Δ and P-δ effects, is

$$v(x)'''' + k^2 v(x)'' = 0 \tag{6.2}$$

where $v(x)$ is the lateral deflection of the column at location x, $'$ indicates derivative with respect to x, and $k = \sqrt{P/EI}$, where P is the axial compression force and EI is the flexural stiffness of the column.

The general solution of this differential equation is

$$v(x) = A + Bx + C\sin kx + D\cos kx \tag{6.3}$$

where A, B, C, and D are constants to be solved for specific boundary conditions.

6.3.2 Two-Span Bridge

Consider the case of a two-span bridge with one column of length L_{col} that is fixed at the base as shown in Figure 6.27. Because of the fixity, there will be no deflection or rotation at the base, resulting in the first two boundary conditions.

$$v(0) = 0 \tag{6.4}$$

$$v'(0) = 0 \tag{6.5}$$

The abutment does not restrain sway, so translation at the top of the column is free, resulting in the third boundary condition.

$$v'''(L_{col}) + k^2 v'(L_{col}) = 0 \tag{6.6}$$

Rotation at the top of column is restrained by the torsional stiffness of the superstructure, neither perfectly free nor perfectly fixed. Assuming linear elastic behavior of the superstructure, the moment at the top of the column is proportional to rotation at the top of the column. The proportionality constant is based on the torsional stiffness of the superstructure, resulting in the fourth boundary condition.

$$-EIv''(L_{col}) = 2(GJ/L)_{super}v'(L_{col}) \tag{6.7}$$

where $(GJ/L)_{super}$ is the torsional stiffness of the superstructure and the factor of two accounts for both spans restraining the rotation of the column.
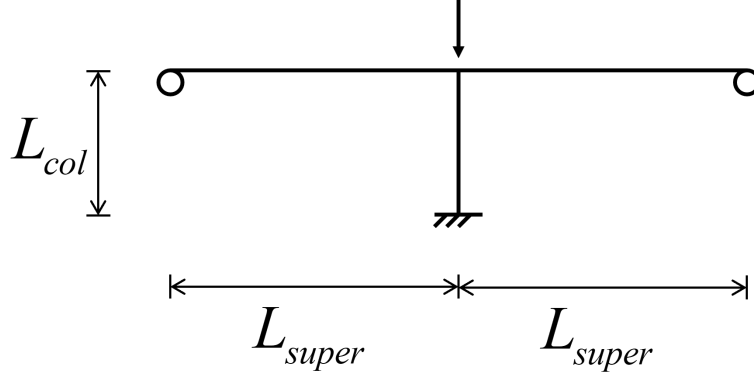
Figure 6.27: Schematic elevation view of two-span bridge

Defining a non-dimensional parameter g for the relative stiffness of the superstructure as

$$g = \frac{(GJ/L)_{super}}{(EI/L)_{col}} \tag{6.8}$$

results in a simplified version of the fourth boundary condition.

$$v''(L_{col}) + \frac{2g}{L_{col}} v'(L_{col}) = 0 \tag{6.9}$$

By combining the four boundary conditions with the general solution of the differential equation, it can be shown that equilibrium is satisfied for arbitrarily large deflections, i.e., buckling occurs at a critical load, P_{cr}. Defining P_{cr} as

$$P_{cr} = \frac{\pi^2 EI_{col}}{(KL_{col})^2} \tag{6.10}$$

allows quantification of the effective length factor, K.

Using the definition in Eq. (6.10) and the solution of the governing differential equation, a relationship between the stiffness parameter, g, and the effective length factor, K, can be determined as

$$g = \frac{-(\pi/K)}{2\tan(\pi/K)} \tag{6.11}$$

A plot of this relationship is shown in Figure 6.28. As expected, $K = 2$ when the normalized superstructure torsional stiffness equals zero and K approaches 1 as the superstructure torsional stiffness approaches infinity. The relationship was verified against results of eigenvalue buckling analyses performed using MASTAN2.

An analysis to assess the bounds of g for Caltrans bridges indicated that values less than 1 are possible, as are values greater than 20. Accordingly, use of a single prescribed value less than 2 for the effective length factor is not advisable. Nonetheless, the stiffness parameter, g, can be computed and the effective length factor, K, can be determined from g with relative ease. However, Eq. (6.11) only applies to two-span bridges.

Figure 6.28: Relationship between normalized superstructure torsional stiffness and effective length factor for a two-span bridge

6.3.3 Three-Span Bridge

For a three-span bridge with two columns of length L_{col}, each fixed at the base as shown in Figure 6.29, the boundary conditions and thus buckling loads and effective length factors will be different than for the two-span bridge. With two columns, two differential equations need to be solved simultaneously.

$$v_1(x)'''' + k^2 v_1(x)'' = 0 \tag{6.12}$$

$$v_2(x)'''' + k^2 v_2(x)'' = 0 \tag{6.13}$$

where $v_1(x)$ is the lateral deflection of a first column and $v_2(x)$ is the lateral deflection of a second column. The parameter k is used for both columns because it is assumed the columns have the same axial compression force and flexural stiffness.

Again, the columns are assumed to have a fixed base

$$v_1(0) = v_2(0) = 0 \tag{6.14}$$

$$v_1'(0) = v_2'(0) = 0 \tag{6.15}$$

and the columns are assumed to be free to translate at the top.

$$v_1'''(L_{col}) + k^2 v_1'(L_{col}) = v_2'''(L_{col}) + k^2 v_2'(L_{col}) = 0 \tag{6.16}$$
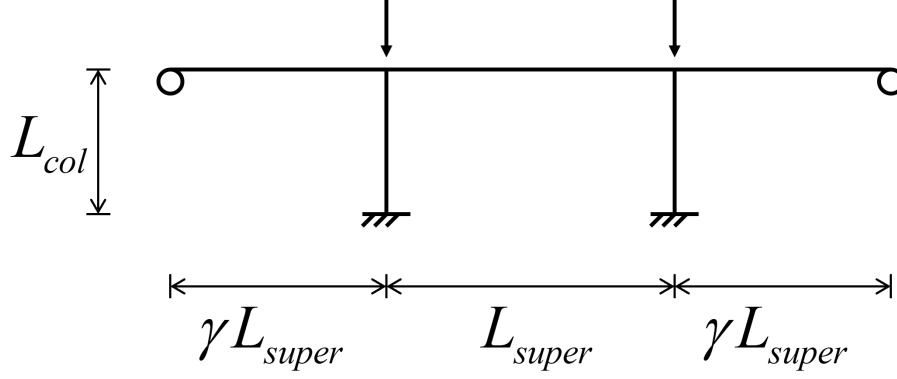
Figure 6.29: Schematic elevation view of three-span bridge

Out-of-plane rotation at the top of the columns is restrained by the torsional stiffness as before. The moment at the top of each column is proportional to the rotation at the top of the column relative to either the abutment (i.e., zero rotation) or to the rotation at the top of the adjacent column, resulting in the following two boundary conditions.

$$v_1''(L_{col}) + \frac{g}{\gamma L_{col}} v_1'(L_{col}) + \frac{g}{L_{col}}[v_1'(L_{col}) - v_2'(L_{col})] = 0 \tag{6.17}$$

$$v_2''(L_{col}) + \frac{g}{\gamma L_{col}} v_2'(L_{col}) + \frac{g}{L_{col}}[v_2'(L_{col}) - v_1'(L_{col})] = 0 \tag{6.18}$$

Note that the end spans of the bridge are assumed to have a different length than the center span (γL_{super} vs L_{super}).

Solving the differential equation leads to two modes of buckling, where the mode with the lower critical load, and thus higher effective length factor, is the controlling mode. The controlling mode is expressed as a function of the stiffness parameter, g, and the effective length factor, K, as follows

$$g = \frac{-\gamma(\pi/K)}{\tan \pi/K} \tag{6.19}$$

The relationship for both buckling modes is presented in Figure 6.30. Again, the relationship was verified against results of eigenvalue buckling analyses performed using MASTAN2.

6.3.4 Additional Spans

Repeating the process for four-span and five-span bridges results in Eq. (6.20) and Eq. (6.21), respectively.

$$g = -\frac{1}{8}\left[\frac{(2+6\gamma)(\pi/K)}{\tan(\pi/K)} + \frac{\sqrt{1-2\gamma+9\gamma^2}(\pi/K)\sin(2\pi/K)}{\sin^2(\pi/K)}\right] \tag{6.20}$$

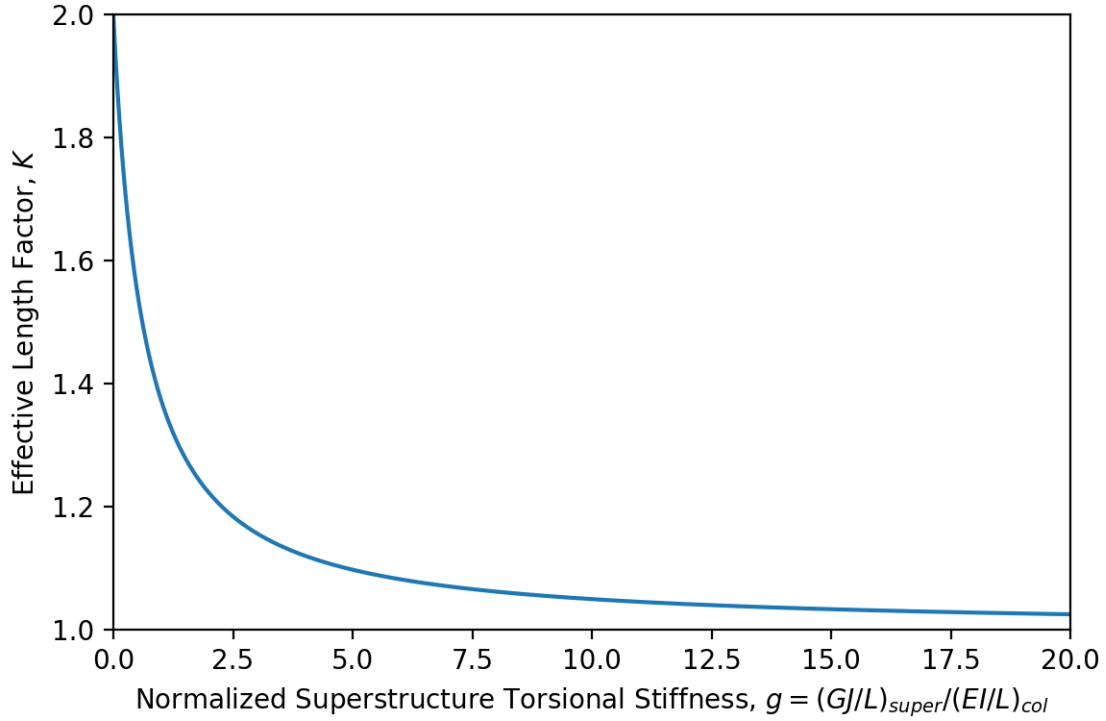$$g = -\frac{1}{2}(\pi/K)\left[\frac{1+2\gamma+\sqrt{(1+4\gamma^2)}}{\tan(\pi/K)}\right] \tag{6.21}$$

128

Figure 6.30: Relationship between normalized superstructure torsional stiffness and effective length factor for a three-span bridge ($\gamma = 0.75$)

Closed form expressions for additional spans become increasingly complex.

The relationships between the normalized superstructure torsional stiffness and effective length factor for the controlling mode for two-, three-, four-, and five-span bridges are presented in Figure 6.31. The effective length factor increases with number of spans since, as the number of spans increases, the total length of the bridge increases and the superstructure is responsible for restraining the rotation of more columns. Both of these factors lead to less restraint of the columns.

6.3.5 Base Flexibility

The evaluation in the previous sections assumes idealized boundary conditions at the base of the columns, specifically zero translation and rotation. It is common in design to recognize that full rotational fixity will not exist at base connections. For example, in AASHTO LRFD Table C4.6.2.5-1 (Figure 6.26), two sets of effective length values are provided: those that assume idealized boundary conditions, the "theoretical K values", and those that assume some amount of rotational flexibility at nominally rotation fixed ends, the "design values of K when ideal conditions are approximated". For cases with a rotation fixed end, the design values of K are higher. Case "(e)" in the table is for a cantilever column. The theoretical effective length factor is 2.0 and the design effective length factor is 2.1.

Rotational flexibility at the base can be considered in the derivation of effective length factors in
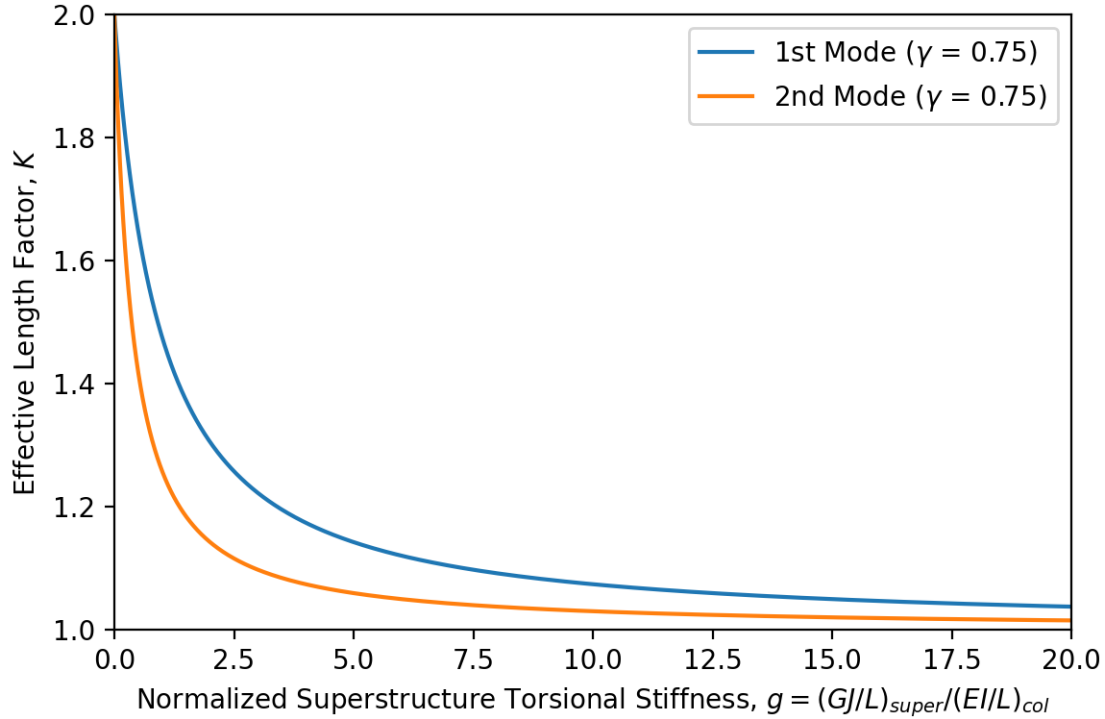
129
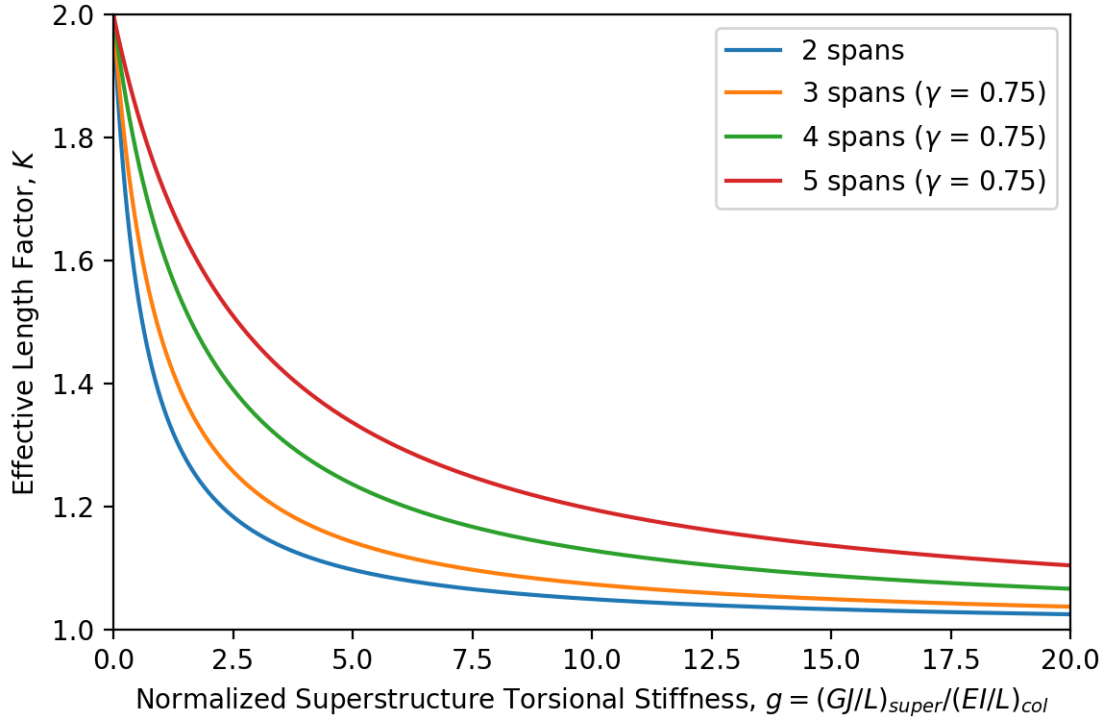
Figure 6.31: Relationship between normalized superstructure torsional stiffness and effective length factor for all spans investigated ($\gamma = 0.75$)

this work by replacing the boundary condition $v'(x) = 0$ with Eq. (6.22) which relates the moment in the column at the base to rotation at the base.

$$EIv''(0) = k_\theta v'(0) \tag{6.22}$$

where, k_θ is the rotational stiffness at the base expressed in relation to the flexural stiffness of the column as follows

$$k_\theta = \frac{EI}{G_{base}L_{col}} \tag{6.23}$$

where, G_{base} is a non-dimensional parameter relating the rotational stiffness of the base to the flexural stiffness of the column.

The parameter G_{base} is similar to the parameter G defined in AASHTO LRFD Equation C4.6.2.5-3 and used in the effective length factor alignment charts of AASHTO LRFD Figures C4.6.2.5-1 and C4.6.2.5-2. For a cantilever column, i.e., case (e) of Figure 6.26, a value of $G_{base} = 0.05$ results in the design values of the effective length factor when ideal conditional are approximated, i.e., $K = 2.1$.

With revised boundary conditions, new characteristic equations that depend on the parameter G_{base} can be developed. The revised equations are Eq. (6.24) for two-span bridges, Eq. (6.25) for three-span bridges, Eq. (6.26) for four-span bridges, and Eq. (6.27) for five-span bridges.

$$g = \frac{G_{base}(\pi/K)^2 \sin(\pi/K) - (\pi/K)\cos(\pi/K)}{2\left[G_{base}(\pi/K)\cos(\pi/K) + \sin(\pi/K)\right]} \qquad (6.24)$$

$$g = \frac{\gamma(\pi/K)\left[G_{base}(\pi/K)\sin(\pi/K) - \cos(\pi/K)\right]}{G_{base}(\pi/K)\cos(\pi/K) + \sin(\pi/K)} \qquad (6.25)$$

$$g = \frac{\left\{\begin{array}{l} -2(\pi/K)^2 G_{base}\cos(2\pi/K) - 6(\pi/K)^2 G_{base}\gamma\cos(2\pi/K) - (\pi/K)\sin(2\pi/K) \\ -3(\pi/K)\gamma\sin(2\pi/K) + (\pi/K)^3 G_{base}^2 \sin(2\pi/K) + 3(\pi/K)^3 G_{base}^2 \gamma\sin(2\pi/K) \\ +(\pi/K)\sqrt{1-2\gamma+9\gamma^2}\left[-2(\pi/K)G_{base}\cos(2\pi/K) - \sin(2\pi/K) + (\pi/K)^2 G_{base}^2 \sin(2\pi/K)\right] \end{array}\right\}}{2\left[2 + 2(\pi/K)^2 G_{base}^2 - 2\cos(2\pi/K) + 2(\pi/K)^2 G_{base}^2\cos(2\pi/K) + 4(\pi/K)G_{base}\sin(2\pi/K)\right]} \qquad (6.26)$$

$$g = (\pi/K)\left(1 + 2\gamma + \sqrt{1+4\gamma^2}\right)\frac{G_{base}(\pi/K)\sin(\pi/K) - \cos(\pi/K)}{2\left[G_{base}(\pi/K)\cos(\pi/K) + \sin(\pi/K)\right]} \qquad (6.27)$$

6.3.6   Design Tool and Recommendations

To enable easy determination of the proposed effective length factor for the transverse buckling mode of single column bents in design, a Microsoft Excel based design tool was created. The tool has tabulated data relating normalized superstructure torsional stiffness, g, to the effective length factor, K, for bridges with 2, 3, 4, and 5 spans; end span ratios, γ, of 0.5, 0.6, 0.7, 0.8. 0.9, and 1.0; and with and without base flexibility. For given normalized superstructure torsional stiffness, g, and end span ratio, γ, the tool linearly interpolates the tabulated data to compute and display the effective length factor, K, for each of the number of spans between 2 and 5 and with an idealized fixed base and with a practical fixed base. A screenshot of the tool is shown in Figure 6.32.

The tool will also calculate the normalized superstructure torsional stiffness, g, given more fundamental input values such as Poisson's ratio of concrete, superstructure span length, and column moment of inertia.

It is common to account for cracking in the determination of elastic properties of RC members. The tool allows input of separate crack factors (i.e., the ratio between cracked and uncracked section stiffness) for the column and the superstructure. In general, it is conservative to use a higher effective length factor in design. Thus, overestimates of column stiffness and underestimates of superstructure stiffness are generally conservative in this analysis. The recommended value of column crack factor of 0.7 is a reasonable upper bound of the cracked stiffness and permitted by ACI 318 for elastic analysis at the factored load level. The recommended value of crack factor is 0.5 for nonprestrssed RC box girders and 1.0 for prestressed RC box girders based on Section 4.2.5.1(a) of Caltrans Bridge Design Practice 4 (Caltrans, 2022). Note that the values for the superstructure are based on the reduction in torsional stiffness due to flexural cracking. The reduction in torsional stiffness due to torsional cracking can be much more severe (Tavio and Teng, 2004; Katsaras et al., 2009), but torsional cracking is not expected to occur because of column buckling.

For columns on pile caps or spread footings, it is recommended that the effective length of the column be determined as the length of the column down to the top of the foundation times the

Effective Length Factor for Transverse Buckling Mode of Single Column Bents

Version 1.4 (September 25, 2024)

Compute Normalized Superstructure Torsional Stiffness

Concrete Modulus of Elasticity, E_c	3605.00	psi
Concrete Poisson Ratio, v	0.20	---
Concrete Shear Modulus, G_c	1,502.08	psi
Superstructure Torsional Constant, J	530.00	ft^4
Superstructure Span Length	200.00	ft
Superstructure Crack Factor	0.50	---
Column Moment of Inertia, I	12.50	ft^4
Column Height	40.00	ft
Column Crack Factor	0.70	---

Override Normalized Superstructure Torsional Stiffness

(leave blank to use computed torsional stiffness)		---

Effective Length Factor Calculation

Normalized Superstructure Torsional Stiffness	2.524	---
End Span Ratio	0.50	---

Number of Spans	Effective Length Factor, K	
	Idealized Fixed Base	Practical Fixed Base
2	1.18	1.23
3	1.18	1.23
4	1.32	1.37
5	1.45	1.51

Notes

1. Effective length factors are linearly interpolated from tabulated solutions to the governing differential equation.
2. Idealized fixed base assumes infinite rotational stiffness at the base.
3. Practical fixed base assumes rotational stiffness at the base equal to the value that results in $K = 2.1$ when the normalized superstructure torsional stiffness is zero.
4. For columns on pile caps or spread footings, it is recommended that the effective length of the column be taken as the length of the column down to the top of the foundation times the effective length factor, K, for a practical fixed base. For columns on shafts, it is recommended that the effective length of the column be taken as the length of the column down to the equivalent point of fixity times the effective length factor, K, for an idealized fixed base. See image below.
5. The equations are based on equal interior span lengths and equal end span lengths. For bridges with three or more spans, the span length should be the arithmetic mean of the interior span lengths and the end span ratio should be the arithmetic mean of the end span lengths divided by the span length. For bridges with two spans, the span length should be the arithmetic mean of the two span lengths. Variations in individual spans from the arithmetic mean of up to 20% will cause minimal error. See image below for example.
6. See Section 6.3 of [[REFERENCE TO PROJECT REPORT]] for background information.
7. The password to unlock the spreadsheet is "Caltrans".

Figure 6.32: Screenshot of the interface for the Microsoft Excel based tool for determining the effective length factor for the transverse buckling mode of single column bents

effective length factor for a practical fixed base. For columns on shafts, it is recommended that the effective length of the column be determined as the length of the column down to the equivalent point of fixity times the effective length factor for a idealized fixed base. These recommendations are illustrated in Figure 6.33.
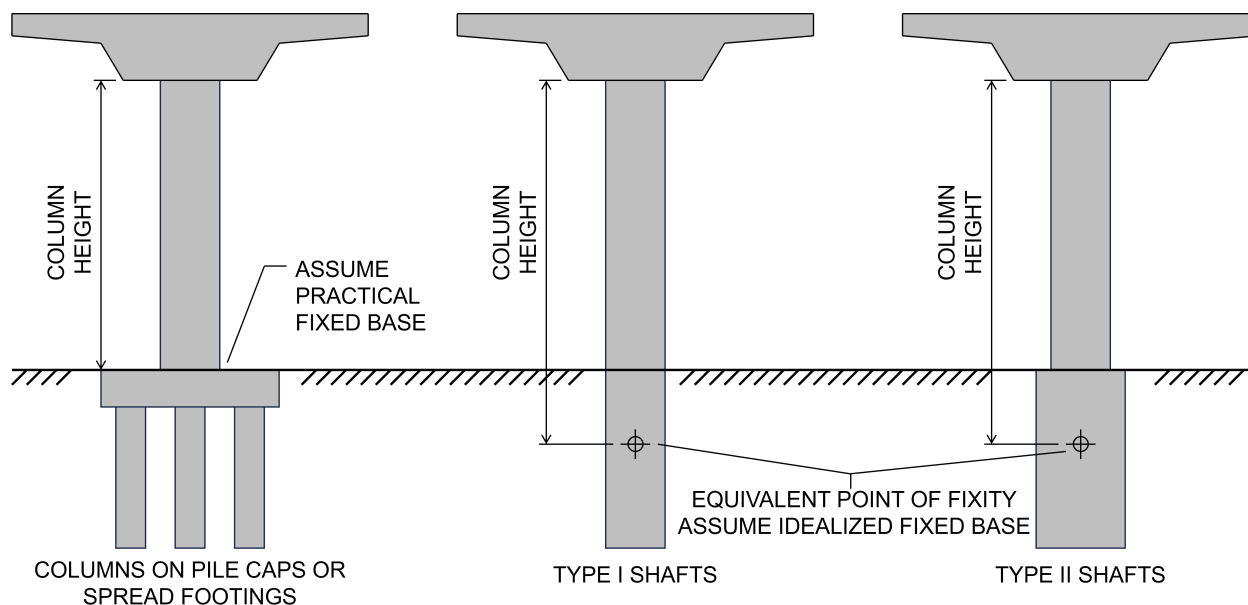
Figure 6.33: Schematic of different bridge column base conditions and recommendations for column height and base fixity

While the end span ratio, γ, accounts for differences between the end span and the interior spans for bridges with three spans or more, differences in span lengths assumed equal in this derivation can still exist. Minor differences in span lengths can be accommodated by using the average length in the equations. Specifically, for bridges with three or more spans, the span length should be the arithmetic mean of the interior spans and the end span ratio should be the arithmetic mean of the end spans divided by the span length. For bridges with two spans, the span length should be the arithmetic mean of the two span lengths (note, however, that using the harmonic mean of the span lengths is more accurate). When defined this way, variation in individual spans from the arithmetic mean of up to 20% will cause minimal error as shown in Table 6.17.

Table 6.17 shows a comparison between the proposed effective length factor and effective length factors computed from eigenvalue buckling analysis in MASTAN2 for for various configurations with 20% variation in span length. For these analyses, the column had a height of 40 ft, cross-sectional area of 1,800 in^2, moment of inertia about both axes of 260,000 in^4, and torsional constant of 520,000 in^4. The superstructure had a cross-sectional area of 9,000 in^2, moment of inertia about the horizontal axis of 4,000,000 in^4, moment of inertia about the vertical axis of 180,000,000 in^4, and torsional constant of 2,000,000 in^4. The concrete for both the column and the superstructure has a modulus of elasticity of 3,605 ksi and shear modulus of 1,502 ksi. The difference between the proposed effective length factor and the effective length factor compute from the eigenvalue buckling analysis is less than 3% for all the cases examined.

133

For variations greater than 20%, the longer span length should be used or the effective length factor should be determined from eigenvalue buckling analysis.

Table 6.17: Comparison between proposed effective length factor and effective length factor computed from eigenvalue buckling analysis in MASTAN2 for bridges with unequal span lengths

| Span Length (ft) | | | | MASTAN2 | | Proposed | | Percent |
Span 1	Span 2	Span 3	Span 4	P_{cr} (kips)	K	g	K	Difference
100	100	—	—	23,345	1.31	1.282	1.31	-0.1%
80	120	—	—	23,683	1.30	1.282	1.31	0.6%
75	100	75	—	20,188	1.41	1.282	1.41	0.0%
60	100	90	—	20,308	1.41	1.282	1.41	0.3%
75	100	100	75	17,071	1.53	1.282	1.56	1.7%
60	100	100	90	17,105	1.53	1.282	1.56	1.8%
60	80	120	90	17,224	1.53	1.282	1.56	2.2%
60	120	80	90	16,958	1.54	1.282	1.56	1.4%

6.4 Tools for Preliminary Design

Preliminary design of bridges helps engineers understand the general parameters of a bridge early in the design process. Current practice for preliminary design of bridge columns is focused on rules of thumb based on axial load. Preliminary designs could be improved by considering bending moment if appropriate simplified analysis methods are available.

This section describes the development of two tools. The first is a rule of thumb to approximate the moment strength of an RC cross section. The second is a rule of thumb to approximate the moment magnification factor.

6.4.1 Moment Strength

The moment strength at zero axial load, M_n, was determined for each of the 36 cross sections described in Section 5.1.1 using the strain compatibility approach described in Section 5.1.2. Additionally, moment strength of 216 similar cross sections but with six different pairs of steel and concrete strength was determined. The pairs of f_y and f_c' were 50 and 3, 50 and 4, 60 and 3, 60 and 5, 70 and 4, and 70 and 5, all in units of ksi, making the total number of cross sections 252. Then, using `PySR`, an open-source software for symbolic regression (Cranmer, 2023), a new equation was developed to approximate the moment strength. The regression software was provided with calculated moment strength, steel ratio, nominal axial strength of cross section, depth to reinforcing, concrete strength, and steel strength, and output different equations to approximate the moment strength with varying accuracy and complexity. Eq. (6.28) was selected from the output equations for its balance of simplicity and accuracy.

$$M_n \approx \left(\frac{A_{st}}{A_g} \right)^{0.6} P_0 d \tag{6.28}$$

where

M_n = approximate moment strength of cross section

A_{st} = total area of longitudinal reinforcement

A_g = gross area of concrete section

P_0 = nominal axial strength of cross section, Eq. (5.3)

d = distance from the extreme compression fiber to the centroid of the extreme tensile reinforcement

To quantify the accuracy of the approximate formula, the moment strength computed from the strain compatibility method, $M_{n(SC)}$, was compared to the moment strength according to Eq. (6.28), $M_{n(eqn)}$ for the 252 cross sections in the training set. For each case, an error value was calculated using Eq. (6.29).

$$\varepsilon = \frac{M_{n(SC)} - M_{n(eqn)}}{M_{n(SC)}} \tag{6.29}$$

Summary statistics of the errors computed using Eq. (6.29) are listed in Table 6.18 by cross section type and bending axes. Note that positive values of error indicate that the approximate equation underpredicts the moment strength calculated from the strain compatibility method.

The proposed equation has an average error less than 1% for circular cross sections. Greater error is observed for obround cross sections. These errors are related to the shape of the cross section and the distribution of reinforcing. For example, for obround sections bending about their x-axis, the distribution of reinforcing bars is more favorable with more bars located farther from the neutral axis. Capturing these effects in the approximate equation and achieving additional accuracy would require additional terms and complexity in the equation which may not be suitable for initial design.

Although the average errors are positive for all cross section types, error for individual cases can be negative or positive, resulting in either an overprediction or underprediction of strength. The maximum and minimum errors are listed in Table 6.18. Moreover, the equation is noted to be less accurate when higher strength steel is employed with lower strength concrete, or conversely, when lower strength steel is used with higher strength concrete.

Table 6.18: Error values for the results obtained from Eq. (6.29)

Cross Section Type	Bending Axis	Average Error	Standard Deviation of Error	Minimum Error	Maximum Error
Circle	-	0.95%	9.64%	-21.70%	20.98%
Obround	x	23.36%	10.72%	-7.88%	44.99%
Obround	y	12.79%	10.53%	-16.63%	35.76%

6.4.2 Moment Magnification Factor

The moment magnification approach defined in AASHTO LRFD Section 4.5.3.2.2b is relatively simple, but can be further simplified for preliminary design. By assuming $C_m = 1$ and the ratio P_u/P_e is the same for all columns, the nonsway and sway moment magnifiers become equal and can be written as:

$$\delta = \frac{1}{1 - \dfrac{P_u}{\phi_K P_e}} \tag{6.30}$$

The term $P_u/\phi_K P_e$ can be expanded by substituting in the definition of P_e (Eq. 5.10) and an expression for EI (Eq. 2.1).

$$\frac{P_u}{\phi_K P_e} = \frac{P_u}{\phi_K \dfrac{\pi^2 EI}{(KL)^2}} = \frac{P_u}{\phi_K \dfrac{\pi^2 0.4 E_c I_g}{(1 + \beta_d)(KL)^2}} \tag{6.31}$$

Multiplying the numerator by P_{0g}/P_{0g} where $P_{0g} = 0.85 f_c' A_g$ yields

$$\frac{P_u}{\phi_K P_e} = \frac{\dfrac{P_u}{P_{0g}} 0.85 f_c' A_g}{\phi_K \dfrac{\pi^2 0.4 E_c I_g}{(1 + \beta_d)(KL)^2}} \tag{6.32}$$

Substituting in expressions for the area and moment of inertia of a circle yields

$$\frac{P_u}{\phi_K P_e} = \frac{\dfrac{P_u}{P_{0g}} 0.85 f_c' \dfrac{\pi}{4} D^2}{\phi_K \dfrac{\pi^2 0.4 E_c \dfrac{\pi}{64} D^4}{(1 + \beta_d)(KL)^2}} \tag{6.33}$$

Canceling common terms, substituting in $\phi_K = 0.75$, and simplifying yields

$$\frac{P_u}{\phi_K P_e} = 4.6 \frac{f_c'}{E_c}(1 + \beta_d)\frac{P_u}{P_{0g}}\left(\frac{KL}{D}\right)^2 \tag{6.34}$$

Substituting back into the moment magnification factor equation yields

$$\delta = \frac{1}{1 - 4.6 \dfrac{f_c'}{E_c}(1 + \beta_d)\dfrac{P_u}{P_{0g}}\left(\dfrac{KL}{D}\right)^2} \tag{6.35}$$

Eq. (6.35) is tabulated for $f_c' = 4$ ksi, $E_c = 3{,}605$ ksi based on Eq. (3.1), and $\beta_d = 0.5$ in Table 6.19. While derived for circular shapes, this approximate moment magnifier can also be

applied to obround shapes if D is taken as the cross-sectional dimension perpendicular to the axis of bending. However, the approximation is less accurate for bending about the minor axis of obround shapes.

Together with Eq. (6.28), the approximate moment magnifier can aid preliminary design of bridge columns by providing an approximate size column size or by identifying when the size of a column should be increased due to slenderness effects.

Table 6.19: Approximate moment magnifier for $f'_c = 4$ ksi and $\beta_d = 0.5$. Values greater than 3 are not shown.

$\mathbf{P_u}/\mathbf{P_{0g}}$	$\mathbf{KL}/\mathbf{D}$					
	0	**5**	**10**	**15**	**20**	**25**
0.00	1.00	1.00	1.00	1.00	1.00	1.00
0.05	1.00	1.01	1.04	1.09	1.18	1.31
0.10	1.00	1.02	1.08	1.21	1.44	1.92
0.15	1.00	1.03	1.13	1.35	1.85	—
0.20	1.00	1.04	1.18	1.53	2.58	—
0.25	1.00	1.05	1.24	1.76	—	—
0.30	1.00	1.06	1.30	2.07	—	—
0.35	1.00	1.07	1.37	2.52	—	—
0.40	1.00	1.08	1.44	—	—	—
0.45	1.00	1.09	1.53	—	—	—
0.50	1.00	1.11	1.62	—	—	—

Chapter 7

Conclusions

The importance of second-order effects has long been recognized in the design of slender RC bridge columns. While the decades old moment magnification method remains a robust approach to account for second-order effects in most cases, it is important for engineers to understand the limitations of the methods they employ and be aware of alternatives to the simplifications they use as highlighted in this work.

For stability design, the AASHTO LRFD allows, within certain slenderness limits, calculation of required strengths using moment magnification. However, this method is approximate. Use of simplified equations for the flexural rigidity of RC sections, especially the equations in the AASHTO LRFD, is a major source of error in the approximate method. Use of simplified effective length factors that do not fully account for the restraint provided by the bridge superstructure can also be a major source of error in the approximate method. Use of a refined method in design is permitted regardless of member slenderness, but refined methods based on second-order analysis requires many modeling choices that can be unclear.

A numerical investigation was undertaken to improve the accuracy of the approximate approach and develop guidance on how to address second-order effects in the design of slender RC bridge columns. An advanced second-order inelastic model for RC bridge columns was developed and validated against the results of hundreds of physical experiments. The model considers geometric nonlinearity, including P-δ and P-Δ effects; material nonlinearity, including concrete cracking and crushing and steel yielding; as well as long-term effects such as creep and shrinkage. A parametric study was performed to generate data on the strength of columns. This data was used as a benchmark against which the accuracy of design methods was quantified. The results of these comparisons show that the simplified equations for flexural rigidity in the AASHTO LRFD are generally conservative but can result in unconservative error especially for more slender members with relatively low axial load and high bending moments. Evaluation of other available equations for the flexural rigidity, including those that depend on the axial load and bending moment in the column were found to be more accurate on average but with even greater unconservative errors over a broader range than the AASHTO LRFD equations. New equations for flexural rigidity were developed to minimize unconservative error while controlling overall error.

Slenderness limits in the AASHTO LRFD were reevaluated as a means to limit unconservative

138

error. The results indicated that the proposed equations could be safely used in the moment magnification approach for members with slenderness much greater than the current limit of 100. Refined analysis, which is required to be used for members that exceed the slenderness limit, was not explicitly studied in this work. With the proposed EI equations and greater slenderness limits, it may be appropriate to simply not design columns with slenderness exceeding the slenderness limit. However, it is anticipated that refined analysis is still necessary for irregular geometries or to model the stiffness more accurately. Simply using matrix structural analysis instead of the moment magnification approach may not improve accuracy. Further investigation is required to develop robust procedures and requirements for refined analysis.

Guidance was also developed on the effective length factor. Using eigenvalue buckling analyses of three-dimensional models of basic bridge types, current Caltrans practice for selecting effective length factors was found to be appropriate for multi-column bents and single-column bents for buckling in the plane of the bridge, i.e., in the longitudinal direction. Current Caltrans practice for selecting the effective length factor for single-column bents for buckling out of the plane of the bridge, i.e., in the transverse direction, was found to be conservative as it neglected the torsional stiffness of the superstructure, which can be substantial in many cases. A new effective length factor for out-of-plane buckling of single-column bents was developed based on closed-form solutions to the governing differential equation. The effective length factor was implemented in a spreadsheet-based design tool for easy use by engineers.

Further evaluation of long-term effects and the use of analysis models to account for the restraint provided by the superstructure and foundation is recommended. Nonetheless, given the thorough evaluation of the flexural rigidity and effective length factor, the identification and quantification of errors due to simplifications, and the rigorously justified and practical recommendations to reduce error, this work will help engineers make more confident, accurate decisions when designing slender RC columns.

Several avenues for future study have been identified.

- This study focused primarily on relatively simple bridges where the restraint of the columns can readily be idealized. Research to develop detailed guidance for efficiently incorporating restraint from the foundation, superstructure, abutment, etc. in a "refined" second-order elastic analysis for the design of the columns would be beneficial. The research could identify how the various components should be modeled and what simplifications are appropriate. The research could also help identify under what conditions a refined analysis is the best approach. Ideally, the research would cover a range of bridge types (including curved), foundation types, abutment types (including integral).

- This study found that that the use of β_d in the flexural rigidity equations may overestimate the impact of long-term effects. Research to further these observations and to develop recommendations for design would be beneficial.

- This study focused on columns subject to combined axial compression and bending about one axis. Research to confirm the applicability of the recommendations when the column is subject to combined axial compression and bending about two axes would be beneficial.

- This study focused on traditional elastic analyses where the flexural stiffness is defined *a priori*. Elastic analyses can also be performed with fiber sections where the steel is defined

139

with an elastic stress-strain relationship and the concrete is defined with an elastic-no-tension stress-strain relationship. These nonlinear elastic analyses could be advantageous because they would track the level of cracking explicitly within a second-order analysis and could be performed efficiently for regular bridge types with an app powered by OpenSees. However, research is needed to develop the analysis approach and the app.

Appendix A

Second-Order Analysis Using CSiBridge

Where the foregoing research results based on OpenSees may be too cumbersome for design floor use, this appendix shows how results similar to those from OpenSees can be obtained using CSiBridge (v24).

A.1 Bridge Model

The canonical bridge model shown in Figure A.1 is used for analyses in both OpenSees and CSiBridge. The model is defined in three dimensions (3D) with three spans with 100 ft main span and 75 foot approach spans.
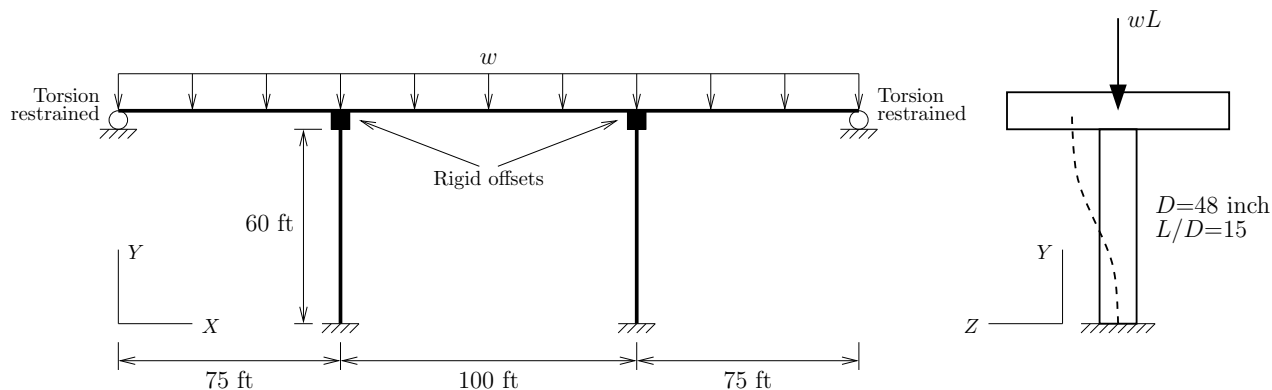

Figure A.1: Bridge model for second order analysis using OpenSees and CSiBridge.

The column section is round with diameter D=48 inch and 2% longitudinal reinforcing steel (24 #11 Grade 60 bars) with 2 inch clear cover. Concrete compressive strength is f_c'= 4 ksi.

Rigid beam offsets connect the top of the columns to the centerline of the superstructure (half of the superstructure depth). The flexible column length is 60 ft (aspect ratio L/D=15). The superstructure is elastic with the following properties:

- Elastic modulus, $E_{ss} = 4000$ ksi; Poisson ratio, $\nu = 0.3$

- Area, $A_{ss} = 63.5$ ft^2

- Second moment of area (local z, global Z) $I_{zss} = 182$ ft^4

- Second moment of area (local y, global Y) $I_{yss} = 8570$ ft^4

- Polar second moment of area, $J_{ss} = 550$ ft^4

The abutment boundary conditions are rollers with torsion restrained in the superstructure.

A.2   Bridge Loading

A series of analyses will be performed in OpenSees and CSiBridge for a reference load pattern of uniform distributed load across the bridge superstructure. In the vertical direction (along global $-Y$ axis), the reference distributed load magnitude is w. For analyses cases that include out-of-plumbness, the columns are defined with an initial offset $L/500 = 1.44$ inch in the global Z-direction.

A.2.1   Geometric and Material Nonlinear Analysis (GMNIA)

An analysis that includes both material and geometric nonlinearity is the "best guess" at true behavior. Using fiber sections for the columns with EPP steel fibers and `Concrete04` for the concrete, consistent with the models used for short-term loading in this report, an analysis with geometric nonlinearity (corotational mesh of column elements) predicts a peak load of w=78 kip/ft. The analysis includes $L/500$ out of plumbness for the columns and the load-displacement response is shown in Figure A.2.
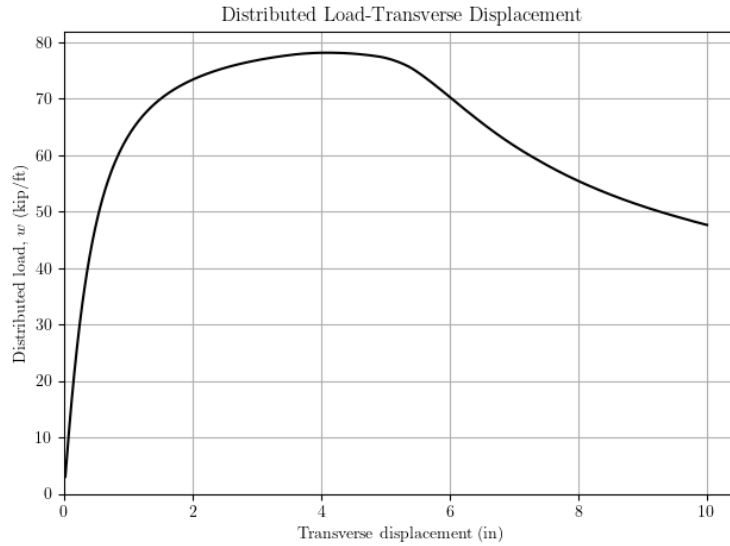

Figure A.2: Transverse load-displacement response based on GMNIA in OpenSees.

Although this analysis (GMNIA) was performed only in OpenSees, the following analyses were performed in CSiBridge.

A.2.2 Geometric Nonlinear Analysis (GNA)

Accounting for only geometric nonlinearity with elastic column response, analyses were performed in CSiBridge to determine the distributed loading, w, on the bridge that placed the column demands at the interaction curve shown in Figure A.3. For all cases, the column moment is the resultant of the moment about the local axes 2 and 3 in CSiBridge.

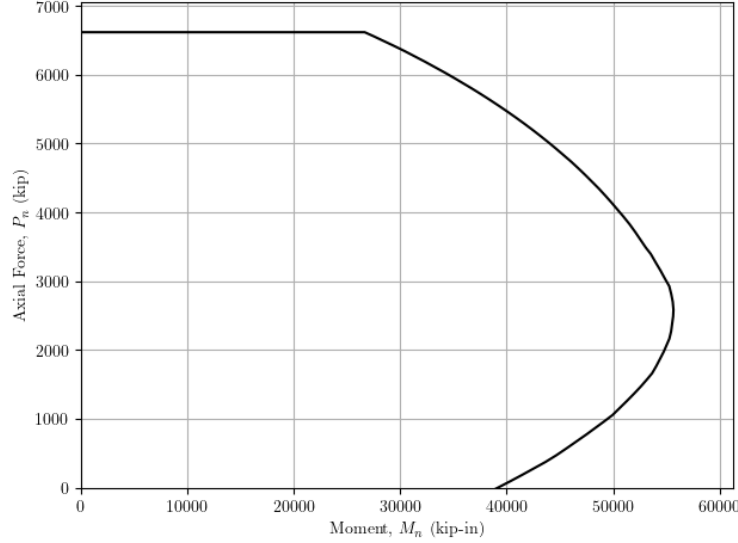The nominal P-M interaction curve for this section is shown in Figure A.3.

Figure A.3: Nominal P-M interaction curve for column section used in bridge analysis.

Four cases of GNA were performed in CSiBridge to estimate the maximum distributed load the bridge model can support:

- $EI_{eff} = 0.4E_cI_g$ with $L/500$ out-of-plumbness

- $EI_{eff} = 0.4E_cI_g$ with no out-of-plumbness

- EI_{eff} based on Eq. (6.1) with $L/500$ out-of-plumbness

- EI_{eff} based on Eq. (6.1) with no out-of-plumbness

Although EI_{eff} depends on the applied axial load according to Eq. (6.1), the value of EI_{eff} used for the two cases of GNA is based on axial load where $P/P_o \approx 1$. In this case, $EI_{eff} = 0.52E_cI_g$ for the columns in this bridge model.

The EI_{eff} values are input in CSiBridge using E_c=3605 ksi (for 4000 psi concrete), I_g based on the column diameter, and appropriate section modifiers (0.4 or 0.52) on the I values about the section 2 and 3 axes. The distributed load is applied as a reference uniform load pattern up to a peak value of w=68 kip/ft (corresponds to P_o on axial-moment interaction curve in Figure A.3). Loads are applied in 10 steps and the CSiBridge analysis uses both P-Δ and P-δ effects in the column elements.

For GNA with $EI_{eff} = 0.4E_cI_g$ and $L/500$ out-of-plumbness, the distributed load that leads to

axial-moment demands on the column interaction curve is $w{=}62$ kip/ft. For the other three GNA cases, the maximum distributed load is $w{=}67$ kip/ft. With no out-of-plumbness, the higher EI_{eff} leads to higher column demands as "stiffness attracts load"; however, when out-of-plumbness is included in the analysis, the lower EI_{eff} leads to a lower maximum distributed load because the lower flexural stiffness leads to higher deflections and thus higher second order moments.
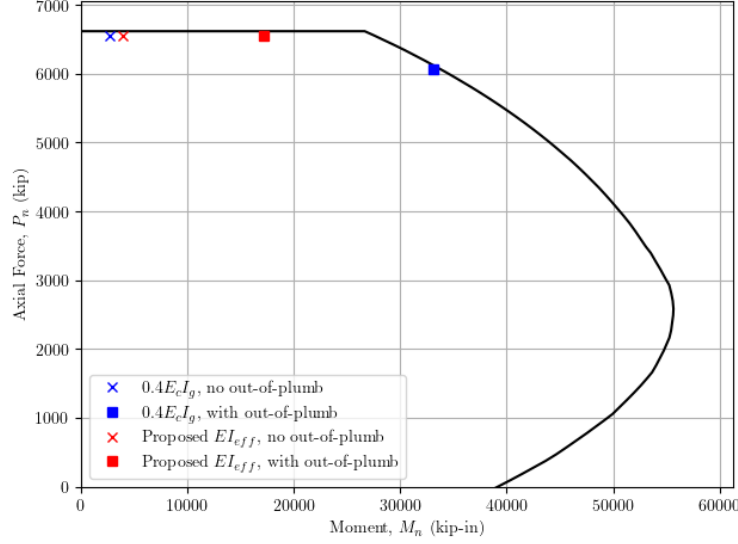

Figure A.4: Geometrically nonlinear analysis (GNA) with column effective stiffness $EI_{eff} = 0.4E_cI_g$.

A.3 Key Steps for CSiBridge Analysis

While the OpenSees analyses for the example bridge analysis closely follow the methods presented in this report, the CSiBridge analyses require different considerations, the highlights of which are summarized in this section.

For the analysis presented in this appendix, the bridge model consists of line elements as shown in Figure A.5. The base of each column is completely fixed (restrained in all six DOFs) while the ends of the superstructure are on rollers but with the torsional DOF constrained. In CSiBridge, the nodal restraint at the ends of the superstructure (nodes 2 and 8 in Figure A.5) is "u3,r1", i.e., fixed in both Z-direction translation and rotation about the X-axis.

Additional modeling details for the superstructure are omitted here and the focus is on the columns.

- Define column sections as elastic and use property/stiffness modifiers to achieve the desired effective flexural stiffness. For example, to set the effective flexural stiffness for the columns to $0.52E_cI_g$, use the inputs shown in Figure A.6. Note that the modifiers should be set for both axes of bending.

- For analysis cases that require out-of-plumbness for the columns, the Y-coordinate of the column base nodes was adjusted manually to achieve $L/500$.
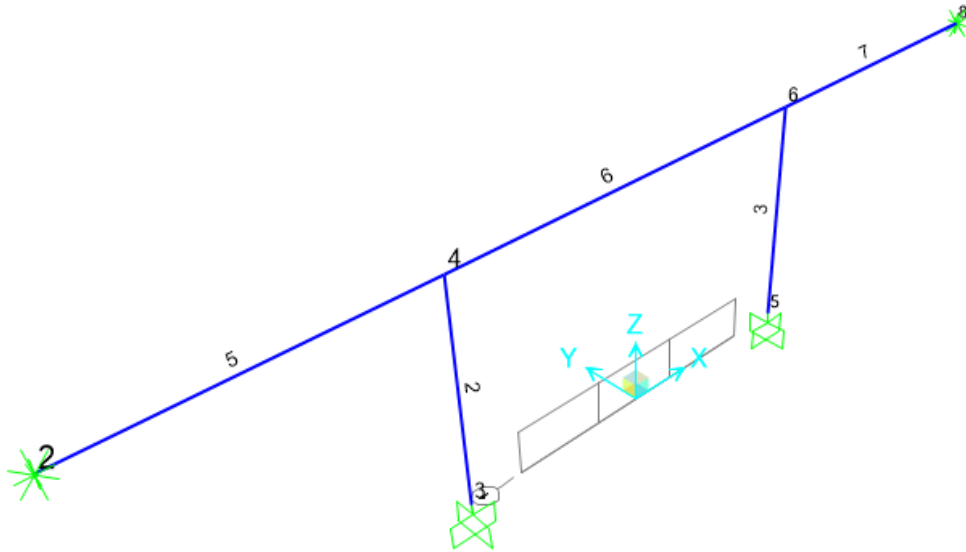
Figure A.5: CSiBridge model using line elements for the example bridge.

- Reference distributed loads of magnitude 1 kip/ft were applied as line loads along the longitudinal direction the superstructure.

- Geometric nonlinear analysis was defined as a load case with the options shown in Figure A.7. The main points are:

  - The Load Case Type (upper right of Figure A.7) should be "Multi-step Static".

  - The Analysis Type (just below Load Case Type in Figure A.7) should be set to "Nonlinear".

  - The Geometric Nonlinearity Parameters (lower right of Figure A.7) should be set to "P-Delta plus Large Displacements".

  - The Loads Applied information (middle section of Figure A.7) should refer to the reference load pattern (distributed load on superstructure) and include a maximum scale factor, e.g., 62, meaning the final analysis step will apply 62 times the reference load pattern. Some trial and error may be required in order to determine a suitable scale factor for the analysis.

Figure A.6: Frame property/stiffness modifiers in CSiBridge.

Figure A.7: Options for geometric nonlinear analysis in CSiBridge.

A.4 Moment Magnification Analysis

To apply the moment magnification method, a first order analysis is performed with $w=1$ kip/ft vertical distributed load and no out-of-plumbness. In the first order analysis, the flexural stiffness of the columns is $EI_{eff} = 0.7E_cI_g$, which is achieved by setting the column I_2 and I_3 modifiers to 0.7 in CSiBridge.

The column demands from the first order analysis are:

- Axial force, $P=97.7$ kip

- Bending moment, M_{1b}=-50.3 kip-in, M_{2b}=101 kip-in (double curvature)

These demands are then scaled up via moment magnification for two cases:

- $EI_{eff} = 0.4E_cI_g$ in the moment magnifier equations.

- The EI_{eff} proposed in Eq. (6.1) for the moment magnifier equations, accounting for modified magnifier coefficients as the axial load increases and effects the flexural stiffness. For the columns in this bridge model, the flexural stiffness is $EI_{eff} = 0.52E_cI_g$.
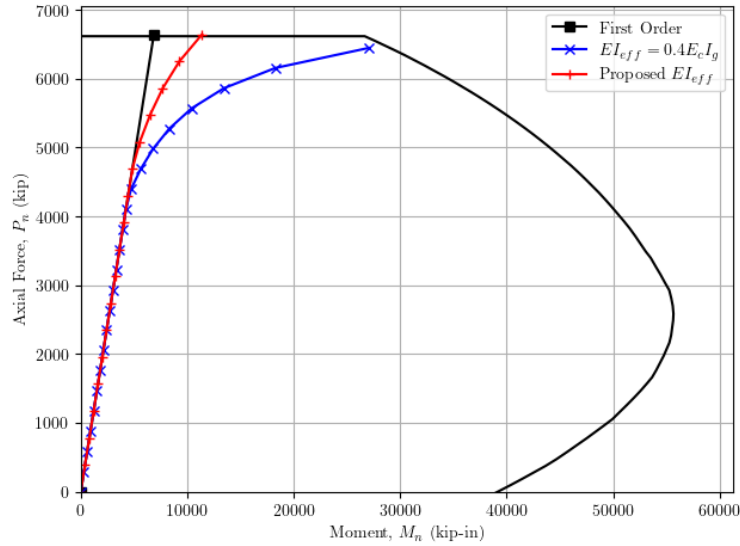
Figure A.8: Moment magnification method with column effective stiffness $EI_{eff} = 0.7E_cI_g$ in first order analysis and $EI_{eff} = 0.4E_cI_g$ and EI_{eff} proposed in Eq. (6.1) in the moment magnification procedure.

With a large effective stiffness, the moment magnification using the proposed EI_{eff} is not as significant as the case of $EI_{eff} = 0.4E_cI_g$. The maximum distributed load predicted by moment magnification is $w=67$ kip/ft using the proposed EI_{eff} and $w=66$ kip/ft using $0.4E_cI_g$.

A.5 Commentary

The foregoing analyses show that the analysis methods proposed in this report can be carried out using CSiBridge. The slenderness of the columns for the chosen bridge model was moderate

($L/D = 15$) and the moment magnifier analysis and all but one GNA case showed the column demands reaching the peak axial strength. For more slender columns, the moment amplification would be more significant. In all GNA and moment magnification cases, the predicted maximum distributed load was less than the "best guess of true behavior" of $w = 78$ kip/ft predicted by GMNIA, indicating these methods gave conservative results for this sample bridge model. While advanced analysis software such as CSiBridge and OpenSees are not required in order to model second order effects in standard bridges where moment magnification does a good job, the analysis methods presented in this appendix may be necessary for bridges with irregular geometries, e.g., due to skewed or curved superstructures.

Bibliography

AASHTO (2017). *AASHTO LRFD Bridge Design Specifications, 8th ed.* American Association of State Highway Officials, Washington, DC.

ACI (2019). *Building Code Requirements for Structural Concrete and Commentary (ACI 318-19).* American Concrete Institute, Farmington Hills, MI.

ACI Committee 209 (1997). Prediction of Creep, Shrinkage, and Temperature Effects in Concrete Structures (ACI 209R-92). Technical report, American Concrete Institute, Farmington Hills, MI.

Adams, A., Galindez, N., Hopper, T., Murphy, T., Ritchie, P., Storlie, V., and Weisman, J. (2019). *Manual for refined analysis in bridge design and evaluation.* United States Federal Highway Administration, Office of Infrastructure, Washington, DC.

Alemdar, B. N. and White, D. W. (2005). Displacement, flexibility, and mixed beam-column finite element formulations for distributed plasticity analysis. *Journal of Structural Engineering*, 131(12):1811–1819.

ASCE (1997). *Effective length and notional load approaches for assessing frame stability: Implications for American steel design.* American Society of Civil Engineers, New York, New York.

Babazadeh, A., Burgueño, R., and Silva, P. F. (2016). Evaluation of the critical plastic region length in slender reinforced concrete bridge columns. *Engineering Structures*, 125:280–293.

Babazadeh, A., Burgueño, R., and Silva, P. F. (2017). Model for the Plastic Region in Slender RC Columns with Nonlinear Moment and Stiffness Profiles. *Journal of Structural Engineering*, 143(9):04017119.

Babazadeh-Naseri, A. (2017). *Nonlinear Inelastic Response of Slender Reinforced Concrete Bridge Columns.* Ph.D. dissertation, Michigan State University, East Lansing, Michigan.

Barrera, A. C., Bonet, J. L., Romero, M. L., and Miguel, P. F. (2011). Experimental tests of slender reinforced concrete columns under combined axial load and lateral force. *Engineering Structures*, 33(12):3676–3689.

Bažant, Z. P., Cedolin, L., and Tabbara, M. R. (1991). New Method of Analysis for Slender Columns. *ACI Structural Journal*, 88(4):391–401.

Breen, J. E. and Ferguson, P. M. (1969). Long cantilever columns subject to lateral forces. In *Long Reinforced Concrete Columns*, pages 137–146, Reston, Virginia. ASCE.

Burgueño, R., Babazadeh, A., Fedak, L. K., and Silva, P. F. (2016). Second-order effects on seismic response of slender bridge columns. *ACI Structural Journal*, 113(4):735–46.

Caltrans (2019). *California Amendments to AASHTO LRFD Bridge Design Specifications – 8th edition*. State of California, Department of Transportation, Sacramento, California.

Caltrans (2022). Structural modeling and analysis. In *Bridge Design Practice*, chapter 4. California Department of Transportation, Sacramento, California.

CEN (2004). *Eurocode 2: Design of concrete structures – Part 1-1: General rules and rules for buildings*. European Committee for Standardization, Brussels, Belgium.

CEN (2005). *Eurocode 2: Design of concrete structures – Part 2: Concrete bridges - Design and detailing rules*. European Committee for Standardization, Brussels, Belgium.

Chang, G. A. and Mander, J. B. (1994). Seismic energy based fatigue damage analysis of bridge columns: Part 1–evaluation of seismic capacity. Technical Report NCEER-94-0006, National Center for Earthquake Engineering Research, Department of Civil Engineering, State University of New York at Buffalo, Buffalo, New York.

Chang, W. F. and Ferguson, P. M. (1963). Long-hinged reinforced concrete columns. *Journal Proceedings*, 60:1–26.

Chuang, P. H. and Kong, F. K. (1997). Large-scale tests on slender, reinforced concrete columns. *Structural Engineer*, 75(23):410–16.

Claeson, C. and Gylltoft, K. (1998). Slender high-strength concrete columns subjected to eccentric loading. *Journal of Structural Engineering*, 124(3):233–240.

Claeson, C. and Gylltoft, K. (2000). Slender concrete columns subjected to sustained and short-term eccentric loading. *Structural Journal*, 97(1):45–52.

Cranmer, M. (2023). Interpretable Machine Learning for Science with PySR and SymbolicRegression.jl. (arXiv:2305.01582).

Crisfield, M. (1991). *Non-linear Finite Element Analysis of Solids and Structures, Volume 1*. Wiley, Chichester, UK.

Dracos, A. (1982). *Long Slender Reinforced Concrete Columns*. PhD Thesis, University of Bradford, Bradford, England.

Drysdale, R. G. and Huggins, M. W. (1971). Sustained biaxial load on slender concrete columns. *Journal of the Structural Division*, 97(5):1423–1443.

fib (2013). *fib Model Code for Concrete Structures 2010*. Wiley, Lausanne.

Foster, S. J. and Attard, M. M. (1997). Experimental tests on eccentrically loaded high strength concrete columns. *Structural Journal*, 94(3):295–303.

Germain, O. and Espion, B. (2005). Slender high-strength RC columns under eccentric compression. *Magazine of Concrete Research*, 57(6):361–370.

Geschwindner, L. F., Liu, J., and Carter, C. J. (2017). *Unified Design of Steel Structures*. John Wiley & Sons, New York City, New York.

Goel, R., Kumar, R., and Paul, D. K. (2007). Comparative Study of Various Creep and Shrinkage Prediction Models for Concrete. *Journal of Materials in Civil Engineering*, 19(3):249–260.

Goyal, B. B. and Jackson, N. (1971). Slender concrete columns under sustained load. *Journal of the structural division*, 97(11):2729–2750.

Green, R. and Breen, J. E. (1969). Eccentrically loaded concrete columns under sustained load. *Journal Proceedings*, 66:866–874.

Hjelmstad, K. D. (2005). *Fundamentals of Structural Mechanics*. Springer, New York City, New York.

Hjelmstad, K. D. and Taciroglu, E. (2003). Mixed variational methods for finite element analysis of geometrically non-linear, inelastic Bernoulli-Euler beams. *Communications in Numerical Methods in Engineering*, 19:809–832.

Hsu, C.-T., Hsu, L. S. M., and Tsao, W.-H. (1995). Biaxially loaded slender high-strength reinforced concrete columns with and without steel fibres. *Magazine of concrete Research*, 47(173):299–310.

Hung, C.-C., Yuen, T. Y., Mosalam, K. M., et al. (2024). Full-scale cyclic testing of slender rc columns bent in double curvature under high axial load. *Journal of Building Engineering*, 82:108186.

Ibrahim, H. H. and MacGregor, J. G. (1996). Flexural behavior of laterally reinforced high-strength concrete sections. *Structural Journal*, 93(6):674–684.

Iwai, S., Minami, K., and Wakabayashi, M. (1986). Stability of slender reinforced concrete columns subjected to biaxially eccentric loads. *Bulletin of the disaster prevention research institute*, 36(3-4):137–157.

Jenkins, R. W. and Frosch, R. J. (2015). Improved Procedures for the Design of Slender Structural Concrete Columns. CRC Report 67, Purdue University, West Lafayette, Indiana.

Katsaras, C. P., Panagiotakos, T. B., and Kolias, B. (2009). Effect of torsional stiffness of prestressed concrete box girders and uplift of abutment bearings on seismic performance of bridges. *Bulletin of Earthquake Engineering*, 7(2):363–375.

Kent, D. C. and Park, R. (1971). Flexural members with confined concrete. *Journal of the Structural Division*, 97(7):1969–1990.

Khalil, N., Cusens, A., and Parker, M. (2001). Tests on slender reinforced concrete columns. *Structural Engineer*, 79:21–30.

Khuntia, M. and Ghosh, S. K. (2004). Flexural Stiffness of Reinforced Concrete Columns and Beams: Analytical Approach. *ACI Structural Journal*, 101(3):351–363.

Kim, J.-K. and Lee, S.-S. (2000). The behavior of reinforced concrete columns subjected to axial force and biaxial bending. *Engineering Structures*, 22(11):1518–1528.

Kim, J.-K. and Yang, J.-K. (1995). Buckling behaviour of slender high-strength concrete columns. *Engineering structures*, 17(1):39–51.

Knaack, A. M. and Kurama, Y. C. (2018). Modeling Time-Dependent Deformations: Application for Reinforced Concrete Beams with Recycled Concrete Aggregates. *Structural Journal*, 115(1):175–190.

Kostic, S. M. and Filippou, F. C. (2012). Section discretization of fiber beam-column elements for cyclic inelastic response. *Journal of Structural Engineering*, 138(5):592–601.

Lee, J.-H. and Son, H.-S. (2000). Failure and strength of high-strength concrete columns subjected to eccentric loads. *ACI Structural Journal*, 97(1):75–85.

Lloyd, N. A. and Rangan, B. V. (1996). Studies on high-strength concrete columns under eccentric compression. *Structural Journal*, 93(6):631–638.

MacGregor, J. G. and Barter, S. L. (1966). Long eccentrically loaded concrete columns bent in double curvature. *Special Publication*, 13:139–156.

Mander, J. B., Priestley, M. J. N., and Park, R. (1988). Theoretical Stress-Strain Model for Confined Concrete. *Journal of Structural Engineering*, 114(8):1804–1826.

Martin, I. and Olivieri, E. (1966). Test of slender reinforced concrete columns bent in double curvature. *Special Publication*, 13:121–138.

Mavichak, V. and Furlong, R. W. (1976). *Strength and Stiffness of Reinforced Concrete Columns under Biaxial Bending*. Center for Highway Research, The University of Texas at Austin, Austin, Texas.

McKenna, F., Scott, M. H., and Fenves, G. L. (2010). Nonlinear finite-element analysis software architecture using object composition. *Journal of Computing in Civil Engineering*, 24(1):95–107.

Mirza, S. A. (1990). Flexural Stiffness of Rectangular Reinforced Concrete Columns. *ACI Structural Journal*, 87(4):425–435.

Mirza, S. A. and MacGregor, J. G. (1989). Slenderness and strength reliability of reinforced concrete columns. *ACI Structural Journal*, 86(4):428–438.

Neuenhofer, A. and Filippou, F. C. (1998). Geometrically nonlinear flexibility-based frame finite element. *Journal of Structural Engineering*, 124(6):704–711.

Pallarés, L., Bonet, J. L., Miguel, P. F., and Prada, M. F. (2008). Experimental research on high strength concrete slender columns subjected to compression and biaxial bending forces. *Engineering Structures*, 30(7):1879–1894.

Pancholi, V. R. (1977). *The Instability of Slender Reinforced Concrete Columns. A Buckling Study of Very Slender Reinforced Concrete Columns between the Slenderness Ratios of 30 and 79 Including Essential Creep Investigations, and Leading to Design Recommendations*. PhD thesis, University of Bradford, Bradford, England.

Ramamurthy, L. N. (1966). Investigation of the ultimate strength of square and rectangular columns under biaxially eccentric loads. *Special Publication*, 13:263–298.

Reineck, K.-H., Kuchma, D. A., Kim, K. S., and Marx, S. (2003). Shear database for reinforced concrete members without shear reinforcement. *Structural Journal*, 100(2):240–249.

Saenz, L. P. and Martin, I. (1963). Test of reinforced concrete columns with high slenderness ratios. *ACI Journal Proceedings*, 60:589–616.

Sarker, P. K., Adolphus, S., Patterson, S., and Rangan, B. V. (2001). High-strength concrete columns under biaxial bending. *Special Publication*, 200:217–234.

Sarker, P. K. and Rangan, B. V. (2003). Reinforced concrete columns under unequal load eccentricities. *Structural Journal*, 100(4):519–528.

Schofield, D. (1983). *Slender Reinforced Concrete Columns under Load and Movement*. PhD Thesis, University of Bradford, Bradford, England.

Taso, W. H. and Hsu, C.-T. (1994). Behaviour of biaxially loaded square and L-shaped slender reinforced concrete columns. *Magazine of Concrete Research*, 46(169):257–267.

Tavio and Teng, S. (2004). Effective Torsional Rigidity of Reinforced Concrete Members. *ACI Structural Journal*, 101(2):252–260.

Tošić, N., Knaack, A., and Kurama, Y. (2020). Supporting documentation for time-dependent concrete material models in OpenSees. *Mendeley Data Set*.

Viest, I. M., Elstner, R. C., and Hognestad, E. (1956). Sustained load strength of eccentrically loaded short reinforced concrete columns. *Journal Proceedings*, 52:727–755.

Wang, G. G. and Hsu, C.-T. T. (1992). Complete Biaxial Load-Deformation Behavior or RC Columns. *Journal of Structural Engineering*, 118(9):2590–2609.

Wu, H. and Huggins, M. W. (1977). Size and Sustained Load Effects in Concrete Columns. *Journal of the Structural Division*, 103(3):493–506.

Zhu, M., McKenna, F., and Scott, M. H. (2018). OpenSeesPy: Python library for the OpenSees finite element framework. *SoftwareX*, 7:6–11.